Coupling of numerical methods for the forward problem in Magneto- and Electro-Encephalography

Emmanuel Olivi

UNIVERSITY OF NICE - SOPHIA ANTIPOLIS

DOCTORAL SCHOOL STIC

SCIENCES ET TECHNOLOGIES DE L'INFORMATION
ET DE LA COMMUNICATION

P H D T H E S I S

to obtain the title of

PhD of Sciences

of the University of Nice - Sophia Antipolis

Specialty : Control, Signal and Image Processing

Defended by

Emmanuel Olivi

Coupling of numerical methods for the forward problem in Magneto- and Electro-EncephaloGraphy

prepared at INRIA Sophia Antipolis, Athena Project Team

defended on December, 14th 2011

Advisor :	Maureen Clerc	-	INRIA, Sophia Antipolis
Reviewers :	Abderrahmane Bendali	-	INSA, Toulouse
	Marc Bonnet	-	ENSTA, Paris
Examiners :	Christian Bénar	-	INSERM, Marseille
	Olivier Bertrand	-	INSERM, Lyon
	Stéphane Lanteri	-	INRIA, Sophia Antipolis
Invited member:	Hervé Delingette	-	INRIA, Sophia Antipolis

UNIVERSITÉ DE NICE - SOPHIA ANTIPOLIS

ÉCOLE DOCTORALE STIC
SCIENCES ET TECHNOLOGIES DE L'INFORMATION
ET DE LA COMMUNICATION

T H È S E DE D O C T O R A T

pour obtenir le titre de

Docteur en Sciences

de l'Université de Nice - Sophia Antipolis
Spécialté : Automatique, Traitement du signal et des images

défendue par

Emmanuel Olivi

Couplage de méthodes numériques pour le problème direct en Magnéto- et Électro-Encéphalographie

préparée à l'INRIA Sophia Antipolis

soutenue le 14 décembre 2011

Directeur :	Maureen Clerc	-	INRIA, Sophia Antipolis
Rapporteurs :	Abderrahmane Bendali	-	INSA, Toulouse
	Marc Bonnet	-	ENSTA, Paris
Examinateurs :	Christian Bénar	-	INSERM, Marseille
	Olivier Bertrand	-	INSERM, Lyon
	Stéphane Lanteri	-	INRIA, Sophia Antipolis
Invités :	Hervé Delingette	-	INRIA, Sophia Antipolis

Remerciements

INRIA Quelle joie de m'être trouvé pendant 3 années dans ce laboratoire avec cette thèse. Après une première expérience en 2007 où j'avais pu faire un stage de 2 mois au sein de l'équipe Odyssée, je souhaitais vivement y revenir en thèse pour la qualité de l'institut et la motivation des personnes y travaillant. Plus particulièrement l'équipe Odyssée et ses thèmes de recherches motivants.

Encadrants Un grand merci à ma directrice Maureen Clerc, tout d'abord pour m'avoir choisi; et surtout pour avoir su me guider tout au long de cette thèse sans rien imposer et toujours de manière très constructive et efficace. La qualité du travail qu'elle accomplit au sein de l'équipe m'a beaucoup impressionné.
Je remercie également Théodore Papadopoulo, avec qui j'ai passé beaucoup de temps et avec qui il était facile de partager et obtenir des éclaircissements tant au niveau de la programmation que sur d'autres idées bien plus diverses: ma thèse, la vision 3D, l'astrophysique, ...
Merci à notre directeur, de l'équipe-projet Athena, Rachid Deriche qui permet un bon environnement de travail pour ses étudiants, et stimule nos interactions par des réunions ainsi que par des réceptions toujours appréciées au bord de sa piscine.
Enfin merci à Marie-Cécile Lafont et Claire Sénica pour m'avoir soutenu sur le plan administratif dès mon arrivée, ainsi que pour leur bonne compagnie au cours de ces années.

Collaborateurs Mariette Yvinec que je connaissais de part mon premier stage, puisqu'elle était mon encadrante, m'a maintes fois aidé et débloqué concernant CGAL le logiciel de maillage de l'équipe Geometrica. Merci également pour sa bonne humeur contagieuse.
Jean-Michel Badier, responsable MEEG à l'hôpital de la Timone de Marseille, m'a invité a utilisé ses données, notamment IRM, CT-scan et EEG. Je l'en remercie, même si je n'ai pu faire de ces données que de jolies images que l'on voit dans l'introduction car je n'ai pas pu obtenir de bonnes segmentations de l'IRM de sa patiente. Je remercie également Christian Bénar qui m'avait parlé de ses travaux sur les inhomogénéités du crâne en BEM.
Enfin je remercie Martine Olivi avec qui j'ai pu faire de l'enseignement.

Athena Team Une belle pensée à tous mes nombreux collègues du labo, avec qui on a passé de très bons moments au sein et en dehors de l'INRIA. Cette convivialité qui est indispensable à une santé mentale correcte au cours de la thèse a parfois donné lieu à une profonde amitié; merci à vous: Emilien, Alexandre, Emmanuel, Romain, Aurobrata, Sylvain, James, Nicolas, Hassan, Jaime, Diego, Vivien, ... Tout particulièrement à Joan et Anne-Charlotte.

Amitiés Merci à ma famille pour leur présence vitale, et mes amis pour leur soutien. Pour la qualité de son air pur, merci au parapente et à tous mes amis ailés du club de la Colmiane et celui de St Vallier, notamment Axel, mais également aux constructeurs de ma voile qui font du bon boulot.

Membres du jury Pour l'attention qu'ils ont portés à la lecture de cette thèse et les rapports fournis, merci à mes deux rapporteurs Marc Bonnet, et mon ancien professeur Abderrahmane Bendali. Enfin merci aux autres membres du jury, Olivier Bertrand, Christian Bénar, Stéphane Lantéri et Hervé Delingette pour leur présence ainsi que pour les précédentes interactions.

Overview

Résumé

L'électro- et la magnéto-encéphalographie sont deux techniques très utiles pour observer l'activité électrique du cerveau de par leur résolution temporelle et leur caractère non invasif. Les mesures sont faites sur la surface extérieure de la tête (électrodes pour l'EEG et magnétomètres pour la MEG); afin de retrouver les sources responsables du signal mesuré, un problème inverse de localisation doit être résolu. Celui-ci requiert une bonne résolution du problème direct, ce qui demande une bonne modélisation des tissus de la tête, ainsi qu'une représentation fidèle de ce modèle électro-physiologique par une méthode numérique comme la FEM ou la BEM. Dans cette thèse, nous nous intéressons au choix critique d'un modèle et de sa représentation par une méthode numérique notamment pour prendre en compte l'inhomogénéité de la conductivité du crâne et celle de la matière blanche qui est proche des sources. Après avoir mis en évidence les avantages et inconvénients des méthodes courantes, nous exposons une méthode duale de résolution du problème direct: c'est la méthode adjointe applicable quel que soit la méthode numérique choisie. Puis en utilisant une approche de décomposition de domaine nous formulons plusieurs méthodes de couplage de méthodes numériques visant à tirer parti de leurs avantages dans des sous domaines. Cela permet de coupler la BEM avec la FEM, et implique de nombreux aspects intéressants notamment pour une bonne prise en compte du crâne. Finalement, nous proposons une nouvelle méthode permettant de traiter des conductivités localement anisotropes ou inhomogènes avec la BEM.

Abstract

Electro- and Magneto-Encephalography are precious tools for studying brain activity, notably due to their time resolution and their non invasive nature. Acquisitions are done on the exterior of the head (scalp electrodes for EEG, and magnetometers for MEG); in order to recover the sources responsible of the measured signal, an inverse problem must be solved, for which accurate solutions of the forward problem must be available. This requires a good modeling of the head tissues, and an appropriate representation of this electrophysiological model within numerical methods such as the BEM or FEM. In this thesis we focus on this dual problem of modeling and numerical resolution, notably to handle the skull region which must often be considered anisotropic or highly inhomogeneous in clinical applications, and for the white matter anisotropy which surrounds the sources in the brain. In this thesis we first see the common numerical solvers for solving the forward problem, and expose their strengths and weaknesses. Then, a dual point of view for solving the forward problem using any numerical method is exposed; which is the adjoint method of our

forward problem. Its application within a BEM framework is given. Later using a domain decomposition (DD) framework, we present different coupling procedures of the main methods BEM and FEM, in order to get both methods advantages regarding the resolution of the forward problem (notably for handling the skull). This is done within a DD framework, which appears to be interesting in many points. Finally, we propose a new method for dealing with locally anisotropic or inhomogeneous conductivities using a BEM.

Contributions

The main contributions of this thesis are the following:

in Chapter 2: Implementation of the adjoint method for solving, in BEM, the EEG and MEG forward problem for point-like sensors.

in Chapter 3-4-5: Studying coupling algorithms notably Neumann-Dirichlet. Implementation of a coupling library, which allows for many different couplings, between BEM and BEM, BEM with tetrahedral FEM, and also BEM with implicit FEM (Cartesian grid).

in Chapter 6: The handling of perturbations in the conductivity profile within a BEM framework.

others: Implementation of functionalities for the BEM such as: internal operators for any sub-domains, implementation of sources within any sub-domains. For the tetrahedral FEM: handling of anisotropic conductivities such as the one of the skull, or the one of a white matter fiber. Meshing tools: using CGAL for generating surfacic meshes out of segmented MRI, or re-meshing of very fined mesh. Volumic meshes generation with special features such as multi-compartment model, or approximating at boundaries a given surfacic mesh, or matching exactly this surfacic mesh (sharp edges).

Publications

Conferences

Emmanuel Olivi, Maureen Clerc and Théodore Papadopoulo. 'Domain decomposition for coupling finite and boundary element methods in EEG.' In Proceedings of Biomag, 2010. Biomag 2010 Fellowship winner. [Olivi et al., 2010a]

Emmanuel Olivi, Maureen Clerc and Théodore Papadopoulo. 'Domain decomposition for coupling finite and boundary element methods with non-matching grids in Electro-Encephalography.' In Proceedings of ECCM, 2010. [Olivi et al., 2010b]

Emmanuel Olivi, Maureen Clerc and Théodore Papadopoulo. 'Handling white-matter anisotropy in BEM for the EEG forward problem.' In Proceedings of ISBI, 2011. [Olivi et al., 2011a]

Emmanuel Olivi, Alexandre Gramfort, Théodore Papadopoulo and Maureen Clerc. 'Adjoint method for lead-fields computation in MEEG.' Human Brain Mapping (HBM), jun 2011. [Olivi et al., 2011b]

Maureen Clerc, Alexandre Gramfort, Emmanuel Olivi and Théodore Papadopoulo. 'The symmetric BEM: bringing in more variables for better accuracy.' In Proceedings of Biomag, 2010. [Clerc et al., 2010]

Maureen Clerc, Jean-Michel Badier, Emmanuel Olivi, Alexandre Gramfort and Théodore Papadopoulo. 'OpenMEEG for calibrating the conductivity of nested compartment models.' In EIT conference, 2011. [Clerc et al., 2011]

Journals

Alexandre Gramfort, Théodore Papadopoulo, Emmanuel Olivi and Maureen Clerc. 'OpenMEEG: opensource software for quasistatic bioelectromagnetics. ' BioMedical Engineering OnLine, 9(45), sep 2010.[Gramfort et al., 2010]

Alexandre Gramfort, Théodore Papadopoulo, Emmanuel Olivi and Maureen Clerc. 'Forward Field Computation with OpenMEEG.' Computational Intelligence and Neuroscience 2011. [Gramfort et al., 2011]

Emmanuel Olivi, Théodore Papadopoulo, Mariette Yvinec and Maureen Clerc. 'Coupling numerical methods in the EEG forward problem via Domain Decomposition'. Submitted. 2011

Reports

Emmanuel Olivi, Maureen Clerc, Mariette Yvinec and Théodore Papadopoulo. 'Quantitative comparisons of forward problems in MEEG.' 2007 [Olivi et al., 2007] (internship report done one year before the begining of the PhD thesis)

Notations and units:

Mathematical notations:

$\mathbf{r}$ denotes a vector in $\mathbb{R}^3$.

$f : \mathbf{r} \in \mathbb{R}^3 \mapsto f(\mathbf{r}) \in \mathbb{R}$ a scalar function.

$\mathbf{F} : \mathbf{r} \in \mathbb{R}^3 \mapsto \mathbf{F}(\mathbf{r}) \in \mathbb{R}^3$ a function returning a vector (*i.e.* a vector field).

$\nabla = \left(\frac{\partial}{\partial x}, \quad \frac{\partial}{\partial y}, \quad \frac{\partial}{\partial z}\right)^T$ 'nabla', a first-order differential operator.

$\Delta = \nabla \cdot \nabla$ the Laplace operator (or Laplacian), a second-order differential operator which can be applied to a scalar or vector field.

∇f denotes the gradient of f.

$\nabla \cdot \mathbf{F}$ denotes the divergence of the vector field $\mathbf{F}$, a scalar function of $\mathbb{R}^3$.

$\nabla \times \mathbf{F}$ denotes the curl of $\mathbf{F}$, a vector field.

$\frac{\partial}{\partial t}$ denotes the (partial-) derivative operator with respect to time.

Ω a compact subset of $\mathbb{R}^3$.

$\partial\Omega$ its (Lipshitz) boundary, and $\bar{\Omega}$ its closure *i.e.* $\bar{\Omega} = \Omega \cup \partial\Omega$.

$\int_\Omega d\mathbf{r}'$ denotes a volumic integral.

$\int_S d\mathbf{s}'$ an integral over the surface S.

$\delta(\mathbf{r}) = \delta_0(\mathbf{r})$ the Dirac distribution centered at 0.

Physical notations:

$V(\mathbf{r})$ the electric potential at point $\mathbf{r}$ (expressed in $[V]$: Volts).

$\mathbf{E}$ the electric field (expressed in $[V.m^{-1}]$).

$\mathbf{B}$ the magnetic field (expressed in $[T]$: Tesla).

ρ the electric charge density $[C.m^{-3}]$.

$\mathbf{J}$ the total current density $[A.m^{-2}]$.

$\mathbf{J}^{\mathrm{p}}$ the primary current source $[A.m^{-2}]$.

constants:

$\mu_0 = 4\pi.10^{-7}$ the magnetic permeability of the vacuum space (expressed in $[V.s.A^{-1}.m^{-1}]$).

$\varepsilon_0 = \frac{1}{\mu_0 \cdot c_0}$ the electrical permittivity of the vacuum space.

Contents

Chapter 1

Introduction française

Au fur et à mesure que l'homme progresse dans sa compréhension de la nature, le cerveau fascine. Sa complexité au niveau structurel est hors de portée de nos compétences techniques actuelles, un ordinateur ne peut rivaliser avec $10^{11} = 100$ milliards de neurones, chacun interagissant avec des milliers de voisins, le tout avec une consommation énergétique faible puisqu'il ne consomme que 25 watts au maximum [Kandel et al., 2000].

Contents

1.1 Contexte

Dans le cerveau se trouvent des cellules qui assurent la transmission de signaux bio-électriques: les neurones. Des charges électriques sont transmises par l'axone, puis le signal est relayée à ses synapses par des molécules qui assurent le lien entre un neurone et ses afférents: un neurotransmetteur (voir Fig.1.1).

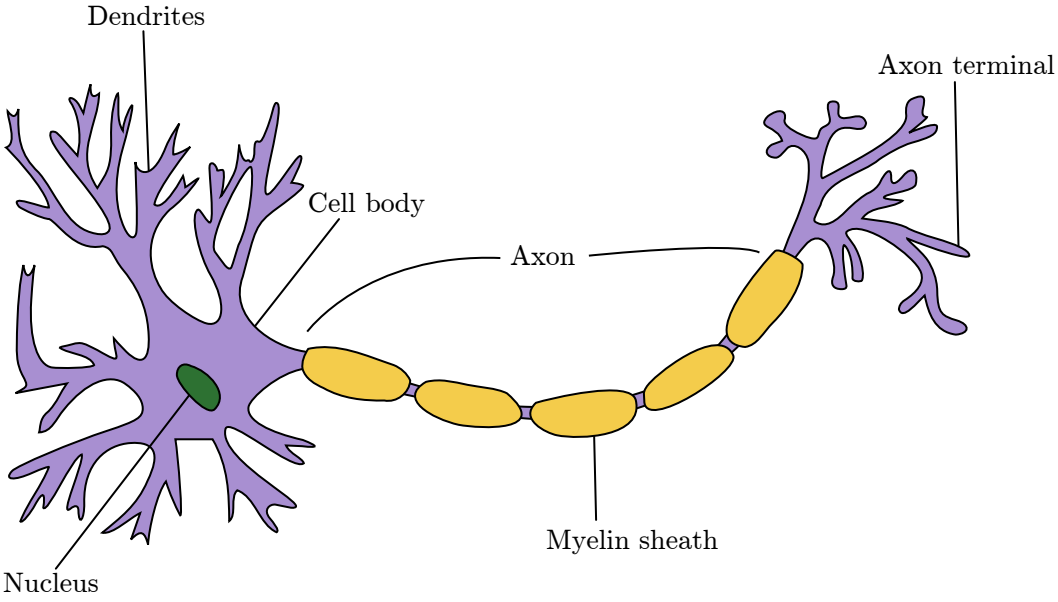

Figure 1.1 – *Schéma d'un neurone.*[WIKIPEDIA]

Le cerveau est également composé de cellules gliales encore plus nombreuses que les neurones (10 à 50 fois plus). Même si ces cellules ne transmettent pas directement l'information, elles apportent des nutriments et de l'oxygène aux neurones. De plus, elles produisent de la myéline qui permet aux neurones d'être isolés les uns des autres. Le rôle des cellules gliales n'est pas complètement établi, mais la myéline produite étant blanche baptisa la 'matière blanche', où leur concentration est la plus importante, car cette région contient un grand nombre d'axones contrairement à la matière grise qui elle contient les corps cellulaires des neurones.
Depuis les début de l'odyssée du cerveau, l'homme essaye d'établir différentes relations entre l'organisation cellulaire et des fonctions cognitives. Un des buts majeurs serait la conception d'une carte hautement détaillée du cerveau avec les fonctions cognitives associées.

1.1.1 L'anatomie du cerveau

Le cerveau est l'organe central du système nerveux. Il flotte dans le liquide céphalo-rachidien (LCR) et est entouré du crâne qui le protège de l'extérieur et . Il se

compose de deux hémisphères qui chacun peut être divisé en 4 lobes comme l'indique la figure 1.2. Ces lobes sont séparés par des fissures que tous les individus partagent. On peut en première approximation associer ces lobes avec les fonctions suivantes:

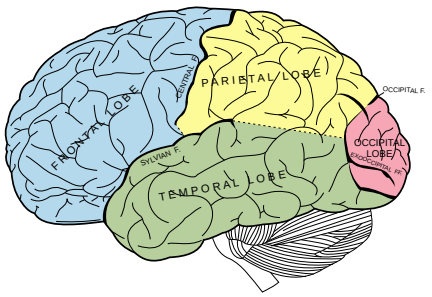

Figure 1.2 – *Coupe sagittale d'un cerveau humain.*[WIKIPEDIA]

le lobe frontal: dont la fonction est l'aptitude à la prise de décision, l'établissement de raisonnements, le siège des émotions; des fonctions cognitives de haut niveau.

le lobe pariétal: intègre les informations sensorielles, également associé à l'orientation, la reconnaissance, le langage.

le lobe temporel: impliqué dans la perception auditive, la sémantique, le langage, la mémoire.

le lobe occipital: dédié à la vision.

La région hachurée (sous le lobe occipital) est le cervelet qui est impliqué dans l'équilibre, la posture, ... Bien qu'il ne génère pas ces mouvements, il les calibre et les rend précis [Ghez and Fahn, 1985]. La partie extérieure du cerveau est nommé le cortex ou matière grise, sur lequel l'on voit des circonvolutions appelés gyrus ou sulci pour respectivement des plis convexes ou concaves. Sous la matière grise qui représente l'interface du cerveau avec le LCR, se trouve la matière blanche composées de faisceaux de fibres (regroupement d'axones myélénisés).

1.1.2 Motivations

Historiquement, on a commencé à établir des relations entre ses différentes régions et l'observation de manifestations extérieures, notamment à la suite de lésions. De telles lésions peuvent, en effet, amener des pertes de mémoire (court termes et long terme), la cécité, ou l'impossibilité de prendre une décision, l'obésité, ... De telles observations ont amené les premiers expérimentateurs à penser que la vision n'était pas simplement le fait des yeux, l'obésité de l'alimentation, ... mais tous contrôlés par le cerveau. D'un autre coté, les maladies neuro-dégénératives comme Alzheimer ou Parkinson, sont causés par la mort de neurones entraînant celles des fonctions

associées, comme la mémoire, la mouvement,....
L'épilepsie quant à elle, est une activité hyper-synchrone neuronale générée par une petite région du cerveau (spécifique à chaque patient). L'étude de telles maladies constitue également une motivation principale.

Mais dans certains cas, souvent rencontrés sur des personnes ayant des troubles du développement, le cerveau fascine par son habilité à stocker de l'information, comme par l'exemple des livres entiers ligne par ligne, ou encore pour ses aptitudes au calcul arithmétique bien plus avancées qu'un individu 'normal'.

Certains pensent qu'en étudiant et comprenant la manière dont est traitée l'information dans le cerveau, la construction d'une intelligence artificielle serait possible. Une autre motivation séduisante consiste à établir une communication du cerveau vers une machine: de l'ICM (Interface Cerveau-Machine). En analysant les signaux générés par le cerveau (comme avec de l'EEG), on peut traduire ces informations en commandes en vue de contrôler un ordinateur. Cette alternative offre un grand espoir aux personnes dans l'incapacité partielle ou totale de communiquer (souffrant de syndrome d'enfermement).

1.1.3 L'imagerie médicale

Les techniques d'imageries médicales visent à produire des images 1D, 2D, 3D ou 3D+temps de parties ou de la totalité du cerveau en vue d'une étude clinique de cet organe. La plupart reposent sur des phénomènes électromagnétiques, d'autres sur la radioactivité, ou les ondes acoustiques. Chacune possède naturellement des avantages et inconvénients, et produit ainsi des images à différentes résolutions spatiale, temporelle ou de différent tissus. À partir de ces données collectées, une image peut être reconstruite. Les techniques de reconstruction sont un champ de recherche propre à chaque modalité d'imagerie.

1.1.3.1 L'imagerie par résonance magnétique: l'IRM

La plus connue des modalités d'imagerie pour observer le cerveau est l'IRM, qui pourvoit les meilleures résolutions de tissus contenant des molécules d'eau (comme les tissus cérébraux). l'IRM est basée sur l'interaction des protons contenus dans les molécules d'eau (proton de l'atome d'hydrogène H) avec un champ magnétique généré par la machine. Ces interactions directement liées aux proportions d'eau dans les tissus, permettent d'en déduire des images tri-dimensionnelles où le contraste représente cette hétérogénéité de la concentration d'eau dans les tissus. En variant le type d'acquisition (champ magnétique et l'impulsion radio-fréquence émise: séquence T1 et T2 par exemple) on obtient des images de contraste différent pour la peau, la graisse, le LCR, le crâne, ... bien que le crâne reste difficilement visible sur une IRM: voir Fig.(1.3).
Le principe de l'IRM a donné lieu à d'autres modalités comme l'IRM fonctionnelle (IRMf) qui permet de mesurer certaines quantités liées à l'activité du cerveau.

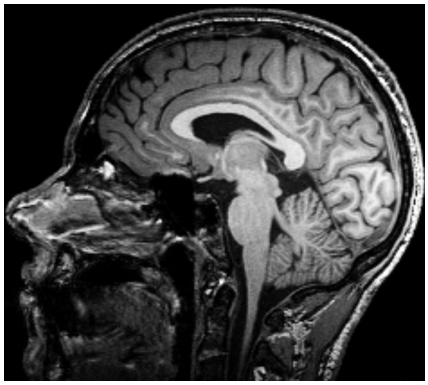

Figure 1.3 – *Coupe sagittale d'une IRM T1.*

Cette modalité sera détaillée section.1.1.4.2.

L'IRM de diffusion (IRMd) mesure quant à elle la diffusion des molécules d'eau dans le cerveau dans des directions spécifiées. Cette diffusion serait isotrope dans un milieu homogène; l'anisotropie de la diffusion reflète ainsi les faisceaux de fibres présents notamment dans la matière blanche. Cette anisotropie est mise en évidence en calculant une valeur scalaire l'anisotropie fractionnaire (la FA:fractional anisotropy) en chaque voxel. En intégrant plusieurs images obtenues dans des directions différentes, on peut construire un modèle de diffusion en chaque voxel, le plus simple étant un modèle de tenseur (DTI pour Diffusion Tensor Imaging). Le modèle de tenseur étant symétrique, il n'a que six inconnues et peut être représenté par une ellipsoïde. HARDI (pour High-Angular-Resolution Diffusion Tensor Imaging) est une représentation plus fine permettant l'observation de croisement de fibres. La Fig.(1.4) représente la FA dans la direction principale (le vecteur propre du tenseur de diffusion), où le codage couleur en RGB encode les composantes x-y-z du vecteur propre. Le tenseur de diffusion en chaque voxel de l'image 3D est d'un grand intérêt pour étudier les connectivités au sein du cerveau. En effet, à partir de l'expression du tenseur de diffusion (DTI), on peut estimer les fibres qui suivent les directions principales de ces ellipsoïdes. Manipulant ces tenseurs de diffusion a permis l'établissement d'une nouvelle technique d'imagerie, la tractographie [Mori et al., 1999]-[Basser et al., 2000] (voir Fig.(2.5)). On peut également reconstruire une tractographie à partir de représentations plus fine de la diffusion en utilisant HARDI (High Angular Resolution Diffusion Imaging) [Descoteaux et al., 2009].

1.1.3.2 Autres techniques d'imagerie

Comme le crâne est composé de peu de molécules d'eau, il est difficile de le reconstruire à partir d'IRM. D'un autre côté, les rayons-X interagissent bien avec les os. Ces ondes électromagnétiques furent découvertes en 1895 par Wilhelm Röntgen

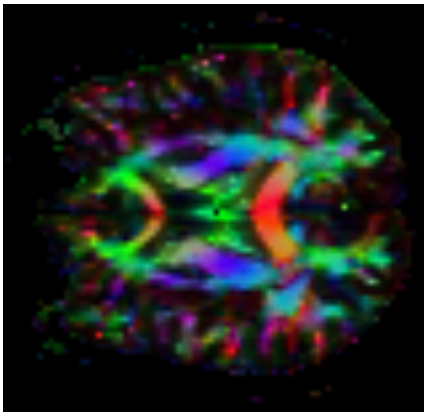

Figure 1.4 – *Coupe axiale d'une DWI colorée en FA.*

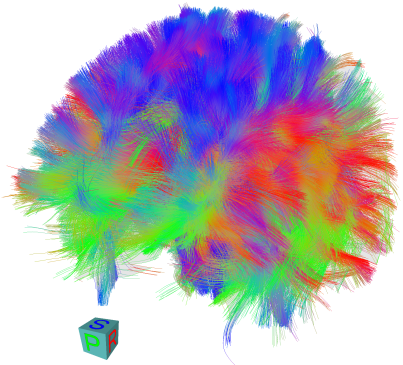

Figure 1.5 – *Une vue 3D d'une tractographie.*

et sont considérées comme la première technique d'imagerie. Même si les rayons-X sont à première vue inoffensifs pour l'homme, une exposition longue ou répétée peut entraîner des conséquences négatives sur les corps cellulaires. Sur la Fig.(1.6) est affichée un CT-scan du crâne, où les artefacts visibles sont dû à certains composants de la machine.

Les ultra-sons ne pénétrant pas dans le cerveau à cause du crâne, l'imagerie du cerveau par ultra-sons est impossible. Néanmoins pour des tissus plus souples, les muscles, liquides, ... les ultra-sons peuvent fournir de belles images en 2D+temps (Échographie)

Ces techniques permettent l'observation anatomique du cerveau et non son étude fonctionnelle.

1.1.4 Observer l'activité du cerveau

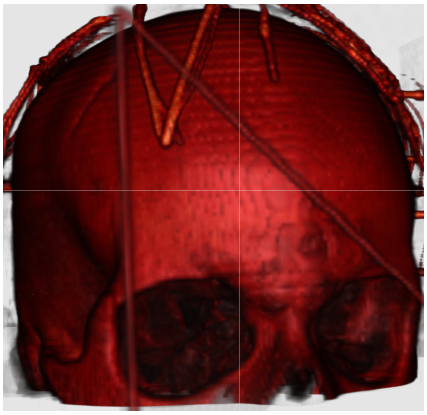

Figure 1.6 – *Computed tomography.*

1.1.4.1 Techniques invasives

La Tomographie à Émission de Positron (TEP) requiert l'injection d'une substance radioactive et permet de reconstruire une image en mesurant la désintégration radioactive de cet élément introduit et diffusé dans une région d'intérêt. En TEP, le traceur radioactif injecté dans le corps se concentre sur le glucose qui est différemment consommé dans les différentes région du cerveau. Ce traceur émet des positrons que le système mesure indirectement grâce aux paires de rayons-gamma produits lorsque le positron s'annule avec l'électron: $e^- + e^+ \longrightarrow \gamma + \gamma$. Une image en 3D peut ainsi être reconstruite grâce à des techniques de reconstruction par tomographie: une coupe d'une telle image est affichée en Fig.(1.7). Les zones rouges correspondent à une accumulation de radioactivité, ce qui trahit l'activité du cerveau de par sa consommation en glucose.

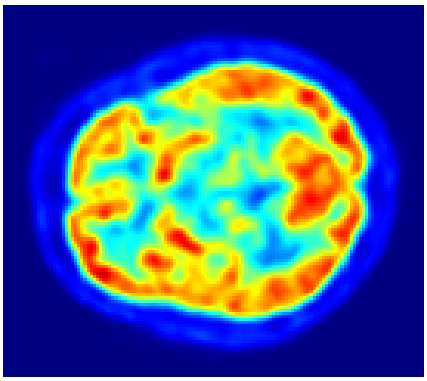

Figure 1.7 – *Scan TEP d'une tête humaine.*[WIKIPEDIA]

L'ElectroCorticoGraphie (EcoG) est une technique très proche de l'électroencéphalographie, pour laquelle les électrodes sont directement placées sur une grille disposée sur la surface du cortex[1] afin de mesurer l'activité électrique de la région alentour aux électrodes.

Encore plus profondément dans le cerveau, la stéréo Encéphalographie (sEEG) permet d'obtenir le potentiel électrique sur des électrodes placées sur un tige implanté en profondeur dans le cortex.

Ces deux techniques requièrent donc un trou dans le crâne pour y placer les électrodes, bien que la craniotomie requise pour la sEEG soit plus réduite. Ces techniques sont utilisées pour les patients atteint d'épilepsie pharmaco-résistante. Le signal obtenu est traité afin de localiser la zone epileptogène pendant une crise. Dans certains cas cette zone peut être enlevée et permet une guérison complète de la maladie. Au préalable, on doit avoir une idée sur la zone a-priori responsable afin d'insérer les électrodes non loin de cette zone, car elles ne peuvent qu'inférer localement l'activité du cerveau.

1.1.4.2 Techniques non-invasives

L'IRM fonctionnelle (IRMf) L'IRM fonctionnelle est une séquence spéciale d'IRM qui permet de mesurer la réponse hémodynamique locale. Cette activité est reliée à l'activité du cerveau. L'oxygène est délivrée aux neurones via l'oxyhémoglobine qui est une molécule diamagnétique contenue dans le sang.

À leur activation, les neurones transforment l'oxyhémoglobine en désoxyhémoglobine qui est elle paramagnétique. D'un autre côté le débit sanguin local augmente également mais de manière plus importante, ce qui entraîne une diminution relative de la desoxyhémoglobine. Cette différence de concentration relative produit des changements observables par la résonance magnétique: c'est le signal BOLD (Blood-Oxygen-Level Dependent).

Ces changements ne sont pas instantanés, ce qui limite la résolution temporelle de l'IRMf à quelques secondes. IRMf est attractive de par sa résolution spatiale (voir Fig.(1.8)), qui est de l'ordre de $2-3$ mm et indépendante de la localisation de la source, ce qui permet l'observation de phénomènes profonds dans le cerveau ce qui n'est pas possible en EEG.

Enfin, ajoutons que les résultats obtenus avec l'IRMf restent difficiles à interpréter car la relation entre le signal BOLD mesuré et l'activité des neurones est seulement une corrélation et non une implication.

L'ÉlectroEncéphalographie (EEG) et la MagnétoEncéphalographie (MEG) sont deux modalités hautement non-invasives puisque passives: elles n'appliquent aucun champ externe mais visent à capter le faible champ électromagnétique généré par l'activité neuronale. Seules les sources superficielles du cerveau sont mesurables *càd* les sources non loin de la surface du cortex. L'EEG et la MEG permettent

[1] soit en-dessus de la dure mère (épidurale) ou en-dessous (subdurale), mais dans tout les cas, sous le crâne.

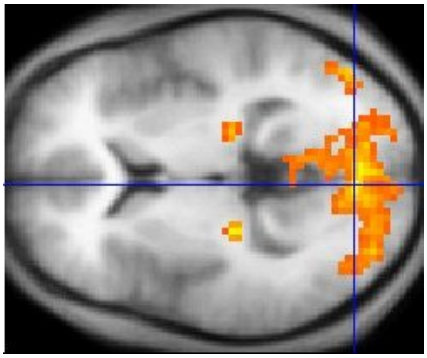

Figure 1.8 – *IRMf statistique (orange) superposée à une coupe d'IRMa.*[WIKIPEDIA]

toutes deux d'obtenir une très bonne résolution temporelle (1ms dépendant de la fréquence échantillonnage). Quant à la résolution spatiale, après une localisation de sources, l'erreur estimée est de l'ordre du centimètre.

Ajoutons également que la MEG ne peut détecter que très faiblement les sources radiales à la surface interne du crâne, tandis que l'EEG n'a pas cette limitation. Ces modalités seront plus en détails exposées sec.(1.2.2).

La Fig.(1.9) présente les différentes résolutions spatiales et temporelles des modalités présentées ci-dessus. Les résolutions spatiales de l'EEG,MEG,EcoG,sEEG sont des estimations de l'erreur spatiale commise en localisation de sources (*càd* une fois le signal acquis); puisque rappelons-le ces modalités ne fournissent pas une image 3D comme l'IRMf, mais un signal aux électrodes qui est traité afin de recouvrer les sources responsables de ce signal. Ajoutons également que l'abscisse des temps est logarithmique.

Enfin, cette figure ne présente pas les différentes sensibilités des modalités à la position (ou orientation) des sources, par exemple la MEG ne voit pas les sources radiales, l'EEG ne permet pas de voir les sources profondes, et l'IRMf n'apporte qu'une corrélation avec l'activité électrique, enfin l'EcoG-sEEG ont un champ de vision très local.

1.2 EEG-MEG: concept physique et applications courantes.

1.2.1 Les générateurs électromagnétiques

1.2.1.1 Comportement électrique d'un seul neurone

Comme expliqué en sec.(1.1), les neurones transmettent des signaux. Le signal se propageant le long de l'axone s'appelle un Potentiel d'Action (PA). Un neurone reçoit de multiple signaux (des potentiels d'action) en entrée de la part de ses neurones voisins qui ont leurs dendrites connectées à ses synapses ou directement sur le soma. À partir de ces entrées, le neurones va émettre ou non un potentiel d'action,

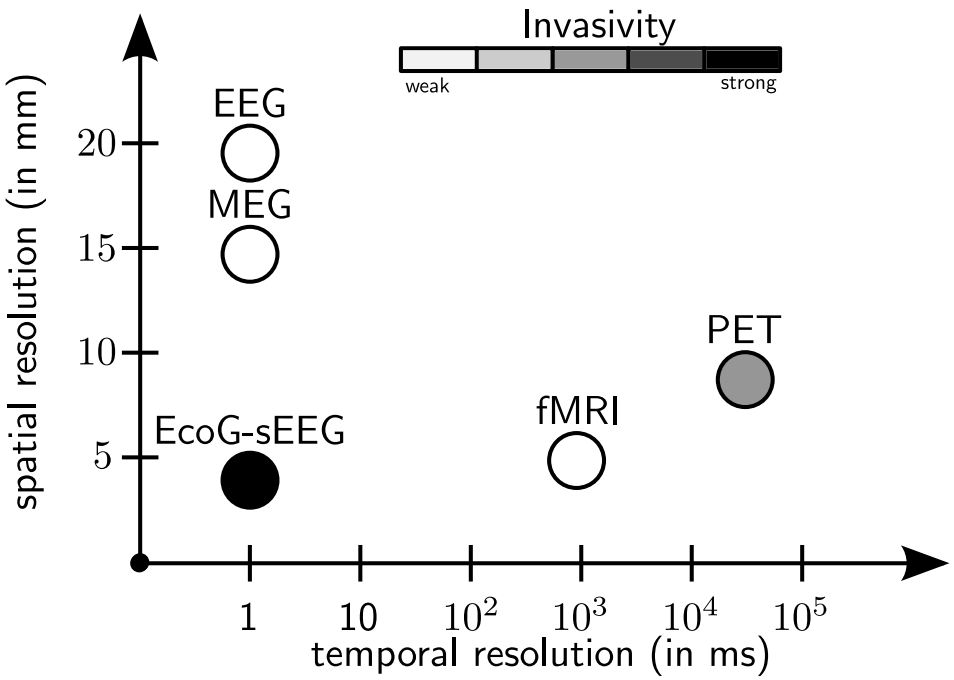

Figure 1.9 – *Résolutions spatiale et temporelle pour différentes modalités d'imagerie fonctionnelle du cerveau. La noirceur du cercle donne une idée de l'invasivité de la modalité.*

càd transmettre l'information le long de l'axone à d'autres neurones. La plupart des liaisons inter-neuronales sont biochimiques (relaxation d'un neurotransmetteur), même si certains sont purement électriques.

Le Potentiel Post-Synaptique : (PPS) Quand un potentiel d'action atteint une terminaison de l'axone, celui-ci relâche des neurotransmetteurs, et ces molécules voyagent jusqu'à atteindre les synapses d'autres neurones. Puis ces molécules changent subitement la perméabilité de la membrane de telles sorte que les ions Na^+ et K^+ pénètrent la cellule et modifient la différence de potentiel intra-extracellulaire de état de repos. Cette différence de potentiel est augmentée de 10mV pendant 10ms environ. Ce phénomène est nommé un PPS.

Le Potentiel Action : (PA) Si beaucoup de PPS s'additionnent, le potentiel atteint un seuil critique et un PA est généré. Ce PA correspond à une augmentation de 100mV du potentiel de repos en 1ms pendant $2-3$ms. Le potentiel de repos étant la différence transmembranaire due aux différentes concentration en ions Ca^+ et K^+. Après ce PA, l'état de repos est recouvré en quelques ms; le temps total du phénomène est de l'ordre de 10ms. La Fig.(1.10) retrace ce processus. Ajoutons que l'amplitude des PA est toujours la même, ainsi le codage de l'information au sein du cerveau se fait en modulation de fréquence et non modulation d'amplitude.

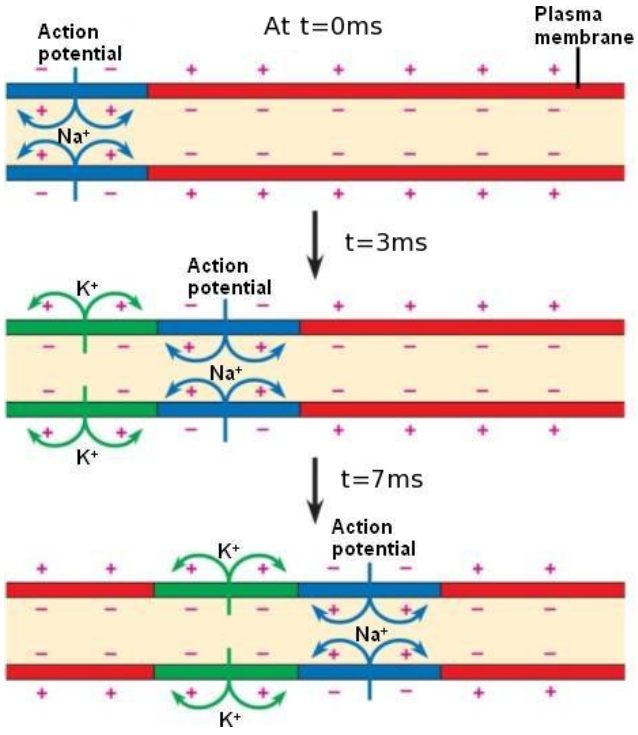

Figure 1.10 – *Potentiel d'action se propageant le long d'un axone. Le rouge code les états de repos, le bleu le PA, et le vert le recouvrement.* `http://soe.ucdavis.edu`

Ces potentiels créés lors de l'activation de neurones (PPS et PA) engendrent un déplacement de charges et ainsi la création de petits courants appelés courant primaires (ou intracellulaires). Afin de détecter à une certaine distance ces petits champs électromagnétiques générés par les neurones, ces champs doivent s'additionner à un temps donné. Les courants primaires dues aux PA durent 1ms, ce qui les rend peut susceptibles de se synchroniser. D'un autre côté, les PPS engendrent des courants durant 10ms. De plus, le champ électromagnétique créé par un PA peut être assimilé à celui d'un quadripôle *càd* la somme de deux dipôles opposés légèrement déplacés l'un de l'autre.

On peut observer Fig.(1.10) (milieu) cette configuration; les charges positives sont entourées de charges négatives, ce qui créé des courants opposés. À une distance r, l'influence d'un quadripôle décroît en r^3, tandis que celle d'un dipôle décroît en r^2. En contraste, les PPS génèrent des courants dans une seule direction (de la synapse vers le soma). Finalement, afin que ces PPS se somment, ils doivent être dans la même direction. Heureusement, de telles structures sont présentes dans le cerveau: ces neurones à dendrites longues et parallèles s'appellent des neurones pyramidaux. Selon les estimations (voir [Murakami and Okada, 2006]), 10^4 neurones doivent être conjointement actifs pour obtenir un signal mesurable en EEG et MEG.

1.2.1.2 Les neurones pyramidaux

Les neurones pyramidaux sont des cellules dans la matière grise qui présentent des dendrites orientées vers la surface externe du cortex (dendrites apicales.) On peut voir Fig.(1.11) de telles structures dont le comportement électromagnétique peut être assimilé à celui d'un dipôle de courant. Dans les expériences relatées

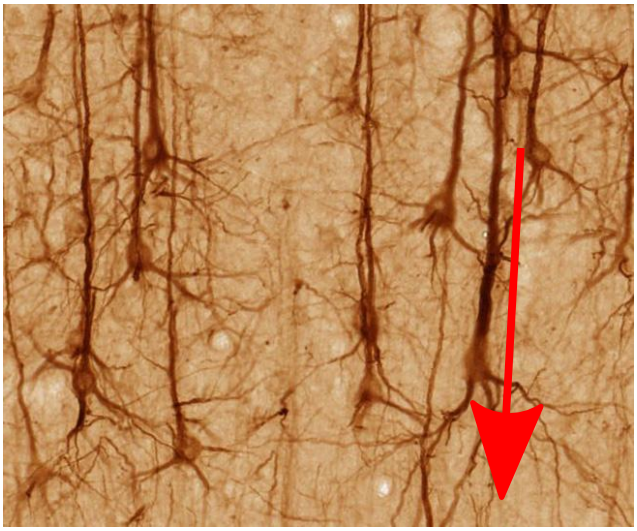

Figure 1.11 – *Neurones pyramidaux d'un macaque où un dipôle de courant superposé représente un PPS.* `http://brainmaps.org`

par [Murakami and Okada, 2006], différents types de neurones ont été modélisés et leur courant équivalent calculé. Un dipôle de courant peut être défini comme un dipôle électrique où au lieu de considérer deux charges de différents signes, on considère deux courants opposés: un puits et une source. Voir Fig.(1.12) pour une superposition du potentiel et courant généré par un dipôle de courant sur une dendrite apicale. Dans ces expériences, les auteurs ([Murakami and Okada, 2006]), estiment à 1pA pour le moment d'un dipôle de courant représentant un simple neurone pyramidal. Il a été estimé à 1mm^2 la surface du cortex nécessaire à l'obtention d'un signal mesurable, même si les expériences augmente cette estimation à 100mm^2 [Hämäläinen et al., 1993].

Soit un dipôle de courant à la position $\mathbf{r}$, d'orientation $\mathbf{m}$ et d'amplitude $m = \|\mathbf{m}\|$. On peut voir Fig.(1.13), les iso-lignes du champ électrique généré par un dipôle (une vue 2D avec une symétrie axiale). Pour le cas du champ magnétique, on note que le champ est contenu dans les plans normaux à $\mathbf{m}$ (vue 3D). Cela explique l'incapacité de la MEG à détecter des sources radiales (champ magnétique nul).

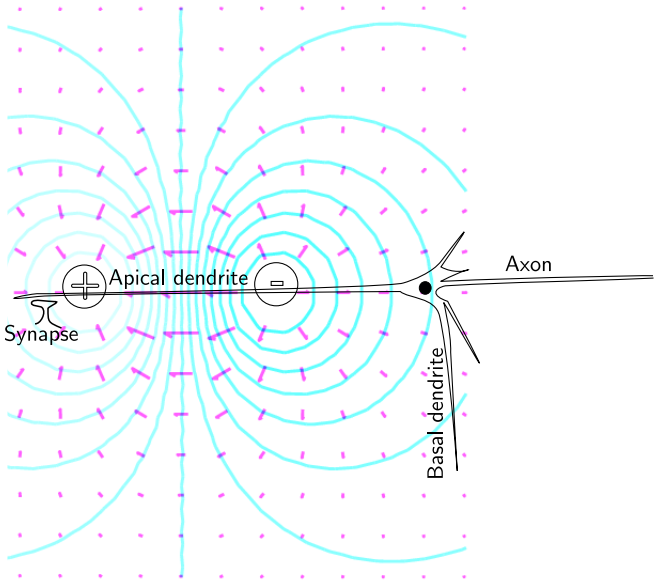

Figure 1.12 – *Champ électrique (flèches violettes) généré par un dipôle de courant (modèle de courant PPS). Les lignes bleues représentent les iso-courbes du potentiel.*

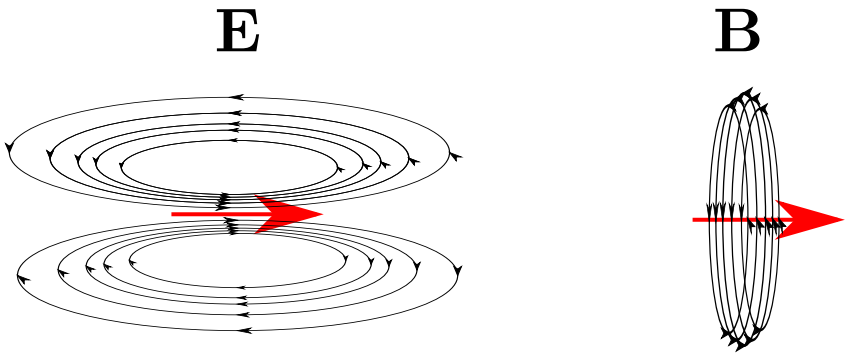

Figure 1.13 – *Champ électrique (gauche) et magnétique (droite) généré par un dipôle de courant (en rouge).*

1.2.2 L'EEG et la MEG

L'Électroencéphalographie (EEG) est une technique non-invasive très utile a l'observation fonctionnelle du cerveau. Sa haute résolution temporelle est bien

meilleure que celle de l'IRMf (*cf.* Fig.(1.9)), et sa haute non-invasivité la rend très utilisée depuis plusieurs décennies. L'EEG enregistre le potentiel électrique au niveau des électrodes disposées sur le scalp. L'EEG mesure les fluctuations du potentiel qui résultent des courants générés par les neurones dans le cerveau. Le premier enregistrement EEG sur un humain a été réalisé en 1929 par le physiologiste Allemand Hans Berger. Grâce aux enregistrements effectués entre seulement 2 électrodes, il a pu observer différentes activités du cerveau d'un patient selon qu'il avait les yeux fermés ou pas. Plus tard, il mesura également l'activité lors d'une crise épileptique. Ces analyses du signal étaient faites visuellement en regardant la courbe du potentiel; le tout sur un encéphalogramme de mauvaise définition (voir Fig.(1.14)). En fait, les électrodes utilisées n'étaient pas des capteurs placés sur

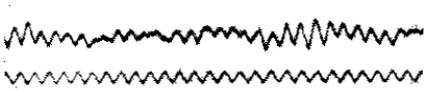

Figure 1.14 – *Un des tout premier enregistrement EEG. EEG d'un enfant superposé sur un signal a* $10Hz$.[WIKIPEDIA]

le scalp, mais de fins fils d'argent introduits sous le scalp. Cette technique permettait une bonne conduction entre le fil et la tête. De nos jours, les bonnets EEG peuvent compter de 19 à 256 électrodes et le contact entre les électrodes et le scalp est assuré par une solution électrolytique qui se diffuse sur une petite surface autour de l'électrode. Des électrodes sèches sont également en cours de recherche [Taheri et al., 1994], ce qui permettra notamment d'augmenter leur nombre.

Avoir plus d'électrodes permet d'obtenir des cartes de plus hautes résolutions de l'activité électrique sur le scalp.
À la question: *Combien d'électrodes devons nous mettre pour obtenir une bonne topographie?*, il convient de remarquer que le potentiel sur le scalp est très lisse, de plus l'emploi de gel électrolytique ne permet pas de placer des électrodes proches.

Les signaux enregistrés en EEG sont de l'ordre de quelques μV, et sont amplifiés et numérisés avec un taux d'échantillonnage allant jusqu'à 25kHz La Fig.(1.15) représente un enregistrement EEG actuel.

La magnetoencéphalographie (MEG) est apparue 40 ans après l'EEG en 1968. Si l'activité électrique du cerveau génère un champ électrique, elle génère également un champ magnétique (ou d'une manière plus générale un champ électromagnétique). Bien-que le champ magnétique soit très faible (quelques fT (10^{-15}Tesla)), il se propage hors de la tête. David Cohen en 1968 a inventé la MEG. En réalité ce fut la MCG (MagnetoCardiographie) inventée premièrement, lorsqu'il observa avec un seul capteur (une bobine d'induction en cuivre) le champ magnétique créé par un cœur battant. Avec de telles faibles valeurs du champ magnétique l'on doit avoir

Figure 1.15 – *Enregistrement EEG de plusieurs électrodes au cours du temps (en abscisse). On y voit une crise épileptique.*[WIKIPEDIA]

des capteurs de très haute sensibilité. En effet, sachant que le champ magnétique terrestre est autour de 50μT=5.10^{-5}T (un milliard de fois le champ magnétique créé par le cerveau), et un bruit magnétique urbain est de 1μT, cela a conduit les scientifiques à travailler dans des espaces protégés des champs extérieurs. Un an après, James E. Zimmerman inventa le SQUID (Superconducting QUantum Interference Device) qui est un détecteur ultra-sensible (jusqu'à 5.10^{-18}T). David Cohen a vite vu l'avantage de tels capteurs et pu observer le cerveau dans une chambre isolée du MIT. Les MEG actuelles comportent des centaine de SQUIDS, souvent appariées afin de mesurer un gradient de champ magnétique (gradiomètres) moins sensibles aux bruits. Elles ont autour de 200 capteurs et certaines installations permettent d'avoir un casque EEG simultanément (voir Fig.(1.16)).

1.2.3 Imagerie fonctionnelle du cerveau avec l'EEG et la MEG

L'intérêt majeur de l'EEG est d'analyser les fonctions du cerveau. Avec seulement 2 capteurs, Hans Berger a pu observer différents rythmes cérébraux. Dans son expérience, il a pu observer que lorsqu'un individu ferme les yeux, un rythme dominant de $10Hz$ apparaissait. C'est ainsi que l'on commença à étudier les rythmes du cerveau, tout d'abord en déduisant un état cognitif seulement en regardant les fréquences principales présentes (voir Fig.(1.17)).

L'étude des rythmes cérébraux ne nécessite que peu d'électrodes (un casque de 19 électrodes suffit), en appliquant une FFT (Fast Fourier Transform) sur les données acquises, on obtient les fréquences contenues. L'inférence d'un rythme avec un état peut dépendre de la position des électrodes. L'on peut vérifier les affirmations suivantes:

Ondes γ: Activités cérébrales de haut niveau telles que lors de calcul mental ou de résolution de problèmes.

Figure 1.16 – *Un système MEG couplé à un EEG moderne.*

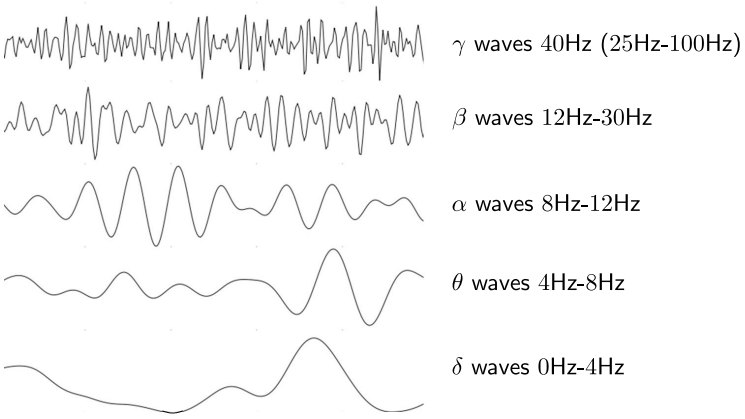

Figure 1.17 – *Rythmes du cerveau.*

Ondes β: État occupé, conversations, pensées, ... état normal.

Ondes α: Au niveau du lobe occipital (à l'arrière au dessus du cou). Elles sont signes d'états calmes, ou yeux clos. Elles ont les amplitudes les plus élevées (c'est pourquoi elles ont été les premières ondes observées).

Ondes μ: Apparaissent aux mêmes fréquences que les ondes α mais se situent au niveau du cortex moteur (centre du scalp); elles disparaissent quand le sujet bouge ou pense à bouger.

Ondes θ: Sont plus difficiles à caractériser, elles apparaissent durant le sommeil profond, et sont probablement dues à l'hippocampe qui se trouve pourtant

loin des capteurs EEG [Buzsáki, 2002].

En regardant une topographie EEG ou MEG, on peut parfois avoir une vague idée de la position de la source représentant l'activité prépondérante (voir Fig.(1.18)). Visuellement, on peut estimer grossièrement la position: antéro-

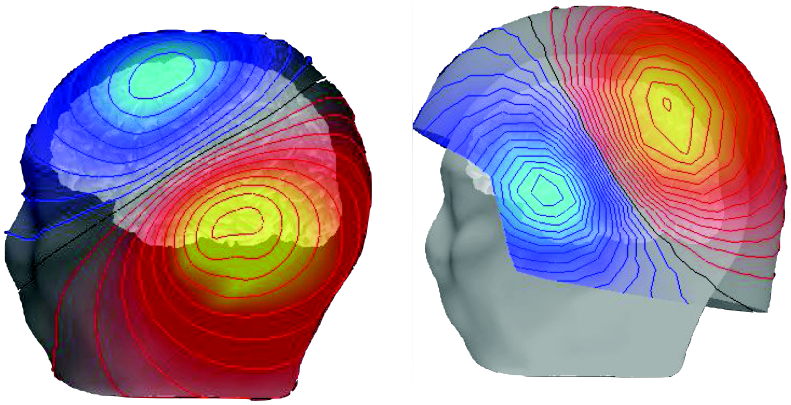

Figure 1.18 – *Topographie EEG et MEG. extraite d'une présentation de Matti Hämäläinen.*

postérieure, droite/gauche, ainsi que l'orientation de la source principale. Par exemple, à partir de la Fig.1.18, un médecin verrait une source tangentielle localisée dans la zone temporale ou au niveau du cortex moteur, sur la gauche du patient. À partir des données collectées l'on souhaiterait trouver les sources du signal mesurés, et ce, à chaque instant, ce qui produirait une image 3D+temps montrant les zones du cerveau actives. Hélas ce n'est pas possible tant que nous avons plus d'inconnues que de données. D'où l'intérêt d'augmenter le nombre de capteurs évoqué en sec.1.2.2.
En réalité, on peut estimer les paramètres (position, orientation) des différentes sources, c'est le problème de localisation de sources en MEEG:

Étant donné des valeurs du potentiel sur le scalp, trouver les sources responsables de ce signal.

1.2.4 Localisation de sources en MEEG

À partir d'enregistrements EEG ou MEG, l'on souhaite retrouver les sources dans le cerveau responsables de certaines composantes du champ électromagnétique mesuré. C'est un problème inverse de localisation. Soit $\mathbf{J}$ la variable représentant la source primaire (un dipôle de courant) dans le cerveau, et soit f une fonction qui donne la stricte relation des sources avec le potentiel aux capteurs V_s. f est le résultat du problème direct qui étant donné une source dans le cerveau donne la composante souhaitée du champ électromagnétique. Le problème inverse est fondé sur

le problème direct. En EEG il s'écrit:

$$\text{trouver } \mathbf{J} \text{ t.q } V_s = f(\mathbf{J}) \ . \tag{1.1}$$

Si l'on pouvait inverser la fonction f, le problème serait résolu en écrivant:

$$\mathbf{J} = f^{-1}(V_s).$$

Mais comme le problème est sous déterminé puisqu'on ne dispose quelques centaines de capteurs pour des milliers de sources possibles.(*p.ex.* en considérant $\mathbf{J} \in \mathbb{R}^3 \times \mathbb{R}^3$ un champ de vecteurs échantillonné dans tout le cerveau sur une image cartésienne de 128x128x128).
On doit donc se résigner à trouver une solution approchée $\tilde{\mathbf{J}}$ de $\mathbf{J}$ en ajoutant de l'*a-priori* sur les sources; c'est le champ de recherche des problèmes inverses en MEEG.

1.2.4.1 Modèles de sources

Une hypothèse sur l'activité électrique du cerveau souvent appliquée, est qu'à chaque instant, elle est clairsemée (sparse): *càd* seules quelques sources sont actives simultanément. 'Actives' signifie électriquement actives et détectables par l'EEG ou la MEG. Les modèles de sources sont de deux types:

sources dipolaires elles représentent l'activité conjointe d'un grand nombre de PPS voisins d'une position (10^6 [Hämäläinen et al., 1993][Nunez, 1981]). Chaque source a 6 paramètres (3 pour la position et 3 pour l'orientation).

sources distribuées représentent l'activité d'une petite surface. Le plus souvent, la position est contrainte à vivre sur une surface imaginaire située entre l'interface matière grise/LCR et Matière blanche/matière grise. L'orientation est contrainte par la surface car les PPS sont perpendiculaires à la surface externe du cortex. Cela permet de réduire le nombre d'inconnues.

1.2.5 Le problème inverse

Le problème inverse est résolu en cherchant une solution $\tilde{V_s} = f(\tilde{\mathbf{J}})$ approchée des données mesurées V_s:

$$\tilde{\mathbf{J}} = \arg\min_{\mathbf{J}} \|V_s - \tilde{V_s}\| = \arg\min_{\mathbf{J}} \|V_s - f(\mathbf{J})\| \ . \tag{1.2}$$

Ce problème est mal posé (au sens d'Hadamard), selon les critères suivants définissant un problème bien posé:

- Il existe une unique solution;
- Elle dépend continûment des données (dans une certaine topologie).

Le problème (1.2) ne remplit pas ces conditions car il est largement sous déterminé, on procède donc à une régularisation traitée ici en ajoutant de l'*a-priori* sur la solution. On pourrait également augmenter le nombre d'électrodes, mais comme expliqué en [Ryynänen et al., 2004], cela dépend beaucoup de la conductivité du crâne qui lisse les potentiels spatialement; dans le cas de l'EEG, il ne sert à rien d'aller au delà de 256 électrodes. On ajoute donc de l'*a-priori* sur la solution.
Plusieurs techniques sont envisageable, ajouter de l'*a-priori* sur les positions des sources au cours du temps, sur leur orientation, ... Ces méthodes peuvent se classer dans ces différentes catégories:

dipole fitting On place des dipôles sur une région d'intérêt, et l'on essaye d'estimer leur moment afin de satisfaire au mieux l'Eq.(1.2). Par exemple, pour une tâche somato-sensorielle, on place des dipôles dans le cortex sensori-moteur. Quelques méthodes sont: rotating dipôles, moving dipôles, Minimum Norm, ...

filtrage l'espace est échantillonné (souvent sur une grille cartésienne), et l'on essaie de filtrer le bruit et les inter-corrélations (beamforming methods). On peut également essayer de décomposer le signal en multiple composantes (avec une SVD), c'est le but des méthodes MUSIC (MUltiple SIgnal Classification).

sources distribuées de manière plus générale on échantillonne l'espace des sources (grille cartésienne ou surface imaginaire), où à chaque noeud sont placés 3 dipôles (pour couvrir toutes les orientations). Les méthodes de MinimumNorm ajoutent de l'a-priori sur la régularité des sources, avec soit une norme L^0 (nombre de sources spécifié), norme L^1 (sparsité), norme L^2 (énergie bornée), ... ou combinaison de plusieurs normes [Gramfort et al., 2008].

1.3 Le problème direct

Le problème direct simule une source dans le cerveau afin de calculer la composante d'intérêt aux capteurs (f dans Eq.(1.1)). Cette résolution est faite grâce aux équations de Maxwell en quasi-statique sur une géométrie particulière au patient. Ainsi, ce problème dépend de chaque sujet, *càd* on doit avoir pour chaque patient la définition de ses tissus cérébraux et leur conductivités. La plupart des surfaces peuvent être obtenus en segmentant une IRM anatomique; le crâne est cependant difficile à obtenir et est souvent estimé (inflation du cerveau ou érosion du scalp). Les conductivités des différentes couches sont évaluées de différentes manières ; conductivités estimées *in-vivo*, *ex-vivo*, *in-vitro*, ... ou grâce à l'EIT (Tomographie par Impédance Électrique) [Clerc et al., 2005a].

1.3.1 Les équations de Maxwell

Les équations de Maxwell sont des EDP (équations aux dérivées partielles), qui relient dans tout milieu, le champ électrique, le champ magnétique avec les sources

électriques, ou les distributions de courants. Ces variables dépendent du temps et de l'espace. Voir page.vii concernant les notations utilisées.

Une formulation locale: En partant des relations établies par Ampère, Gauss, et Faraday, Maxwell les a rassemblées et complétées. Dans leur forme locale, elles s'écrivent dans le vide:

$$\begin{cases} \nabla \cdot \mathbf{E} = \frac{\rho}{\varepsilon_0} \\ \nabla \cdot \mathbf{B} = 0 \\ \nabla \times \mathbf{E} = -\frac{\partial \mathbf{B}}{\partial t} \\ \nabla \times \mathbf{B} = \mu_0 \mathbf{J} + \mu_0 \varepsilon_0 \frac{\partial \mathbf{E}}{\partial t} \end{cases} \tag{1.3}$$

Pour les tissus humains, la perméabilité magnétique est la même que celle du vide. La permittivité électrique ε varie beaucoup de ε_0 selon le tissu considéré et les fréquences étudiées.

Soit $\varepsilon_r = \frac{\varepsilon}{\varepsilon_0}$ la permittivité relative d'un milieu de permittivité ε, ce facteur est de 4.10^8 pour la matière grise, 1.10^5 pour la peau à 10Hz [Gabriel et al., 1996b]. Dans leur forme locale, pour un milieu de permittivité ε et perméabilité $\mu = \mu_0$, Eq.(1.3.a) et Eq.(1.3.d) s'écrivent:

$$\nabla \cdot \mathbf{E} = \frac{\rho}{\varepsilon} \tag{1.4}$$

$$\nabla \times \mathbf{B} = \mu_0 \mathbf{J} + \mu_0 \varepsilon \frac{\partial \mathbf{E}}{\partial t} \tag{1.5}$$

$$\tag{1.6}$$

L'approximation quasi-statique : Pour l'EEG et la MEG, on peut négliger les dérivées en temps (voir [Hämäläinen et al., 1993]). Ceci est dû aux échelles de notre problème, un diamètre de tête inférieur au mètre, des échelles de temps de l'ordre de quelques ms (PPS). On peut ré-écrire ces équations (1.3):

$$\begin{cases} \nabla \cdot \mathbf{E} = \frac{\rho}{\varepsilon} & (a) \\ \nabla \times \mathbf{E} = 0 & (b) \\ \nabla \cdot \mathbf{B} = 0 & (c) \\ \nabla \times \mathbf{B} = \mu_0 \mathbf{J} & (d) \end{cases} \tag{1.7}$$

Le champ magnétique et le champ électrique sont découplés et peuvent donc être résolus indépendamment.

1.3.1.1 Une équation de Poisson pour le potentiel électrique

L'équation.(1.7b.) implique que $\mathbf{E}$ dérive d'un champ scalaire, le potentiel électrique V, et va par définition des hauts potentiels vers les bas:

$$\nabla \times \mathbf{E} = 0 \Longrightarrow \mathbf{E} = -\nabla V \tag{1.8}$$

Ce champ $\mathbf{E}$ est entièrement déterminé par la connaissance de V, et V est ainsi défini à une constante près. On applique une divergence sur l'Eq.(1.7d.):

$$\nabla \cdot (\nabla \times \mathbf{B}) = \nabla \cdot (\mu_0 \mathbf{J}) = 0$$

Ainsi le courant total est de divergence nulle. On décompose maintenant $\mathbf{J}$ en sa composante primaire due à la source primaire, noté $\mathbf{J}^{\mathrm{p}}$ (générée par les PPS) et sa composante passive due aux courants passifs (ou Ohmique) car le matériau est résistif (de conductivité σ):

$$\nabla \cdot \mathbf{J} = \nabla \cdot \mathbf{J}^{\mathrm{p}} + \nabla \cdot (\sigma \mathbf{E}) = 0$$

Cette équation est une équation de Poisson qui relie le potentiel à la source primaire $\mathbf{J}^{\mathrm{p}}$. En utilisant l'Eq.(1.8) on obtient l'équation que va s'attacher à résoudre cette thèse:

$$\boxed{\nabla \cdot (\sigma \nabla V) = \nabla \cdot \mathbf{J}^{\mathrm{p}}} \tag{1.9}$$

1.3.1.2 La loi de Biot-Savart pour le champ magnétique

En prenant le rotationel de l'Eq.(1.7d.), et utilisant l'Eq.(1.7c.):

$$\nabla \times \nabla \times \mathbf{B} = \nabla(\nabla \cdot \mathbf{B}) - \Delta \mathbf{B} = -\Delta \mathbf{B} = \mu_0 \nabla \times \mathbf{J}, \tag{1.10}$$

On obtient des équations de Poisson pour chaque composante du champ magnétique $\mathbf{B}$. La solution fondamentale de l'équation de Laplace qui vérifie $\Delta G = \delta$: est la fonction de Green

$$G(\mathbf{r}) = \frac{-1}{4\pi \|\mathbf{r}\|}$$

On utilise le produit de convolution de cette solution fondamentale avec le terme source, ainsi l'Eq.(1.10) s'écrie:

$$\mathbf{B}(\mathbf{r}) = \frac{\mu_0}{4\pi} \int_{\mathbb{R}^3} \nabla \times \mathbf{J}(\mathbf{r}') \frac{1}{\|\mathbf{r} - \mathbf{r}'\|} d\mathbf{r}' + \mathbf{B}_H,$$

où $\mathbf{B}_H$ est la solution homogène de l'Eq.(1.10). Finalement, on impose un champ magnétique nul à l'infini et donc $\mathbf{B}_H = 0$, et en intégrant par partie:

$$\begin{aligned}
\mathbf{B}(\mathbf{r}) &= \frac{\mu_0}{4\pi} \int_{\mathbb{R}^3} \mathbf{J}(\mathbf{r}') \times \nabla \left(\frac{1}{\|\mathbf{r} - \mathbf{r}'\|} \right) d\mathbf{r}' \\
&= \frac{\mu_0}{4\pi} \int_{\mathbb{R}^3} \mathbf{J}(\mathbf{r}') \times \left(\frac{\mathbf{r} - \mathbf{r}'}{\|\mathbf{r} - \mathbf{r}'\|^3} \right) d\mathbf{r}' \\
&= \frac{\mu_0}{4\pi} \int_{\mathbb{R}^3} \mathbf{J}^{\mathrm{p}}(\mathbf{r}') \times \left(\frac{\mathbf{r} - \mathbf{r}'}{\|\mathbf{r} - \mathbf{r}'\|^3} \right) d\mathbf{r}' - \frac{\mu_0}{4\pi} \int_{\mathbb{R}^3} \sigma \nabla V(\mathbf{r}') \times \left(\frac{\mathbf{r} - \mathbf{r}'}{\|\mathbf{r} - \mathbf{r}'\|^3} \right) d\mathbf{r}' \\
\mathbf{B}(\mathbf{r}) &= \mathbf{B}_0(\mathbf{r}) - \frac{\mu_0}{4\pi} \int_{\mathbb{R}^3} \sigma \nabla V(\mathbf{r}') \times \left(\frac{\mathbf{r} - \mathbf{r}'}{\|\mathbf{r} - \mathbf{r}'\|^3} \right) d\mathbf{r}' \,, \qquad (1.11) \\
\text{où} \quad \mathbf{B}_0(\mathbf{r}) &= \frac{\mu_0}{4\pi} \int_{\mathbb{R}^3} \mathbf{J}^{\mathrm{p}}(\mathbf{r}') \times \left(\frac{\mathbf{r} - \mathbf{r}'}{\|\mathbf{r} - \mathbf{r}'\|^3} \right) d\mathbf{r}' \,. \qquad (1.12)
\end{aligned}$$

C'est la loi de Biot et Savart.
Le champ magnétique à chaque point $\mathbf{r}$ peut donc s'écrire comme la somme des contributions des 2 courants. On appelle $\mathbf{B}_0$ le champ magnétique primaire qui ne dépend que de la source primaire et pas du milieu. C'est là une distinction entre la MEG et l'EEG puisque en EEG on a une très forte dépendance aux milieu traversé tandis qu'en MEG la composante primaire est indépendante de ces paramètres et est de plus prépondérante.

1.3.2 Les modèles électrophysiologiques

Afin de résoudre le problème direct avec l'équation de Poisson (1.9), ou l'équation de Biot-Savart (1.12), il faut avoir la description de la géométrie et les conductivités des tissus de la tête du patient. Les problèmes directs en MEG et EEG ne partagent pas les mêmes sensibilités à l'égard de la modélisation géométrique ou du profil de conductivité. En fait, le champ magnétique primaire est prépondérant dans l'expression de $\mathbf{B}$, et peut être calculé analytiquement, sans un modèle de tête. Toutefois, on pourrait introduire des erreurs considérables, en ne calculant pas la contribution passive ohmique dans le champ magnétique. Une tête humaine peut être considérée comme un volume conducteur borné si l'on néglige le courant à travers le cou. Le courant électrique ne se propage pas en dehors de la tête, car l'air a une conductivité négligeable.
On peut alors définir une tête comme un ensemble de volumes conducteurs qui partitionent la tête en régions de profil de conductivité différent. Le crâne ayant une conductivité nettement inférieure à celle des autres tissus, il convient de le définir en domaine à part entière. De plus, le profil de conductivité du crâne est crucial lorsqu'il s'agit de résoudre un problème direct en EEG, car il se situe entre les sources et les capteurs. D'autre part, pour le problème direct en MEG, il est moins important de prendre en compte le crâne. En effet le champ magnétique primaire est indépendant de la conductivité, et le champ passif est lui proportionnel à la conductivité de la couche considérée. Par conséquent le champ magnétique n'est que peu affecté par le crâne, ni par le cuir chevelu (dans lequel, en raison de l'effet protecteur de la boîte crânienne, ne contient pas d'importants courants). L'affectation de conductivités isotropes ou anisotropes à chaque région est encore discutée aujourd'hui, les mesures *in-vivo* étant presque impossibles et souvent sujettes à une haute variabilité [Baysal and Haueisen, 2004, Lai et al., 2005], ce problème sera abordé plus tard, pour l'instant on envisage une conductivité du crâne entre 15 et 80 fois inférieure à celle du cuir chevelu [Bashar et al., 2009].

Dans le reste de cette section, nous présentons maintenant différents modèles électrophysiologiques, en partant de la description géométrique d'une tête grossière avec des volumes conducteurs sphériques imbriqués et des conductivités constantes et homogènes par morceaux, puis allant jusqu'à une forme réaliste de tête extraite d'une IRM anatomique et associée à des profils de conductivité appropriés pour chaque région considérée.

1.3.2.1 Volumes conducteurs sphériques

Le premier modèle utilisé pour résoudre le problème direct en EEG était un modèle de sphères emboîtées comme montré Fig.(2.19) [Rush and Driscoll, 1968, Meijs and Peters, 1987]. Sur cette figure, le domaine de la tête Ω est décomposé en 3 régions $\Omega_1, \Omega_2, \Omega_3$ de conductivités respectives $\sigma_1, \sigma_2, \sigma_3$. On considère communément Ω_1 représentant le 'cerveau', Ω_2 le crâne et Ω_3 la peau du scalp avec des rayons respectifs $0.87, 0.92, 1$.

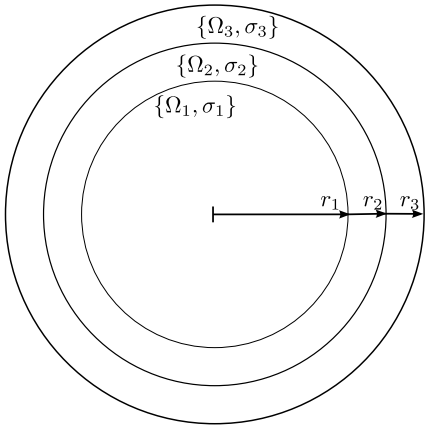

Figure 1.19 – *Un modèle de tête sphérique à 3 couches.*

Ce modèle présente plusieurs avantages. Tout d'abord, on ne requiert pas d'extraction de la géométrie de la tête du patient, seulement une disposition approchée d'une sphère sur une surface. Deuxièmement, la solution des problèmes directs Eq.(1.9)-(1.12) peut être obtenue analytiquement, et donc très rapidement [Spinelli et al., 2000]. Mais naturellement l'approximation d'une tête par des sphères est grossière et conduit à des erreurs considérables. Les modèles elliptiques sont légèrement plus intéressants (voir Fig.(2.20)), et les équations peuvent encore se résoudre analytiquement [De Munck, 1988, Kariotou, 2004].

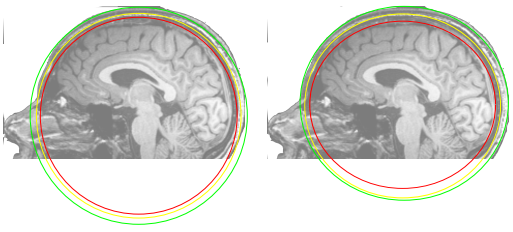

Figure 1.20 – *Un modèle sphérique sur la gauche et ellipsoïdal sur la droite.*

L'approximation géométrique faite amène des erreurs considérables pour la résolution du problème direct [Cuffin, 1996, Huiskamp et al., 1999]. Même pour

la MEG, on considère les modèles sphériques comme trop grossiers comparés aux modèles réalistes [Van Uitert and Johnson, 2002]. On utilise également des modèles de sphères centrés pour chaque capteur MEG, ce qui minimise mieux certaines erreurs géométriques [Huang et al., 1999]-[Lalancette et al., 2011].
Un pas en avant dans la modélisation est de considérer des géométries réalistes.

1.3.2.2 Conducteurs homogènes constants par morceaux

En segmentant une IRMa, on peut extraire différentes surfaces du cerveau, comme l'interface matière grise/blanche, grise/LCR, LCR/crâne, crâne/scalp, et scalp/air. Sur la Fig.(1.21), On peut voir différentes surfaces extraites obtenues en utilisant le logiciel Freesurfer [Dale et al., 1999, Fischl et al., 1999] qui fonctionne à base d'atlas. En utilisant une IRM pondérée en T2, on peut deviner l'interface LCR-

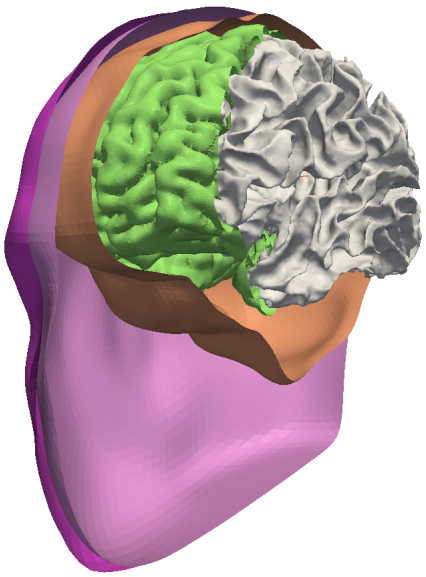

Figure 1.21 – *Surfaces triangulées de hautes définitions de segmentations d'IRMa: (fushia)-scalp-(mauve)-crâne-(orange)-LCR-(green)-matière grise-(gray)-matière blanche.*

crâne, sinon une IRM en densité de proton (un autre type de séquence) peut être utilisée pour définir le crâne.
En utilisant un modèle constant par morceau avec une géométrie réaliste, on a désormais moins d'erreur géométriques. Si l'IRM n'est pas disponible, une approche consiste à adapter des modèles génériques calculés sur des IRMa moyennées [Darvas et al., 2006].
Dans ce type de modèle, la conductivité est constante et homogène par morceau. C'est la limitation de ce modèle, puisque certains tissus ont une conductivité anisotrope et inhomogène.

1.3.2.3 Modèles inhomogènes et anisotropes

Le crâne est composé de plusieurs couches, et dans les parties les plus épaisses, contient de l'os spongieux. L'os spongieux a une conductivité 4 à 7 fois supérieur à l'os dur [Akhtari et al., 2002, Ramon et al., 2006]. Cette augmentation subite de la conductivité au milieu du crâne a conduit les scientifiques à utiliser des modèles de conductivités anisotropes pour le crâne, afin d'approximer cette inhomogénéité. Le modèle précédent (de conductivités constantes par morceaux) pourrait modéliser un tel compartiment si l'on pouvait définir ces aires spongieuses (avec un CT-scan, T2-MRI). De plus, de petites régions engendreraient de petits volumes difficiles à discrétiser et utiliser avec des méthodes numériques.
La matière blanche est elle aussi source d'anisotropie. En effet, sa structure fibreuse due aux axones des neurones, conduit mieux dans la direction de la fibre que dans son plan normal. Cela introduit donc une anisotropie forte du tenseur de conductivité à prendre en compte.

1.3.2.4 Définir les conductivités des tissus cérébraux

Afin d'avoir une bonne résolution du problème direct il faut introduire naturellement de bonnes valeurs de conductivités. Ces valeurs sont souvent difficiles à obtenir.

Mesures in-vivo, et in-vitro Les mesures in-vivo sont très rares car elles nécessitent des expériences invasives, les mesures in-vitro sont elles plus fréquentes [Gabriel et al., 1996a]-[Gabriel et al., 1996b]. La principale interrogation au sujet de mesures de conductivité in-vitro, est que le tissu se comporte différemment que dans son milieu naturel à la température corporelle. Les mesures in-vivo sont plus proches des conductivités réelles, et ont conduit à des corrections majeures, par exemple, dans [Baumann et al., 1997], nous apprenons que la conductivité du LCR a été sous-estimés d'environ 44 % entre 1977-1997. Dans [Hoekema et al., 2003], la conductivité du crâne de plusieurs sujets épileptiques a été mesurée ainsi que celle d'un morceau de crâne post-mortem. Ces conductivités issues de craniotomies sont beaucoup plus grandes que celle utilisées par la communauté et que celle du crâne post-mortem, mais montrent surtout une forte variabilité entre les sujets. De plus, la conductivité du crâne dépend fortement de l'âge de la personne. C'est pourquoi les méthodes suivantes sont séduisantes. Voir [Lai et al., 2005] concernant le rapport de conductivité cerveau-crâne.

La tomographie par impédance électrique est une technique similaire à l'EEG. Au lieu de mesurer le potentiel à des capteurs pour mesurer l'activité électrique du cerveau, on injecte un courant connu à une paire d'électrodes de sorte que l'on peut calibrer les valeurs de conductivité en considérant le potentiel mesuré sur les autres capteurs. C'est ce qu'on appelle l'EIT (voir [Kybic et al., 2006] pour Electrical Impedance Tomography). On peut estimer les conductivités des tissus de manière non invasive pour chaque patient en particulier, avant une expérience clinique ou

de recherche. Une étude sur la sensibilité de ces conductivités avec l'EIT est faite dans [Vallaghé and Clerc, 2009].

Les potentiels évoqués Afin de calibrer les conductivités des autres tissus, on peut envisager d'avoir la solution du problème inverse, puis estimer la conductivité, de telle sorte que le problème direct est en accord avec les mesures. Par exemple, en connaissant l'emplacement de la zone somato-sensorielle gauche, on peut stimuler le patient dans cette région, et analyser les résultats, de sorte qu'ils conviennent à la résolution du problème direct [Gonçalves et al., 2003].

Conductivités utilisées dans nos expériences Le tableau (1.1) énumère les conductivités que nous allons utiliser. Il est basé sur les articles précédents et de la vaste enquête effectuée dans [Dannhauer et al., 2010]. Nous montrons aussi les conductivités normalisés qui sont couramment utilisés pour résoudre un problème direct sur un ordinateur qui peut être fait de même avec conductivités réelles ou normalisées. Le ratio anisotrope est, pour le crâne, le rapport de la conductivité radiale sur la conductivité tangentielle *càd* $\frac{\sigma_{radiale}}{\sigma_{tangentielle}}$. Et pour la substance blanche il correspond au ratio de $\frac{\sigma_{transversale}}{\sigma_{longitudinale}}$ qui multiplie la conductivité le long des fibres de matière blanche. Au chapitre 7 nous étudierons cette question plus en détail.

Tissus	**Conductivités S/m**	**Isotropes normalisées**	**Ratio Anisotrope**
Cerveau	0.33	1.	
Matière grise	0.33	1.	
Matière blanche	0.33	1	1 : 10
Crane	0.01	0.03	1 : 1.5
Scalp	0.33	1.	

Table 1.1 – *Conductivités des tissus d'une tête humaine.*

Les modèles électrophysiologiques étant présentés, ainsi que les modèles de sources, il faut représenter ces modèles dans une formulation numérique. Plusieurs outils sont disponibles, nous nous attachons en section.2.4 à présenter ces divers outils numériques afin de résoudre le problème direct en MEEG. Après avoir introduits ces méthodes numériques nous proposons le couplage de certaines, afin d'obtenir une méthode couplées présentant plusieurs avantages. Enfin une extension d'une méthode permettant généralement de traiter que des domaines isotropes sera introduite. Suite en section.2.4

Chapter 2

Introduction

As we go deeper in the understanding of Nature and Man, the brain keeps on fascinating more and more. Its complexity at a structural level, is way beyond what one could achieve nowadays with computers, at least for a human brain: 10^{11} = 100 billions of neurons, and each of them interacting with up to several thousands of neighbors, and quite economic from an energy point of view with 25 watt at peak [Kandel et al., 2000].

Contents

2.1 Context

In the brain lie neurons which are cells ensuring the transmission of information with bio-electrical signals. The electrical part being the transmission of charges along the axon, then relayed by the biochemical part: neurotransmitters at synapse (see fig.2.1). The synapse is the junction between an axon terminal of one neuron with the dendrites of another neuron.

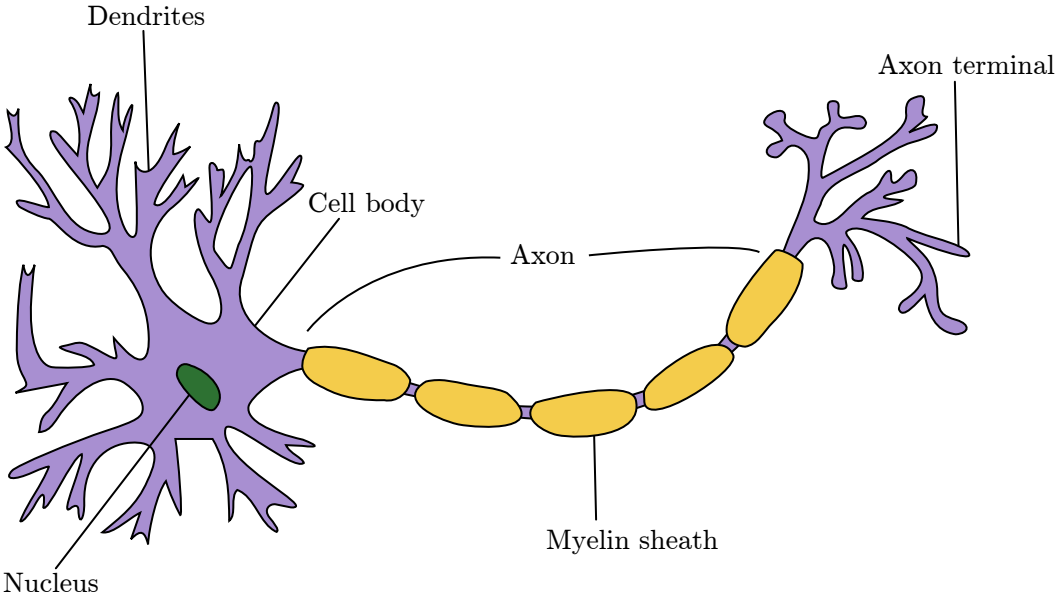

Figure 2.1 – *Simple neuron sketch.*[WIKIPEDIA]

The brain is also composed of glial cells (or glia) even more numerous than the neurons (10 to 50 times more). Even if they do not transmit information, besides other functionalities, they bring nutrients and oxygen to neurons, and insulate them from each other, as they all carry electric charges. Their role is not fully understood yet, but the myelin they produce to insulate the neurons, being white, gave the name to the white matter region, where mainly the axon part of the neurons lie. On the other hand, in the gray matter lies the body of the neurons cells.
Since the beginning of the Odyssey of the brain, scientists endeavor to establish maps of brain cells organization, as well as functional maps. One of the main goals being to obtain a fully detailed map of the brain regions with the functions they play in cognitive processes.

2.1.1 Brain anatomy

The brain is an organ at the center of the nervous system. It is enclosed in the skull and 'floats' in the CSF (CerebroSpinal Fluid). It is composed of two hemispheres,

each of which can be divided into 4 lobes as Fig.(2.2) shows. These lobes are separated by fissures which all individuals share. These lobes can represent roughly

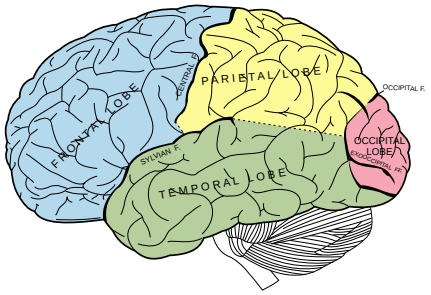

Figure 2.2 – *Sagittal view of a human brain.*[WIKIPEDIA]

the following functions:

the frontal lobe: involves the ability to make decisions, plans, reasonings, emotions; higher mental functions;

the parietal lobe: integrates sensory information, also associated with orientation, recognition, speech;

the temporal lobe: is involved in auditory perception, semantic, speech, memory;

the occipital lobe: is mainly dedicated to vision.

The hashed region is the cerebellum which is involved in the balance or posture position, it does not generate these movements but rather calibrates them and makes them precise [Ghez and Fahn, 1985]. The exterior of the brain is called cortex or gray matter, on which we can see convolutions called gyri and sulci for convex resp. concave folds. Under the gray matter layer, which represents the interface between the brain and the CSF, lies the white matter which is mainly composed of bundles of myelinated axons.

2.1.2 Motivations

What is the main motivation for studying the brain ? It is simply the most fascinating organ, for which, historically, one has begun to establish relationship between its regions and their function, through observation of patients suffering from brain lesions. Such lesions can lead to loss of memory (short term or long term), blindness, impossibility of taking critical decisions, obesity, and many other syndromes. Studying such patients has led scientists to think that the vision process, the body weight ... were all controlled by the brain. On the other hand, neurodegenerative diseases, such as Alzheimer's disease, Parkinson's disease are caused by death of neurons leading to diminution of control, memory, ...

Epilepsy is an abnormal hyper-synchronous neuronal activity often generated by a small region within the brain (specific to each patient). Studying these diseases is a main motivation for research. But in a few cases, often encountered in people with developmental disorders, the brain can fascinate by its ability to stock information, such as entire books line by line, or for arithmetic calculations way beyond those one can achieve normally. Some researchers believe that studying it, and understanding the way information is treated could lead to the creation of artificial intelligence for machines. Another very seductive interest is emerging with Brain-Computer Interface (BCI), where scientists analyze in real time the brain signals most often measured with EEG, in order to control a computer. This could be of great interest for everyone but most surely for people suffering from locked-in syndrome who cannot interact easily with their environment (through talking and gestures).

2.1.3 Medical imaging

Medical imaging techniques regroup all the processes used to create images (1D, 2D, 3D, 3D+time) of parts of the (human) body for their clinical study. Most of them rely on electromagnetic waves, some on radioactivity and some on acoustic waves. They all have strengths and weaknesses, and provide images with different spatial and time resolutions, and moreover they are sensitive to specific tissues. Once data are collected by the machine, they need to be processed to reconstruct an image. Reconstruction techniques have been a very active field in research for every imaging modality since its origin.

2.1.3.1 Magnetic resonance imaging

The most famous modality for studying the brain anatomy is the MRI, which achieves the best resolution for tissues containing water molecules such as the brain. Magnetic Resonance Imaging is based on the interaction of the protons contained in the water (proton of H atoms) of the head tissues with a magnetic field generated by the machine. These interactions measured by the machine reveal the proportion of water molecules in the tissues, and after image reconstruction, lead to accurate description of the tissues containing water. Different acquisition sequences can be designed by varying the main magnetic field, and the radio frequency emitted (mainly T1, and T2 sequences) yielding different contrast for fat, water, skin, bones ; although the skull cannot be perfectly resolved on a MRI see Fig.(2.3).
MRI has given rise to new imaging techniques, such as functional MRI (fMRI) which is able to measure a certain activity of the brain. This will be discussed section.2.1.4.2.
Diffusion MRI (dMRI) allows to measure the water molecules diffusion within the brain along a specified direction. This diffusion would be isotropic in a homogeneous material, but is strongly anisotropic in the brain betraying the presence of elongated structures such as the neuron axons since water molecules do not propagate through them. This anisotropy can be revealed computing a scalar value,

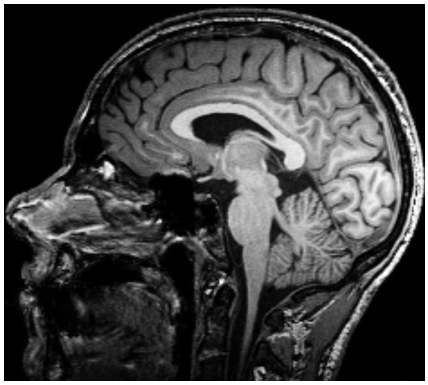

Figure 2.3 – *Sagittal slice of an T1-MRI.*[Joan's head]

the fractional anisotropy (FA) for each voxel. Having several images for different directions allows to construct models of this diffusion process within each voxel, the easiest being a tensor model (DTI for Diffusion Tensor Imaging). The tensor model being symmetric has six unknowns and can be represented as an ellipsoid. HARDI (for High-Angular-Resolution Diffusion Tensor Imaging) which is a finer representation allowing the visualization of fiber crossings. In Fig.(2.4), is displayed the FA along the principal eigenvector of the reconstructed tensor, where the RGB color map encodes the x-y-z coordinates of the principal eigenvector.

This gives the diffusion tensor for each voxel of the 3D image, which can be of great interest for studying the brain connectivity. From the expression of the DTI, one can estimate the fibers following the principal directions of the ellipsoids. This has create a brand new imaging technique, the tractography [Mori et al., 1999]-[Basser et al., 2000] (see Fig.(2.5)). One can also get a tractography based on HARDI (High Angular Resolution Diffusion Imaging) [Descoteaux et al., 2009].

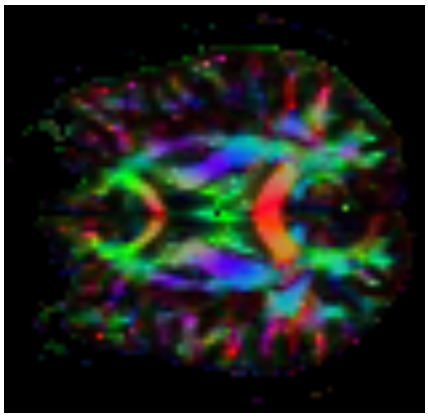

Figure 2.4 – *Axial slice of a FA colored DWI.*

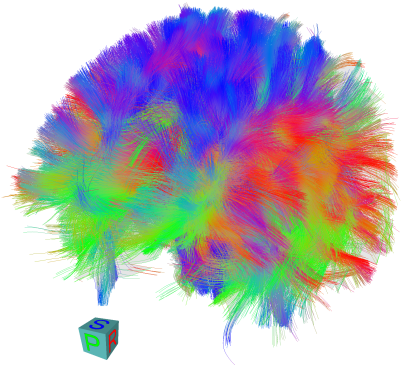

Figure 2.5 – *A 3D view of a tractography via DTI.*

2.1.3.2 Other imaging techniques

Since the skull does not contain much water, it is difficult to reconstruct it from classical MRI. On the other hand, X-rays do interact with the skull. These electromagnetic waves were discovered in 1895 by Wilhelm Röntgen and are considered to be the first medical imaging technique. Even if techniques using X-rays such as the CT (Computed Tomography) appear to be harmless, a long or repeated exposition to these waves can interact negatively with body cells. In Fig.(2.6) is displayed a CT scan of a skull, where the artifacts are some machine components.

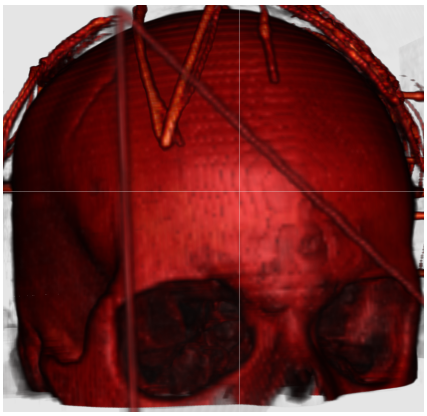

Figure 2.6 – *Computed tomography.*

Ultrasound techniques do not allow for brain imaging, since the skull is very resistant to it. It works fine for soft tissues, muscles and liquids.

These techniques used for brain imaging all provide a scan at one moment, and do not permit the functional study of the organ.

2.1.4 Observing the brain activity

2.1.4.1 Invasive techniques

Positron Emission Tomography (PET) requires the injection of a radioactive material, and obtains images by measuring the radioactive disintegration of the elements introduced and diffused in regions of interest. In PET imaging, the radioactive tracer injected into the body focuses on glucose cells that are consumed in different manner in brain regions. This tracer emits positrons that the system can indirectly measure when they annihilate with electrons through the pair of gamma rays produced: $e^- + e^+ \longrightarrow \gamma + \gamma$. A 3D image is reconstructed through tomography reconstruction, a slice of which can be seen in Fig.(2.7). Red areas correspond to an accumulated radioactivity, then showing indirectly the brain activity through its glucose consumption.

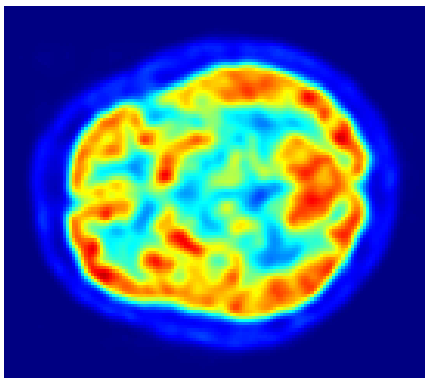

Figure 2.7 – *PET scan of the human brain.*[WIKIPEDIA]

ElectroCorticoGraphy (EcoG) is an imaging technique very close to electroencephalography, for which electrodes are directly placed on a grid onto the exposed surface[1] of the brain in order to record electrical activity of the cortex. A still more invasive technique is stereo electroencephalography (sEEG), in which are inserted depth electrodes within the cortical layers. These techniques thus require a craniotomy, to place the set of electrodes. These modalities are very used nowadays on patients with pharmaco-resistant epilepsy. The signal is treated to get the localization of the epileptogenic zone during a seizure, which can in some cases be removed in order to cure definitively the disease. One must have an insight on the location of the epileptogenic zone a-priori since the measurements can only infer a local activity.

[1]Electrodes may be placed either outside the dura mater (epidural) or under the dura mater (subdural), but in all cases, under the skull.

2.1.4.2 Non invasive techniques

functional MRI (fMRI) Functional MRI is a special MRI scan used to measure the hemodynamic response, which is related to the neural activity of the brain. Oxygen is delivered to neurons via oxyhemoglobin which is a diamagnetic molecule carried by the blood. When neurons are very active, they transform these molecules into desoxyhemoglobin which is paramagnetic. This change leads to small differences in the MR signal, and is called the BOLD signal (Blood-Oxygen-Level Dependence). This change does not operate instantaneously and thus limits the temporal resolution of the fMRI to a few seconds. fMRI is especially appealing for the spatial resolution of the reconstructed map (see Fig.(2.8)), which is at most $2-3$mm, and independent on the location of the sources, which allows for deep source observations which is not possible with EEG. Furthermore, results obtained by fMRI are difficult to interpret since the relation between the neural activity and the BOLD signal is only a correlation, and one cannot infer one from the other.

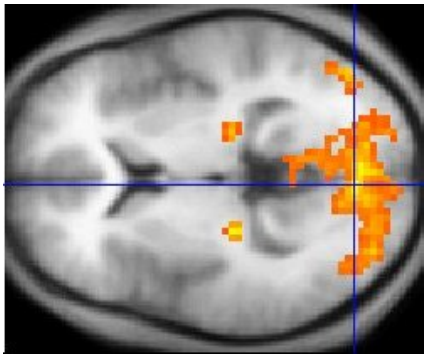

Figure 2.8 – *fMRI statistics (orange) overlaid on an averaged brain.*[WIKIPEDIA]

ElectroEncephalography (EEG) and MagnetoEncephalography (MEG) are two highly non invasive modalities, since they are passive: they do not rely on any externally applied field but directly measure the electromagnetic fields generated by neural activities. Only superficial sources of the brain can be measured, the ones located close to the cortical surface. Both EEG and MEG achieve a very good temporal resolution, about 1ms depending on the sampling frequency. The source localization achieved with their signal has a spatial resolution close to 1cm. Furthermore, the MEG cannot detect sources radially oriented with respect to the skull surface such as sources on top of gyri, while EEG can detect all cortical sources. These modalities will be detailed in sec.(2.2.2).

Fig.(2.9) displays the spatio-temporal resolution of the presented modalities for brain functional imaging. The spatial resolutions for EEG-MEG and EcoG, are the estimated spatial errors when doing source localization from the measured signal, since these modalities do not give a 3D image as PET or fMRI, but rather a

signal which must be interpreted to recover the sources within the brain producing it. Note that the time axis (x-axis) is logarithmic. This graph does not show the different sensitivities with regard to the sources, *e.g.* the MEG does not see radially oriented sources, the EEG only sees superficial sources, and the fMRI signal only measures a correlation correlated with sources activation, the EcoG and sEEG are only sensitive to their immediate neighborhoods.

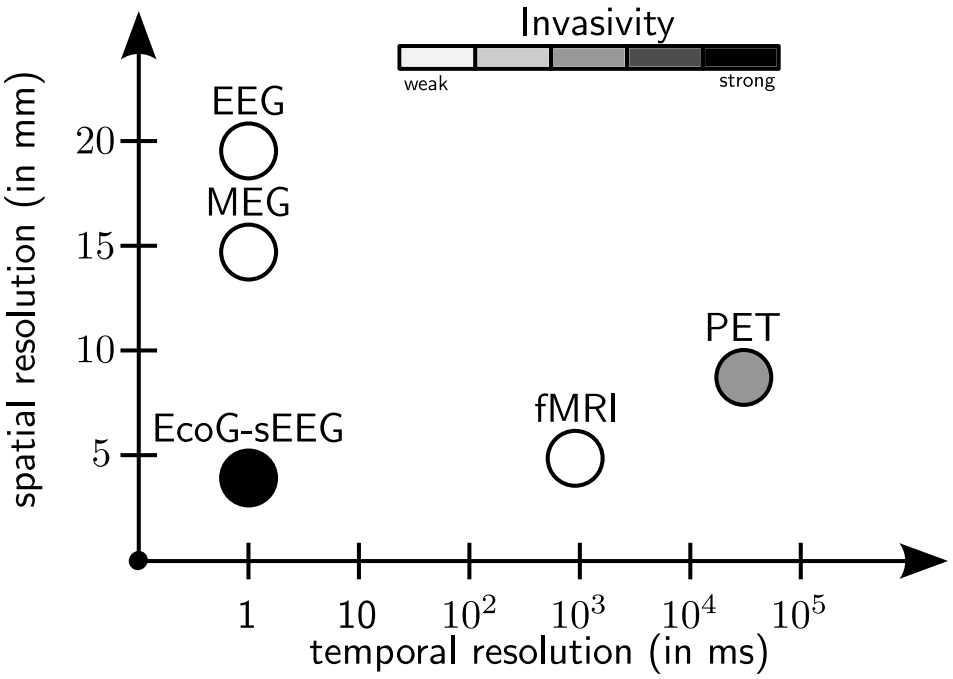

Figure 2.9 – *Spatial and temporal resolutions for functional brain imaging modalities. The darkness of the circles show the degree of invasivity of the technique.*

2.2 EEG-MEG: physical concept, and current applications.

2.2.1 Electromagnetism generators

2.2.1.1 Electrical behavior of a single neuron

As stated section.(2.1), neurons propagate signals called action potentials. A neuron receives multiple input signals (action potentials) through the synapses of its afferent neurons connected to its dendrites or directly to its cell body. From these inputs, the neuron will 'spike' or not *i.e.* transmit action potentials that will then be transmitted through the neuron synapses to other neurons. For most of the neurons the transmission at synapses is done with chemical molecules, neurotransmitters, even if some of them can be electrical synapses. Let us have a look at the mechanism of transmission from one neuron to the other.

Post-Synaptic Potential: (PSP) When an action potential reaches the end of an axon terminal, it releases neurotransmitters, these molecules navigate until they reach another neuron, then their biochemical properties affect the membrane's permeability, so that the ions Na^+ and K^+ penetrate the cell and disturb it from its resting ionic equilibrium. This increases the inner cell potential by 10mV for about 10ms. This phenomena is called the post-synaptic potential.

Action Potential: (AP) If many post-synaptic potentials sum up, the cell's body can reach a threshold which will make it spike. This action potential consists of an increase of 100mV from its resting potential in only 1ms and lasts 2-3ms. The resting potential being the transmembrane voltage which is due to different concentrations in Ca^+ and K^+ inside and outside of the cell. After spiking the resting state is recovered in a few ms, so that the whole phenomenon lasts about 10ms. All processes can be seen in Fig.(2.10). Let us note that the amplitude of the spiking is always the same. Hence, the brain encodes information by frequency modulation and not amplitude modulation.

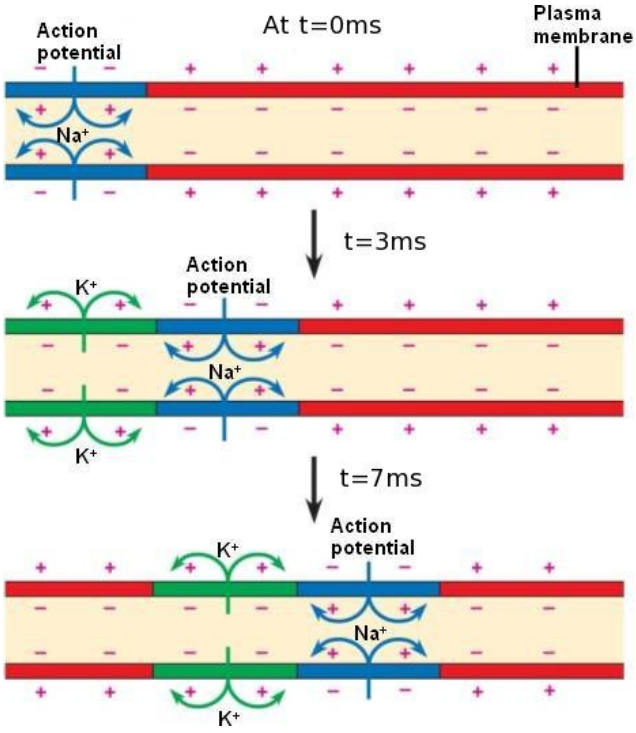

Figure 2.10 – *Action potential propagation along the axon. Red codes for the resting states, Blue for the Action potential, and Green for the recovery.* `http://soe.ucdavis.edu`

The potentials created when the neurons become active, (PSP and AP) create then a displacement of charges and therefore some tiny currents called intracellular or primary current. In order to be able to detect at a distance the electromagnetic

field generated by neurons, these tiny electromagnetic fields have to sum up at a given time. Primary currents due to AP have a temporal duration of about 1 ms, which make them hard to synchronize. On the other hand, the PSP leads to currents with 10 ms duration. Furthermore, when looking at the electromagnetic field created by an AP, it can be represented as a quadrupole *i.e.* the sum of two opposite dipoles at a slightly different position. One can see in Fig.(2.10) middle row this configuration; the positive charges are surrounded by negative ones, which create these opposite currents. At a distance r, a quadrupole influence decreases in r^3, whereas that of a dipole decreases in r^2, this is again a bad point for the AP. In contrast, the PSP generates currents in only one direction (from the synapse to the cell body), and thus have a radius of visibility higher. Finally, for all these PSP currents to sum up, they need to be in the same direction. Such structures do occur in the brain: these well organized and parallel oriented neurons are called pyramidal neurons (cells). It has been estimated that 10^4 neurons must be jointly active to produce a signal detectable by EEG or MEG (see [Murakami and Okada, 2006]).

2.2.1.2 Pyramidal neurons

Pyramidal neurons are cells located in the gray matter which present elongated dendrites all oriented toward the gray matter/CSF interface (apical dendrites). One can see in Fig.(2.11), such a structure whose electric behavior is well represented by a dipole. In the experiments related in [Murakami and Okada, 2006], different

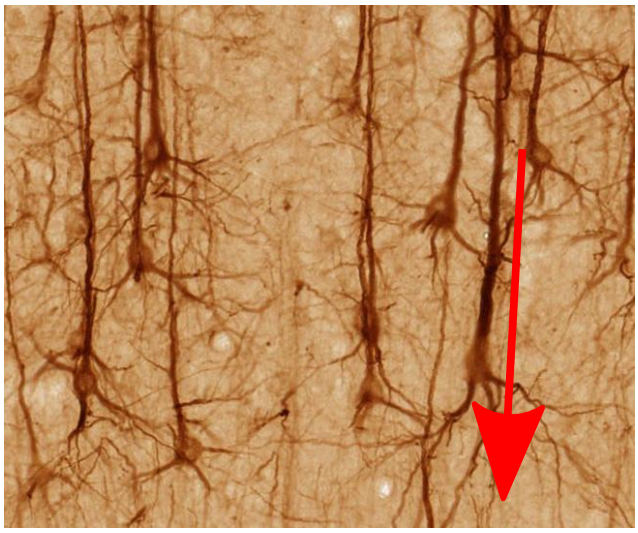

Figure 2.11 – *Pyramidal neurons of a macaque with overlaid a current dipole representing a PSP.* `http://brainmaps.org`

types of neuron have been modeled, and equivalent current dipoles were computed. A current dipole is similar to an electrical dipole except that instead of considering two charges of opposite signs, one considers a current sink and a current source.

See Fig.(2.12) for a superposition of a current dipole on an apical dendrite. In

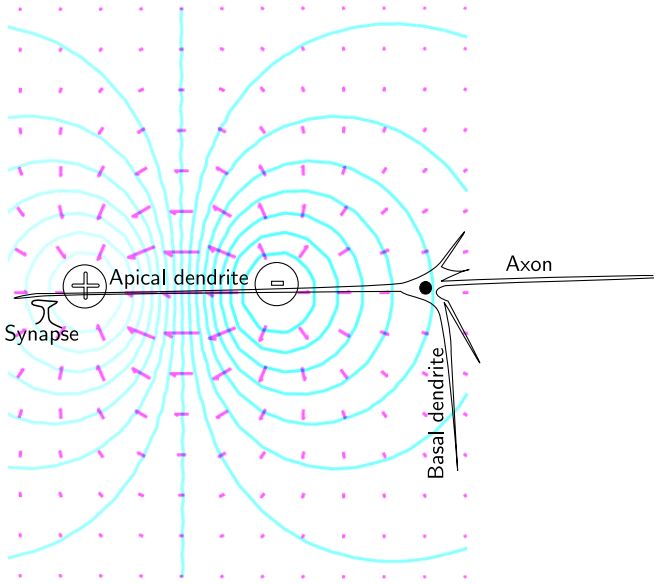

Figure 2.12 – *Electric field (purple arrows) generated by an electric dipole (model for a PSP current). Blue lines represents iso-lines of the potential.*

their experiments, the authors of [Murakami and Okada, 2006] estimated a current dipole with a moment of 1pA for a single pyramidal neuron. The pyramidal cells are very numerous in the gray matter: it has been estimated that an area of $1mm^2$ of the cortex would be detectable, even if in the experiments the minimal detectable area was closer to $100mm^2$ [Hämäläinen et al., 1993].
Let us define a current dipole at location $\mathbf{r}$, and orientation $\mathbf{m}$, its strength is simply the norm of $\mathbf{m}$. One can see Fig.(2.13), the iso current lines for the electric field generated by a dipole (a 2D view, with axial symmetry). For the case of the magnetic field, one can see that the field is only in the plane normal to $\mathbf{m}$ (3D view), this will explain the incapacity of the MEG to detect radial sources (null magnetic field).

2.2.2 EEG and MEG modalities

Electroencephalography (EEG) is a non-invasive technique very useful for studying brain functional activity because of its non invasivity and its high temporal resolution (several orders of magnitude higher than that of the functional MRI on

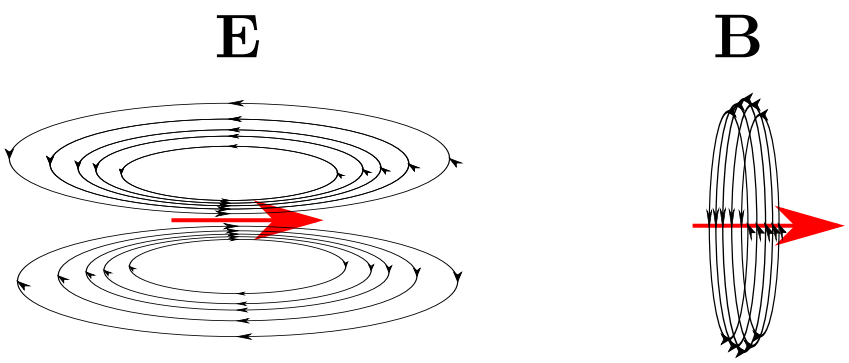

Figure 2.13 – *Electric field (left) and magnetic field (right) generated by a current dipole (in red).*

Fig.(2.9)). Electroencephalography records electrical activity on the scalp. EEG measures voltage fluctuations which result from current flows within the neurons of the brain. The first EEG recording on a human was made in 1929 by the German physiologist Hans Berger. Thanks to the recordings he made with only two electrodes, he could observe changing brain activities depending on whether or not the patient had eyes opened. Later, he also discovered a different electrical phenomenon when recording an epileptic seizure. This analysis was done by analyzing visually the curve shape defined by the poor definition encephalogram (see Fig.(2.14)). Actually, he did not use electrodes placed on the scalp at first, but tiny silver wires

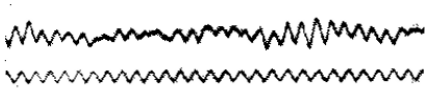

Figure 2.14 – *One of the first EEG signal of a young boy overlaid on a 10Hz signal.*[WIKIPEDIA]

introduced under the scalp. This technique was convenient for assuring a good electrical contact between the device and the head. Nowadays, one can get an EEG recording wearing a helmet with 19 to 256 electrodes (even 512 in some research cases). The electrical contact between electrodes and the scalp is ensured using an electrolyte solution which spreads the contact over a small scalp area. Technical researchers now try to build dry electrodes for convenience [Taheri et al., 1994]. Having more electrodes allows for constructing higher resolutions map of the electrical activity on the scalp.

How far do we need go in adding electrodes on the scalp ?

Actually, the potential on the scalp is quite smooth, furthermore technical limita-

tions due to the use of electrolyte solutions do not allow for too close electrodes. EEG amplitude is less than 10μV, and EEG is amplified by an amplifier that can sample and convert numerically the data with a sampling rate up to 2kHz. Fig.(2.15) displays a typical EEG recording.

Figure 2.15 – *EEG recording for several sensors along time showing an epileptic seizure.*[WIKIPEDIA]

Magnetoencephalography (MEG) appeared 40 years after EEG in 1968. If the brain electrical activity generates an electrical field through the head, it also generates a magnetic field (or from a more general point of view an electromagnetic field). Although this field is very weak (some fT (10^{-15}Tesla)), it propagates outside the head. David Cohen in 1968, invented the field of biomagnetism looking at the magnetic field generated by a pulsing heart with one sensor, a copper induction coil. With such tiny values for the magnetic field one must have highly sensitive detectors. Recalling that the Earth magnetic field is around 50μT=5.10^{-5}T (a billion times larger than brain generated magnetic field), and a typical urban magnetic noise is up to 1μT, have led experimenters to practice in very well shielded rooms. One year later, James E. Zimmerman invented the SQUIDs (Superconducting QUantum Interference Device) which are highly sensitive magnetometers able to measure fields down to 5.10^{-18}T ! David Cohen took advantage of these detectors to measure the first brain activity through magnetic field in a better shielded room at MIT. Current MEG machines work on the same description, but now with a very high number of SQUIDS, often packaged by two to measure a component of the gradient of the magnetic field (gradiometers), that is less noise sensitive. They have around 200 detectors, and some allow for a simultaneous EEG recordings such as shown in Fig.(2.16).

Figure 2.16 – *Modern MEG device and a simultaneous EEG 64-electrode helmet.*

2.2.3 Brain functional imaging with EEG and MEG

The purpose of EEG research is to analyze the brain functions. From a two-sensor EEG recording, Hans Berger could observe different brain rhythms. In this experiment, he observed that the signal contained an important 10Hz oscillation when the subject had his eyes closed. This was the birth of the brain rhythms studies, where only looking at the main brain frequency one has been able to deduce different cognitive states (see Fig.(2.17)). To study brain rhythms, one only needs

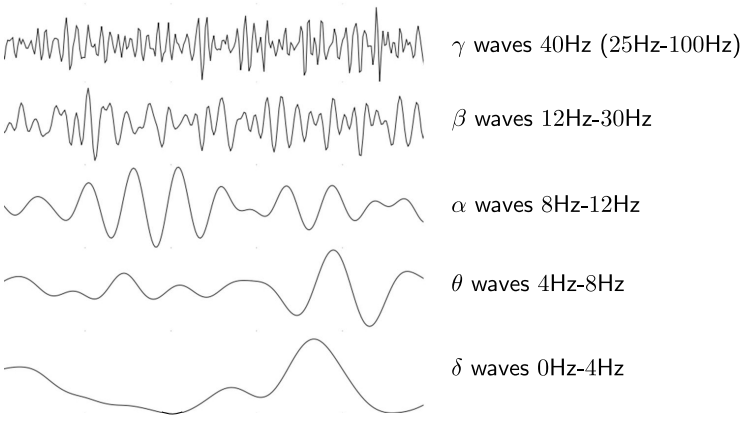

Figure 2.17 – *Brain rhythms.*

a few electrodes (*e.g.* a 19-electrode helmet), and to apply an FFT (Fast Fourier Transform) on the data to get the main frequencies. Inference sometimes depends

on electrode locations. With such simple procedures one established the following observations:

γ **waves:** High brain activity, such as when problem solving or arithmetic calculations.

β **waves:** Busy state, conversation, anxious thinking, 'normal' state.

α **waves:** Occur at the occipital lobes (above the neck), and are signs of a resting state, or closing eyes. They offer the highest amplitude (which is why they were the first to be observed in recordings).

μ **waves:** Appear with the same frequencies as the α waves but at the motor cortex (central scalp), and disappear when the subject is moving or intending to move.

θ **waves:** Are harder to characterize, they appear during REM sleep, and are probably due to the hippocampus which is far from the EEG sensors [Buzsáki, 2002].

By looking at a (EEG or MEG) topography, one can get an insight on the localization of the main brain electrical activity (see Fig.(2.18)). Visually, one gets

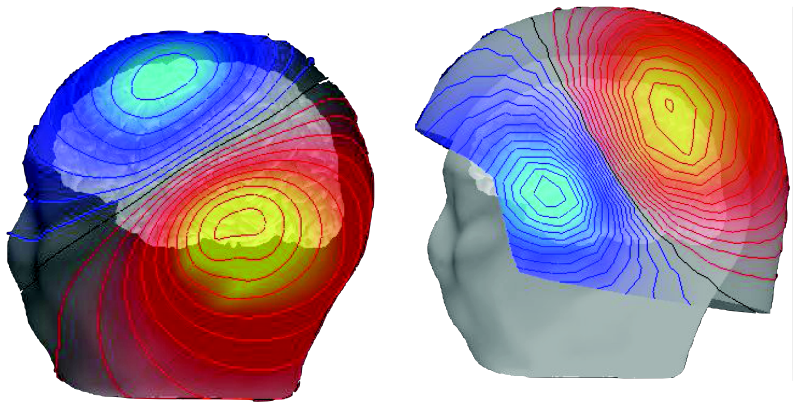

Figure 2.18 – *EEG and MEG topography. from Hämäläinen presentation.*

a rough estimate on the lateralization or the anterior-posterior position, of the source. For example, a physicist could guess from these topographies that the main source present in the signal is oriented tangentially, and located somewhere in the temporal lobe or motor cortex on the left of the patient. From the data acquired, ideally, one would like to localize all the sources within the brain active at a given time. This would have the form of a 3D image (as in fMRI), showing the activity of each part of the brain. Such a case cannot occur as long as we have less data than unknowns. This would tend to answer the question in sec.2.2.2 about the number

of sensors. Following this observation one would need as many sensors as unknowns (at least).
In absence of such a case, one can estimate the parameters (positions/orientations) of dominant sources, this problem is called the MEEG source localization problem:

Given some data on the boundary, find the sources responsible for this signal.

2.2.4 Source localization in MEEG

From MEG or EEG acquisitions, one wishes to recover the electrical sources inside the brain that are responsible for the measured components of the electromagnetic field. This problem is called an inverse problem of localization. Denoting $\mathbf{J}$ the variable representing the brain source activity within the brain volume, we introduce the function f which gives the strict relation between brain sources and the potential at sensors V_s. f indeed comes from the forward problem, which given a source, gives the estimated data that one would observe at sensors. The inverse problem is based on this forward problem. The inverse problem can be formulated for the EEG case as:

$$\text{find } \mathbf{J} \text{ s.t } V_s = f(\mathbf{J}) \ . \tag{2.1}$$

If one could invert the function f, the inverse problem would be solved writing:

$$\mathbf{J} = f^{-1}(V_s).$$

But this problem is largely under-determined, we only have a few hundred data for millions of unknowns (*e.g.* considering $\mathbf{J} \in \mathbb{R}^3 \times \mathbb{R}^3$ a vector field and sampling the brain volume into a 3D image of dimension 128x128x128). One must then resort to finding an approximate solution $\tilde{\mathbf{J}}$ of $\mathbf{J}$, adding *a-priori* hypothesis on the sources; this is the field of inverse problem for source localization in MEEG.

2.2.4.1 What kind of model for sources ?

An *a-priori* hypothesis for the brain electrical activity, is that at a given time, it is sparse spatially; *i.e.* only a few regions of the brain are active simultaneously. 'Active' in the previous sentence means active electrically and detectable by EEG or MEG. One can distinguish two types of model for sources:

dipolar sources represent the PSP activity within a small volume (10^6 neurons [Hämäläinen et al., 1993][Nunez, 1981]). It has 6 parameters for each dipole (3, for the position, 3 for the moment).

distributed sources represent the activity of a small area on a surface. Most often an imaginary interface between the gray-CSF interface and white-gray interface is chosen. The sources are then constrained by the normal of the surface since PSP are oriented normally to the exterior cortex surface. It restrains the number of parameters to estimate.

2.2.5 Inverse problem

The inverse problem of localization is tackled as follow: one seeks to find a solution $\tilde{V_s} = f(\tilde{\mathbf{J}})$ that is close to the measured data V_s:

$$\tilde{\mathbf{J}} = \arg\min_{\mathbf{J}} \|V_s - \tilde{V_s}\| = \arg\min_{\mathbf{J}} \|V_s - f(\mathbf{J})\| \ . \tag{2.2}$$

This problem is ill-posed (Hadamard's sense). A well-posed problem follows the requirements:

- A unique solution exists;
- This solution depends continuously on the data (in some metric).

Problem (2.2) does not fulfill the first requirement since it is an under-determined problem, it thus needs regularization which is achieved adding *a-priori* on the solution. Actually one could think about adding measurements *i.e.* scalp electrodes for EEG, but as discussed in [Ryynänen et al., 2004] it depends on the skull conductivity which blurs the signal, and may not be useful in our case to go beyond 256 electrodes, which is much lower than our number of unknowns. One must then add *a-priori* on the solution.
Many techniques are then possible, adding *a-priori* on the source position through time, or source orientation, or more complex schemes. The methods can be placed in the following categories:

dipole fitting methods Where we place a set of dipoles in a region of interest, and try to estimate their position and moment to fulfill as well as possible the Eq.2.2. For a somato-sensory task, for example, one places dipoles within the region *a-priori* responsible of these task (somato-sensory cortex). Methods of this category include: rotating dipoles, moving dipoles, Minimum Norm,

filtering approaches the space is sampled (often with a Cartesian grid), and one tries to spatially filter the sources from noise and inter-correlation (beam-forming methods). An alternative is to extract multiple signals from the data (using a SVD: Singular Value Decomposition), this is the goal of MUSIC methods (MUltiple SIgnal Classification).

distributed sources the space is sampled on a Cartesian grid in the brain region or the gray matter (with constrained orientations or not). Dipoles are placed at these grid points (often 3 dipoles per grid point, so that all orientations are covered). MinimumNorm methods try to solve the minimization problem enforcing a-priori regularity on the solution; either with L^1 norm (sparsity), L^2 norm (limited energy), ... or combination of these [Gramfort et al., 2008].

2.3 The forward problem

The forward problem consists in simulating sources inside the brain and computing the resulting field at the sensor positions (f in Eq.(2.1)). This resolution is done

by solving Maxwell's equations in their quasi-static approximation on a geometry specific to the subject. Hence, for each subject, one needs the definition of the tissues, *i.e.* the geometry of the different layers and their conductivities. Most of the layers of the head can be extracted from anatomical MRI (Magnetic Resonance Imaging); the skull still presents some difficulties to be extracted and is often approximated by inflating the brain. Conductivities of the layers can be evaluated in different ways ; one can use reference conductivities that have been measured in vivo on test subjects, or one can estimate the conductivity for each subject using Electrical Impedance Tomography [Clerc et al., 2005a].

2.3.1 Maxwell's equations

Maxwell's equation are a set of PDE (partial differential equations), that relate in any medium, the electric field, the magnetic field, the distribution of electrical charges, and the distribution of the currents. These relations are given through partial differential operators with respect to space and time. We refer the reader to page.vii concerning the notations used.

A local formulation: Starting from the relations established by Ampère, Gauss, and Faraday, Maxwell summarized and completed these equations. In their local form, in a vacuum they write:

$$\begin{cases} \nabla \cdot \mathbf{E} = \frac{\rho}{\varepsilon_0} & (a) \\ \nabla \cdot \mathbf{B} = 0 & (b) \\ \nabla \times \mathbf{E} = -\frac{\partial \mathbf{B}}{\partial t} & (c) \\ \nabla \times \mathbf{B} = \mu_0 \mathbf{J} + \mu_0 \varepsilon_0 \frac{\partial \mathbf{E}}{\partial t} & (d) \end{cases} \tag{2.3}$$

For human tissues, the magnetic permeability is the same as the one in the vacuum. For the electric permittivity however, it varies a lot from ε_0 depending on the tissue and frequency studied. Writing $\varepsilon_r = \frac{\varepsilon}{\varepsilon_0}$ the relative permittivity of a medium of permittivity ε, this ratio is around 4.10^8 for gray matter, 1.10^5 for skin at 10Hz [Gabriel et al., 1996b]. In their local form, for a medium with permittivity ε and permeability $\mu = \mu_0$, Eq.(2.3.a) and Eq.(2.3.d) write:

$$\nabla \cdot \mathbf{E} = \frac{\rho}{\varepsilon} \tag{2.4}$$

$$\nabla \times \mathbf{B} = \mu_0 \mathbf{J} + \mu_0 \varepsilon \frac{\partial \mathbf{E}}{\partial t} \tag{2.5}$$

$$\tag{2.6}$$

The Quasi-static assumption: When considering these equations for EEG or MEG problems, one can neglect the time derivatives (see [Hämäläinen et al., 1993]). This is due to the typical scale of our problems; a head is less than a meter diameter, and the time scale of about 10ms (typical electrical activity of PSP). One can

then re-write equations (2.3):

$$\begin{cases} \nabla \cdot \mathbf{E} = \frac{\rho}{\varepsilon} & (a) \\ \nabla \times \mathbf{E} = 0 & (b) \\ \nabla \cdot \mathbf{B} = 0 & (c) \\ \nabla \times \mathbf{B} = \mu_0 \mathbf{J} & (d) \end{cases} \tag{2.7}$$

The magnetic field and the electric field are then decoupled, and which makes it possible to solve them independently.

2.3.1.1 A Poisson equation for the electric potential

Equation.(2.7b.) implies that $\mathbf{E}$ derives from a scalar potential field, which is the electrical potential V, and also by definition, the electric field points from high potentials to region with low potentials:

$$\nabla \times \mathbf{E} = 0 \Longrightarrow \mathbf{E} = -\nabla V \tag{2.8}$$

The field $\mathbf{E}$ is fully determined by V, and V is defined up to a constant. Using now Eq.(2.7d.), and taking its divergence yields:

$$\nabla \cdot (\nabla \times \mathbf{B}) = \nabla \cdot (\mu_0 \mathbf{J}) = 0.$$

Thus the total amount of current density is divergence free. Now splitting $\mathbf{J}$ into its component due to the primary current source, denoted $\mathbf{J}^{\mathrm{p}}$ (the one generated by the PSP), and the passive Ohmic current due to the resistive material (of conductivity σ) being crossed writes:

$$\nabla \cdot \mathbf{J} = \nabla \cdot \mathbf{J}^{\mathrm{p}} + \nabla \cdot (\sigma \mathbf{E}) = 0$$

This equation is a Poisson equation relating the potential in the head domain, and the primary current source $\mathbf{J}^{\mathrm{p}}$, using Eq.(2.8) we obtain the following equation which this thesis will aim at solving: to solve:

$$\boxed{\nabla \cdot (\sigma \nabla V) = \nabla \cdot \mathbf{J}^{\mathrm{p}}} \tag{2.9}$$

2.3.1.2 The Biot-Savart law for a magnetic field equation

Taking the curl of Eq.(2.7d.) and expanding it with the use of Eq.(2.7c.):

$$\nabla \times \nabla \times \mathbf{B} = \nabla(\nabla \cdot \mathbf{B}) - \Delta \mathbf{B} = -\Delta \mathbf{B} = \mu_0 \nabla \times \mathbf{J}, \tag{2.10}$$

we obtain a set of Poisson equations on the three coordinates of the vector field $\mathbf{B}$. Knowing the fundamental solution of the Laplace equation $\Delta G = \delta$ to be: the Green function

$$G(\mathbf{r}) = \frac{-1}{4\pi \|\mathbf{r}\|}$$

We now use the convolution product in the sense of distribution, so that the solution to Eq.(2.10) writes:

$$\mathbf{B}(\mathbf{r}) = \frac{\mu_0}{4\pi}\int_{\mathbb{R}^3} \nabla \times \mathbf{J}(\mathbf{r}')\frac{1}{\|\mathbf{r}-\mathbf{r}'\|}d\mathbf{r}' + \mathbf{B}_H,$$

where $\mathbf{B}_H$ is an homogeneous solution to Eq.(2.10). Imposing a null magnetic field at infinity leads to set $\mathbf{B}_H$ to zero, we then integrate by parts and get:

$$\begin{aligned}
\mathbf{B}(\mathbf{r}) &= \frac{\mu_0}{4\pi}\int_{\mathbb{R}^3} \mathbf{J}(\mathbf{r}') \times \nabla\left(\frac{1}{\|\mathbf{r}-\mathbf{r}'\|}\right) d\mathbf{r}' \\
&= \frac{\mu_0}{4\pi}\int_{\mathbb{R}^3} \mathbf{J}(\mathbf{r}') \times \left(\frac{\mathbf{r}-\mathbf{r}'}{\|\mathbf{r}-\mathbf{r}'\|^3}\right) d\mathbf{r}' \\
&\quad \{\text{now splitting } \mathbf{J} \text{ into its primary current and passive components}\} \\
&= \frac{\mu_0}{4\pi}\int_{\mathbb{R}^3} \mathbf{J}^{\mathrm{p}}(\mathbf{r}') \times \left(\frac{\mathbf{r}-\mathbf{r}'}{\|\mathbf{r}-\mathbf{r}'\|^3}\right) d\mathbf{r}' - \frac{\mu_0}{4\pi}\int_{\mathbb{R}^3} \sigma\nabla V(\mathbf{r}') \times \left(\frac{\mathbf{r}-\mathbf{r}'}{\|\mathbf{r}-\mathbf{r}'\|^3}\right) d\mathbf{r}' \\
\mathbf{B}(\mathbf{r}) &= \mathbf{B}_0(\mathbf{r}) - \frac{\mu_0}{4\pi}\int_{\mathbb{R}^3} \sigma\nabla V(\mathbf{r}') \times \left(\frac{\mathbf{r}-\mathbf{r}'}{\|\mathbf{r}-\mathbf{r}'\|^3}\right) d\mathbf{r}' \ , \qquad (2.11)
\end{aligned}$$

$$\text{where} \qquad \mathbf{B}_0(\mathbf{r}) = \frac{\mu_0}{4\pi}\int_{\mathbb{R}^3} \mathbf{J}^{\mathrm{p}}(\mathbf{r}') \times \left(\frac{\mathbf{r}-\mathbf{r}'}{\|\mathbf{r}-\mathbf{r}'\|^3}\right) d\mathbf{r}' \ . \qquad (2.12)$$

The magnetic field at any point $\mathbf{r}$ can then be written summing up the contributions of the two currents. Let us note that the term $\mathbf{B}_0$, called the primary magnetic field, only depends on the primary current and not on the conductivities of the crossed media, thus not either on the patient head geometry. This will be a main difference between MEG and EEG when solving their forward problems, since the Poisson equation in (2.9) strongly depends on the patient head modeling (geometry and conductivity), while the primary magnetic field is not sensitive to it.

2.3.2 Electrophysiological models

In order to solve the forward problem with the Poisson equation.(2.9), or the Biot-Savart equation.(2.12), one must have the description of the geometry shape and the conductivities of the tissues of the patient head. MEG and EEG forward problems do not share the same sensitivity with regards to the geometric modeling or the conductivity profile. Actually, the primary magnetic field is paramount in the expression of $\mathbf{B}$, and can be computed analytically without a head model. However, one would introduce considerable errors not computing the passive Ohmic current contribution to the magnetic field. A human head can be considered to be a bounded volume conductor when neglecting the current flow through the neck. The electric current does not propagate outside the head since the air has negligible conductivity.
One can then define a head as a set of volume conductors, partitioning where it is relevant, the head into regions with different conductivity profiles. We define a relevant partitioning as a splitting of the head domain into regions of very changing conductivity profile. Considering an homogeneous volume conductor for

the head would be a really coarse approximation since the skull structure makes it very low-conductive when compared to other head tissues. Considering the skull conductivity profile is crucial when solving a forward EEG problem, since it lies in between the sources and the sensors. On the other hand, for the forward MEG problem it less important to take the skull into account. Since the primary magnetic field is independent of the conductivities, and the passive Ohmic current is proportional to the conductivity of the medium considered, thus not really affected by the skull nor by the scalp in which, because of the shielding effect of the skull, do not lie big Ohmic currents. Assigning isotropic or anisotropic conductivities to each region is still challenging today, in-vivo measurements being almost impossible and subject to variability [Baysal and Haueisen, 2004, Lai et al., 2005], this problem will be addressed later, considering for the moment that the conductivity of the skull is considered to be between 15 and 80 times lower than the one of the scalp [Bashar et al., 2009].

In the rest of this section we now present different electrophysiological models, starting from a coarse geometric description of a head with nested spherical volume conductors and piecewise homogeneous conductivities, and ending with a realistic head shape extracted from anatomical MRI and associated with appropriate conductivity profiles for each region considered.

2.3.2.1 Spherical volume conductors

Considering the head as nested spherical conductors such as shown Fig.(2.19) has been the first model for solving the forward EEG problem [Rush and Driscoll, 1968, Meijs and Peters, 1987]. In this figure, the head domain Ω is split into three different regions $\Omega_1, \Omega_2, \Omega_3$ with respective conductivities $\sigma_1, \sigma_2, \sigma_3$. The common model used for a forward EEG problem considers Ω_1 to be the 'brain', Ω_2 the skull and Ω_3 the scalp with respective relative radii $0.87, 0.92, 1$. This model presents several

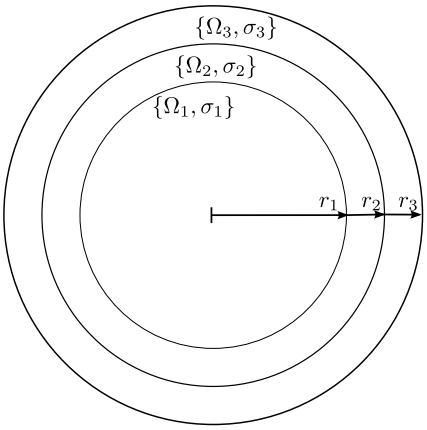

Figure 2.19 – *A three-layer spherical head model.*

advantages. The geometry of the patient does not have to be known, we only need to fit approximately one sphere on the patient head. The solution of the forward problem equations (2.9)-(2.12) can be solved analytically, and thus very fast, which is a pro for real time source localization for example [Spinelli et al., 2000]. But the main con is on the geometry modeling, which does not conform exactly to any surface. A step forward in the head modeling has been done considering ellipsoidal description for the volume conductors (see Fig.(2.20)), equations can still be solved analytically [De Munck, 1988, Kariotou, 2004].

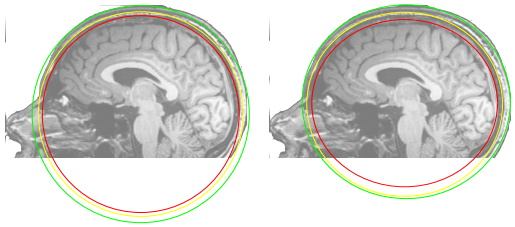

Figure 2.20 – *A spheroidal model on the left and ellipsoidal on the right approximating the head geometry.*

But still, the geometry approximation leads to considerable errors at least for the forward EEG problem [Cuffin, 1996, Huiskamp et al., 1999]. Even for the MEG forward problem, it is considered that concentric spherical models are not good enough when compared to realistic one [Van Uitert and Johnson, 2002], instead a spherical model per squid centered is used, which minimize some geometric errors [Huang et al., 1999] (see [Lalancette et al., 2011] for other similar cases). A step forward in the geometrical head modeling is to consider realistic geometries.

2.3.2.2 Piecewise homogeneous volume conductors

Segmenting an anatomical MRI, one can extract different surfaces of a head, such as the white/gray matter interface, the gray-CSF interface, the CSF-skull interface, the skull-scalp interface and finally the scalp-air interface. In Fig.(2.21), one can see some of the extracted surfaces obtained using the open-source software Freesurfer [Dale et al., 1999, Fischl et al., 1999] which uses a brain atlas. Using a T2-weighted MRI, one can detect the CSF and the soft bone, the skull is often inferred from these. For acquisition of the hard bone people rather use proton density MRI (a kind of sequence).
Using such a piecewise model, the geometry description now conforms with the patient head but requires at least the anatomical MRI. If the MRI is not available, a common approach considers using template meshes generated on the average of several segmented MRI [Darvas et al., 2006].
In such a model a scalar conductivity is assigned for each region. One limitation of this model comes from the fact that some of the head tissues cannot be consid-

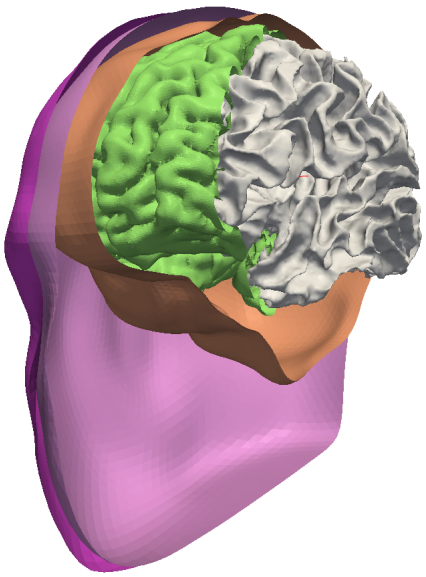

Figure 2.21 – *High definition of triangulated surfaces from segmented MRI: (fushia)-scalp-(mauve)-skull-(orange)-CSF-(green)-gray matter-(gray)-white matter.*

ered to have a constant and isotropic conductivity. This lead us to more refined modeling, allowing now for all kinds of conductivity profiles.

2.3.2.3 Inhomogeneous and anisotropic models

The skull has a layered structure, and in some parts, where it is thickest, it is composed of a layer of soft bone lying in between two layers of hard bone. The soft bone conductivity can be 4 to 7 times higher than the hard one [Akhtari et al., 2002, Ramon et al., 2006]. This increases the tangential conductivity which has led the community to consider an anisotropic description for the skull conductivity. The piecewise model previously discussed could represent the skull with tiny compartments for the soft bone, but it will require an accurate geometry of the skull (with soft and hard bone, thus CT-scan, T2-MRI as well the T1-MRI), and then such small regions will lead in the numerical methods solving the EEG forward equation to very tiny elements which can be annoying in some cases.
The white matter is also another example of tissue showing anisotropy. As it is composed of bundle of fibers due to the neuron axons, it conducts more in the direction of the fibers than in the tangential one. This should be dealt with an accurate description of the inhomogeneous electrical tensor.

2.3.2.4 Assigning conductivities to brain tissues

In order to get a proper forward problem resolution, one must estimate precisely the different conductivities. This is a challenging task and different opinions can be considered.

In-vivo, and in-vitro measurements In-vivo measurements are very rare because they require invasive experiments, in-vitro measurements are however more common [Gabriel et al., 1996a]-[Gabriel et al., 1996b]. The main issue regarding in vitro conductivities measurements, is that the tissue behaves differently than in its living environment, and at body temperature. In-vivo measurements are closer to real conductivities, and have led to corrections, for example, in [Baumann et al., 1997], we learn that the CSF conductivity was under-estimated of about 44% between 1977-1997. In [Hoekema et al., 2003], the skull conductivity of several subjects in epilepsy surgery was measured as well as a post-mortem piece of skull. The conductivities of the craniotomy was much bigger than the one used by the community and also the one of the post-mortem skull, but suffered from high variability between subjects. Actually, the skull conductivity highly depends on the age of the person. That is why the next methods are seductive. See [Lai et al., 2005] for the brain to skull conductivity ratio.

Electrical impedance tomography (EIT) is a technique similar to EEG. Instead of measuring the potential at sensors due to the brain electrical activity, one can consider injecting a current at a pair of electrodes so that, one can calibrate the conductivity values by considering the potential measured on the other sensors. This is called EIT (see [Kybic et al., 2006]). One can estimate the tissues conductivities for each patient specifically, before the clinical or research experiment. A study on the sensitivity on these conductivities with EIT is done in [Vallaghé and Clerc, 2009], where it is shown that the scalp/skull ratio of conductivities can be well estimated.

Evoked potential In order to calibrate the conductivities of the other tissues, one can consider having the solution of the inverse problem, and then estimate the conductivities, such that the forward problem agrees with the measurements in terms of their topography. For example, knowing the location of the left somatosensory sensitivity, one can make an experiment, where the subject is stimulated in this region, and analyze the results, so that they agree with the forward modeling [Gonçalves et al., 2003].

Conductivities used in our experiments Table (2.1) lists the conductivities we will use. It is based on the previous articles and the extensive survey done in [Dannhauer et al., 2010]. We also show the normalized conductivities which are commonly used since solving a forward problem on a computer can be done similarly with real conductivities or normalized ones. The anisotropic ratio is, for the skull, the radial conductivity compared to the tangential one *i.e.* $\frac{\sigma_{radial}}{\sigma_{tangential}}$. And

for the white matter it corresponds to the ratio $\frac{\sigma_{transverse}}{\sigma_{longitudinal}}$ which multiplies the conductivity along the white matter fibers. In Chap.7 we will study this matter in more detail.

Tissues	Conductivities S/m	Normalized isotropic	Anisotropic ratio
Brain	0.33	1.	
Gray Matter	0.33	1.	
White Matter	0.33	1	1 : 10
Skull	0.01	0.03	1 : 1.5
Scalp	0.33	1.	

Table 2.1 – *Conductivities of the human head tissues.*

2.4 Solving the forward problems

Let us recall the forward EEG problem to be solved for V in a domain Ω with boundary Γ (scalp-air interface):

$$\begin{cases} \nabla \cdot \sigma \nabla V = \nabla \cdot \mathbf{J}^{\mathrm{p}} & \text{in } \Omega \\ \sigma \nabla V \cdot \mathbf{n} = 0 & \text{on } \Gamma \end{cases}, \tag{2.13}$$

where $\mathbf{n}$ denotes the normal to the external surface.

On simple geometries such as an unbounded homogeneous medium, or spherical/elliptic head models with piecewise constant conductivities, one can derive the analytical formulas. These solutions provide a very high accuracy compared to the ideal solution, since no hypothesis are introduced, neither on the model, nor on the solution. For the case of EEG for example, the analytical expression requires an infinite sum which is truncated in real situations and thus approximated.

2.4.1 Analytical solutions in spherical geometry

2.4.1.1 EEG spherical model

In a spherical geometry, the use of spherical harmonics is judicious. A harmonic function f (*i.e.* *s.t* $\Delta f = 0$) can be written in spherical coordinates (r, θ, ϕ) as:

$$f(r,\theta,\phi) = \sum_{l=0}^{\infty} \sum_{m=-l}^{l} \left(A_{lm} r^{-l-1} + B_{lm} r^{l} \right) P_l^m(\cos(\theta)) \cos(m\phi) \ , \tag{2.14}$$

where A_{lm} and B_{lm}, are the coefficients which will be determined so that boundary conditions and continuity through interfaces hold. P_m^l is an associated Legendre function:

$$P_m^l(\cos(\theta)) = (-1)^m \sin^m(\theta) \frac{d^m P_l(\cos(\theta))}{d \cos^m(\theta)}, \tag{2.15}$$

and P_l are Legendre polynomials.
Such functions can be used to represent the potential V in each domain where it is harmonic. In the domain where the source term is located, one gets a slightly different expression to represent the potential. This leads to a linear system to be solved whose unknowns are the coefficients A, B for each domain.
Such methods can be found in [Hédou, 1997]. Other formulations which appear to be faster, are possible when one only wants the potential at some points (or sensors) lying on the external surface, this was done by [Berg and Scherg, 1994]. It consist in adding dipole terms in a 1-layer homogeneous model, so that it approximates a multi-layer model. This can also be done for anisotropic layers (tangential/normal anisotropy) [Zhang, 1995]. This is the formulation we will use to validate other methods on spherical models for EEG.

2.4.1.2 MEG spherical model

Let us recall the Biot-Savart equation (stated in Eq.(2.12)) which the magnetic field satisfies:

$$\mathbf{B}(\mathbf{r}) = \mathbf{B}_0(\mathbf{r}) - \frac{\mu_0}{4\pi} \int_{\mathbb{R}^3} \sigma \nabla V(\mathbf{r}') \times \left(\frac{\mathbf{r} - \mathbf{r}'}{\|\mathbf{r} - \mathbf{r}'\|^3} \right) d\mathbf{r}' \ . \tag{2.16}$$

Consider the geometry described in Fig.2.22. First of all, the integral in Eq.(2.16)

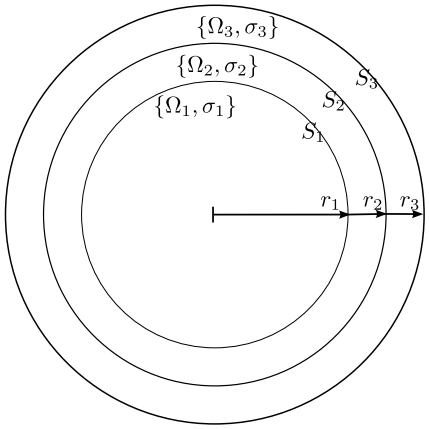

Figure 2.22 – *A three-layer spherical head model.*

does not need to be computed in all 3D space, since σ is zero in the air. Then one can split the integral over the total computational domain Ω, into the sum of the integrals over the constant sub-domains Ω_k in order to use the Stokes theorem, and get to a surfacic writing of the previous equation on each interface $S_k = \partial\Omega_k \cap \partial\Omega_{k+1}$ with normal $\mathbf{n}_k(\mathbf{r}') = \frac{\mathbf{r}'}{\|\mathbf{r}'\|}$:

$$
\begin{aligned}
\mathbf{B}(\mathbf{r}) &= \mathbf{B}_0(\mathbf{r}) - \frac{\mu_0}{4\pi}\sum_k \sigma_k \int_{\Omega_k} \nabla V(\mathbf{r}') \times \left(\frac{\mathbf{r}-\mathbf{r}'}{\|\mathbf{r}-\mathbf{r}'\|^3}\right) d\mathbf{r}' \\
&= \mathbf{B}_0(\mathbf{r}) - \frac{\mu_0}{4\pi}\sum_k \sigma_k \int_{\Omega_k} \nabla V(\mathbf{r}') \times \nabla \left(\frac{1}{\|\mathbf{r}-\mathbf{r}'\|}\right) d\mathbf{r}' \\
&= \mathbf{B}_0(\mathbf{r}) - \frac{\mu_0}{4\pi}\sum_k \sigma_k \int_{\Omega_k} \nabla \times \left(V(\mathbf{r}')\nabla\left(\frac{1}{\|\mathbf{r}-\mathbf{r}'\|}\right)\right) - V(\mathbf{r}')\nabla \times \nabla \left(\frac{1}{\|\mathbf{r}-\mathbf{r}'\|}\right) d\mathbf{r}' \\
&= \mathbf{B}_0(\mathbf{r}) - \frac{\mu_0}{4\pi}\sum_k \sigma_k \int_{\Omega_k} \nabla \times \left(V(\mathbf{r}')\left(-\frac{\mathbf{r}-\mathbf{r}'}{\|\mathbf{r}-\mathbf{r}'\|^3}\right)\right) d\mathbf{r}' \\
&= \mathbf{B}_0(\mathbf{r}) - \frac{\mu_0}{4\pi}\sum_k \sigma_k \int_{\partial\Omega_k} \left(V(\mathbf{r}')\left(\frac{\mathbf{r}-\mathbf{r}'}{\|\mathbf{r}-\mathbf{r}'\|^3}\right)\right) \times \mathbf{ds}' \\
&\quad \{ \text{ as we are dealing with nested geometries: } \} \\
&\quad \int_{\partial\Omega_k} \mathbf{ds}' = \int_{S_k} \mathbf{n}_k(\mathbf{r}')d\mathbf{s}' - \int_{S_{k-1}} \mathbf{n}_k(\mathbf{r}')d\mathbf{s}' \text{ if } S_{k-1} \text{ exists} \\
&= \mathbf{B}_0(\mathbf{r}) + \frac{\mu_0}{4\pi}\sum_k (\sigma_{k+1}-\sigma_k) \int_{S_k} V(\mathbf{r}') \left(\frac{\mathbf{r}-\mathbf{r}'}{\|\mathbf{r}-\mathbf{r}'\|^3}\right) \times \mathbf{n}_k(\mathbf{r}')d\mathbf{s}' \qquad (2.17)
\end{aligned}
$$

Expression (2.17) for the magnetic field is due to [Geselowitz, 1970], and also holds for non-spherical geometries.
As all SQUID sensors, magnetometers and gradiometers, provided by manufacturers are generally oriented radially with respect to the patient scalp, let us look at the radial component of the magnetic field $\mathbf{B}(\mathbf{r}) \cdot \frac{\mathbf{r}}{\|\mathbf{r}\|}$, which is easy to express, since this scalar product with a vector normal to $\mathbf{n}_k$ is zero. Which means that only the primary magnetic field is involved in the radial component of the magnetic field: $\mathbf{B}(\mathbf{r}) \cdot \frac{\mathbf{r}}{\|\mathbf{r}\|} = \mathbf{B}_0(\mathbf{r}) \cdot \frac{\mathbf{r}}{\|\mathbf{r}\|}$.

Concerning the total magnetic field outside of a spherical head model generated by a dipole, there exists a really simple closed form due to [Sarvas, 1987] which does not even depend on the conductivity of each layer. Let us derive it for a dipolar source $\mathbf{J}^{\mathrm{p}} = \mathbf{m}\delta_{\mathbf{r}_0}$, first noticing that $\nabla \times \mathbf{B} = 0$ outside Ω (because of Eq.(2.7)d). Then $\mathbf{B}$ derives from a magnetic scalar potential which we call U, such that: $\mathbf{B} = -\nabla U$. Since Eq.(2.7)c), U is harmonic *i.e.* $\Delta U = 0$, and one can select it so that U vanishes at infinity. Starting from a point $\mathbf{r} \notin \Omega$, and integrating along the radial direction ($\mathbf{e}_r = \frac{\mathbf{r}}{\|\mathbf{r}\|}$) to infinity, permits us to write $U(r)$ with the

following line integral:

$$\begin{aligned}
U(\mathbf{r}) &= -\int_0^{+\infty} \nabla U(\mathbf{r}+t\mathbf{e}_r)\cdot\mathbf{e}_r dt \\
&= \int_0^{+\infty} \mathbf{B}(\mathbf{r}+t\mathbf{e}_r)\cdot\mathbf{e}_r dt \\
&= \int_0^{+\infty} \mathbf{B}_0(\mathbf{r}+t\mathbf{e}_r)\cdot\mathbf{e}_r dt \\
&= \int_0^{+\infty} \frac{\mu_0}{4\pi}\int_{\mathbb{R}^3} \mathbf{m}\delta_{\mathbf{r}_0}(\mathbf{r}')\times\left(\frac{\mathbf{r}+t\mathbf{e}_r-\mathbf{r}'}{\|\mathbf{r}+t\mathbf{e}_r-\mathbf{r}'\|^3}\right)d\mathbf{r}'\cdot\mathbf{e}_r dt \\
&= \frac{\mu_0}{4\pi}\int_0^{+\infty} \mathbf{m}\times\left(\frac{\mathbf{r}+t\mathbf{e}_r-\mathbf{r}_0}{\|\mathbf{r}+t\mathbf{e}_r-\mathbf{r}_0\|^3}\right)\cdot\mathbf{e}_r dt \\
&= \frac{\mu_0}{4\pi}\left(\mathbf{m}\times(\mathbf{r}-\mathbf{r}_0)\right)\cdot\mathbf{e}_r\int_0^{+\infty}\left(\frac{1}{\|\mathbf{r}+t\mathbf{e}_r-\mathbf{r}_0\|^3}\right)\cdot dt \\
&= \frac{-\mu_0}{4\pi}\frac{(\mathbf{m}\times\mathbf{r}_0)\cdot\mathbf{r}}{F},
\end{aligned}$$

where the expression of F is, denoting $\mathbf{a}=\mathbf{r}-\mathbf{r}_0$, $a=\|\mathbf{a}\|$ and $r=\|\mathbf{r}\|$: $F = a(ra+r^2-\mathbf{r}_0\cdot\mathbf{r})$. Then the total magnetic field $\mathbf{B}$ writes:

$$\mathbf{B}(\mathbf{r}) = \frac{\mu_0}{4\pi F^2}\left(F\mathbf{m}\times\mathbf{r}_0 - (\mathbf{m}\times\mathbf{r}_0\cdot\mathbf{r})\nabla F\right), \tag{2.18}$$

where $\nabla F = (r^{-1}a^2 + a^{-1}\mathbf{a}\cdot\mathbf{r} + 2a + 2r)\mathbf{r} - (a+2r+a^{-1}\mathbf{a}\cdot\mathbf{r})\mathbf{r}_0$. This formulation is due to [Sarvas, 1987].

The computation of the magnetic field generated by a dipole in a spherical model then leads to a closed form which can be evaluated by hand.
This case is an exception, and nowadays computations are done on computer, in which everything stored is finite, one need to discretize each parameter of the forward problem to solve it: the geometry, the conductivity values, the sensors and the sources, and even harder, represent the partial differential equation in Eq.(2.13) in a discrete form.
The simplest way to discretize a PDE is writing the differential operator as finite differences which approximate these operators. In the following section we will introduce several numerical methods to solve our Poisson equation, namely the FDM (finite difference method), FEM (finite element method), and BEM (boundary element method).

2.4.2 Finite Difference Method

It consists in discretizing each element of the equations stated in (2.13)-(2.12), most of the time, sampling the 3 directions of the space with a length h, so that a derivative in one axis direction writes:

$$\frac{\partial f}{\partial x}(\mathbf{r}_0) = \lim_{\varepsilon\to 0}\frac{f(\mathbf{r}_0+\frac{\varepsilon}{2})-f(\mathbf{r}_0-\frac{\varepsilon}{2})}{\varepsilon} \simeq \frac{f(\mathbf{r}_0+\frac{h}{2})-f(\mathbf{r}_0-\frac{h}{2})}{h} \tag{2.19}$$

One can get the value of f at point $x+\frac{h}{2}$ with x a grid point, interpolating between the two values of its neighbors.
The operator $\nabla \cdot \sigma \nabla V$ can be discretized using a seven-point scheme:

$$\alpha_0 V(\mathbf{r}_0) - \sum_{i=1}^{6} \alpha_i V(\mathbf{r}_i) \ , \tag{2.20}$$

where the $\mathbf{r}_i$ are the neighbors of $\mathbf{r}_0$ on a 3D Cartesian grid. Coefficients α_i and α_0 depend on the conductivities σ_i at positions $\mathbf{r}_i$:

$$\alpha_i = 2h\frac{\sigma_0\sigma_i}{\sigma_0+\sigma_i} \quad \alpha_0 = \sum_{i=1}^{6} \alpha_i \tag{2.21}$$

It can be seen as the Kirchoff's law, which states that at a point in an electrical circuit, the sum of the in and out currents is zero. The divergence operator can be discretized using a similar scheme. A dipolar source term is enforced strongly, most often assigning a high value at two grid points (to represent the two poles). Doing this for all grid points yields a linear system which is very well structured (band matrix), and very sparse. See [Hédou-Rouillier, 1999] and [Dang and Ng, 2011] for fast implementations.

2.4.3 Boundary Element Method

2.4.3.1 Common formalism

Let us introduce some notations regarding the solving of the electric Poisson equation defined in Eq.(2.13). Considering the nested geometry displayed in Fig.(2.23), this equation can broken down in each sub-domain Ω_i. As the conductivity σ is considered to be constant in each sub-domain, the potential V satisfies in each domain Ω_i:

$$\sigma_i \Delta V = f_i \ , \forall i \in \{1..N\}, \tag{2.22}$$

The term f_i defines the restriction of the source term $\nabla \cdot \mathbf{J}^{\mathrm{p}}$ to Ω_i; *i.e.* the dipoles inside the layer Ω_i. At interfaces, here denoted S_i, we enforce the continuity of the variable V as well as the normal current $\sigma\partial_n V$, it means that the 'jump' across S_i (between two sub-domains) is zero:

$$[V]_{S_i} = 0 \tag{2.23}$$

$$[\sigma\partial_n V]_{S_i} = 0. \tag{2.24}$$

In this expression, the jump of a function f is defined as the difference between the value of the function f at all points $\mathbf{r} \in S_i$ from one side to the other:

$$[f]_{S_i} = f^-_{S_i} - f^+_{S_i} \tag{2.25}$$

$$\text{with} \quad f^{\pm}_{S_i} = \lim_{\alpha \to 0^{\pm}} f(\mathbf{r}+\alpha\mathbf{n}) \tag{2.26}$$

where $\mathbf{n}$ denotes the outward normal of the surface, as seen in Fig.(2.23) with black arrows.

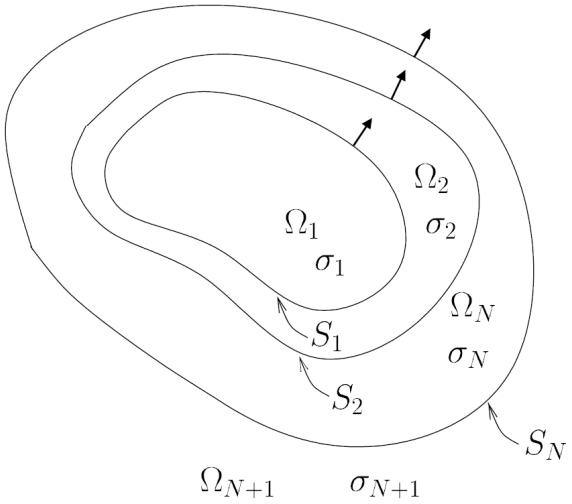

Figure 2.23 – *Nested regions with constant conductivities.*

2.4.3.2 A Green formula and its application to EEG due to Geselowitz

Green's equations Taking two functions u and v twice continuous and differentiable on the open set $\Omega \subset \mathbb{R}^3$, and writing the divergence theorem for the functions $u\nabla v$ and $v\nabla u$ successively gives:

$$\begin{aligned}\int_\Omega \nabla\cdot(u\nabla v)d\mathbf{r}' &= \int_{\partial\Omega}(u\nabla v)\cdot\mathbf{n}'\,d\mathbf{s}' = \int_\Omega \nabla u\cdot\nabla v d\mathbf{r}' + \int_\Omega u\Delta v d\mathbf{r}'\\ \int_\Omega \nabla\cdot(v\nabla u)d\mathbf{r}' &= \int_{\partial\Omega}(v\nabla u)\cdot\mathbf{n}'\,d\mathbf{s}' = \int_\Omega \nabla v\cdot\nabla u d\mathbf{r}' + \int_\Omega v\Delta u d\mathbf{r}'\end{aligned}$$

Subtracting the two equations leads to the second Green identity:

$$\int_\Omega (u\Delta v - v\Delta u)\,d\mathbf{r}' = \int_{\partial\Omega}\left(u\frac{\partial v}{\partial\mathbf{n}'} - v\frac{\partial u}{\partial\mathbf{n}'}\right)\,d\mathbf{s}' \tag{2.27}$$

Let us now consider u as a harmonic function (*s.t.* $\Delta u = 0$ in $\mathbb{R}^3\setminus\partial\Omega$); and $v(\mathbf{r},\mathbf{r}') = -G(\mathbf{r}-\mathbf{r}') = \frac{-1}{4\pi\|\mathbf{r}-\mathbf{r}'\|}$, with $G(\mathbf{r})$ the Green solution of the equation $-\Delta G = \delta_0$ (δ_0 is defined p.vii). The previous Eq.(2.27) now writes:

$$\int_\Omega u(\mathbf{r}')\,\delta_0(\mathbf{r}-\mathbf{r}')d\mathbf{r}' = \int_{\partial\Omega}\left(\partial_{\mathbf{n}'}uG(\mathbf{r}-\mathbf{r}') - u\partial_{\mathbf{n}'}G(\mathbf{r}-\mathbf{r}')\right)\,d\mathbf{s}' \tag{2.28}$$

If $\mathbf{r}\in\Omega$, the first term is simply $u(\mathbf{r})$, conversely if $\mathbf{r}\in\mathbb{R}^3\setminus\bar{\Omega}$, then it is zero. Considering $\mathbf{r}\in\partial\Omega$, one must integrate on a ball centered on $\mathbf{r}$ with an infinitely small radius ε, the domain of this ball $\Omega_B = B_\varepsilon(\mathbf{r})$, is split between $\bar{\Omega}$ and $\mathbb{R}^3\setminus\bar{\Omega}$ with a plane interface. The computation of this integral leads to the mean of $u(\mathbf{r})$ on both sides which is then: $\frac{1}{2}u^-(\mathbf{r})$ since u^+ is zero (see [Nédélec, 2001] for a formal

proof). The values of the first term in Eq.(2.28) denoted $I(\mathbf{r})$ are summarized here:

$$I(\mathbf{r}) = \begin{cases} u(\mathbf{r}) & \mathbf{r} \in \Omega \\ \frac{1}{2}u^-(\mathbf{r}) & \mathbf{r} \in \partial\Omega \\ 0. & \mathbf{r} \in \mathbb{R}^3 \setminus \bar{\Omega} \end{cases}$$

Seen from inside the domain Ω, it writes:

$$I(\mathbf{r}) = \int_{\partial\Omega} \left(\partial_{\mathbf{n}'} u^-(\mathbf{r}')G(\mathbf{r}-\mathbf{r}') - u^-(\mathbf{r}')\partial_{\mathbf{n}'}G(\mathbf{r}-\mathbf{r}')\right)\, d\mathbf{s}'.$$

Doing exactly the same for the domain $\Omega' = \mathbb{R}^3 \setminus \bar{\Omega}$ also an open subset of $\mathbb{R}^3$, this time denoting $J(\mathbf{r})$ in place of $I(\mathbf{r})$, we get:

$$J(\mathbf{r}) = \begin{cases} 0. & \mathbf{r} \in \Omega \\ \frac{1}{2}u^+(\mathbf{r}) & \mathbf{r} \in \partial\Omega \\ u(\mathbf{r}) & \mathbf{r} \in \mathbb{R}^3 \setminus \bar{\Omega} \end{cases}$$

$$J(\mathbf{r}) = \int_{\partial\Omega} \left(\partial_{\mathbf{n}'} u^+(\mathbf{r}')G(\mathbf{r}-\mathbf{r}') - u^+(\mathbf{r}')\partial_{\mathbf{n}'}G(\mathbf{r}-\mathbf{r}')\right)\, d\mathbf{s}'.$$

When summing up with the expression of $I(\mathbf{r})$ yields:

$$\int_{\partial\Omega} \left([\partial_{\mathbf{n}'} u]\, G(\mathbf{r}-\mathbf{r}') - [u]\, \partial_{\mathbf{n}'}G(\mathbf{r}-\mathbf{r}')\right)\, d\mathbf{s}' = \begin{cases} u(\mathbf{r}) & \text{if } \mathbf{r} \in \Omega \\ \frac{u^-(\mathbf{r})+u^+(\mathbf{r})}{2} & \text{if } \mathbf{r} \in \partial\Omega \end{cases} \tag{2.29}$$

One can then reconstruct a piecewise harmonic function in all of $\mathbb{R}^3$ considering by only its jump on the interface. For ease of notation, we introduce the two operators respectively called the single- and double-layer potentials which map a scalar function f defined on $\partial\Omega$ to another scalar function:

$$\begin{aligned} (\mathcal{D}f)(\mathbf{r}) &= \int_{\partial\Omega} \partial_{\mathbf{n}'}G(\mathbf{r}-\mathbf{r}')f(\mathbf{r}')d\mathbf{s}' \\ (\mathcal{S}f)(\mathbf{r}) &= \int_{\partial\Omega} G(\mathbf{r}-\mathbf{r}')f(\mathbf{r}')d\mathbf{s}' \end{aligned} \tag{2.30}$$

From Eq.(2.29) we now write:

$$u(\mathbf{r}) = -\mathcal{D}[u](\mathbf{r}) + \mathcal{S}[\partial_{\mathbf{n}}u](\mathbf{r}) \qquad \forall \mathbf{r} \in \Omega \tag{2.31}$$

$$u^{\mp}(\mathbf{r}) = \left(\pm\tfrac{\mathcal{I}}{2} - \mathcal{D}\right)[u](\mathbf{r}) + \mathcal{S}[\partial_{\mathbf{n}}u](\mathbf{r}) \qquad \forall \mathbf{r} \in \partial\Omega, \tag{2.32}$$

where $\mathcal{I}$ denotes the identity operator. Considering multiple regions such as the piecewise constant head model of Fig.(2.23), we can write the same set of equations for each sub-domain Ω_i.

Geselowitz Starting from the formula previously established, one has to find a harmonic function which could allow for the computation of the potential V on the different surfaces. Let us start with the restriction of f the source term to Ω_i, and v_{Ω_i} the solution of $\Delta v_{\Omega_i} = f_i$ in Ω_i, and harmonic outside. Hence it is continuous as well as its normal derivative for each surface S_j, and the function $v_d = \sum_{i=1}^{N} v_{\Omega_i}$ satisfies $\Delta v_d = f$. Now, let $u_d = \sigma V - v_d$. It is a harmonic function, since $\forall i$: $\Delta u_d = \sigma_i \Delta V - \Delta v_{\Omega_i} = f_i - f_i = 0$, even for $\mathbf{r} \in \mathbb{R}^3 \setminus \Omega_i$. The jump of its normal derivative is 0 since $\sigma \partial_n V$ is continuous across interfaces, and also is v_d by construction. Last the jump $[u_d]_{S_i} = [\sigma V - v_d]_{S_i} = \sigma_i V_i - \sigma_{i+1} V_i$, which allows us to write for each surface S_j by applying Eq.(2.32):

$$v_d = \frac{\sigma_i + \sigma_{i+1}}{2} V_{S_j} - \sum_{i=1}^{N} (\sigma_{i+1} - \sigma_i) V_{S_i}, \tag{2.33}$$

This formulation is the one given by Geselowitz [Geselowitz, 1967], and can be called the double-layer formulation since it uses double-layer potentials. It is still commonly used today, but is prone to certain numerical errors when implemented, especially when the conductivity value drops significantly between two neighboring regions, which is exactly the case for the EEG problem (because of the skull). A special care for this change of conductivity has been studied in [Hämäläinen and Sarvas, 1989].

Single-layer formulation Similarly to what has been done for the double-layer potentials approach, one can construct a harmonic function $u_s = V - \sum_i^N \frac{v_{\Omega_i}}{\sigma_i}$, and will get a formulation giving an expression for the normal derivative of u_s. The solution u_s is then computed out of the jumps of $\partial_{\mathbf{n}} u_s$ through the integral operator $\mathcal{S}$ defined in Eq.(2.30) (see [Kybic et al., 2005]).

Extending the Green representation theorem see in Eq.(2.32), by computing the partial derivative toward $\mathbf{n}$, has led Nédélec et al [Nédélec, 2001] to their representation theorem (see also [Bonnet, 1995]):

Representation Theorem We introduce two more integral operators $\mathcal{N}, \mathcal{D}^*$, and recall the two previous ones introduced in Eq.(2.30):

$$\begin{aligned}
\big(\mathcal{D} f\big)(\mathbf{r}) &= \int_{\partial\Omega} \partial_{\mathbf{n}'} G(\mathbf{r} - \mathbf{r}') f(\mathbf{r}') \, \mathrm{d}s(\mathbf{r}') \ , \\
\big(\mathcal{S} f\big)(\mathbf{r}) &= \int_{\partial\Omega} G(\mathbf{r} - \mathbf{r}') f(\mathbf{r}') \, \mathrm{d}s(\mathbf{r}') \ , \\
\big(\mathcal{N} f\big)(\mathbf{r}) &= \int_{\partial\Omega} \partial^2_{\mathbf{n},\mathbf{n}'} G(\mathbf{r} - \mathbf{r}') f(\mathbf{r}') \, \mathrm{d}s(\mathbf{r}') \ , \\
\big(\mathcal{D}^* f\big)(\mathbf{r}) &= \int_{\partial\Omega} \partial_{\mathbf{n}} G(\mathbf{r} - \mathbf{r}') f(\mathbf{r}') \, \mathrm{d}s(\mathbf{r}') \ ,
\end{aligned} \tag{2.34}$$

where $\mathbf{n}$, resp. $\mathbf{n}'$, is the outward normal vector at position $\mathbf{r}$, resp. $\mathbf{r}'$. Operator $\mathcal{D}^*$ is the (L^2-)dual of operator $\mathcal{D}$, whence its name. We will say that a function u satisfies condition $\mathscr{H}$, if it simultaneously satisfies:

$$\mathscr{H} : \begin{cases} \lim_{r\to\infty} r\,|u(\mathbf{r})| < \infty \\ \lim_{r\to\infty} r\dfrac{\partial u}{\partial \mathbf{r}}(\mathbf{r}) = 0 \end{cases} ,$$

where $r = \|\mathbf{r}\|$, and $\dfrac{\partial u}{\partial \mathbf{r}}(\mathbf{r})$ denotes the partial derivative of u in the radial direction. The Green function G satisfies the $\mathscr{H}$ condition. To condition $\mathscr{H}$ corresponds the physical intuition that an electrostatic field is zero far away from charges. The fundamental representation theorem on which the Boundary Element Method is then formulated as:

Theorem 1 (Representation Theorem) *Let $\Omega \subseteq \mathbb{R}^3$ be a bounded open set with a regular boundary $\partial\Omega$. Let $u : (\mathbb{R}^3\backslash\partial\Omega) \to \mathbb{R}$ be a harmonic function ($\Delta u = 0$ in $\mathbb{R}^3\backslash\partial\Omega$), satisfying the $\mathscr{H}$ condition, and let further $p(\mathbf{r}) \overset{def}{=} \partial_{\mathbf{n}} u(\mathbf{r})$. Then*

$$\begin{aligned} -p = \quad & +\mathcal{N}[u] && -\mathcal{D}^*[p] && \text{for } \mathbf{r} \notin \partial\Omega \\ u = \quad & -\mathcal{D}[u] && +\mathcal{S}[p] \\ \\ -p^{\pm} = \quad & +\mathcal{N}[u] && + \left(\pm\frac{\mathcal{I}}{2} - \mathcal{D}^*\right)[p] && \text{for } \mathbf{r} \in \partial\Omega \\ u^{\pm} = \quad & \left(\mp\frac{\mathcal{I}}{2} - \mathcal{D}\right)[u] && +\mathcal{S}[p] \end{aligned} \tag{2.35}$$

The Theorem holds in particular for the hollow ball topology depicted in Figure 2.23, *i.e.* for disjoint open sets Ω_i such that $\Omega = \cup_{i\in\{1..N\}}\Omega_i$ From this theorem, one can recover the two previous formulations (single and double). This result is the basis of a third formulation, the symmetric BEM formulation which involves $\mathcal{N}$, and $\mathcal{D}^*$.

The symmetric BEM developed in [Kybic et al., 2005], considers in each $\Omega_1, \ldots, \Omega_N$ the function:

$$u_{\Omega_i} = \begin{cases} V - v_{\Omega_i}/\sigma_i & \text{in } \Omega_i \\ -v_{\Omega_i}/\sigma_i & \text{in } \mathbb{R}^3\backslash\overline{\Omega}_i \ . \end{cases} \tag{2.36}$$

The notation is the one introduced above as Eq.(2.33). Each u_{Ω_i} is harmonic in $\mathbb{R}^3\backslash\partial\Omega_i$. Considering the nested volume model, the boundary of Ω_i is $\partial\Omega_i = S_{i-1} \cup S_i$. With respect to the orientations of normals indicated in Fig. 2.23, the jumps of u_{Ω_i} across S_i satisfy the relations

$$[u_{\Omega_i}]_i = V_{S_i}, \qquad [u_{\Omega_i}]_{i-1} = -V_{S_{i-1}} \ , \tag{2.37a}$$

and the jumps of their derivatives

$$[\partial_{\mathbf{n}} u_{\Omega_i}]_i = (\partial_{\mathbf{n}} V)^-_{S_i}, \quad [\partial_{\mathbf{n}} u_{\Omega_i}]_{i-1} = -(\partial_{\mathbf{n}} V)^+_{S_{i-1}} \ . \tag{2.37b}$$

In contrast to the previous approaches, none of the jumps are null. We define $p_{S_i} = \sigma_i [\partial_{\mathbf{n}} u_{\Omega_i}]_i = \sigma_i (\partial_{\mathbf{n}} V)^-_{S_i}$. Note that since $[\sigma \partial_{\mathbf{n}} V] = 0$ from the continuity of the current, we have: $p_{S_i} = \sigma_i (\partial_{\mathbf{n}} V)^-_{S_i} = \sigma_{i+1} (\partial_{\mathbf{n}} V)^+_{S_i}$ at the interface S_i. As u_{Ω_i} is harmonic in $\mathbb{R}^3 \backslash \partial\Omega_i$ and satisfies the condition $\mathscr{H}$, we apply Theorem 1 to u_{Ω_i}, and get the following for $i = 1, \ldots, N$:

$$\begin{aligned} \sigma_{i+1}^{-1} (v_{\Omega_{i+1}})_{S_i} - \sigma_i^{-1} (v_{\Omega_i})_{S_i} = \\ \mathcal{D}_{i,i-1} V_{S_{i-1}} - 2\mathcal{D}_{ii} V_{S_i} + \mathcal{D}_{i,i+1} V_{S_{i+1}} - \sigma_i^{-1} \mathcal{S}_{i,i-1} p_{S_{i-1}} \\ + (\sigma_i^{-1} + \sigma_{i+1}^{-1}) \mathcal{S}_{ii} p_{S_i} - \sigma_{i+1}^{-1} \mathcal{S}_{i,i+1} p_{S_{i+1}} \ , \end{aligned} \tag{2.38}$$

Using the same approach, we evaluate the quantities $\left(\sigma_i \partial_{\mathbf{n}} u_{\Omega_i}\right)^-_{S_i} = \left(p - \partial_{\mathbf{n}} v_{\Omega_i}\right)^-_{S_i}$ and $\left(\sigma_{i+1} \partial_{\mathbf{n}} u_{\Omega_{i+1}}\right)^+_{S_i} = \left(p - \partial_{\mathbf{n}} v_{\Omega_{i+1}}\right)^+_{S_i}$ and subtracting the resulting expressions yields:

$$\begin{aligned} (\partial_{\mathbf{n}} v_{\Omega_{i+1}})_{S_i} - (\partial_{\mathbf{n}} v_{\Omega_i})_{S_i} = \\ \sigma_i \mathcal{N}_{i,i-1} V_{S_{i-1}} - (\sigma_i + \sigma_{i+1}) \mathcal{N}_{ii} V_{S_i} + \sigma_{i+1} \mathcal{N}_{i,i+1} V_{S_{i+1}} - \\ \mathcal{D}^*_{i,i-1} p_{S_{i-1}} + 2\mathcal{D}^*_{ii} p_{S_i} - \mathcal{D}^*_{i,i+1} p_{S_{i+1}} \ , \end{aligned} \tag{2.39}$$

for $i = 1, \ldots, N$. Here (and in (2.38)) the terms corresponding to non-existing surfaces S_0, S_{N+1} are to be set to zero. Terms involving p_{S_N} must also be set to zero, since $\sigma_{N+1} = 0$ implies $p_{S_N} = 0$. This formulation used for the forward EEG problem is carried out in [Kybic et al., 2005], and is also compatible for non nested geometries [Kybic et al., 2006], as well as the EIT problem [Clerc et al., 2005b].

Variational formulation Introducing the shape functions ϕ, and ψ that will be used to represent respectively the potential at vertices and the normal current for each triangle, we multiply Eq.(2.38) by the ψ test function, and integrate over the surfaces, and similarly we multiply Eq.(2.39) by the ϕ test function and integrate. It is not exactly Galerkin's method, since we do not put against same functions to represent the variable and test it, but it is the same idea, since it is done to keep the same order of precision for the scalar products. Indeed, our operators acting on the variables (the potential V and p) have different regularity behavior, since $\mathcal{S}$ increases the regularity of the function (due to the integral), whereas $\mathcal{N}$ decreases it (double derivative and only one integration), and finally operators $\mathcal{D}, \mathcal{D}^*$ do not change it. When discretizing, ϕ and ψ will be chosen as piecewise polynomial functions, and ϕ will be chosen 1-higher order than the other set of shape function ψ. Indexing the shape functions with the surface they belong to, these equations (2.38)-(2.39) now write in weak form:
Using the notation of the $L^2(S)$ scalar product defined as: $\langle f, g \rangle = \int_S f(\mathbf{r})\, g(\mathbf{r}) d\mathbf{s}$,

we multiply Eq.(2.38)-(2.39) with the test functions ψ and ϕ respectively and integrate over each surface: $\forall(\phi_i,\psi_i)\in(L^2(S_i))^2$,

$$\begin{aligned}\big\langle\sigma_{i+1}^{-1}(v_{\Omega_{i+1}})_{S_i}-\sigma_i^{-1}(v_{\Omega_i})_{S_i},\psi_i\big\rangle=\\ \big\langle\mathcal{D}_{i,i-1}V_{S_{i-1}},\psi_i\big\rangle-2\big\langle\mathcal{D}_{ii}V_{S_i},\psi_i\big\rangle+\big\langle\mathcal{D}_{i,i+1}V_{S_{i+1}},\psi_i\big\rangle-\big\langle\sigma_i^{-1}\mathcal{S}_{i,i-1}p_{S_{i-1}},\psi_i\big\rangle\\ +\big\langle(\sigma_i^{-1}+\sigma_{i+1}^{-1})\mathcal{S}_{ii}p_{S_i},\psi_i\big\rangle-\big\langle\sigma_{i+1}^{-1}\mathcal{S}_{i,i+1}p_{S_{i+1}},\psi_i\big\rangle\,,\end{aligned}\tag{2.40}$$

$$\begin{aligned}\big\langle(\partial_{\mathbf{n}}v_{\Omega_{i+1}})_{S_i}-(\partial_{\mathbf{n}}v_{\Omega_i})_{S_i},\phi_i\big\rangle=\\ \big\langle\sigma_i\mathcal{N}_{i,i-1}V_{S_{i-1}},\phi_i\big\rangle-\big\langle(\sigma_i+\sigma_{i+1})\mathcal{N}_{ii}V_{S_i},\phi_i\big\rangle+\big\langle\sigma_{i+1}\mathcal{N}_{i,i+1}V_{S_{i+1}},\phi_i\big\rangle-\\ \big\langle\mathcal{D}^*_{i,i-1}p_{S_{i-1}},\phi_i\big\rangle+2\big\langle\mathcal{D}^*_{ii}p_{S_i},\phi_i\big\rangle-\big\langle\mathcal{D}^*_{i,i+1}p_{S_{i+1}},\phi_i\big\rangle\,,\end{aligned}\tag{2.41}$$

for $i=1,\dots,N$.

Discretization From Eq.(2.40)-(2.41), we set ϕ to be P1 shape functions (piecewise linear) to describe the potential at each vertex *i.e.* $V_{S_k}(\mathbf{r})=\sum_i v_i^{(k)}\phi_i^{(k)}(\mathbf{r})$ and choose ψ as P0 functions (piecewise constant) on each triangle to represent the current *i.e.* $p_{S_k}(\mathbf{r})=\sum_i c_i^{(k)}\psi_i^{(k)}(\mathbf{r})$. We can define discretized operators:

$$\begin{aligned}(\mathsf{N}_{kl})_{ij}&=\big\langle\mathcal{N}_{kl}\phi_j^{(l)},\phi_i^{(k)}\big\rangle & (\mathsf{S}_{kl})_{ij}&=\big\langle\mathcal{S}_{kl}\psi_j^{(l)},\psi_i^{(k)}\big\rangle\\ (\mathsf{D}_{kl})_{ij}&=(\mathsf{D}^*_{lk})_{ji}=\big\langle\mathcal{D}_{kl}\phi_j^{(l)},\psi_i^{(k)}\big\rangle\\ (\mathbf{b}_k)_i&=\Big\langle\partial_{\mathbf{n}}v_{\Omega_k}-\partial_{\mathbf{n}}v_{\Omega_{k+1}},\phi_i^{(k)}\Big\rangle & (\mathbf{d}_k)_i&=\Big\langle\sigma_{k+1}^{-1}v_{\Omega_{k+1}}-\sigma_k^{-1}v_{\Omega_k},\psi_i^{(k)}\Big\rangle\\ (\mathbf{v}_k)_i&=v_i^{(k)} & (\mathbf{c}_k)_i&=c_i^{(k)}\end{aligned}$$

and end up with the symmetric linear system:

$$\underbrace{\begin{bmatrix}(\sigma_1+\sigma_2)\mathsf{N}_{11} & -2\mathsf{D}^*_{11} & -\sigma_2\mathsf{N}_{12} & \mathsf{D}^*_{12} & & & \\ -2\mathsf{D}_{11} & (\sigma_1^{-1}+\sigma_2^{-1})\mathsf{S}_{11} & \mathsf{D}_{12} & -\sigma_2^{-1}\mathsf{S}_{12} & & & \\ -\sigma_2\mathsf{N}_{21} & \mathsf{D}^*_{21} & (\sigma_2+\sigma_3)\mathsf{N}_{22} & -2\mathsf{D}^*_{22} & -\sigma_3\mathsf{N}_{23} & \mathsf{D}^*_{23} & \\ \mathsf{D}_{21} & -\sigma_2^{-1}\mathsf{S}_{21} & -2\mathsf{D}_{22} & (\sigma_2^{-1}+\sigma_3^{-1})\mathsf{S}_{22} & \mathsf{D}_{23} & -\sigma_3^{-1}\mathsf{S}_{23} & \\ & & -\sigma_3\mathsf{N}_{32} & \mathsf{D}^*_{32} & (\sigma_3+\sigma_4)\mathsf{N}_{33} & -2\mathsf{D}^*_{33} & \dots\\ & & \mathsf{D}_{32} & -\sigma_3^{-1}\mathsf{S}_{32} & -2\mathsf{D}_{33} & (\sigma_3^{-1}+\sigma_4^{-1})\mathsf{S}_{33} & \dots\\ & & & & \vdots & \vdots & \ddots\end{bmatrix}}_{\mathsf{A}}\underbrace{\begin{bmatrix}\mathbf{v}_1\\ \mathbf{c}_1\\ \mathbf{v}_2\\ \mathbf{c}_2\\ \mathbf{v}_3\\ \mathbf{c}_3\\ \vdots\end{bmatrix}}_{\mathbf{w}}=\underbrace{\begin{bmatrix}\mathbf{b}_1\\ \mathbf{d}_1\\ \mathbf{b}_2\\ \mathbf{d}_2\\ \mathbf{b}_3\\ \mathbf{d}_3\\ \vdots\end{bmatrix}}_{\mathbf{z}}\tag{2.42}$$

Extension for non-nested geometries Actually the BEM does not require nested geometries. This extension is described in [Kybic et al., 2006]. The handling for a hole in the skull is there described. This hole has a much higher conductivity than the skull, and shares common boundaries with the skull-scalp and brain-skull interface. These common boundaries are sharp, and can lead to numerical errors if not discretized finely enough, as discussed in the paper.

2.4.4 Finite Element Method

2.4.4.1 Common formalism

In finite element methods, as has been done previously for the BEM, we look for an approximate solution of our problem considering the weak formulation of the problem. But instead of considering the weak form of the integral equations, we directly start from the PDE defined on all the computational domain Ω. The solution is *a-priori* regular (except at the exact location of the dipole), which is in our case a good hypothesis. Considering the forward EEG problem in Eq.(2.13), we multiply by a test function $\phi \in H^1(\Omega)$, where $H^1(\Omega)$ denotes the Sobolev functional space:

$$H^1(\Omega) = \left\{ f \in L^2(\Omega), \frac{\partial f}{\partial x^k} \in L^2(\Omega), \forall k \in \{1,2,3\} \right\}. \tag{2.43}$$

The forward EEG problem with its boundary condition is given Eq.(2.13). We multiply this equation by ϕ and integrate over Ω, which gives the weak formulation:

$$\int_\Omega \nabla \cdot (\sigma \nabla V)\phi \; d\mathbf{r} = \int_\Omega \nabla \cdot \mathbf{J}^{\mathrm{p}} \phi \; d\mathbf{r} \tag{2.44}$$

$$\int_\Omega (\sigma \nabla V) \cdot \nabla \phi \; d\mathbf{r} = \int_\Omega \mathbf{J}^{\mathrm{p}} \cdot \nabla \phi \; d\mathbf{r} \tag{2.45}$$

It can be stated as:

$$a(V, \phi) = f(\phi) \tag{2.46}$$

where $a(u, v)$ is a (symmetric) bilinear form, which can be shown easily to be coercive (or H^1-elliptic), and thus thanks to the Lax-Milgram theorem, this weak problem is assured to have a unique solution $V \in H^1(\Omega)$.
In Galerkin's method the same shape functions are used for the test functions ϕ, and to represent the potential variable, here V. These shape functions are commonly chosen with a very small support in Ω, so that the integrals to be computed are easy, and lead to solving a sparse linear system. The computational domain is discretized into small volumic elements (tetrahedra, voxels[2], hexahedrons), and the shape function are supported over only a few elements. One often considers shape functions that are 1 for one vertex, zero for others, and linear in between (P1 shape functions). Let consider this case for sake of simplicity and write N the total number of vertices (*i.e.* the total number of unknowns or degrees of freedom), and C_k the k-cell of the mesh.
When concerning the right hand side with a dipolar source $\mathbf{J}^{\mathrm{p}} = \mathbf{m}\delta_{\mathbf{r}_0}$ at location $\mathbf{r}_0$, and momentum $\mathbf{m}$, the delta function is spread over the vertices of the cell, it is then smoothed, and only represented by these vertex values, *i.e.* 4 points for a tetrahedron, 8 for a voxel... its good representation then depends strongly on the shape, the size of the cell and its relative orientation with regard to the dipole momentum. The source term (RHS of Eq.(2.46)) when considering one dipole at

[2] voxles are cubic elements, *i.e.* generalization of pixel for 3D image.

position $\mathbf{r}_0$ lying in one cell indexed j is :

$$f(\phi) = \sum_{i=1}^{N} \mathbf{m} \cdot \nabla\phi_i(\mathbf{r}_0),$$

where most of the $\phi_i(\mathbf{r}_0)$ are zero since this $\mathbf{r}_0$ is not in their support, and as the ϕ_i have been chosen piecewise linear, their gradient are constant over the cell and thus the description of a dipole is at an over-cell resolution.
Regarding the discretization of the conductivity, all conductivity models can be considered (inhomogeneous, anisotropic,...) as long as it is constant within each cell. An anisotropic conductivity defined by the tensor Σ, is incorporated in the bilinear form as:

$$a(V, \phi) = \int_{\Omega} \nabla V \cdot (\Sigma \nabla \phi)\ d\mathbf{r}\ .$$

Using Galerkin's method, we represent the potential with the same shape functions as the test functions ϕ, V then writes:

$$V(\mathbf{r}) = \sum_{i=1}^{N} V_i \phi_i(\mathbf{r})\ .$$

One can now re-write the bilinear form discretized A with these shape functions; the coefficients of matrix A are:

$$A_{ij} = \sum_{k \in C} a_{ij}^k\ ,$$

where k runs along the cells of the mesh, and a_{ij}^k is:

$$a_{ij}^k = \int_{C_k} \nabla\phi_i(\mathbf{r}) \cdot (\Sigma_k \nabla\phi_j(\mathbf{r}))d\mathbf{r}\ .$$

Different discretization of the domain can be imagined, leading to different approximation of the geometry, different elements, different accuracies.

2.4.4.2 The tetrahedral FEM

In a tetrahedral FEM the domain is split into tetrahedra, the geometry description of the surface is then piecewise linear and continuous. We refer to sec.2.6, concerning the mesh generation. Let us take a look at the RHS term of (2.46):

$$f(\phi) = \sum_{i=1}^{N} \mathbf{m} \cdot \nabla\phi_i(\mathbf{r}_0) = \mathbf{m} \cdot (\nabla\phi_a(\mathbf{r}_0) + \nabla\phi_b(\mathbf{r}_0) + \nabla\phi_c(\mathbf{r}_0) + \nabla\phi_d(\mathbf{r}_0)),$$

where the ϕ indexed with a, b, c, d are the non null shape functions at point $\mathbf{r}_0$. We end up with a linear system, where the unknowns are V at each vertex:

$$A \cdot \begin{pmatrix} V_1 \\ V_2 \\ \vdots \\ V_N \end{pmatrix} = F\ , \tag{2.47}$$

where F has only 4 non-zero coefficients.

2.4.4.3 The implicit FEM

The implicit FEM was developed in [Papadopoulo et al., 2006]-[Vallaghé and Papadopoulo, 2010], and is based on a mesh-free concept. Actually, since meshing can be a difficult task, notably for the case of a human head, this FEM uses a Cartesian grid as the one of the MRI. It then deals with voxels *i.e.* cubic elements, but the main difference with the FDM, is the good handling of the interfaces through the use of level-set. A level-set is a function which is zero only for $\mathbf{r}$ on the surface, and gives the distance to the surface elsewhere. The implicit FEM takes as input the dimension of the grid, and the level-sets (one for each surface) constructed from the segmented MRI and then bypasses the mesh generation step. It then computes the FEM integral over these voxels using Q1 elements with specific integrals in case of voxels crossed by surfaces.

2.5 An ideal numerical resolution of the forward problems

These methods all provide a solution of the forward problem (EEG or MEG), but at what cost ? And how well do they solve the equation ? Since most of them are numerical methods, they thus introduce errors, approximation when discretizing the electrophysiological model. Furthermore, once the numerical system is built, they might be instable at solving, which can increase significantly the numerical errors. Finally, they are not able able to represent the same models, since for each of them special assumptions are made to derive the numerical scheme. Let first see what are the pros and cons of each of them for the MEEG forward problems.

2.5.1 Pros and cons of the previous numerical methods

Analytical methods: represent their electrophysiological model in the best manner, since most often they allow for having a closed form (like the magnetic field computation in Eq.(2.18)) which then leads to an exact calculations (at the machine precision $\sim 10^{-16}$). For the EEG problem resolution, one gets a formula containing an infinite sum which must be truncated. The user then defines the desired accuracy giving the number of terms. Analytical solutions on multi-layer spheres designed in [Zhang, 1995] are designed to have a strong convergence rate, and are thus very fast for given precision. Even if they do represent the model quite well, the model is very poor, the coarse geometrical approximation of the head by spheres or ellipsoids lead to considerable errors for EEG and is still discussed now for MEG [Van Uitert and Johnson, 2002]. The community is starting to accept that realistic models should be used for MEG also [Lalancette et al., 2011].

BEM: handle the patient's head geometry through the use of triangulated surfaces representing the domain boundaries (like Brain-Skull interface, Skull-Skin,

. . .), but the handling of complicated geometries such as the gray/CSF interface leads to sharp edges or to a very high number of nodes. Sharp edges can lead to numerical errors in the BEM's operators, and having too many nodes (beyond 30 000 vertices for the symmetric BEM) leads to huge systems that cannot be solved nowadays without using grid computing techniques which are most of the time not available for clinicians. Despite its geometric approximation (it requires smooth surfaces), the symmetric BEM achieves very good accuracy when compared to FEM for a given computation time [Olivi, 2007]. The main limitation of the BEM is its incapacity to handle anisotropic media, or small compartments such as those in the skull.

FDM: can deal with anisotropy, but the convergence rate of the geometric error with regard to the grid size is slow since the FDM uses a Cartesian grid; the way the geometry is approximated leads to a staircase description of the interfaces. Furthermore it does not allow for having local refinement of the grid where it is needed such as the dipole location or close to interfaces. On the other hand, the implementation is very easy and the stiffness matrix is well structured which gives access to fast solvers [Dang and Ng, 2011].

FEM: can deal with anisotropy, very local refinement, and good approximation of the geometry. They lead to huge but sparse systems, in our case, symmetric positive definite stiffness matrices, which allows for the use of fast iterative methods such as the (preconditioned-) conjugated gradient method. Its main pro is its flexibility (with regard to the domain description or the conductivity profiles), and its main drawback resides in its poor handling of sharp source term (such as the Dirac). The mesh generation is also a crucial step, since it can be sometimes difficult to generate, and the resulting mesh should not contain badly shaped elements. The reader can refer to [Wolters et al., 2007], for a way of generating hexahedral meshes out of Cartesian grid and segmentations.

Fig.(2.24) represents the fidelity of the numerical methods to their input model after a forward problem resolution. We imagine that through the filter of analytical methods on the left the result is very faithful to the concentric spheres model; in the middle, we get a slight blurring representing the numerical errors, on the BEM's representation of the piecewise constant model (notably the skull). And finally, on the right, we estimate the solution on a multi-compartment head model which is very detailed, but the FEM 'filter' is not sharp at all, and thus compromises the overall accuracy.

2.5.2 What method and model to choose for the forward problem ?

Knowing the above pros and cons of each method makes the choice difficult. On the one hand, one would like to have an accurate electrophysiological model of the subject's head, incorporating as faithfully as possible the different head regions

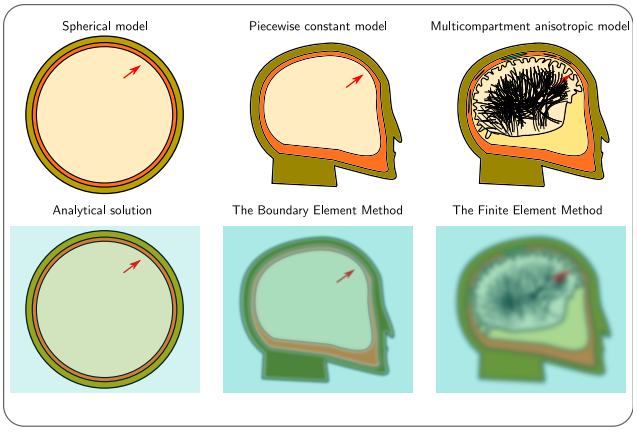

Figure 2.24 – *Sketch on models represented by their numerical method.*

with conductivity profiles closest to reality. On the other hand, if the numerical errors compromise this good description when solving a forward model, it is not sensible to go further in modeling the head, because a coarser model well solved numerically may lead to better results. One has better choose the best **couple** *i.e.* the electrophysiological model and the numerical method which best represents it.

2.5.2.1 Choosing models and methods

Let us first state the case of the MEG forward problem.

MEG As discussed in sec.(2.3.1.2), the magnetic field is less distorted by the skull than the electric field. Actually, the primary source term is dominant in the magnetic field computation. Furthermore, as the Ohmic current contribution to the magnetic field is proportional to the Ohmic current, and thus to the conductivity of the region, the Ohmic current lying in the skull does not contribute much to the magnetic field. Then, a valid approach is to simply remove from the computational domain, the skull and scalp regions [Gramfort et al., 2010]. We can conclude that for the magnetic field computation, one only needs to consider the brain region, eventually with the anisotropy brought by the white matter fibers since it can be of great influence [Wolters et al., 2006]. Still considering the anisotropic fibers, with the FEM, and the good BEM handling of the source for isotropic media, might lead to different results which are difficult to analyze. These results may be biased due to the numerical errors of the FEM, or to the absence of fibers in the BEM modeling. Thus the choice is still not obvious and needs to be investigated by validating both methods.

EEG For the EEG problem resolution, it is non avoidable to consider the skull, and scalp, since electricity needs to propagate through these tissues to reach the sensors. The structure of the skull must be well taken into account, since it is on the

direct path between the source and the sensors. As seen in sec.(2.3.2), the skull can be modeled as a multi-compartment region, or as an equivalent anisotropic conductivity, or as an isotropic conductor. The FEM can deal with the three descriptions, the BEM, on the other hand cannot handle many small regions such as the soft bone within the skull, thus it is limited to the isotropic case. Another common case in clinical applications, is the modeling of a hole in the skull due to a surgery. Such holes lead to inhomogeneous skull, which can considerably change the forward solutions, and cannot be easily taken into account in BEM. The sharp contours of the hole with the skull boundaries require many elements to be discretized correctly, thus leading to the memory limitation for the BEM case [Kybic et al., 2006]. It has nevertheless been successfully applied with standard BEM (double-layer formulation) in [Oostenveld and Oostendorp, 2002]-[Bénar and Gotman, 2002].

2.5.2.2 An ideal case

An ideal numerical method should have the following features:

1. optimal meshing with local refinement where it is needed for a given forward problem.
2. correct handling of the dipolar source.
3. a faithful description of the conductivity profiles, and finite elements elongated in the direction of their anisotropy.
4. minimal numerical errors when solving the system.
5. reasonable time and memory consumption.

These features might be contradictory in some cases. For example, the FEM would need tiny elements for the correct description of the white matter fibers, also for the dipolar source modeling, which would then lead to very huge systems. Having an optimal mesh for a given forward problem might be achievable, but would need to be reiterated for the thousands of sources when building a leadfield. The symmetric BEM is a good candidate with regards to the numerical error, but still would need a broader range of conductivity profiles available.

2.5.2.3 A realistic ideal case

Choosing between these methods might be a difficult task because of their respective pros and cons. One would like a method with both advantages, the BEM's ability for dealing with sources, and the FEM's flexibility for handling conductivities. Decomposition domain methods (DDM) allow for the splitting of the computational domain, to be dealt by independent solvers. In Chap.4-6 will be exposed an application of DDM for the forward EEG problem, where the brain region containing the sources will be dealt with the BEM, and the other domains by the FEM. We will see that this coupled method answers partially to the previous requirement,

notably concerning the correct source modeling and the skull conductivity profile. In Chap.7, will be introduced a method which should lead to the handling of a kind of local anisotropy or local inhomogeneities within a BEM framework.

2.5.2.4 Validations

When developing a new method, numerical validation is crucial and can sometimes be difficult. Most of the time the numerical solvers will be first compared to analytical solution on spherical models which can include the normal-tangential anisotropy of the skull [Zhang, 1995]. As soon as inhomogeneities or local anisotropy are introduced, we will use a high resolution FEM to validate the other methods; the FEM converges toward the true solution when the mesh size decreases. When comparing the result of a method which is a vector V_{num}, with regard to a reference solution V_{ref}, we will compute the RDM and MAG [Meijs et al., 1989]:

RDM: Relative difference measure, which is a topographical error independent of the magnitude of the solutions:

$$\texttt{RDM}(V_{ref}, V_{num}) = \left\| \frac{V_{ref}}{\|V_{ref}\|} - \frac{V_{num}}{\|V_{num}\|} \right\| \tag{2.48}$$

MAG: Magnification error, which gives what is missing in the RDM, *i.e.* the comparison of their magnitudes:

$$\texttt{MAG}(V_{ref}, V_{num}) = \frac{\|V_{num}\|}{\|V_{ref}\|} \ , \tag{2.49}$$

where the norm $\|.\|$ denotes the l^2 norm for vectors, *i.e.* $\|V\| = \sqrt{\sum_i V_i^2}$.

2.6 From MRI to mesh generation

2.6.0.5 Segmentation

Segmenting a medical image is challenging due to the sometimes poor resolution of MRI:s. It consists of extracting a surface of a 3D volume which matches some features in the images, such a high contrast. Regularity and/or topology can be imposed sometimes [Piovano and Papadopoulo, 2008]. The best segmenting algorithm we have at our disposal is based on a brain atlas, so that it already knows what kind of surface one is looking for. Freesurfer[3] is a software suite for medical image processing (see [Dale et al., 1999] for cortical surface segmentation). It has allowed us to obtain from a T1 anatomical MRI of resolution 256x176x256, high resolution surfaces of the white and gray matter, the brain envelope, the inner skull, the outer skull, and outer skin.
These surfaces can be defined as very-high resolution meshes (see Fig.(2.25)), or level-sets.

[3] http://surfer.nmr.mgh.harvard.edu

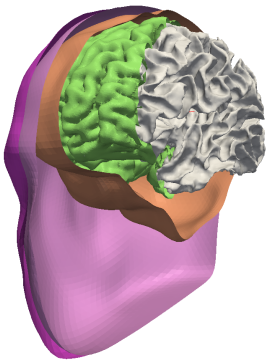

Figure 2.25 – *Surfaces segmentated by Freesurfer.*

2.6.1 What is a good mesh

Many criteria can be defined, such as the correct representation of the boundaries, the local refinement in places where the solution we seek varies a lot, or the good properties for the numerical conditioning when using these meshes in FEM. The good conditioning is important because it increases the convergence rate of the iterative solver, and allows for more stable schemes (less numerical errors). Another constraint one would want is the good agreement with the equation parameters such as the anisotropy of the conductivity, which should lead to elongated elements in some directions, since the solution should vary more in one direction than the other.

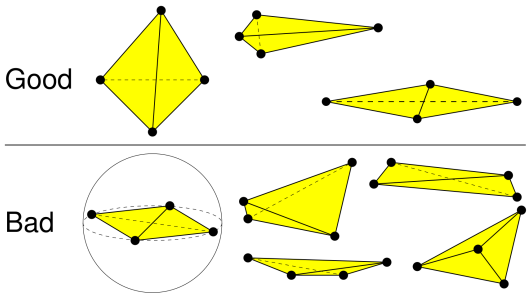

Figure 2.26 – *Good and bad finite elements for conditioning (from [Shewchuk, 2002a]).*

For that, a good mesh must be composed of good elements, that can be hard to guarantee, see Fig.(2.26). In Delaunay triangulations, some bad tetrahedra persist, these are called slivers (or flat tets) and are responsible of bad conditioning in FEM [Shewchuk, 2002b]. A triangulation is Delaunay, if no point lies in the circumsphere of any cell.

2.6.2 Meshing with CGAL

CGAL[4] is an open-source project providing easy access to efficient and reliable geometric algorithms in the form of a C++ library. It is based on Delaunay triangulation, and weighted Delaunay. It allows the generation of surfacic meshes from the definition of gray level image, re-meshing a more complicated geometry, or simply an implicit function (such as sphere functions) [Rineau and Yvinec, 2011]. And it also provides 3D meshes [Alliez et al., 2011], with labeled domain, for the different region such as in Fig.(2.27).

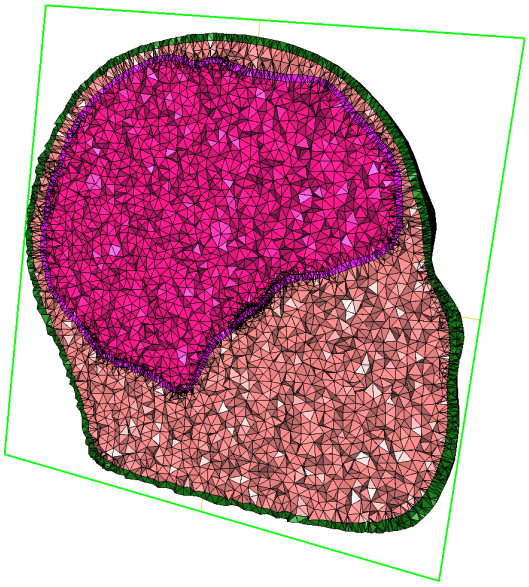

Figure 2.27 – *A realistic 4-layer head mesh (with 297 822 vertices).*

The mesh quality can be controlled through several criteria such as: on the surface, the max distance of the elements to the input surface, the edge length of triangles, their minimum angles, and for the volumic elements, the cell size, the minimum dihedral angle (which prevents slivers), ...

2.7 OpenMEEG: Implementation of the symmetric BEM

OpenMEEG is an open-source multi-platform software which implements the symmetric BEM (sBEM) for the EEG and MEG forward problem resolution. Given a geometric model, and the desired piecewise constant conductivities, OpenMEEG builds and solves the forward problems through a pipeline. The user must supply the surfacic meshes defining the regions, the sensor locations, the sources which can either be distributed on an input surface or punctual (dipoles), and finally the conductivities.

[4] http://www.cgal.org

2.7.1 Implementation

The symmetric BEM (sBEM) as described in sec.(2.4.3) has two types of unknowns, the potential at vertices which will be denoted V or indexed on each surface with $\mathbf{v}_i$, the normal current noted p or $\mathbf{c}_i$. The sBEM in OpenMEEG is implemented using P1 shape functions for the potential at each vertex x_j *i.e.*:

$$\phi_j(x) = \begin{cases} 1 & \text{if } x = x_j \\ 0 & \text{if } x = x_k \ , k \neq j \\ linear & \text{if } x \in T(x_j) \\ 0 & \text{elsewhere} \end{cases},$$

where the notation $T(x_j)$ defines the union of triangles which have x_j as vertex. P0 shape functions are used for the current on each triangle T_j: $\psi(x) = \mathbb{1}_{T_j}(x)$. The main matrices are then:

H: the main head matrix which is symmetric (denoted A in Eq.(2.42)).

X: the unknowns, the potential V and the normal current p.

D: the matrix containing the projection of the sources onto the BEM surfaces (a column of which is denoted z for a single dipole in Eq.(2.42)).

$\mathbf{S}_{eeg}$**:** the projection matrix which simply uses the P1 approximation of the potential to interpolate it at EEG sensors on the outer surface.

$\mathbf{S}_{meg}$ the matrix which is applied to $\mathbf{X}$ to yield the (Ohmic-) magnetic contribution to the MEG sensors.

$\mathbf{T}_{meg}$ the matrix which computes the primary source magnetic contribution to the MEG sensors.

A typical forward problem resolution is then achieved solving the system:

$$\mathbf{H} \cdot \mathbf{X} = \mathbf{D} \tag{2.50}$$

which is most of the time done inverting the matrix $\mathbf{H}$ with LAPACK. In order to obtain the leadfields one applies the selection matrix to the previously computed matrix $\mathbf{X}$ and one adds the primary contribution for the MEG leadfield:

$$\mathbf{L}_{eeg} = \mathbf{S}_{eeg}\mathbf{X} \quad , \quad \mathbf{L}_{meg} = \mathbf{S}_{meg}\mathbf{X} + \mathbf{T}_{meg} \tag{2.51}$$

A more efficient way of solving these systems will be explained in the next chapter.

Boundary current injection When solving an EIT forward problem, another source matrix due to the non-zero boundary condition is built instead of $\mathbf{D}$. This will be used in chapter 4 for solving Neumann boundary value problems.

Internal operators To model electrodes inserted within the brain (sEEG), one can obtain the potential there using another operator also derived from the representation theorem. This can also be useful in other cases which will be discussed in the last chapter 5. Let us derive the formula which derives from the Green's representation theorem. It says that for a harmonic function u_{Ω_i}, its value inside the domain Ω_i can be given by its jump $[u_{\Omega_i}]$ and the one of its normal derivative $[p_{\Omega_i}]$ at the boundary $\partial\Omega_i$ (refer Eq.(2.31) and (2.35)):

$$u_{\Omega_i} = -\mathcal{D}[u_{\Omega_i}] + \mathcal{S}[p_{\Omega_i}].$$

And since in the symmetric BEM $u_{\Omega_i} = V_i - \frac{v_{\Omega_i}}{\sigma_i}$, then the potential V_i writes as the sum $u_{\Omega_i} + \frac{v_{\Omega_i}}{\sigma_i}$.
Using the notations introduced in sec.(2.4.3), with the sBEM variables, in order to get the potentials V_j at points $\mathbf{r}_j \in \Omega$ which can be located in any sub-domains Ω_i, we take the scalar product of the previous equation with a Dirac (collocation method) δ_j located at $\mathbf{r}_j$. We recall that we are still in a nested geometry, and that $\partial\Omega_i = S_i \cap S_{i+1}$. The previous equation then writes:

$$\begin{aligned} V_j &= \frac{v_{\Omega_i}(\mathbf{r}_j)}{\sigma_i} + \langle u_{\Omega_i}, \delta_j \rangle \\ &= \frac{v_{\Omega_i}(\mathbf{r}_j)}{\sigma_i} - \langle \mathcal{D}_{ji} V_{S_i}, \delta_j \rangle + \langle \mathcal{D}_{ji+1} V_{S_{i+1}}, \delta_j \rangle + \frac{1}{\sigma_j} \left(\langle \mathcal{S}_{ji} p_{S_i}, \delta_j \rangle - \langle \mathcal{S}_{ji+1} p_{S_{i+1}}, \delta_j \rangle \right) \end{aligned} \tag{2.52}$$

For example, let us take a 3-layer model where the only primary source lies in the first volume, and ask for the potential at several points within each volume. The internal operator which acts on the sBEM unknowns $\mathbf{X}$ can be constructed applying the previous formula for each point. Let $\mathbf{v}_a, \mathbf{v}_b, \mathbf{v}_c$ be the vectors containing the potentials requested in domain a, b, c respectively. We also write the BEM's unknowns as: $\mathbf{X} = [\mathbf{v}_1\ \mathbf{p}_1\ \mathbf{v}_2\ \mathbf{p}_2\ \mathbf{v}_3]^T$, and denote by v_a^1 the potential generated by the dipole in Ω_1 as if it was an infinite medium, at the desired a locations. This writes using the internal operators:

$$\begin{bmatrix} \mathbf{v}_a \\ \mathbf{v}_b \\ \mathbf{v}_c \end{bmatrix} = \begin{bmatrix} -\mathcal{D}_{a1} & \frac{1}{\sigma_a}\mathcal{S}_{a1} & 0 & 0 & 0 \\ \mathcal{D}_{b1} & -\frac{1}{\sigma_b}\mathcal{S}_{b1} & -\mathcal{D}_{b2} & \frac{1}{\sigma_b}\mathcal{S}_{b2} & 0 \\ 0 & 0 & \mathcal{D}_{c2} & -\frac{1}{\sigma_c}\mathcal{S}_{c2} & -\mathcal{D}_{c3} \end{bmatrix} \begin{bmatrix} \mathbf{v}_1 \\ \mathbf{p}_1 \\ \mathbf{v}_2 \\ \mathbf{p}_2 \\ \mathbf{v}_3 \end{bmatrix} + \frac{1}{\sigma_1} \begin{bmatrix} v_a^1 \\ 0 \\ 0 \end{bmatrix}. \tag{2.53}$$

2.7.2 Performances:

OpenMEEG has been compared to other BEM solvers implemented in freely available softwares in term of accuracy and precision for a given number of mesh nodes, or given number of unknowns. Concerning the forward EEG problem resolution, OpenMEEG achieves the best accuracies and precisions when compared to 4 other softwares [Gramfort et al., 2010]. Excellent results were also obtained for the MEG forward problem resolution.

Commands We refer to [Gramfort et al., 2011] for a manual of OpenMEEG.

Chapter 3

The adjoint method for the forward problem resolution

In this chapter is presented a method which allows for a smarter and faster computation of the leadfield than the classical approach. The leadfield is defined as the linear operator (introduced in sec.(2.2.5)) which associates with one unitary source the resulting set of measurements at each sensor. An accurate computation of the leadfield results from the good resolution of the forward problem where we model a source, and the potential (for EEG) or some component of the magnetic field (for MEG) is computed at sensors. A good leadfield thus requires the use of an appropriate physiological model represented by a pertinent numerical method; this implies realistic geometries and thus numerical methods such as the FDM, FEM or BEM. Furthermore, in order to build the leadfield in the classical approach, the forward problem is solved for each source, which can represent more than 10 000 dipoles in clinical applications. A clever idea for such an assembly has been given thanks to reciprocity theorems which consider the problem from the viewpoint of sensors instead of sources. This drops down the number of resolutions to a few hundred (number of sensors), and can be as straightforward as solving a classical forward problem.

Summary

Goals: Accelerate the MEG and EEG forward problem resolution.

Tools: The adjoint operator of the forward problem.

Results: A simple and effective adjoint resolution using the sBEM.

Contents

3.1 The adjoint operator

From a mathematical point of view, when a linear operator $\mathbf{A}$ maps an element of H, an Hilbert space, to another element of H, then due to the Riesz(-Fréchet) representation theorem, it admits a unique adjoint $\mathbf{A}^*$ such that:

$$\langle \mathbf{A}u, v\rangle = \langle u, \mathbf{A}^* v\rangle \ , \ \forall (u,v) \in H \times H \tag{3.1}$$

where the notation $\langle ., . \rangle$ denotes the inner product in H. Before finding what is the adjoint operator of the EEG forward operator or the MEG one, let us first get an insight physically of the main idea, expressing reciprocity theorems.

3.1.1 Reciprocity theorems

In electromagnetism, one can find many reciprocity theorems. All of them involve the interchange of the source of an electromagnetic field and the measurement of this field. The most famous being the Lorentz reciprocity theorem, which states that the relationship between an oscillating current and its resulting field is unchanged if one interchanges the point source of the current with the place where the field is being measured. Helmholtz reciprocity theorem states analogously that an emitting light (source) measured at one place (sensor) can be interchanged keeping the same relation. This concept was applied to EEG [Rush and Driscoll, 1969] and MEG [Malmivuo, 1980] since its very beginning (also it was already known before for the similar case in electrocardiography (ECG) [Plonsey, 1963]). Let us take a look at the EIT (Electrical Impedance Tomography) problem, where instead of measuring the electrical activity of the brain, we inject a tiny current at some sensors in order to estimate the tissues conductivity. This method can be used to state the reciprocity theorem as done in [Clerc et al., 2005b]. In case of EEG, solving the classical formulation of the forward problem for V_f amounts to solving the Poisson equation:

$$\begin{cases} \nabla \cdot (\sigma \nabla V_f) & = f = \nabla \cdot (\mathbf{m}\delta_{\mathbf{r}_0}) \text{ in } \Omega \\ \sigma \nabla V_f \cdot \mathbf{n} & = 0 \text{ on } \Gamma \end{cases} , \tag{3.2}$$

where Γ denotes the boundary of Ω *i.e.* the scalp where the measurements are made. The EIT problem solves for V_j while injecting a (unit) current at location $\mathbf{r}_i$ ($\delta(\mathbf{r}_i)$), and the opposite one at $\mathbf{r}_e$ ($\delta(\mathbf{r}_e)$) :

$$\begin{cases} \nabla \cdot (\sigma \nabla V_j) & = 0 \text{ in } \Omega \\ \sigma \nabla V_j \cdot \mathbf{n} & = j = \delta(\mathbf{r}_i) - \delta(\mathbf{r}_e) \text{ on } \Gamma \end{cases} , \tag{3.3}$$

where the $\delta(\mathbf{r}_i)$ distribution is defined such that $\int_\Gamma \delta(\mathbf{r}_i)\, d\mathbf{s} = 1$ and $supp(\delta(\mathbf{r}_i)) = \mathbf{r}_i$.

Writing the divergence theorem for function $\sigma V_j \nabla V_f$ gives:

$$\begin{aligned}\int_\Gamma V_j(\sigma\nabla V_f \cdot \mathbf{n})d\mathbf{s} &= 0 = \int_\Omega \nabla\cdot(\sigma V_j \nabla V_f)\ d\mathbf{r} \\ &= \int_\Omega \sigma\nabla V_j\cdot\nabla V_f\ d\mathbf{r} + \int_\Omega V_j\nabla\cdot(\sigma\nabla V_f)\ d\mathbf{r} \\ &= \int_\Omega \sigma\nabla V_j\cdot\nabla V_f\ d\mathbf{r} + \int_\Omega V_j\, f\ d\mathbf{r} \end{aligned} \tag{3.4}$$

Similarly, we write the same for the function $\sigma V_f \nabla V_j$:

$$\int_\Gamma V_f\, j d\mathbf{s} = \int_\Omega \sigma\nabla V_j\cdot\nabla V_f\ d\mathbf{r} \tag{3.5}$$

Subtracting the two previous equations leads to:

$$\int_\Omega f\, V_j\ d\mathbf{r} = -\int_\Gamma V_f\, j d\mathbf{s}\ , \tag{3.6}$$

which gives:

$$\mathbf{m}\cdot\nabla V_j(\mathbf{r}_0) = V_f(\mathbf{r}_i) - V_f(\mathbf{r}_e) \tag{3.7}$$

This shows that the gradient of the EIT solution is a leadfield for the EEG forward problem. Using the reciprocity concept, one can construct the leadfield by solving n_s (number of sensors) times the system (3.3), and each time evaluating the gradient of the solution at the desired dipole locations. This can be of prime importance, since $n_s \ll n_d$, where n_d is the number of dipoles.

3.1.2 The adjoint method for the EEG forward problem

In this section, we will derive the adjoint of the EEG forward operator in a continuous framework. With the adjoint method, we will recover the previous Eq.(3.7), and extend it. We will describe the method formally, so that the MEG case could be treated in a similar manner.
Consider $H(\Omega)$ to be the Hilbert space $L^2(\Omega)$ with the inner product defined by: $\langle u, v\rangle_{L^2(\Omega)} = \int_\Omega u(\mathbf{r})v(\mathbf{r})\ d\mathbf{r}$. We define a subspace of $H(\Omega)$ called:

$$W(\Omega) = \{v \in H(\Omega)\cap \mathcal{C}^1(\bar{\Omega}),\ \frac{\partial v}{\partial x_i} \in L^2(\Omega)\ \forall i \in \{1,2,3\}\}, \tag{3.8}$$

which is a Sobolev space (derivatives are in a weak sense). We consider a measurement operator m (linear continuous) of the potential $V \in W(\Omega)$. For example, in EEG this corresponds to the measurement of the potential on the scalp between locations $\mathbf{r}_1$ and $\mathbf{r}_2$, *i.e.* m is a trace operator which evaluates V at these location, through two Dirac distributions of opposite signs:

$$\langle m, V\rangle_{L^2(\Omega)} = \int_\Gamma (\delta_1 - \delta_2)V(\mathbf{r})d\mathbf{r} = V(\mathbf{r}_1) - V(\mathbf{r}_2)\ , \tag{3.9}$$

where δ_1 (resp. δ_2) denotes surface Dirac distributions at position $\mathbf{r}_1$ (resp. $\mathbf{r}_2$).

The leadfield expression $\mathbf{L}$ can be formulated [Nolte, 2003]-[Weinstein et al., 2000] as a linear operator with the dipole parameter $\mathbf{J}^{\mathrm{p}} \in H$ (due to Riesz-Fréchet representation theorem):

$$\mathbf{L}(\mathbf{J}^{\mathrm{p}}) = \int_{\Omega} \frac{\partial \mathbf{L}}{\partial \mathbf{J}^{\mathrm{p}}}(\mathbf{r}) \cdot \mathbf{J}^{\mathrm{p}}(\mathbf{r}) \; d\mathbf{r} \; , \tag{3.10}$$

such that a measurement of V is just a projection of the leadfield at the desired sensors.

We now decide to build up a functional $L(p, v, w)$ adding the measurement of a variable $v \in W$ to a constraint enforced weakly through the parameter w, where the constraint expresses:

$$\langle \mathbf{A}v, w \rangle = \int_{\Omega} \mathbf{A}v \; w \; d\mathbf{r} = \langle b(p), w \rangle \tag{3.11}$$

As a first stage, we will stay with the notations of $\mathbf{A}$ for the linear operator defined as, in the case of EEG:

$$\mathbf{A}v = \nabla \cdot (\sigma \nabla v) \tag{3.12}$$

and with the linear operator $b(.)$ acting on p the source term:

$$b(p) = \nabla \cdot p \tag{3.13}$$

The constraint is then expressed as the weak formulation of our forward EEG problem, which has a unique solution due to Lax-Milgram theorem for all $w \in W$. The functional L is defined as:

$$L(p, v, w) = \langle m, v \rangle + \langle \mathbf{A}v - b(p), w \rangle, \tag{3.14}$$

We assume it to be differentiable in all 3 variables. When $v = v(p) = V$ where V is the forward problem solution with p as source, this system reduces to the measurement, *i.e.* $g(p) = L(p, V, w) = \langle m, V \rangle$. We introduced the function $g(p)$ since the measurement can be, as seen in Eq.(3.10), expressed as a linear function of p. And thus taking the derivative with regard to p writes the leadfield $\mathbf{L}$ projected onto the measure. This functional expression can be seen as a Lagrangian, where usually we have a function to minimize while enforcing some constraint on the solution through the Lagrange parameter w. Loosely, the space of functions matching the constraint generally called U_{ad} for admissible functions, is quite big. The functional introduced here could be seen as a Lagrangian, where we do not want to minimize anything, but the space U_{ad} is reduced to the singleton $U_{ad} = \{V\}$. We use this form to get to the adjoint problem easily.

This functional is not linear with respect to v (nor to p neither w), we want the differential of this functional with regard to v around the point $v = v(p) = V$ to be zero, since the $g(p)$ should only depend on p.

$$L(p, v(p) + \delta v, w) - L(p, v(p), w) = \langle m, \delta v \rangle + \langle \mathbf{A}\delta v, w \rangle = 0 \; , \tag{3.15}$$

where δv is a small perturbation around $v(p)$.
Since there exists a unique adjoint $\mathbf{A}^*$ of the linear operator $\mathbf{A}$, it must verify:

$$\mathbf{A}^* w = -m \tag{3.16}$$

We thus choose w to be the solution of this adjoint problem. The differential of g written δg with respect to δp now writes:

$$\begin{aligned} \delta g &= \frac{\partial L(p, v(p), w)}{\partial p} \delta p \\ &= \langle -\frac{\partial b(p)}{\partial p} \delta p, w \rangle \end{aligned} \tag{3.17}$$

One can notice, in this expression, that the derivative of $g(p)$, can be obtained with the derivative of $b(p)$, when w is the solution of the adjoint problem. This can be interesting since the derivative of $g(p)$ is the leadfield, and that sometimes the adjoint problem in Eq.(3.16) can be easier to solve.

Let us now express all the previous equations for the EEG case, where we now call $\mathbf{J}^{\mathrm{p}}$ the variable p; the source term $b(p)$ is: $b(\mathbf{J}^{\mathrm{p}}) = \nabla \cdot \mathbf{J}^{\mathrm{p}}$, with $\mathbf{J}^{\mathrm{p}}$ the dipolar source: $\mathbf{J}^{\mathrm{p}} = \mathbf{m}\delta_{\mathbf{r}_0}$. The adjoint problem using the expression of $\mathbf{A}$ derives from the expression of L, where we use the divergence theorem twice to set up the differentiations on the variable w:

$$\begin{aligned} L(\mathbf{J}^{\mathrm{p}}, v, w) &= \langle m, v \rangle + \langle \nabla \cdot \sigma \nabla v, w \rangle - \langle \nabla \cdot \mathbf{J}^{\mathrm{p}}, w \rangle \\ &= \langle m, v \rangle + \langle v, \nabla \cdot \sigma \nabla w \rangle - \int_\Gamma \sigma \nabla w \cdot \mathbf{n} \; v \; d\mathbf{s} + \langle \mathbf{m}\, \delta_{\mathbf{r}_0}, \nabla w \rangle \\ &= \langle m, v \rangle + \langle v, \nabla \cdot \sigma \nabla w \rangle - \int_\Gamma \sigma \nabla w \cdot \mathbf{n} \; v \; d\mathbf{s} + \nabla w(\mathbf{r}_0) \cdot \mathbf{m} \; . \end{aligned} \tag{3.18}$$

As a consequence, the derivative of L with respect to v around the point $v = V$ leads to the adjoint problem:

$$0 = \langle m, \delta v \rangle + \langle \nabla \cdot \sigma \nabla w, \delta v \rangle - \int_\Gamma \sigma \nabla w \cdot \mathbf{n} \; \delta v \; d\mathbf{s} \; , \tag{3.19}$$

Then, we choose w to be the solution of this problem, and we get the leadfield expression:

$$\frac{\partial L(\mathbf{J}^{\mathrm{p}}, V, w)}{\partial \mathbf{J}^{\mathrm{p}}} = \nabla w(\mathbf{r}_0) \cdot \mathbf{m} \; . \tag{3.20}$$

To link this with the previous reciprocity theorem, let us take the measurement on Γ, as in Eq.(3.9) the adjoint problem is then:

$$\begin{cases} \nabla \cdot \sigma \nabla w &= 0 \text{ in } \Omega \\ \sigma \nabla w \cdot \mathbf{n} &= \delta_1 - \delta_2 \text{ on } \Gamma \end{cases} \tag{3.21}$$

which is exactly the EIT problem for which we had derived the reciprocity theorem. Similarly, taking another measure, this time in Ω would lead to solve the following adjoint problem:

$$\begin{cases} \nabla \cdot \sigma \nabla w & = \delta_1 - \delta_2 \text{ in } \Omega \\ \sigma \nabla w \cdot \mathbf{n} & = 0 \text{ on } \Gamma \end{cases} \tag{3.22}$$

The adjoint problem in Eq.(3.19) has the exact same structure as the forward problem. This comes from the self-adjoint operator $(\nabla \cdot \sigma \nabla \cdot)$, only the source terms change. If one can solve the forward problem numerically, one can then easily solve the adjoint, and get to the same result (the leadfield) faster. Let us also point out, that this continuous framework presents the advantage of providing an expression for the adjoint in case of spatially extended sensors, such as the common EEG electrodes (small patches) or compositions of magnetometers (planar gradiometers, axial gradiometers, ...) for MEG. For sake of simplicity we only present the EEG case of point-like sensors and refer to [Vallaghé et al., 2009]-[Papadopoulo et al., 2010] for the other cases.

Let us now see an application of this method which turns out to be even simpler at a discrete level.

3.2 The adjoint at a discrete level: application to the sBEM

3.2.1 Notations

Using the notations defined in sec.(2.7.1), we now recall the principal matrices used in the sBEM and their dimensions. Let us first define the dimensions encountered:

n_{s_e}, n_{s_m}: the number of sensors for EEG and MEG respectively.

n_d: the total number of dipoles.

N: the total number of sBEM unknowns (degrees of freedom at the discretized potentials and normal currents on surfaces).

A typical order of magnitude for the number of sensors is $n_s \sim 10^2$. On the other hand, a full leadfield computation with dipolar sources requires several thousands of sources; usually around $n_d \sim 10^4$ dipoles. Finally, a typical order for the number of unknowns achievable with the sBEM goes from $N \simeq 6\,000$ (when considering a three-layer head model with 642 vertices per layer) to $N \simeq 25\,000$ unknowns (for a 4-layer model with 2 562 vertices per layer).
The matrices used in OpenMEEG are:

H: the Head matrix which is symmetric: $N \times N$.

D: the Source matrix (RHS): $N \times n_d$.

X: the sBEM's unknowns: $N \times n_d$.

$\mathbf{S}_{eeg}$: the projection matrix from the scalp potentials onto the EEG sensors: $n_{s_e} \times N$

$\mathbf{S}_{meg}$: the projection matrix from the surfaces potentials onto the MEG sensors: $n_{s_m} \times N$.

$\mathbf{T}_{meg}$: the analytical contribution of the primary source to the MEG sensors: $n_{s_m} \times n_d$.

$\mathbf{L}_{eeg}, \mathbf{L}_{meg}$: the desired EEG and MEG leadfield matrices with respective sizes: $n_{s_m} \times n_d$ and $n_{s_m} \times n_d$.

3.2.2 The adjoint EEG problem

Conventional approach When solving an EEG forward problem with the classical formulation, one has to solve the linear system:

$$\mathbf{H} \cdot \mathbf{X} = \mathbf{D}, \tag{3.23}$$

and then to apply the projection (or selection) matrix to get the desired leadfield:

$$\mathbf{L}_{eeg} = \mathbf{S}_{eeg} \cdot \mathbf{X}. \tag{3.24}$$

In the second equation only a matrix product is needed, whereas in the first one a system of size $N \times n_d$ has to be solved. Several methods can be considered to solve this system, right now in OpenMEEG this is done inverting the matrix $\mathbf{H}$.

$$\mathbf{X} = \mathbf{H}^{-1}\mathbf{D}. \tag{3.25}$$

and thus the leadfield is assembled computing:

$$\mathbf{L}_{eeg} = \mathbf{S}_{eeg} \cdot \mathbf{H}^{-1} \cdot \mathbf{D}. \tag{3.26}$$

Adjoint approach Actually, taking the transpose of the EEG leadfield expression (Eq.(3.26)) gives, since the matrix $\mathbf{H}$ is symmetric (and also its inverse):

$$\mathbf{L}_{eeg}^T = \mathbf{D}^T \cdot \mathbf{H}^{-1} \cdot \mathbf{S}_{eeg}^T. \tag{3.27}$$

Now consider computing the term $\mathbf{H}^{-1} \cdot \mathbf{S}_{eeg}^T$, by solving the linear system:

$$\mathbf{H} \cdot \mathbf{Y} = \mathbf{S}_{eeg}^T. \tag{3.28}$$

This linear system is the discrete adjoint equation which can be derived from Eq.(3.16). It has $N \times n_{s_e}$ unknowns, and thus its resolution is much easier than for the classical approach. Once the system solved, the leadfield is then assembled (line-by-line):

$$\mathbf{L}_{eeg}^T = \mathbf{D}^T \cdot \mathbf{Y} \tag{3.29}$$

3.2.3 The adjoint MEG problem

Conventional approach For the MEG forward problem, since the Biot-Savart law (stated in Eq.(2.12)) requires the potentials at surfaces, one also needs to solve Eq.(3.23). One must also add the contribution of the primary source onto the MEG sensors, (primary component field $\mathbf{B}_0$ in Eq.(2.12) given by the operator $\mathbf{T}_{meg}$).

$$\mathbf{L}_{meg} = \mathbf{S}_{meg} \cdot \mathbf{X} + \mathbf{T}_{meg} = \mathbf{S}_{meg} \cdot \mathbf{H}^{-1} \cdot \mathbf{D} + \mathbf{T}_{meg} \tag{3.30}$$

As in Eq.(3.26), the leadfield is built column by column since it is equivalent to treating each dipole separately.

Adjoint approach Let us have a look at the adjoint way for the MEG leadfield computation, one needs to solve:

$$\mathbf{H} \cdot \mathbf{Z} = \mathbf{S}_{meg}^T \ . \tag{3.31}$$

Once this system solved for $\mathbf{Z}$, the leadfield is then assembled with:

$$\mathbf{L}_{meg}^T = \mathbf{D}^T \cdot \mathbf{Z} + \mathbf{T}_{meg}^T \ , \tag{3.32}$$

i.e. line-by-line.

3.2.4 Numerical algebraic solvers

In the classical approaches, for both leadfields the Eq.(3.23) need to be solved. This is a system of size $N \times n_d$. Since $n_d >> N$, OpenMEEG currently inverts the matrix $\mathbf{H}$, which is then a problem of size $N \times N$. This is done using LAPACK a package of linear algebra routines, which are implemented for fast computations and based on BLAS low-level optimized functions (matrix-vector product, matrix-matrix product, ...). LAPACK inversion (DSPTRI routine) requires a factorization of the matrix first (DSPTRF routine). The matrix inversion routine consists in solving a triangular system for an identity matrix as RHS (of size $N \times N$).
For solving the adjoint equations in Eq.(3.28), and Eq.(3.31), inverting the matrix would lead to no improvement compared to the classical approach, we therefore choose to solve the systems which are of size $N \times n_{s_e}$ and $N \times n_{s_m}$ respectively; which are smaller than the conventional system. Next we will present this solution, considering both the LAPACK solver, and the (multi-threaded) GMres solver.
The LAPACK solver also needs the factorized matrix as input, and then solve the triangular system for only n_s RHS (DSPTRS routine).
The GMres (Generalized Minimum Residual) algorithm is an iterative procedure based on the Krylov subspace, which means that it deals with matrix-vector products, and does not try to factorize the whole matrix. This is convenient for large systems. The GMres method is well suited for indefinite matrices which is our case; in our case, it was also optimized for symmetric matrices.
Other algorithms have been tested, such as the MinRes, and QRsym, but led to

slower convergence rate. The main problem was that these solvers asked for a positive definite preconditioner, and it is difficult to get a good preconditioner. For the GMres method, we used a Jacobi preconditioner which was easy to implement, to store, and does not need to be positive definite (diagonal of $\mathbf{H}$). The use of the very fast conjugated-gradient method was not possible since the $\mathbf{H}$ is indefinite. The GMres solver was slower than the LAPACK solver, even if in contrast with the LAPACK, GMres were multi-threaded (one column of RHS per thread).

3.2.5 Numerical results

3.2.5.1 Quantitative comparisons

In the following experiments we study the time comparisons as well as the peak memory consumption for solving a forward EEG problem with the classical way (LAPACK inversion), the adjoint way using the LAPACK solver, and the adjoint way using the GMres solver. These comparisons have been done with different numbers of unknowns (indexed $N_i, i = 1..4$) for 10 242 dipoles, and simulated 256-electrodes helmet. These parameters are shown in table (3.1). Computations

n_{s_e}	256
n_d	10 242
$N1$	206
$N2$	806
$N3$	3 206
$N4$	12 806

Table 3.1 – *Problem parameters.*

were done on a 8-processor Intel-Xeon CPU with a CPU clock of 3.20GHz. Multi-threading with 8 cores was used for the assembly of matrices $\mathbf{H}$, $\mathbf{D}$, and for the system resolution with GMres. The next table (3.2) shows the results obtained in terms of:

Elapsed time: displaying the total elapsed time (total time) in seconds.

User time: the sum of the time spent on each processor in seconds.

Memory: the maximum resident set size (RSS) in MB.

These results are plotted in Fig.(3.1), on a logarithmic scale for the y-axis. One can see that although the GMres solver is the slowest, it is the cheapest in terms of memory usage and could be the only one possible for bigger problem sizes due to the machine memory limits. The adjoint resolution using LAPACK is almost twice faster and twice cheaper than the classical approach. Note that for this experiment, 256 sensors were used which is already a lot, for EEG. In the next section only 128 EEG sensors will be used, which spares computations in the adjoint, while it does not for the classical approach.

Methods	N	Elapsed time	User time	Peak RSS
Classic - Lapack inversion	N1	13.94	39.38	745
	N2	54.17	271.85	1 587
	N3	613.5	3 556.46	5 403
	N4	6 398.72	14 000.00	27 874
Adjoint - Lapack solver	N1	11.45	36.41	462
	N2	26.25	136.28	500
	N3	397.44	2 470.48	1 094
	N4	3 484.99	11 693.79	15 493
Adjoint - GMres solver	N1	12.91	47.30	466
	N2	36.38	210.98	506
	N3	752.71	4 872.75	1 100
	N4	15 148.44	103 907.58	11 196

Table 3.2 – *Time and memory consumptions.*

3.2.5.2 A realistic case

In this section we propose to compare the adjoint and the classical approaches on a realistic model (displayed in Fig.(3.2)), which is the template model provided in the software SPM (SPM canonical mesh[1]). It represents a 3-layer head model with 2 562 vertices per layer ($d.o.f\ N = 12\,806$), and has 20 484 sources.

The number of sensors was 128 for the EEG helmet, and 579 magnetometers (CTF system) for the MEG detectors. Note that this number of magnetometers, represents the total number of computations of the magnetic field needed, in reality most of the CTF sensors are planar gradiometers which measure the derivative of the radial component of the magnetic field in a tangent direction $\frac{\partial \mathbf{B}_r}{\partial \mathbf{n}_t}$, these values are obtained in OpenMEEG by linear combination of magnetometers.
On Fig.(3.3) are shown the elapsed times and memory consumption (RSS) when assembling a leadfield with the classical approach and the adjoint approach. One can see for each method, 3 columns, corresponding to computing a EEG leadfield, a MEG leadfield, and both leadfields together. Actually when computing both leadfields for the classical approach, as we do compute the system unknowns (matrix $\mathbf{X}$) for the EEG leadfield computation, it is faster to get the MEG leadfield, since almost everything has been computed. In contrast, with the adjoint method the system to be solved is now:

$$\mathbf{H} \cdot \begin{pmatrix} \mathbf{Y} \\ \mathbf{Z} \end{pmatrix} = \begin{pmatrix} \mathbf{S}_{eeg}^T \\ \mathbf{S}_{meg}^T \end{pmatrix}$$

Which is still a smaller system than the one obtained with the classical method since: $(n_{s_e} + n_{s_m}) < N$. The leadfields have then been assembled together line-by-line to compute only once the matrix $\mathbf{D}$.

[1]SPM: http://www.fil.ion.ucl.ac.uk/spm/

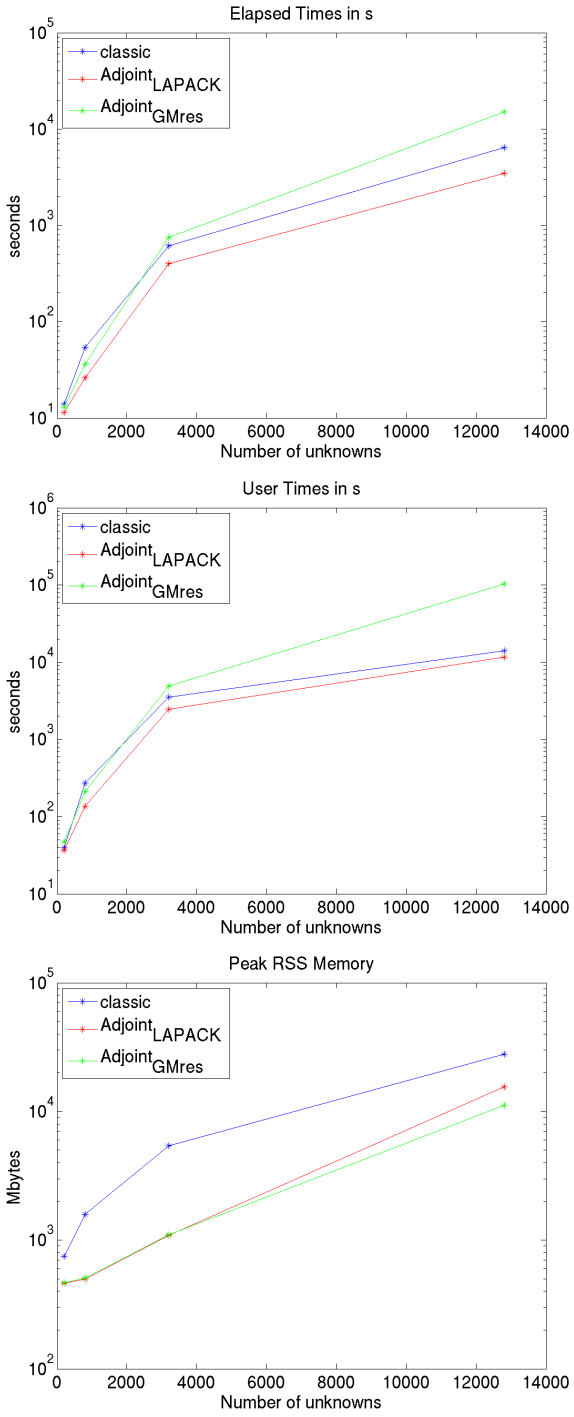

Figure 3.1 – *Times and memory for classical approach vs adjoint approaches.*

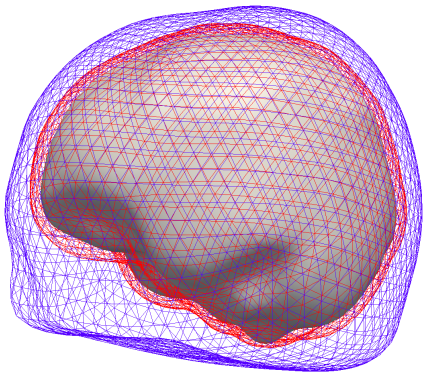

Figure 3.2 – *4-layer realistic (BEM) head model.*

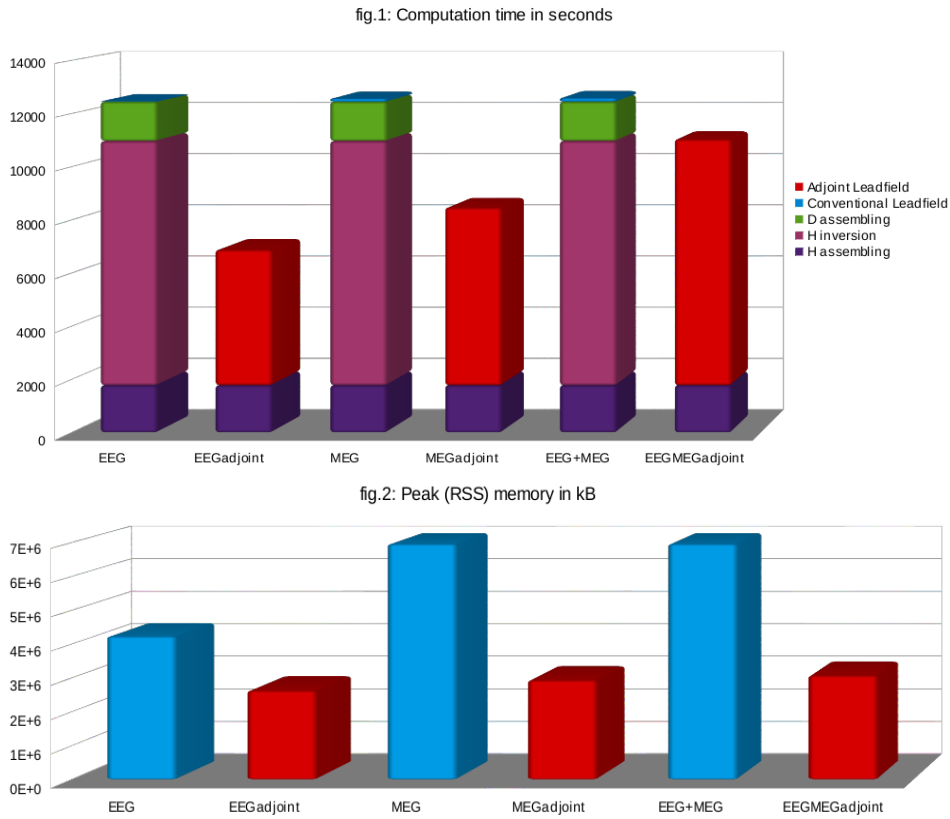

Figure 3.3 – *Times and memory consumption for classical approach vs adjoint approaches.*

3.2.6 Implementation in OpenMEEG

Let us show the commands in OpenMEEG to get to the leadfields using the classical approach and the conventional approach. The input files are:

geometry file (*.geom) which contains the path to the meshes, and their ordering the nested geometry description.

conductivity file (*.cond) which contains the conductivity values of the different regions.

dipole file (*.dip) a file containing the list of position and orientation of each dipole.

sensor files (*.sen) for the EEG sensors locations. For the MEG sensors locations and orientations are written and the linear combination which must be applied to get to gradiometers if needed.

Output files are all matrices (*.mat).

Common part, the assembly of H where one can see the operators introduced in sec.(2.7.1), computed separately.

```
 > om_assemble -HM canonical.geom canonical.cond hm.mat
-----------------------
Sorted List :  1 0 2
Sorted Domains :  Brain Skull Scalp Air
Total number of points    : 7686
Total number of triangles : 15360
OPERATOR S... (arg : mesh m1, mesh m2)
OPERATOR S... (arg : mesh m1, mesh m2)
OPERATOR S... (arg : mesh m1, mesh m2)
OPERATOR N... (arg : mesh m1, mesh m2)
OPERATOR N... (arg : mesh m1, mesh m2)
OPERATOR N... (arg : mesh m1, mesh m2)
OPERATOR D... (arg : mesh m1, mesh m2)
OPERATOR D... (arg : mesh m1, mesh m2)
OPERATOR D... (arg : mesh m1, mesh m2)
OPERATOR D... (arg : mesh m1, mesh m2)
OPERATOR S... (arg : mesh m1, mesh m2)
OPERATOR S... (arg : mesh m1, mesh m2)
OPERATOR N... (arg : mesh m1, mesh m2)
OPERATOR N... (arg : mesh m1, mesh m2)
OPERATOR D... (arg : mesh m1, mesh m2)
-----------------------------------------
| User Time: 9546.66 s.
-----------------------------------------
```

Classical approach for EEG, and MEG leadfields In the classical approach the matrices $\mathbf{H}^{-1}$, $\mathbf{D}$, $\mathbf{S}_{eeg}$, $\mathbf{S}_{meg}$ and $\mathbf{T}_{meg}$ are built separately before being assembled with the 'om_gain' command.

```
>#-------------------------------- CLASSICAL APPROACH
> om_minverser hm.mat hm_inv.mat
-----------------------------------------
| User Time: 9051.4 s.
-----------------------------------------

> om_assemble -DSM canonical.geom canonical.cond cortex_20484.dip dsm.mat
-----------------------
Sorted List :  1 0 2
Sorted Domains :  Brain Skull Scalp Air
Total number of points    : 7686
Total number of triangles : 15360
-----------------------------------------
| User Time: 7101.88 s.
-----------------------------------------

> om_assemble -H2EM canonical.geom canonical.cond eeg_sensors.sen h2em.mat
-----------------------------------------
| User Time: 0.45 s.
-----------------------------------------

> om_gain -EEG hm_inv.mat dsm.mat h2em.mat eeg_leadfield.mat
-----------------------------------------
| User Time: 17.83 s.
-----------------------------------------

> om_assemble -H2MM canonical.geom canonical.cond meg_sensors.sen h2mm.mat
-----------------------------------------
| User Time: 63.74 s.
-----------------------------------------

> om_assemble -DS2MM cortex_20484.dip meg_sensors.sen ds2mm.mat
-----------------------------------------
| User Time: 6.38 s.
-----------------------------------------

> om_gain -MEG hm_inv.mat dsm.mat h2mm.mat ds2mm.mat meg_leadfield.mat
-----------------------------------------
| User Time: 114.71 s.
-----------------------------------------
```

Adjoint approach for EEG, and MEG leadfields For the adjoint approach, only the matrices $\mathbf{S}_{eeg}$, $\mathbf{S}_{meg}$ and $\mathbf{T}_{meg}$ need to be computed first, the leadfield is then

assembled with the command 'om_gain' and an 'adjoint' option.

```
>#---------------------------------- ADJOINT APPROACH
> om_gain -EEGadjoint canonical.geom canonical.cond cortex_20484.dip
hm.mat h2em.mat eeg_leadfield_adjoint.mat
-----------------------
Sorted List :  1 0 2
Sorted Domains :  Brain Skull Scalp Air
Total number of points    : 7686
Total number of triangles : 15360
-----------------------------------------
| User Time: 12152.1 s.
-----------------------------------------

> om_gain -MEGadjoint canonical.geom canonical.cond cortex_20484.dip hm.mat
h2mm.mat ds2mm.mat meg_leadfield_adjoint.mat
-----------------------------------------
| User Time: 15435.4 s.
-----------------------------------------

> om_gain -EEGMEGadjoint canonical.geom canonical.cond cortex_20484.dip hm.mat
h2em.mat  h2mm.mat ds2mm.mat eeg_leadfield_adjoint2.mat meg_leadfield_adjoint2.mat
-----------------------------------------
| User Time: 23651.2 s.
-----------------------------------------
```

Chapter 4

A Domain Decomposition framework for the EEG forward problem

As discussed in sect.2.5.1, each numerical solver has pros and limitations depending on the problem to solve. Ideally, we would like to use the best numerical method possible. On the other hand, once an electrophysiological model has been chosen, one ends up with different conductivity profiles for each sub-domain: either homogeneous, isotropic or inhomogeneous, anisotropic. One could now want to use the most appropriate numerical method for each sub-domain. The domain decomposition framework allows such a splitting of a global computational domain into smaller ones that can be handled with different numerical methods. In this chapter, we propose a decomposition of the domain Ω in Eq.(2.13) in order ultimately to use a BEM for the volume where the sources are (the brain), and a FEM for the rest of the computational domain.

Summary

Goals: Sub-divide the forward EEG problem into smaller ones, to obtain a flexible expression allowing for different numerical solvers.

Tools: Using a domain decomposition framework, dividing the original computational domain in smaller ones where the interfaces are physical interfaces (*e.g.* brain-skull interface).

Results: Coupled formulations through iterative boundary value problems.

Contents

4.1 A domain decomposition framework

The forward EEG problem aims at solving for V the following Poisson equation:

$$\begin{cases} \nabla \cdot (\Sigma \nabla V) = \nabla \cdot \mathbf{J}^{\mathrm{p}} & \text{in } \Omega \\ \Sigma \nabla V \cdot \mathbf{n} = 0 & \text{on } \Gamma_{ext} \end{cases}, \tag{4.1}$$

where Σ denotes the electrical conductivity tensor, which can, depending on the sub-domain, be either a scalar or a 3×3 positive definite matrix. $\Gamma_{ext} = \partial\Omega$ is the exterior surface (*i.e.* the scalp-air interface), where we impose no current outflow (since $\sigma_{air} = 0$).

4.1.1 Introduction

Domain decomposition methods (DDMs) for the numerical solution of partial differential equations is a relatively new field. It is nowadays mostly used to divide a problem into sub-problems defined on sub-domains of the initial computational domain. These techniques allow for the numerical solving of very-large scale problems which could not be solved on a single machine. DDM allow for the use of parallel architecture because the sub-problems they generate can most of the time be solved in parallel. The flexibility of the developed algorithms allow for the use of different numerical solvers within each sub-domain. (This will be of particular interest in our case.) DDM generate sub-problems that need to communicate at their interface somehow. This communication will be done through iterative processes, until the methods 'agree' at their common interface. The sub-domains treated are either overlapping or non-overlapping. The first family of domain decomposition methods, Schwarz methods, uses overlapping domains.

Schwarz methods are the first example of DD approaches, they were introduced by Schwarz in 1869, but mostly gained interest for second order elliptic PDE in the mid-20th century. Let Ω be the computational domain, an overlapping domain decomposition into two regions (Ω_1, Ω_2) is such that: $\Omega = \Omega_1 \cup \Omega_2$ with $\Omega_{1,2}$, the domain defined as $\Omega_{1,2} = \Omega_1 \cap \Omega_2$, non empty. In Fig.(4.1) such a domain partition is displayed, where the spiraled region corresponds to Ω_2, and the gray one to Ω_1. Γ_1, and Γ_2 are the two interfaces defined as: $\Gamma_1 = \partial\Omega_1$, and $\Gamma_2 = \partial\Omega_2 \cap \Omega_1$ Note that the interfaces Γ_1 and Γ_2 do not represent the skull-scalp or CSF-skull interface, but only imaginary interfaces. Solving the forward EEG problem using Schwarz method writes:
Find V_1^k, V_2^k for all $k \geq 1$, so that:

$$\begin{cases} \nabla \cdot \Sigma_1 \nabla V_1^{k+1} &= \nabla \cdot \mathbf{J}_1^{\mathrm{p}} \quad \text{in } \Omega_1 \\ V_1^{k+1} &= V_2^k \quad \text{on } \Gamma_1 \end{cases},$$

$$\begin{cases} \nabla \cdot \Sigma_2 \nabla V_2^{k+1} &= \nabla \cdot \mathbf{J}_2^{\mathrm{p}} \quad \text{in } \Omega_2 \\ V_2^{k+1} &= V_1^{k+1} \quad \text{on } \Gamma_2 \\ \Sigma_2 \nabla V_2^{k+1} \cdot \mathbf{n} &= 0 \quad \text{on } \partial\Omega_2 \cup \partial\Omega \end{cases},$$

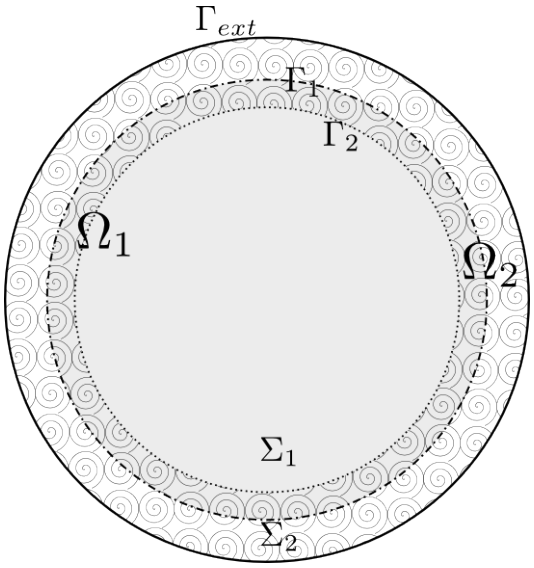

Figure 4.1 – *An overlapping domain partition:* $\Omega = \Omega_1 \cup \Omega_2$ *with* Ω_1 *the gray domain and* Ω_2 *the spiraled one.* Ω_1 *straddles* Γ_2*, and* Ω_2 *straddles* Γ_1*.*

where $V_2^0 = 0$, and $\mathbf{J}_i^{\mathrm{p}}$ for $i = 1, 2$ denote the restriction to Ω_i of the source term $\mathbf{J}^{\mathrm{p}}$. Such an approach is known as the '*multiplicative Schwarz method*'. When looking at these equations, one can see that they cannot be solved in parallel since the second equation (on Ω_2) needs the result V_1^{k+1}. This led to the so called '*additive Schwarz method*', in which the equation $V_2^{k+1} = V_1^{k+1}$ on Γ_2 is replaced by $V_2^{k+1} = V_1^k$. This then allows for parallel algorithms.
The full solution V in Ω is recovered at convergence by taking $V = V_1$ in Ω_1 and $V = V_2$ in Ω_2, (Note that V_1 should be equal to V_2 in $\Omega_1 \cap \Omega_2$). The main problem encountered for the Schwarz techniques, is the convergence rate which directly depends on the 'size' of the shared domain $\Omega_1 \cap \Omega_2$. It thus leads to a critical choice, which is, increase the shared domain to get faster convergence at the expense of heavier computations (since both domains Ω_1 and Ω_2 are bigger). This led the DDM community to investigate further in so-called '*optimized Schwarz methods*', which are techniques that investigate new communications at interface to faster convergence. Some even allow for non-overlapping domain partitions [Lions, 1989].

Fully coupled methods When dealing with non-overlapping domains, such as the one displayed in Fig.(4.2), the problem that one has to solve can be written, when

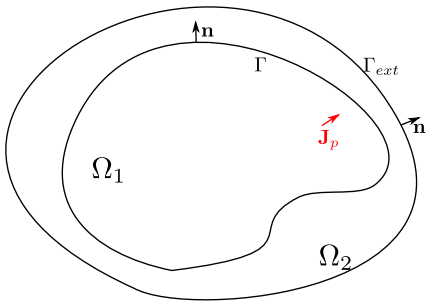

Figure 4.2 – *A non-overlapping domain partition:* $\Omega = \Omega_1 \cup \Omega_2$ *with* $\Gamma = \partial\Omega_1 \cap \partial\Omega_2$.

considering the case of the EEG forward problem for a source located in Ω_1, as:

$$\begin{cases} \nabla \cdot \Sigma_1 \nabla V_1 = \nabla \cdot \mathbf{J}^{\mathrm{p}} & \text{in } \Omega_1 \\ \\ V_1 = V_2 & \text{on } \Gamma \\ \Sigma_1 \nabla V_1 \cdot \mathbf{n} = \Sigma_2 \nabla V_2 \cdot \mathbf{n} & \text{on } \Gamma \\ \\ \nabla \cdot \Sigma_2 \nabla V_2 = 0 & \text{in } \Omega_2 \\ \Sigma_2 \nabla V_2 \cdot \mathbf{n} = 0 & \text{on } \Gamma_{ext} \end{cases} . \tag{4.2}$$

It can be shown that this multi-domain problem is equivalent to the Poisson Eq.(4.1) (see [Quarteroni and Valli, 1999] for a very similar case).
Let us now express, as an example of fully coupled method, the case of a BEM-FEM coupling. Sub-domain Ω_1 will be handled by the BEM (supposing homogeneous isotropic conductivity σ_1), and Ω_2 dealt by the FEM. The key point is to express boundary value problems (b.v.p) in each sub-domain and then to write one b.v.p with the solution of the other. This leads to consider a fully coupled method, where the BEM's equations are incorporated into the FEM stiffness matrix. Such a coupled method was applied successfully in [Fischer et al., 2000] for the case of ECG (Electrocardiography). Let us consider such a BEM-FEM coupling on a realistic head geometry. We suppose that both grids (or meshes) are matching at the interface Γ *i.e.* they share the same vertices. Such a model is displayed Fig.(4.3) (sagittal cut of a head mesh).
The Dirichlet problem in Ω_1 writes:

$$\begin{cases} \sigma_1 \Delta V_1 = \nabla \cdot \mathbf{J}^{\mathrm{p}} & \text{in } \Omega_1 \\ V_1 = V_\Gamma & \text{on } \Gamma \end{cases} \tag{4.3}$$

One can write this Dirichlet b.v.p with the BEM's integral operators. Imposing the potential V_Γ at Γ, we write $\mathbf{A}_B$ the BEM's stiffness matrix corresponding to a Dirichlet problem, $\mathbf{J}_B$ the source term due to the primary source $\mathbf{J}^{\mathrm{p}}$, and $\mathbf{D}_B$ the right hand side which projects the given Dirichlet data on Γ (a vector written $\mathbf{V}_\Gamma$)

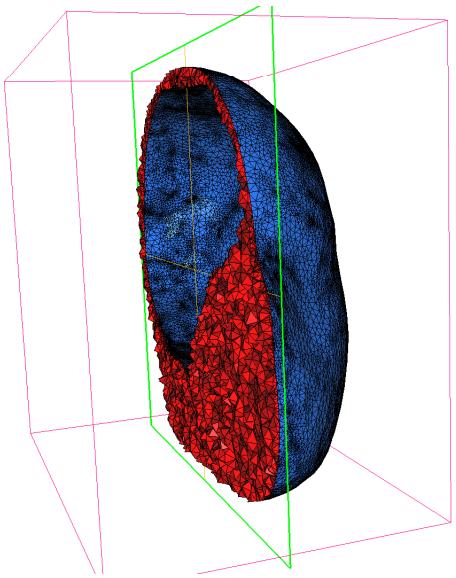

Figure 4.3 – *A non-overlapping partition meshed for a BEM-FEM coupling.*

onto the BEM's variable. We write n the number of vertices on Γ, which is also the number of degrees of freedom for the imposed potential (size of $\mathbf{V}_\Gamma$), we solve for $\mathbf{j}_1 = \sigma_1 \partial_{\mathbf{n}} V_1$, which represents the normal current crossing each of the $2n-2$ triangles of Γ, the equation:

$$\mathbf{A}_B \cdot \mathbf{j}_1 = \mathbf{J}_B \ + \mathbf{D}_B \cdot \mathbf{V}_\Gamma \ , \qquad \text{with } \mathbf{j}_1 = \begin{bmatrix} j_1 \\ j_2 \\ \vdots \\ j_{2n-2} \end{bmatrix} . \tag{4.4}$$

On the other hand, let us solve a Neumann problem in Ω_2:

$$\begin{cases} \nabla \cdot \Sigma_2 \nabla V_2 = 0 & \text{in } \Omega_2 \\ \Sigma_2 \nabla V_2 \cdot \mathbf{n} = j_\Gamma & \text{on } \Gamma \\ \Sigma_2 \nabla V_2 \cdot \mathbf{n} = 0 & \text{on } \Gamma_{ext} \end{cases} \tag{4.5}$$

We denote $\mathbf{A}_F$ the FEM's stiffness matrix corresponding to a Neumann problem whose unknowns are the potential at all mesh vertices denoted $\mathbf{V}_2$ (displayed in red in Fig.(4.3)), including the one on the boundary Γ (in blue in Fig.(4.3)). As there is no source term (except the Neumann boundary data on Γ written $\mathbf{j}_\Gamma$), the

system to solve is:

$$\mathbf{A}_F \cdot \mathbf{V}_2 = \mathbf{T}_F \cdot \mathbf{j}_\Gamma \ , \quad \text{with } \mathbf{V}_2 = \begin{bmatrix} v_1 \\ \vdots \\ v_n \\ v_{n+1} \\ \vdots \\ v_N \end{bmatrix} , \tag{4.6}$$

where $N \gg n$ denotes the total number of vertices in the FEM mesh, and $\mathbf{T}_F$ the operator acting on the Neumann data. Extracting $\mathbf{j}_1$ from Eq.(4.4), and setting $\mathbf{j}_\Gamma = \mathbf{j}_1$ into Eq.(4.6) yields:

$$\mathbf{A}_F \cdot \mathbf{V}_2 - \mathbf{T}_F \mathbf{A}_B^{-1} \cdot (\mathbf{J}_B + \mathbf{D}_B \mathbf{V}_\Gamma) = 0 \tag{4.7}$$

And as we want V_1 to be equal to V_2 at interface *i.e.* $\mathbf{V}_\Gamma = \mathbf{V}_2|_\Gamma$, we write $\mathbf{V}_\Gamma$ as a subset of $\mathbf{V}_2$, such that:

$$\left(\mathbf{A}_F - \begin{bmatrix} \mathbf{T}_F \mathbf{A}_B^{-1} \cdot \mathbf{D}_B & 0 \\ 0 & 0 \end{bmatrix} \right) \cdot \mathbf{V}_2 = \mathbf{T}_F \mathbf{A}_B^{-1} \cdot \mathbf{J}_B, \tag{4.8}$$

where the 0 mean null block matrices with appropriate sizes. Eq.(4.8) is a BEM-FEM fully coupled system. Such a system fulfills the continuity requirements in Eq.(4.2), and allows to obtain the solution in 'one shot' on the global computational domain Ω. But it requires first the assembly of the BEM matrices for the same vertices on Γ as the one of the FEM. This is a bad point since the FEM can handle very detailed mesh because of the sparse structure of its linear system, and thus having too many elements for the BEM might be difficult (or impossible) due to the machine resources. Furthermore, from an algebraic point of view, the solving of the linear system in Eq.(4.8) might be difficult since the coupled matrix (left hand side) is not sparse, and may not be symmetric, nor positive definite, unlike the FEM stiffness matrix. This restrains the choice for algebraic numerical solvers, and the iterative solution may be very slow to converge. Such method should not even be considered as domain decomposition method, but as a coupling technique, since the resulting algorithm is not decomposed into sub-domains.
We next review more flexible methods for solving the multi-domain Eq.(4.2).

Iterative substructuring methods Starting from the multi-domain problem in Eq.(4.2), we will generate sequences of sub-problems posed in $\Omega_i, i \in \{1, 2\}$, for which independent solvers can be used (we consider the same geometry as in Fig.(4.2)). The key point is to express boundary value problems, where the values of the boundary conditions will evolve through iterations until the two numerical methods agree on these boundary values. This family of DDM are often referred to as iterative substructuring methods [Quarteroni and Valli, 1999]. One can express

this iterative process as follow:

$$
\begin{aligned}
&① \begin{cases} \nabla \cdot \Sigma_1 \nabla V_1^{k+1} & = \nabla \cdot \mathbf{J}_1^{\mathrm{p}} \quad \text{in } \Omega_1 \\ f(V_1^{k+1}, \Sigma_1 \nabla V_1^{k+1} \cdot \mathbf{n}) & = B_1^k \quad \text{on } \Gamma \end{cases}, \\
&② \begin{cases} \nabla \cdot \Sigma_2 \nabla V_2^{k+1} & = \nabla \cdot \mathbf{J}_2^{\mathrm{p}} \quad \text{in } \Omega_2 \\ g(V_2^{k+1}, \Sigma_2 \nabla V_2^{k+1} \cdot \mathbf{n}) & = B_2^k \quad \text{on } \Gamma \\ \Sigma_2 \nabla V_2^{k+1} \cdot \mathbf{n} & = 0 \quad \text{on } \Gamma_{ext} \end{cases},
\end{aligned} \tag{4.9}
$$

where the functions f and g represent the type of boundary condition, and B_1^k, B_2^k denote the values of the boundary conditions at iteration k. For example taking $f(V, p) = V$ would state Dirichlet boundary conditions for the first problem (the one on Ω_1).
Such a formulation allows for the solving of a general problem using independent solvers, such as the BEM if we consider an homogeneous and isotropic conductivity (σ_1) for problem ①, and the FEM for ②, without having a requirement on matching grid at interface, provided that the scheme converges to a solution where $V_1 = V_2$, and $\sigma_1 \partial_{\mathbf{n}} V_1 = \Sigma_2 \nabla V_2 \cdot \mathbf{n}$ on Γ. If so, the solution would satisfy the multi-domain Eq.(4.2) and also the global forward EEG problem taking $V = \begin{cases} V_1 & \text{in } \Omega_1 \\ V_2 & \text{in } \Omega_2 \end{cases}$.

In the next section, we will see some of the possibilities for choosing function f and g with appropriate boundary values.

4.1.2 Alternating on boundary value problems

As explained previously one can choose between types of boundary conditions and definition of the sub-problems to be solved, namely boundary conditions will either be Dirichlet (imposing the potential at interface), Neumann (the normal current), or Robin (imposing a linear combination of both potential and normal current at interface). In an iterative substructuring method, the boundary values of the sub-problem evolves, not the type of boundary condition.
Such an algorithm should be designed so that it converges toward the solution of the multi-domain equation (4.2), at the best convergence rate. Let us note that the interface to be defined for the coupling could be anywhere in principle, but will be in our case the brain/skull interface. This choice is led by the conductivity profile of the skull which we want the FEM to handle.

4.1.2.1 Dirichlet-Neumann mapping

The Dirichlet-Neumann coupling described in [Bjorstad and Widlund, 1986]-[Marini and Quarteroni, 1987]-[Marini and Quarteroni, 1989]-[Quarteroni and Valli, 1999] can be defined as follows:

Find V_1^k, V_2^k for all $k \geq 1$, so that:

$$\begin{cases} \nabla \cdot \Sigma_1 \nabla V_1^{k+1} &= \nabla \cdot \mathbf{J}_1^{\mathrm{p}} \quad \text{in } \Omega_1 \\ V_1^{k+1} &= V_2^k \quad \text{on } \Gamma \end{cases}, \tag{4.10}$$

$$\lambda^{k+1} = (1-\omega)\lambda^k + \omega \Sigma_1 \nabla V_1^{k+1} \cdot \mathbf{n} \text{ on } \Gamma \tag{4.11}$$

$$\begin{cases} \nabla \cdot \Sigma_2 \nabla V_2^{k+1} &= \nabla \cdot \mathbf{J}_2^{\mathrm{p}} \quad \text{in } \Omega_2 \\ \Sigma_2 \nabla V_2^{k+1} \cdot \mathbf{n} &= \lambda^{k+1} \quad \text{on } \Gamma \\ \Sigma_2 \nabla V_2^{k+1} \cdot \mathbf{n} &= 0 \quad \text{on } \Gamma_{ext} \end{cases}, \tag{4.12}$$

where the initial conditions are ($V_2^0 = 0$, $\lambda^0 = 0$). In Eq.(4.11) appears a variable λ^k which is the relaxation variable of the iterative scheme, it is homogeneous to a current, and serves for the convergence. In fact, this scheme may or may not converge depending on the parameter ω which controls the strength of the relaxation. ω is chosen in the range $[0, 1]$. The closer to zero, the slower will be the convergence, but the higher probability for it to converge; on the other hand choosing ω close to one, may decrease the number of iterations provided the scheme does not diverge. Considering a relaxation on the Dirichlet data instead of Neumann leads to the exact same convergence considerations.
What about the choice of the Dirichlet or Neumann side ? Are there clues for choosing Ω_1 on which we solve a Dirichlet problem and Ω_2 for the Neumann one ? Either configuration can be chosen, leading to different algorithms. We will see that in the case of the EEG forward problem, the electrophysiological model is better suited to have a Neumann-Dirichlet coupling.

4.1.2.2 Robin-Robin mapping

Find V_1^k, V_2^k for all $k \geq 1$, so that:

$$\begin{cases} \nabla \cdot \Sigma_1 \nabla V_1^{k+1} &= \nabla \cdot \mathbf{J}_1^{\mathrm{p}} \quad &\text{in } \Omega_1 \\ V_1^{k+1} + \gamma_1 \Sigma_1 \nabla V_1^{k+1} \cdot \mathbf{n} &= V_2^k + \gamma_1 \Sigma_2 \nabla V_2^k \cdot \mathbf{n} \quad &\text{on } \Gamma \end{cases}, \tag{4.13}$$

$$\begin{cases} \nabla \cdot \Sigma_2 \nabla V_2^{k+1} &= \nabla \cdot \mathbf{J}_2^{\mathrm{p}} \quad &\text{in } \Omega_2 \\ V_2^{k+1} + \gamma_2 \Sigma_2 \nabla V_2^{k+1} \cdot \mathbf{n} &= V_1^{k+1} + \gamma_2 \Sigma_1 \nabla V_1^{k+1} \cdot \mathbf{n} \text{ on } \Gamma, \quad &\\ \Sigma_2 \nabla V_2^{k+1} \cdot \mathbf{n} &= 0 \quad &\text{on } \Gamma_{ext} \end{cases} \tag{4.14}$$

where the initial condition is ($V_2^0 = 0$), in such a method relaxation is not needed if the Robin parameters γ_i are correctly chosen. We see that setting γ_1 to a high value tends to solve a Neumann problem in Ω_1 while it would be a Dirichlet one for $\gamma_1 = 0$. Even if we do not have to choose a relaxation parameter, the choice for the Robin parameters are not obvious, in [Quarteroni and Valli, 1999] can be seen a proof of convergence when choosing $\gamma_1 = \gamma_2$, or refer to [Lions, 1989] for the general case.

4.1.2.3 Other mapping choices

Other choices of iterative substructuring methods can be made which do not solve equation (4.9), but rather different problems, the solutions can be then recovered out of these subproblem, see for example [Agoshkov and Lebedev, 1990] for Neumann-Neumann coupling, and other formulations which we did not investigate in this thesis.

4.1.2.4 A one dimensional illustration of the Neumann-Dirichlet coupling

Let us look at the following elliptic problem in one dimension:
Find $u \in \mathcal{C}^2([0,1])$ *s.t.*:

$$\begin{cases} \frac{\partial^2}{\partial x^2}\left(\sigma(x)u(x)\right) = 0, \\ u(0) = 0, \\ u(1) = 0. \end{cases}$$

which has a unique solution $u(x) = 0$. We consider a discontinuous conductivity profile σ (see Fig.(4.4)):

$$\sigma(x) = \begin{cases} \sigma_1 \text{ if } x \in [0,\lambda] \\ \sigma_2 \text{ if } x \in [\lambda,1] \end{cases}.$$

Let us consider a Neumann-Dirichlet coupling where we solve iteratively these problems:
Find u_1^k, u_2^k *for all* $k \geq 1$, *s.t.*:

$$\begin{cases} \sigma_1 u_1''^k(x) &= 0, \\ u_1^k(0) &= 0, \\ \sigma_1 u_1'^k(\lambda) &= \theta^{k-1} \end{cases} \text{ and } \begin{cases} \sigma_2 u_2''^k(x) &= 0, \\ u_2^k(\lambda) &= u_1^k(\lambda), \\ u_2^k(1) &= 0 \end{cases}$$

where we look for polynomial solutions: $u_1(x) = a_1x^2 + b_1x + c_1$ and $u_2(x) = a_2x^2 + b_2x + c_2$, and start the iterative scheme with arbitrary parameters. The *b.c.* of the problem 1 is ensured with a relaxation term $\theta^k = (1-\omega)\theta^{k-1} + \omega\sigma_2 u_2'^k(\lambda)$, with $\omega \in [0,1]$ a relaxation parameter. Due to the previous equations we can deduce the following relations:

$$\begin{aligned} \forall k \geq 0\ , \quad a_1^k &= c_1^k = a_2 = 0 \\ b_1^k &= \frac{\theta^{k-1}}{\sigma_1} \\ c_2^k &= -b_2^k \\ b_2^k &= \frac{-b_1^k\lambda}{1-\lambda} \end{aligned}$$

If the iterative scheme converges, the limit solutions u_1 and u_2 are null. Let us

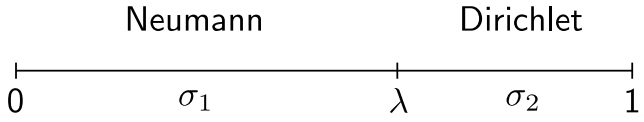

Figure 4.4 – *Description of the 1D domain. The segment* $[0,1]$ *is decomposed into* $[0,\lambda]$ *and* $[\lambda,1]$*, with constant conductivities* σ_1 *and* σ_2 *respectively.*

have a look at the relaxation parameter θ at iteration k:

$$\begin{aligned}\theta^k &= (1-\omega)\theta^{k-1} + \omega\sigma_2 u_2'^k \\ &= (1-\omega)\theta^{k-1} + \omega\sigma_2 b_2^k \\ &= (1-\omega)\theta^{k-1} + \omega\sigma_2 \frac{-b_1^k\lambda}{1-\lambda} \\ &= A\theta^{k-1},\end{aligned}$$

with $A = (1-\omega+\omega\frac{\sigma_2}{\sigma_1}\frac{-\lambda}{(1-\lambda)})$. Thus we can say that this scheme will converge if $\|A\| < 1$, since $\theta^k = A^k\theta^0$. A then defines the convergence rate of the scheme.
Let us first state under which conditions the scheme converges if no relaxation is used *i.e.* $\omega = 1$, then:

$$\|A\| < 1 \Longrightarrow \frac{\sigma_2}{\sigma_1}\frac{\lambda}{(1-\lambda)} < 1 \tag{4.15}$$

For example if $\sigma_1 = \sigma_2$, then the scheme will be convergent with no relaxation provided that the Dirichlet domain is bigger than the Neumann's one.

A numerical example: In Fig.(4.5) are displayed the solutions for 5 iterations of the iterative scheme, where we have set up $\lambda = 0.3$, $\omega = 0.3$, $\sigma_1 = 1.$ and $\theta^0 = 0.1$. Results are displayed varying the parameter σ_2 from 0.1 to 20. The solutions $u_1^k(x)$ are displayed in blue, while $u_2^k(x)$ are in red. One can see that for $\sigma_2 \geq 16$, the scheme is divergent and never reaches the true solution $u(x) = 0$. This is due to the bad choice of the relaxation parameter ω for this conductivity, *i.e.* $\|A\| > 1$. With a lower ω this scheme would be convergent; but taking a too small relaxation parameter leads to a poor convergence rate. The optimal ω could be computed for this 1D problem leading to a total resolution in only one step. ω_{opt} should satisfy $\|A\| = 0 \Longrightarrow \omega_{opt} = \frac{1}{1+\frac{\sigma_2}{\sigma_1}\frac{\lambda}{1-\lambda}}$.

Interpretation: This 1D example of a Neumann-Dirichlet coupling procedure is interesting since it allows to get an idea of the behavior of such a coupling. It can be applied for other coupling strategies such as Robin-Robin method.
From Eq.(4.15), *i.e.* looking at the iterative scheme without relaxation, one can see that for a constant ratio $\frac{\lambda}{1-\lambda}$, the convergence rate depends on the ratio of the conductivities. A very low ratio $\frac{\sigma_2}{\sigma_1} \ll 1$ would imply a high convergence rate. This is in agreement with the following intuition: Viewed from Ω_1, having a (near-)zero

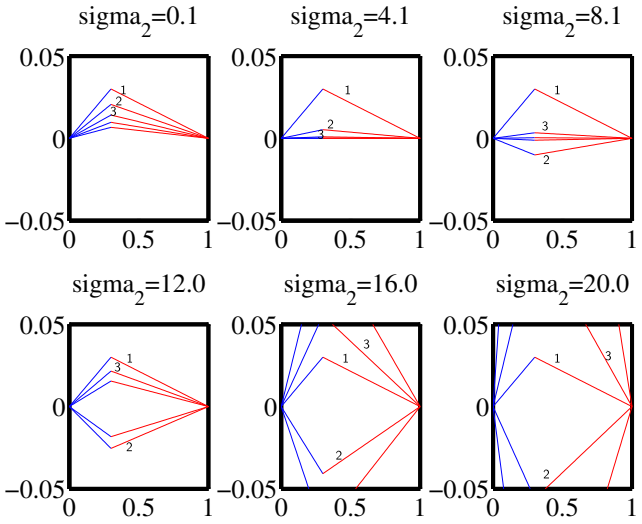

Figure 4.5 – *Solutions through 5 iterations varying σ_2. u_1^k, and u_2^k are plotted in blue and red respectively. Only the first three iterations are indexed i.e. $k = 1, 2, 3$.*

conductivity outside of the domain (in Ω_2) tends to reduces the problem to an homogeneous Neumann problem, since the current crossing the boundary will be (near-) zero.

4.2 Neumann-Dirichlet coupling for solving the forward problem in EEG

4.2.1 From the multi-domain equation to interface equations

In this section we want to split the computational domain (Ω) into several smaller ones (*e.g* Ω_1 and Ω_2). The first step in the decomposition is to write the multi-domain problem equation which we recall here considering an isotropic conductivity σ_1 for domain Ω_1:

$$\begin{cases} \sigma_1 \Delta V_1 = \nabla \cdot \mathbf{J}^{\mathrm{p}} & \text{in } \Omega_1 \\ \\ V_1 = V_2 & \text{on } \Gamma \\ \sigma_1 \nabla V_1 \cdot \mathbf{n} = \Sigma_2 \nabla V_2 \cdot \mathbf{n} & \text{on } \Gamma \\ \\ \nabla \cdot \Sigma_2 \nabla V_2 = 0 & \text{in } \Omega_2 \\ \Sigma_2 \nabla V_2 \cdot \mathbf{n} = 0 & \text{on } \Gamma_{ext} \end{cases} . \tag{4.16}$$

Following the work of [Quarteroni and Valli, 1999], we will develop these equations in order to obtain sub-problems which share a condition on their common interface Γ.

The Steklov-Poincaré operator: Let us write two Dirichlet problems in sub-domains Ω_i, for $i = 1, 2$:
Find w_i *for all* $i = 1, 2$, *s.t.*:

$$\begin{cases} \nabla \cdot \Sigma_i \nabla w_i = f_i & \text{in } \Omega_i \\ w_i = \lambda & \text{on } \Gamma \\ \Sigma_i \nabla w_i \cdot \mathbf{n} = 0 & \text{on } \Gamma_{ext} \end{cases} . \tag{4.17}$$

We see that considering $\Sigma_1 = \sigma_1$, $f_1 = \nabla \cdot \mathbf{J}^{\mathrm{p}}$ and $f_2 = 0$, we have $w_i = V_i$, provided that the second continuity requirement is valid *i.e.* $\sigma_1 \partial_{\mathbf{n}} w_1 = \Sigma_2 \nabla w_2 \cdot \mathbf{n}$ at Γ. The solution w_1 can be written as a harmonic part plus another term handling the source. Writing $\mathcal{H}_1$ the operator which given a Dirichlet data on the boundary associates its harmonic extension in the domain:

$$\begin{array}{lll} \mathcal{H}_1 : H^{\frac{1}{2}}(\Gamma) & \rightarrow H^1(\Omega_1) & \\ \lambda & \mapsto \mathcal{H}_1 \lambda & i.e.\ s.t \begin{cases} \sigma_1 \Delta \mathcal{H}_1 \lambda = 0 & \text{in } \Omega_1 \\ \mathcal{H}_1 \lambda = \lambda & \text{on } \Gamma \end{cases} , \end{array} \tag{4.18}$$

where, $H^{\frac{1}{2}}(\Gamma)$ is the trace space of $H^1(\Omega_1)$. We also introduce still for Ω_1 an operator $\mathcal{G}_1$ *s.t.*:

$$\begin{aligned} \mathcal{G}_1 : L^2(\Omega_1) &\to H^1(\Omega_1) \\ f &\mapsto \mathcal{G}_1 f \quad i.e.\ s.t \begin{cases} \sigma_1 \Delta \mathcal{G}_1 f = f & \text{in } \Omega_1 \\ \mathcal{G}_1 f = 0 & \text{on } \Gamma \end{cases}, \end{aligned} \tag{4.19}$$

and since $\partial\Omega_1 \cap \partial\Omega = \varnothing$, we see that the solution $\mathcal{H}_1\lambda + \mathcal{G}_1 f$ satisfies Eq.(4.17) in Ω_1. And since we have chosen the appropriate Sobolev spaces for the solutions and the data, we can assure the uniqueness of this solution through the Lax-Milgram theorem which is then $w_1 = \mathcal{H}_1\lambda + \mathcal{G}_1 f$.
In Ω_2, we introduce the operator $\mathcal{H}_2$, similar to $\mathcal{H}_1$ but handling the conductivity as a tensor, and ensuring a null Neumann condition on $\Gamma_{ext} = \partial\Omega_2 \cap \partial\Omega$:

$$\begin{aligned} \mathcal{H}_2 : H^{\frac{1}{2}}(\Gamma) &\to H^1(\Omega_2) \\ \lambda &\mapsto \mathcal{H}_2\lambda \quad i.e.\ s.t \begin{cases} \nabla \cdot \Sigma_2 \nabla \mathcal{H}_2\lambda = 0 & \text{in } \Omega_2 \\ \mathcal{H}_2\lambda = \lambda & \text{on } \Gamma \\ \Sigma_2 \nabla \mathcal{H}_2\lambda \cdot \mathbf{n} = 0 & \text{on } \Gamma_{ext} \end{cases}. \end{aligned} \tag{4.20}$$

Similarly we write w_2 thanks to this operator *i.e.* $w_2 = \mathcal{H}_2\lambda$, and the continuity condition is valid: $w_1 = w_2$, since both are λ on Γ. Enforcing the condition for identifying w_i with V_i *i.e.* $\sigma_1 \partial_{\mathbf{n}} w_1 = \Sigma_2 \nabla w_2 \cdot \mathbf{n}$ at Γ, yields:

$$\begin{aligned} \sigma_1 \partial_{\mathbf{n}} \mathcal{H}_1\lambda + \sigma_1 \partial_{\mathbf{n}} \mathcal{G}_1 f &= \Sigma_2 \nabla \mathcal{H}_2\lambda \cdot \mathbf{n} \quad \text{on } \Gamma \\ \left(\sigma_1 \partial_{\mathbf{n}} \mathcal{H}_1 - \Sigma_2 \cdot \mathbf{n}\, \partial_{\mathbf{n}} \mathcal{H}_2\right)\lambda &= -\sigma_1 \partial_{\mathbf{n}} \mathcal{G}_1 f \\ \mathcal{S}\lambda &= \chi \end{aligned} \tag{4.21}$$

The latter equation which holds on Γ is called the Steklov-Poincaré interface equation, with $\mathcal{S}$ the Steklov-Poincaré operator.
If λ satisfies this equation, then solving the sub-problems defined in Eq.(4.17), is equivalent to solving our forward EEG problem. To solve Eq.(4.21), we will consider iterative schemes for solving the multi-domain equation (4.16), which will amounts to expressing an iterative solution of the Steklov-Poincaré equation. But first we introduce a very similar way of handling such a multi-domain problem which is the Poincaré-Steklov operator [Agoshkov and Lebedev, 1990].

The Poincaré-Steklov operator: Instead of two Dirichlet problems (4.17), let us write two Neumann problems in sub-domains Ω_i, for $i = 1, 2$:
Find w_i *for all* $i = 1, 2$, *s.t.*:

$$\begin{cases} \nabla \cdot \Sigma_i \nabla w_i = f_i & \text{in } \Omega_i \\ \Sigma_i \nabla w_i \cdot \mathbf{n} = \lambda & \text{on } \Gamma \\ \Sigma_i \nabla w_i \cdot \mathbf{n} = 0 & \text{on } \partial\Omega_i \cap \partial\Omega \end{cases}, \tag{4.22}$$

where Σ_1 is still equal to σ_1. We have $w_i = V_i$, provided that they share the same value on Γ. In the same spirit, the solution w_i is composed of a harmonic part in Ω_1, *i.e.* writing $\mathcal{N}_1$ the operator which to Neumann data on the boundary associates its harmonic extension in the domain:

$$\begin{array}{lll} \mathcal{N}_1 : H^{-\frac{1}{2}}(\Gamma) & \rightarrow H^1(\Omega_1) & \\ \lambda & \mapsto \mathcal{N}_1\lambda & \textit{i.e. s.t} \begin{cases} \sigma_1 \Delta \mathcal{N}_1\lambda = 0 & \text{in } \Omega_1 \\ \sigma_1 \partial_{\mathbf{n}} \mathcal{N}_1\lambda = \lambda & \text{on } \Gamma \end{cases} . \end{array} \tag{4.23}$$

Operator $\mathcal{G}_1$ is introduced similarly as before, but matches Neumann condition this time on Γ *s.t.*:

$$\begin{array}{lll} \mathcal{G}_1 : L^2(\Omega_1) & \rightarrow H^1(\Omega_1) & \\ f & \mapsto \mathcal{G}_1 f & \textit{i.e. s.t} \begin{cases} \sigma_1 \Delta \mathcal{G}_1 f = f & \text{in } \Omega_1 \\ \sigma_1 \partial_{\mathbf{n}} \mathcal{G}_1 f = 0 & \text{on } \Gamma \end{cases} , \end{array} \tag{4.24}$$

w_1 then writes $w_1 = \mathcal{N}_1\lambda + \mathcal{G}_1 f$. In Ω_2, we introduce the operator $\mathcal{N}_2$, similarly to $\mathcal{N}_1$ but handling the conductivity as a tensor, and ensuring a null Neumann condition on Γ_{ext}:

$$\begin{array}{lll} \mathcal{N}_2 : H^{-\frac{1}{2}}(\Gamma) & \rightarrow H^1(\Omega_2) & \\ \lambda & \mapsto \mathcal{N}_2\lambda & \textit{i.e. s.t} \begin{cases} \nabla \cdot \Sigma_2 \nabla \mathcal{N}_2\lambda = 0 & \text{in } \Omega_2 \\ \Sigma_2 \nabla \mathcal{N}_2\lambda \cdot \mathbf{n} = \lambda & \text{on } \Gamma \\ \Sigma_2 \nabla \mathcal{N}_2\lambda \cdot \mathbf{n} = 0 & \text{on } \Gamma_{ext} \end{cases} , \end{array} \tag{4.25}$$

w_2 writes thanks to this operator: $w_2 = \mathcal{N}_2\lambda$, and the continuity condition $w_1 = w_2$ compulsory to associate w_i to V_i implies:

$$\begin{aligned} \mathcal{N}_1\lambda + \mathcal{G}_1 f &= \mathcal{N}_2\lambda \quad \text{on } \Gamma \\ (\mathcal{N}_1 - \mathcal{N}_2)\,\lambda &= -\mathcal{G}_1 f \\ \mathcal{P}\lambda &= \chi \end{aligned} \tag{4.26}$$

The latter equation which holds on Γ is called the Poincaré-Steklov interface equation, with $\mathcal{P}$ the Poincaré-Steklov operator.
We will later refer to this equation instead of the Steklov-Poincaré one (4.21) in order to study the convergence of the coupled scheme.

4.2.2 The Neumann-Dirichlet coupling

Here we propose a Neumann-Dirichlet problem for a nested geometry as seen Fig.(4.6). We consider a Neumann problem for the innermost domain (Ω_1), and solve a mixed Dirichlet/homogeneous Neumann problem in ($\Omega_2 \cup \Omega_3$), to obtain the (zero-mean) potential on the outermost surface (*e.g.* the scalp Γ_{ext}):

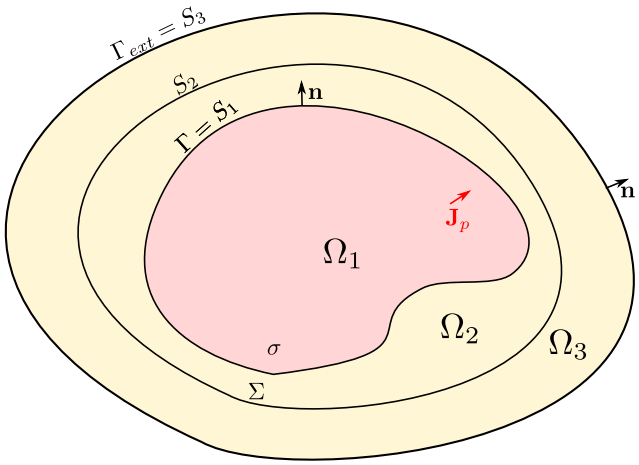

Figure 4.6 – *Domain partition for a Neumann-Dirichlet coupling. A Neumann problem is solved in Ω_1, while a mixed Dirichlet-homogeneous Neumann problem is solved in $\Omega_2 \cup \Omega_3$.*

Find V_1^k, and V_2^k for all $k \geq 1$, s.t.:

$$\text{Neumann b.v.p} \quad \begin{cases} \sigma \Delta V_1^{k+1} = \nabla \cdot \mathbf{J}^{\mathrm{p}} & \text{in } \Omega_1 \\ (\sigma \ \nabla V_1^{k+1}) \cdot \mathbf{n} = \lambda^k & \text{on } \Gamma, \end{cases} \tag{4.27}$$

$$\text{Mixed DhN b.v.p} \quad \begin{cases} \nabla \cdot \Sigma \nabla V_2^{k+1} = 0 & \text{in } \Omega_2 \cup \Omega_3 \\ V_2^{k+1} = V_1^{k+1} & \text{on } \Gamma \\ (\Sigma \nabla V_2^{k+1}) \cdot \mathbf{n} = 0 & \text{on } \Gamma_{ext}, \end{cases} \tag{4.28}$$

where λ is the variable (homogeneous to a current) on which we relax the scheme through iterations.

$$\lambda^{k+1} = (1-\omega)\lambda^k + \omega(\Sigma \ \nabla V_2^{k+1} \cdot \mathbf{n})|_\Gamma \tag{4.29}$$

We will now introduce a different way to write this problem using the previously defined operators for the definition of the Poincaré-Steklov operator in Eq.(4.26). Actually the Neumann problem is known to have a solution defined up to a constant, furthermore, a necessary condition is to have a zero mean data λ on Γ; this is called the *compatibility condition*, and is physically equivalent to the non accumulation of charge. In other words, supposing a solution $v_1 \in H^1(\Omega)$, then applying the divergence theorem in Ω_1 shows that this solution satisfies $\int_\Gamma \sigma \nabla v_1 \cdot \mathbf{ds} = 0$, thus for each homogeneous Neumann problem we will see, we will suppose the Neumann data to be in the space:

$$\lambda \in \hat{H}^{\frac{1}{2}}(\Gamma) \Leftrightarrow \lambda \in \left\{ H^{\frac{1}{2}}(\Gamma) \ s.t \int_\Gamma \lambda ds = 0 \right\}, \tag{4.30}$$

Still, the solution is defined up to a constant which will need to be fixed; one can choose to set one point as reference, or restrained the solution to be zero mean in

total or on some surface. This will be done numerically using the so-called deflation technique.
Using the operators $\mathcal{N}_1$ and $\mathcal{G}_1$ defined in Eq.(4.23) and (4.24) respectively, we write the solution V_1 of problem Eq.(4.27): with the contribution of the source $f = \nabla \cdot \mathbf{J}^{\mathrm{p}}$:

$$V_1 = \mathcal{N}_1 \lambda + \mathcal{G}_1 f \ .$$

Finally let us define operator $\mathcal{D}_2$ for the mixed problem in $\Omega_2 \cup \Omega_3$ (which is simply operator $\mathcal{H}_2$ in the Steklov-Poincaré definition (Eq.(4.20)) extended for two domains):

$$\begin{aligned} \mathcal{D}_2 : H^{\frac{1}{2}}(\Gamma) \quad &\to H^1(\Omega_2 \cup \Omega_3) \\ u \qquad &\mapsto v_2 = \mathcal{D}_2 u \qquad i.e.\ s.t \begin{cases} \nabla \cdot \Sigma \nabla v_2 = 0 & \text{in } \Omega_2 \cup \Omega_3 \\ \Sigma \nabla v_2 \cdot \mathbf{n} = 0 & \text{on } \Gamma_{ext} \\ v_2 = u & \text{on } \Gamma \end{cases} , \end{aligned} \tag{4.31}$$

We can now rewrite the solution of Eq.(4.27)-(4.28), inserting the previously defined operators:

$$\begin{cases} V_1^{k+1} &= \mathcal{N}_1 \lambda^k + \mathcal{G}_1 f \\ V_2^{k+1} &= \mathcal{D}_2 V_1^{k+1}|_\Gamma \end{cases} , \tag{4.32}$$

which now allows us to express Eq.(4.29). Actually we will see later on that in the case of the EEG forward problem such a coupling does not require a relaxation on λ. Let us write down this equation with $\omega = 1$ which also increases readability (although the same can be done with a relaxation parameter):

$$\begin{aligned} \lambda^{k+1} &= \left(\Sigma \nabla V_2^{k+1} \cdot \mathbf{n} \right) \Big|_\Gamma \\ &= \left(\Sigma \nabla (\mathcal{D}_2 \, V_1^{k+1}|_\Gamma) \cdot \mathbf{n} \right) \Big|_\Gamma \\ &= \left(\Sigma \nabla (\mathcal{D}_2 (\mathcal{N}_1 \lambda^k + \mathcal{G}_1 f)|_\Gamma) \cdot \mathbf{n} \right) \Big|_\Gamma \\ &= \left(\Sigma \nabla (\mathcal{D}_2 (\mathcal{N}_1 \lambda^k)|_\Gamma) \cdot \mathbf{n} \right) \Big|_\Gamma + \left(\Sigma \nabla (\mathcal{D}_2 (\mathcal{G}_1 f)|_\Gamma) \cdot \mathbf{n} \right)|_\Gamma \\ &= \mathcal{A} \lambda^k + \mathcal{B} \end{aligned} \tag{4.33}$$

We are thus left with an affine sequence for the Neumann boundary data λ. Where we need some conditions on the operator $\mathcal{A}$ for the sequence to converge. Note that $\mathcal{A}$ does not depend on the source term f.
In fact introducing a variable $\xi^k = \lambda^k + \mathcal{C}$, such that $\mathcal{C}$ verifies:

$$-\mathcal{A}\mathcal{C} + \mathcal{B} + \mathcal{C} = 0 \ ,$$

the convergence of Eq.(4.33)is equivalent to the one of:

$$\begin{aligned} \xi^{k+1} &= \mathcal{A}\xi^k && (4.34)\\ \Longleftrightarrow \xi^k &= \mathcal{A}^k\xi_0 && (4.35) \end{aligned}$$

In order to keep stability the norm of operator $\mathcal{A}$ must satisfy:

$$\begin{aligned} |||\mathcal{A}||| &< 1 && (4.36)\\ |||\left(\Sigma\ \nabla(\mathcal{D}_2(\mathcal{N}_1\ \cdot\ )|_\Gamma)\cdot\mathbf{n}\right)|_\Gamma\ ||| &< 1 && (4.37) \end{aligned}$$

Next, in our experiments we will check the spectral radius of the numerical approximation of $\mathcal{A}$ to verify whether or not the iterative scheme will be converging.

Actually this sequence can be expressed in terms of Steklov-Poincaré operator, and leads to a Richardson procedure for the solving of equation (4.21). We refer to [Quarteroni and Valli, 1999]-[Wohlmuth, 2001], where they provide a proof for the convergence of this iterative scheme, establishing first good properties for the Steklov-Poincaré operator which inherits its properties from the original problem (it is symmetric, positive-definite and coercive). This proof is also given in the finite-dimensional case for the case of matching grids. Let us formulate Eq.(4.29) using the Poincaré-Steklov operator:
We recall that solutions V_1^k, V_2^k can be written using the operators defined in Eq.(4.23)-(4.24)-(4.25):

$$V_1^{k+1} = \mathcal{N}_1\lambda^k + \mathcal{G}_1 f \qquad (4.38)$$

$$V_2^{k+1} = \mathcal{N}_2\left(\Sigma\nabla V_2^{k+1}|_\Gamma\cdot\mathbf{n}\right) \qquad (4.39)$$

The Poincaré-Steklov equation (4.26) writes:

$$\mathcal{N}_2\left(\Sigma_2\nabla V_2^{k+1}\cdot\mathbf{n}\right) = -\chi + \mathcal{N}_1\lambda^k \qquad (4.40)$$

Which now allows us to re-write Eq.(4.29) as:

$$\begin{aligned} \lambda^{k+1} &= (1-\omega)\lambda^k + \omega\left(\Sigma\nabla V_2^{k+1}\cdot\mathbf{n}\right)\\ &= (1-\omega)\lambda^k + \omega\mathcal{N}_2^{-1}\left(\mathcal{N}_1\lambda^k - \chi\right)\\ &= \lambda^k + \omega\mathcal{N}_2^{-1}\left(\mathcal{N}_1\lambda^k - \mathcal{N}_2\lambda^k - \chi\right)\\ &= \lambda^k + \omega\mathcal{N}_2^{-1}\left(\mathcal{P}\lambda^k - \chi\right)\ , && (4.41) \end{aligned}$$

which is then the writing of an iterative procedure called Richardson with operator $\mathcal{N}_2$ acting as preconditioner for the solution of the Poincaré-Steklov equation in Eq.(4.26).

4.2.3 The Dirichlet-Neumann coupling

For sake of completeness, we also present a Dirichlet-Neumann coupling in a similar way as the previous coupling. This coupled method will not be used in practice because of convergence problems.
The Dirichlet-Neumann coupling is defined as:
Find V_1^k, *and* V_2^k *for all* $k \geq 1$, *s.t.*:

$$\text{Dirichlet b.v.p} \quad \begin{cases} \sigma \Delta V_1^{k+1} = \nabla \cdot \mathbf{J}^{\text{p}} & \text{in } \Omega_1 \\ V_1^{k+1} = V_2^k & \text{on } \Gamma \end{cases}, \tag{4.42}$$

$$\lambda^{k+1} = \quad (1-\omega)\lambda^k + \omega(\sigma \partial_{\mathbf{n}} V_1^k) \quad \text{on } \Gamma \tag{4.43}$$

$$\text{Neumann b.v.p} \quad \begin{cases} \nabla \cdot \Sigma \nabla V_2^{k+1} = 0 & \text{in } \Omega_2 \cup \Omega_3 \\ (\Sigma \ \nabla V_2^{k+1}) \cdot \mathbf{n} = \lambda^k & \text{on } \Gamma \\ (\Sigma \nabla V_2^{k+1}) \cdot \mathbf{n} = 0 & \text{on } \Gamma_{ext} \end{cases}, \tag{4.44}$$

where λ is still the relaxation variable (homogeneous to a current). Similarly, one can define operators $\mathcal{D}_1, \mathcal{G}_1, \mathcal{N}_2$ such that the solutions write:

$$V_1 = \mathcal{D}_1 V_2|_\Gamma + \mathcal{G}_1 f \qquad \text{and} \qquad V_2 = \mathcal{N}_2 \lambda \tag{4.45}$$

We thus end up with a similar affine sequence for the relaxation variable λ, where this time we consider the case of a relaxed scheme (*i.e.* $\omega \neq 0$):

$$\begin{aligned} \lambda^{k+1} &= (1-\omega)\lambda^k + \omega \left(\sigma \partial_{\mathbf{n}} V_1^{k+1} \right) \\ &= (1-\omega)\lambda^k + \omega \left(\sigma \partial_{\mathbf{n}} \left(\mathcal{D}_1 V_2^k|_\Gamma + \mathcal{G}_1 f \right) \right) \\ &= (1-\omega)\lambda^k + \omega \left(\sigma \partial_{\mathbf{n}} \left(\mathcal{D}_1 (\mathcal{N}_2 \lambda^k)|_\Gamma \right) \right) + \omega\sigma \left(\partial_{\mathbf{n}} \mathcal{G}_1 f \right) \\ &= \left((1-\omega)\mathcal{I} + \omega\sigma \partial_{\mathbf{n}} \left(\mathcal{D}_1 (\mathcal{N}_2 \ \cdot \ )|_\Gamma \right) \right) \lambda^k + \omega\sigma \left(\partial_{\mathbf{n}} \mathcal{G}_1 f \right) \\ &= \mathcal{A}_{DN} \lambda^k + \mathcal{B}_{DN} \end{aligned} \tag{4.46}$$

We will show next, that $\mathcal{A}_{DN}$ does not have good properties for our electrophysiological problem of EEG.

4.2.4 The Neumann-Dirichlet-Neumann coupling

As our first intention for the coupling is to use the FEM for the skull, we also consider a Neumann-Dirichlet-Neumann coupling, where the FEM is only used for the skull *i.e.* Ω_2 (see Fig.(4.7)). We thus consider isotropic conductivities σ_1, and σ_3 for the sub-domains Ω_1 and Ω_3 respectively, and an inhomogeneous or anisotropic conductivity Σ_2 in Ω_2. The iterative scheme writes:

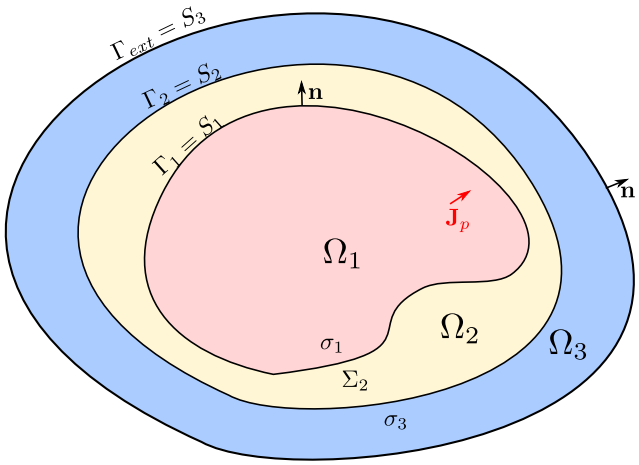

Figure 4.7 – *Domain partition for a Neumann-Dirichlet-Neumann coupling.*

Find V_1^k, V_2^k, V_3^k *for all* $k \geq 1$, *s.t.*:

$$\text{Neumann b.v.p} \quad \begin{cases} \sigma_1 \Delta V_1^{k+1} = \nabla \cdot \mathbf{J}_p & \text{in } \Omega_1 \\ (\sigma_1 \nabla V_1^{k+1}) \cdot \mathbf{n} = \lambda_1^k & \text{on } \Gamma_1, \end{cases} \tag{4.47}$$

$$\text{Dirichlet b.v.p} \quad \begin{cases} \nabla \cdot \Sigma_2 \nabla V_2^{k+1} = 0 & \text{in } \Omega_2 \\ V_2^{k+1} = V_1^{k+1} & \text{on } \Gamma_1 \\ V_2^{k+1} = V_3^k & \text{on } \Gamma_2, \end{cases} \tag{4.48}$$

$$\text{Neumann b.v.p} \quad \begin{cases} \sigma_3 \Delta V_3^{k+1} = 0 & \text{in } \Omega_3 \\ (\sigma_3 \nabla V_3^{k+1}) \cdot \mathbf{n} = \lambda_2^k & \text{on } \Gamma_2, \\ (\sigma_3 \nabla V_3^{k+1}) \cdot \mathbf{n} = 0 & \text{on } \Gamma_3, \end{cases} \tag{4.49}$$

where λ_1^k and λ_2^k are the variables (homogeneous to a current) on which we relax the scheme through iterations.

$$\begin{cases} \lambda_1^{k+1} &= \omega_1 \lambda_1^k + (1-\omega_1)(\sigma_2 \nabla V_2^k \cdot \mathbf{n})|_{\Gamma_1} \\ \lambda_2^{k+1} &= \omega_2 \lambda_2^k + (1-\omega_2)(\sigma_2 \nabla V_2^k \cdot \mathbf{n})|_{\Gamma_2} \end{cases} \tag{4.50}$$

From this point of view this problem seems more difficult to handle, since there are two indefinite problems (two Neumann problems), thus two constants to set, which cannot be independent. Furthermore it seems difficult to express the iterative sequence for the scheme to converge, since there are two relaxation variables.
Instead we choose to consider a Neumann-Dirichlet problem with this time a Neumann problem on the disjoint domain $\Omega_1 \cup \Omega_3$, and a pure Dirichlet problem instead of the mixed Dirichlet-homogeneous Neumann as previously. We call this problem a '*Sandwiched Neumann-Dirichlet*' coupling.

4.2.5 The Sandwiched Neumann-Dirichlet coupling

Variables in the domain $\Omega_{1,3} = \Omega_1 \cup \Omega_3$ will be indexed $_{1,3}$. The iterative scheme writes:
Find $V_{1,3}^k$, *and* V_2^k *for all* $k \geq 1$, *s.t.*:

$$\text{Neumann b.v.p} \quad \begin{cases} \sigma_{1,3}\Delta V_{1,3}^{k+1} = f_{1,3} & \text{in } \Omega_{1,3} \\ (\sigma_{1,3}\nabla V_{1,3}^{k+1}) \cdot \mathbf{n} = \lambda^k & \text{on } \Gamma_{1,3}, \\ (\sigma_{1,3}\nabla V_{1,3}^{k+1}) \cdot \mathbf{n} = 0 & \text{on } \Gamma_{ext}, \end{cases} \tag{4.51}$$

$$\text{Dirichlet b.v.p} \quad \begin{cases} \nabla \cdot \Sigma_2 \nabla V_2^{k+1} = 0 & \text{in } \Omega_2 \\ V_2^{k+1} = V_{1,3}^{k+1} & \text{on } \partial\Omega_2 \end{cases} \tag{4.52}$$

$$\lambda^{k+1} = (1-\omega)\lambda^k + \omega(\Sigma_2 \nabla V_2^{k+1} \cdot \mathbf{n})|_{\partial\Omega_2} \tag{4.53}$$

We write $V_{1,3}$ using similar operators as in Eq.(4.23)-(4.24)-(4.31):

$$V_{1,3}^{k+1} = \mathcal{N}_{1,3}\lambda^k + \mathcal{G}_{1,3} f_{1,3} \tag{4.54}$$

$$V_2^{k+1} = \mathcal{N}_2 \left(\Sigma_2 \nabla V_2^{k+1} \cdot \mathbf{n}|_{\partial\Omega_2} \right) \tag{4.55}$$

Then Eq.(4.53) writes:

$$\begin{aligned} \lambda^{k+1} &= (1-\omega)\lambda^k + \omega(\Sigma_2 \nabla V_2^{k+1} \cdot \mathbf{n})|_{\partial\Omega_2} \\ &= (1-\omega)\lambda^k + \omega\mathcal{N}_2^{-1}\left(\mathcal{N}_{1,3}\lambda^k + \mathcal{G}_{1,3} f_{1,3}\right) \\ &= \lambda^k + \omega\mathcal{N}_2^{-1}\left(\mathcal{P}\lambda^k - \chi\right) \end{aligned} \tag{4.56}$$

In order to study numerically the convergence, we will write this sequence as in Eq.(4.33), with operator $\mathcal{A}$ defined in this case as:

$$\mathcal{A}_{SND} = (1-\omega)\mathcal{I} + \omega \left(\Sigma_2 \nabla (\mathcal{D}_2(\mathcal{N}_{1,3} \ \cdot \ )|_{\partial\Omega_2}) \cdot \mathbf{n}\right)|_{\Gamma_{1,3}} \tag{4.57}$$

4.2.6 Choosing between the different couplings

In the next chapter we consider these coupled formulations using BEM. Such a coupling was a first step (in this thesis) in the establishment of a BEM-FEM coupling, this allowed for using the same mesh for both methods, and trying out the iterative scheme, without the difficulty of using different numerical solvers. We will see that such coupled methods can also be interesting for sparing computation time and dispatching memory.

As seen for the 1D example, the choice of the Dirichlet or Neumann side can be crucial depending on the shape of the space, and the assigned conductivities. The next chapter will show, examining numerically the discrete version of operator $\mathcal{A}$ in Eq.(4.33), that the good choice is to consider a Neumann-Dirichlet coupling. This is

also in agreement with the common physical thinking, since the skull conductivity is very much lower than the brain's, it can be considered that the currents crossing Γ are small (also keeping in mind that the sources lie in the brain), hence the inner problem is close to an homogeneous Neumann problem.

4.3 Conclusion

In this chapter, after introducing the reader with domain decomposition methods, we focused on iterative substructuring methods and mainly on Neumann-Dirichlet coupling. This coupling was first analyzed and described with the Steklov-Poincaré operator, which allow a reduction of the problem to an interface equation, whose resolution ensures the continuity requirements of our physical initial problem. Then we focussed on an operator which will govern the convergence of the iterative scheme. This operator will be studied numerically later, and will allow for choosing a relaxation parameter if needed.

Chapter 5

Implementation of BEM-BEM coupled methods

As a first step, before studying an iterative substructuring method with a BEM coupled with a FEM, we decide to study BEM-BEM couplings. The utility of such a coupling is not obvious regarding our first goal which is to be able to take into account the inhomogeneous conductivity profile of the skull. But we will see that BEM-BEM couplings allow for resolution of bigger (isotropic) problems than the classical BEM, which can be interesting in some cases. Furthermore studying the convergence of the presented schemes is crucial, and this is independent of the numerical methods used, and of the different mesh resolutions used.

Summary

Goals: Try several coupled formulations, as a first step for a BEM-FEM coupling. Establish convergence properties of the different schemes.

Tools: The previously developed formulations for the forward EEG problem, based on domain decomposition methods.

Results: Interesting coupled formulations faster than the classical sBEM formulation.

Contents

5.1 The symmetric BEM operators

We recall here the representation theorem (1) stated p.63:
Let $\Omega \subseteq \mathbb{R}^3$ be a bounded open set with a regular boundary $\partial\Omega$. Let $u : (\mathbb{R}^3 \backslash \partial\Omega) \to \mathbb{R}$ be a harmonic function ($\Delta u = 0$ in $\mathbb{R}^3 \backslash \partial\Omega$), satisfying the $\mathscr{H}$ condition. Then $\forall \mathbf{r} \in \partial\Omega$

$$-\partial_{\mathbf{n}} u^{\pm} = +\mathcal{N}[u] + \big(\pm\frac{\mathcal{I}}{2} - \mathcal{D}^*\big)[\partial_{\mathbf{n}} u] \tag{5.1}$$

$$u^{\pm} = \big(\mp\frac{\mathcal{I}}{2} - \mathcal{D}\big)[u] + \mathcal{S}[\partial_{\mathbf{n}} u] \tag{5.2}$$

which is applied for the symmetric BEM for the harmonic function u_{Ω_i}

$$u_{\Omega_i} = \begin{cases} V - v_{\Omega_i}/\sigma_i & \text{in } \Omega_i \\ -v_{\Omega_i}/\sigma_i & \text{in } \mathbb{R}^3 \backslash \overline{\Omega}_i \end{cases}, \tag{5.3}$$

where the function v_{Ω_i} satisfies the equation: $\Delta v_{\Omega_i} = f_{\Omega_i} = f \cdot \mathbb{1}_{\Omega_i}$, f the source term, which in our case will be considered to be only in the first volume Ω_1.
With regard to the outward normal such as displayed in Fig.(5.1), we have the following jumps for u_{Ω_i}:

$$[u_{\Omega_i}]_i = V_{S_i} \quad , \quad [u_{\Omega_i}]_{i-1} = -V_{S_{i-1}} \ , \tag{5.4}$$

and for $\partial_{\mathbf{n}} u_{\Omega_i}$:

$$[\partial_{\mathbf{n}} u_{\Omega_i}]_i = (\partial_{\mathbf{n}} V)^-_{S_i} \quad , \quad [\partial_{\mathbf{n}} u_{\Omega_i}]_{i-1} = -\,(\partial_{\mathbf{n}} V)^+_{S_{i-1}} \ . \tag{5.5}$$

In the next sections, we will write the BEM equations for different boundary value problems (b.v.p), and we will formulate the equations using the representation theorem. The unknowns will either be the potential V at surface S_i denoted V_i and/or the normal current $p_i = \sigma_i \left[\partial_{\mathbf{n}} u_{\Omega_i}\right]_i = \sigma_i \left(\partial_{\mathbf{n}} V\right)^-_i$, which, as its is continuous, is also equal to $p_i = \sigma_{i+1} \left(\partial_{\mathbf{n}} V\right)^+_i$.
Then we will write the discretized versions of the integral operators to express the matrix systems. The discretized potential V_i at surface S_i will be denoted $\mathbf{V}_i$, which is a vector containing one potential value per mesh node, and $\mathbf{p}_i$ for the normal current (one current value per triangle).
As explained in sec.2.4.3, the potential at surface S_k is discretized with P1 functions $\phi_i^{(k)}$ so that $\mathbf{V}_k = \sum_i v_i \phi_i^{(k)}$, and with P0 functions for the current such that $\mathbf{p}_k = \sum_i \mathfrak{p}_i \psi_i^{(k)}$. And the discretized version of integral operators $\mathcal{N}$, $\mathcal{D}$, $\mathcal{S}$, ... are obtained:

$$\begin{aligned} (\mathbf{N}_{kl})_{ij} &= \langle \mathcal{N}_{kl} \phi_i^{(l)}, \phi_j^{(k)} \rangle \quad , \quad (\mathbf{S}_{kl})_{ij} = \langle \mathcal{S}_{kl} \psi_i^{(l)}, \phi_j^{(k)} \rangle \\ (\mathbf{D}_{kl})_{ij} &= \langle \mathcal{D}_{kl} \phi_i^{(l)}, \psi_j^{(k)} \rangle \quad , \quad (\mathbf{D}^*_{kl})_{ij} = \langle \mathcal{D}^*_{kl} \psi_i^{(l)}, \phi_j^{(k)} \rangle \\ (\mathbf{I}_{kl})_{ij} &= \langle \mathcal{I}_{kl} \phi_i^{(l)}, \psi_j^{(k)} \rangle \quad , \quad (\mathbf{I}^*_{kl})_{ij} = \langle \mathcal{I}^*_{kl} \psi_i^{(l)}, \phi_j^{(k)} \rangle \end{aligned} \tag{5.6}$$

In these equations, one can note that $(\mathbf{D}^*_{kl})_{ij} = (\mathbf{D}_{lk})_{ji}$, since the operator $\mathcal{D}^*$ is the adjoint of $\mathcal{D}$ (it can be seen easily from Eq.(2.34) p.62). Concerning the

discrete version of the identity operator $\mathcal{I}$, it does not represent an identity matrix anymore since it deals with ϕ and ψ functions. If the two functions have disjoint supports, its value is zero, $(\mathbf{I}_{kl})_{ij} = 0$, in particular for disjoint surfaces ($k \neq l$): $(\mathbf{I}_{kl})_{ij} = 0 \ , \forall (i,j)$. Furthermore, as for operator $\mathbf{D}$ the following relation holds: $(\mathbf{I}^*_{kl})_{ij} = (\mathbf{I}_{lk})_{ji}$.

5.2 The BEM's equations for the coupled methods

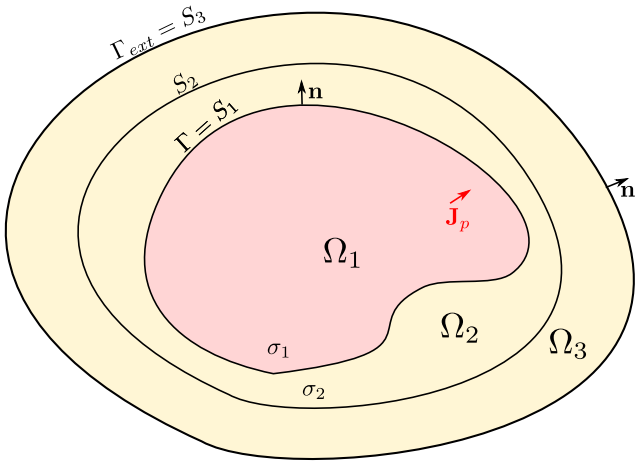

Figure 5.1 – *Domain partition for a BEM-BEM coupling with isotropic conductivities.*

5.2.1 BEM-BEM coupling with the Neumann-Dirichlet coupling

We propose here a domain decomposition such as in Fig.(4.6), where the domain Ω_1 is handled by a BEM with Neumann condition on Γ, and the domains Ω_2 and Ω_3 are handled by a mixed Dirichlet-homogeneous Neumann BEM (denoted DhN). We solve the following iterative problem, to obtain the potential on the outermost surface (*i.e.* the scalp Γ_{ext}):
Find V_1^k, *and* V_2^k *for all* $k \geq 1$, *s.t.*:

$$\text{BEM Neumann} \quad \begin{cases} \sigma_1 \Delta V_1^{k+1} = \nabla \cdot \mathbf{J}_p & \text{in } \Omega_1 \\ \\ \sigma_1 \partial_{\mathbf{n}} V_1^{k+1} = \sigma_2 \partial_{\mathbf{n}} V_2^k & \text{on } \Gamma \end{cases}, \tag{5.7}$$

$$\text{BEM mixed DhN} \quad \begin{cases} \sigma_2 \Delta V_2^{k+1} = 0 & \text{in } \Omega_2 \cup \Omega_3 \\ \\ V_2^{k+1} = V_1^{k+1} & \text{on } \Gamma \\ \sigma_2 \partial_{\mathbf{n}} V_2^{k+1} = 0 & \text{on } \Gamma_{ext}, \end{cases} . \tag{5.8}$$

The previous algorithm is stopped when the relative residual, computed as:

$$\frac{\left\|\sigma_2 \partial_{\mathbf{n}} V_2^{k+1}|_\Gamma - \sigma_2 \partial_{\mathbf{n}} V_2^{k}|_\Gamma\right\|}{\|\sigma_2 \partial_{\mathbf{n}} V_2^{k}|_\Gamma\|}, \tag{5.9}$$

is below 10^{-6}.
We now express these b.v.p in terms of the BEM operators applying the representation theorem, and then get to the discrete problem. First of all, we write the Neumann problem for the inner volume, and next we will see the mixed Dirichlet-Neumann problem for the lasting sub-domains (the skull and scalp).

(exterior-)Neumann problem in Ω_1: From Eq.(5.1)(minus):

$$-\left(\sigma_1 \partial_{\mathbf{n}} u_{\Omega_1}\right)^-_{S_1} = -\left(p - \partial_{\mathbf{n}} v_{\Omega_1}\right)^-_{S_1} = \sigma_1 \mathcal{N}_{\partial\Omega_1}\left[u_{\Omega_1}\right] - \left(\frac{\mathcal{I}_{\partial\Omega_1}}{2} + \mathcal{D}^*_{\partial\Omega_1}\right)\left[\partial_{\mathbf{n}} u_{\Omega_1}\right]_{\partial\Omega_1} \tag{5.10}$$

For the first domain, we have $\partial\Omega_1 = S_1$. Hence the discretized version of this equation writes using the jumps in Eq.(5.4)-(5.5), and the discrete operators in Eq.(5.6):

$$\begin{aligned} -\mathbf{I}^*_{11} \cdot \mathbf{p}_1 + \partial_{\mathbf{n}} \mathbf{v}_1 &= \sigma_1 \mathbf{N}_{11} \cdot \mathbf{V}_1 - (\frac{\mathbf{I}^*_{11}}{2} + \mathbf{D}^*_{11}) \cdot \mathbf{p}_1 \\ \sigma_1 \mathbf{N}_{11} \cdot \mathbf{V}_1 &= (-\frac{\mathbf{I}^*_{11}}{2} + \mathbf{D}^*_{11}) \cdot \mathbf{p}_1 + \partial_{\mathbf{n}} \mathbf{v}_1 \end{aligned}$$

We denote $\mathbf{H}_N$ the symmetric Head matrix (stiffness) for the Neumann problem, $\mathbf{D}_N$ the Neumann operator which acts on the given current on Γ, and $\mathbf{D}_{\mathbf{J}^\mathrm{P}}$ the source term due to the dipole source in Ω_1:

$$\mathbf{H}_N = \left[\sigma_1 \mathbf{N}_{11}\right] \quad , \quad \mathbf{D}_N = \left[-\tfrac{\mathbf{I}^*}{2} + \mathbf{D}^*_{11}\right] \quad , \quad \mathbf{D}_{\mathbf{J}^\mathrm{P}} = \left[\partial_{\mathbf{n}} \mathbf{v}_1\right] \quad . \tag{5.11}$$

We get the following matrix system to solve for $\mathbf{V}_1$:

$$\mathbf{H}_N \cdot \mathbf{V}_1 = \mathbf{D}_N \cdot \mathbf{p}_1 + \mathbf{D}_{\mathbf{J}^\mathrm{P}} \tag{5.12}$$

Note that this problem is defined up to an additive constant, so the matrix $\mathbf{H}_N$ has to be deflated, which is done considering a zero-mean potential on Γ.

Dirichlet-Neumann problem in $\Omega_2 \cup \Omega_3$: Equations for the mixed boundary value problem: Dirichlet data on the inside, and homogeneous Neumann on the outside *i.e.* $\mathbf{p}_3 = 0$.

equation on S_1 From Eq.(5.2)(plus):

$$(u_{\Omega_2})_1^+ = \mathcal{I}_{\partial\Omega_1} V_1 = \left(\frac{-\mathcal{I}_{\partial\Omega_2}}{2} - \mathcal{D}_{\partial\Omega_2}\right)[u_{\Omega_2}]_{\partial\Omega_2} + \sigma_2^{-1}\mathcal{S}_{\partial\Omega_2}[\partial_{\mathbf{n}} u_{\Omega_2}]_{\partial\Omega_2} \tag{5.13}$$

For the second domain, we have $\partial\Omega_2 = S_1 \cup S_2$, hence:

$$\begin{aligned} \mathbf{I}_{11}\mathbf{V}_1 &= \left(\frac{\mathbf{I}_{11}}{2} + \mathbf{D}_{11}\right)\cdot\mathbf{V}_1 - \mathbf{D}_{12}\cdot\mathbf{V}_2 - \sigma_2^{-1}\mathbf{S}_{11}\cdot\mathbf{p}_1 + \sigma_2^{-1}\mathbf{S}_{12}\cdot\mathbf{p}_2 \\ -\sigma_2^{-1}\mathbf{S}_{11}\cdot\mathbf{p}_1 - \mathbf{D}_{12}\cdot\mathbf{V}_2 + \sigma_2^{-1}\mathbf{S}_{12}\cdot\mathbf{p}_2 &= \left(\frac{\mathbf{I}_{11}}{2} - \mathbf{D}_{11}\right)\cdot\mathbf{V}_1 \end{aligned} \tag{5.14}$$

equations on S_2 From Eq.(5.1) (plus-minus):

$$\begin{aligned} \sigma_2\mathbf{N}_{21}\cdot\mathbf{V}_1 - \mathbf{D}_{21}^*\cdot\mathbf{p}_1 - (\sigma_2+\sigma_3)\mathbf{N}_{22}\cdot\mathbf{V}_2 + 2\mathbf{D}_{22}^*\cdot\mathbf{p}_2 + \sigma_3\mathbf{N}_{23}\cdot\mathbf{V}_3 &= 0 \\ -\mathbf{D}_{21}^*\cdot\mathbf{p}_1 - (\sigma_2+\sigma_3)\mathbf{N}_{22}\cdot\mathbf{V}_2 + 2\mathbf{D}_{22}^*\cdot\mathbf{p}_2 + \sigma_3\mathbf{N}_{23}\cdot\mathbf{V}_3 &= -\sigma_2\mathbf{N}_{21}\cdot\mathbf{V}_1 \end{aligned} \tag{5.15}$$

and from Eq.(5.2) (plus-minus):

$$\begin{aligned} \mathbf{D}_{21}\cdot\mathbf{V}_1 - \sigma_2^{-1}\mathbf{S}_{21}\cdot\mathbf{p}_1 - 2\mathbf{D}_{22}\cdot\mathbf{V}_2 + (\sigma_2^{-1}+\sigma_3^{-1})\mathbf{S}_{22}\cdot\mathbf{p}_2 + \mathbf{D}_{23}\cdot\mathbf{V}_3 &= 0 \\ \sigma_2^{-1}\cdot\mathbf{S}_{21}\mathbf{p}_1 + 2\mathbf{D}_{22}\cdot\mathbf{V}_2 - (\sigma_2^{-1}+\sigma_3^{-1})\mathbf{S}_{22}\cdot\mathbf{p}_2 - \mathbf{D}_{23}\cdot\mathbf{V}_3 &= \mathbf{D}_{21}\cdot\mathbf{V}_1 \end{aligned} \tag{5.16}$$

equations on S_3 From Eq.(5.1) (minus):

$$\sigma_3\mathbf{N}_{32}\cdot\mathbf{V}_2 - \mathbf{D}_{32}^*\cdot\mathbf{p}_2 - \sigma_3\mathbf{N}_{33}\cdot\mathbf{V}_3 = 0 \tag{5.17}$$

Writing $\mathbf{H}_{DN}$ the Head matrix for the mixed Dirichlet-homogeneous Neumann problem, and $\mathbf{D}_{DhN}$ its right hand side, *i.e.* the source term due to the potential imposed on S_1, we get the following matrix system to solve for $\mathbf{p}_1,\ \mathbf{V}_2,\ \mathbf{p}_2,\ \mathbf{V}_3$:

$$\mathbf{H}_{DN}\cdot\begin{bmatrix}\mathbf{p}_1\\ \mathbf{V}_2\\ \mathbf{p}_2\\ \mathbf{V}_3\end{bmatrix} = \mathbf{D}_{DhN}\cdot\mathbf{V}_1 \tag{5.18}$$

with the symmetric $\mathbf{H}_{DN}$:

$$\mathbf{H}_{DN} = \begin{bmatrix} -\sigma_2^{-1}\mathbf{S}_{11} & -\mathbf{D}_{12} & \sigma_2^{-1}\mathbf{S}_{12} & \\ -\mathbf{D}_{21}^* & -(\sigma_2+\sigma_3)\mathbf{N}_{22} & 2\mathbf{D}_{22}^* & \sigma_3\mathbf{N}_{23} \\ \sigma_2^{-1}\mathbf{S}_{21} & 2\mathbf{D}_{22} & -(\sigma_2^{-1}+\sigma_3^{-1})\mathbf{S}_{22} & -\mathbf{D}_{23} \\ & \sigma_3\mathbf{N}_{32} & -\mathbf{D}_{32}^* & -\sigma_3\mathbf{N}_{33} \end{bmatrix} \tag{5.19}$$

the $\mathbf{D}_{DhN}$:

$$\mathbf{D}_{DhN} = \begin{bmatrix} \frac{\mathbf{I}_{11}}{2} - \mathbf{D}_{11} \\ -\sigma_2\mathbf{N}_{21} \\ \mathbf{D}_{21} \\ 0 \end{bmatrix} \tag{5.20}$$

We will now write down the convergence of the Neumann data writing Eq.(4.33) with these matrices:

$$\mathcal{A} = (\sigma_2 \partial_{\mathbf{n}}(\mathcal{D}_2(\mathcal{N}_1 \ \cdot \ )|_\Gamma))|_\Gamma \tag{5.21}$$

One can see how to write operators $\mathcal{N}_1$, $\mathcal{D}_2$ with the discretized ones:

$$(\mathcal{N}_1 p_\Gamma)|_\Gamma \implies \mathbf{H}_N^{-1} \cdot \mathbf{D}_N \cdot \mathbf{p}_1 \tag{5.22}$$

$$(\sigma_2 \partial_{\mathbf{n}} \mathcal{D}_2 V_\Gamma)|_\Gamma \implies \mathbf{P} \cdot \mathbf{H}_D^{-1} \cdot \mathbf{D}_D \cdot \mathbf{V}_\Gamma \tag{5.23}$$

We express $\mathcal{A}$ with these operators:

$$\mathbf{A}_{ND} = \mathbf{P} \cdot \mathbf{H}_D^{-1} \cdot \mathbf{D}_D \cdot \mathbf{H}_N^{-1} \cdot \mathbf{D}_N. \tag{5.24}$$

Thus we will study the spectrum of $\mathbf{A}_{ND}$, computing its maximum eigenvalue (in absolute value). Note that $\mathbf{P}$ in the previous equations is just a selection operator, which simply gives a sub-matrix of its input (in this case, it extracts $\mathbf{p}_1$ see Eq.(5.18)).

5.2.2 BEM-BEM coupling with the Dirichlet-Neumann coupling

Still with the domain decomposition shown in Fig.(4.6), the domain Ω_1 will be handled by a BEM with Dirichlet condition on Γ this time, and the domains Ω_2 and Ω_3 by a Neumann-homogeneous Neumann BEM:
Find V_1^k, *and* V_2^k *for all* $k \geq 1$, *s.t.*:

$$\text{BEM Dirichlet} \quad \begin{cases} \sigma_1 \Delta V_1^{k+1} = \nabla \cdot \mathbf{J}_p & \text{in } \Omega_1 \\ V_1^{k+1} = V_2^k & \text{on } \Gamma = S_1 \end{cases}, \tag{5.25}$$

$$\text{BEM Neumann} \quad \begin{cases} \sigma_2 \Delta V_2^{k+1} = 0 & \text{in } \Omega_2 \cup \Omega_3 \\ \sigma_2 \partial_{\mathbf{n}} V_2^{k+1} = \lambda^k & \text{on } \Gamma = S_1 \\ \sigma_2 \partial_{\mathbf{n}} V_2^{k+1} = 0 & \text{on } \Gamma_{ext} = S_3 \end{cases}, \tag{5.26}$$

with λ^k the relaxation variable initialized $\lambda^0 = 0$ and defined as:

$$\lambda^{k+1} = (1-\omega)\lambda^k + \omega(\sigma_1 \partial_{\mathbf{n}} V_1^{k+1})|_\Gamma \tag{5.27}$$

Let us first write down the Dirichlet problem for the innermost volume (the brain), and next the Neumann problem for the lasting sub-domains (skull and scalp).

(exterior-)Dirichlet problem in Ω_1: From Eq.(5.2)(minus):

$$(u_{\Omega_1})^-_{S_1} = \left(V_1 - \frac{v_{\Omega_1}}{\sigma_1}\right)^-_{S_1} = \left(\frac{\mathcal{I}_{\partial\Omega_1}}{2} - \mathcal{D}_{\partial\Omega_1}\right)[u_{\Omega_1}]_1 + \sigma_1^{-1}\mathcal{S}_{\partial\Omega_1}[\partial_{\mathbf{n}} u_{\Omega_1}]_{\partial\Omega_1} \quad (5.28)$$

For the first domain, we have $\partial\Omega_1 = S_1$. Hence:

$$\begin{aligned} \mathbf{I}_{11}\cdot\mathbf{V}_1 - \sigma_1^{-1}\cdot\mathbf{v}_1 &= \left(\frac{\mathbf{I}_{11}}{2} - \mathbf{D}_{11}\right)\cdot\mathbf{V}_1 + \sigma_1^{-1}\mathbf{S}_{11}\cdot\mathbf{p}_1 \\ \sigma_1^{-1}\mathbf{S}_{11}\cdot\mathbf{p}_1 &= \left(\frac{\mathbf{I}_{11}}{2} + \mathbf{D}_{11}\right)\cdot\mathbf{V}_1 - \sigma_1^{-1}\mathbf{v}_1 \end{aligned} \quad (5.29)$$

Writing $\mathbf{H}_D$ the Head matrix for the Dirichlet problem, $\mathbf{D}_D$ the Dirichlet operator which acts on the potential given on Γ, and $\mathbf{D}_{\mathbf{J}^{\mathrm{P}}}$ the source term due to the dipole source in Ω_1, we get the following matrix system to solve for $\mathbf{p}_1$:

$$\mathbf{H}_D\cdot\mathbf{p}_1 = \mathbf{D}_D\cdot\mathbf{V}_1 + \mathbf{D}_{\mathbf{J}^{\mathrm{P}}} \quad (5.30)$$

with the symmetric $\mathbf{H}_D$:

$$\mathbf{H}_D = \left[\sigma_1^{-1}\mathbf{S}_{11}\right] \quad (5.31)$$

the $\mathbf{D}_D$:

$$\mathbf{D}_D = \left[\tfrac{\mathbf{I}_{11}}{2} + \mathbf{D}_{11}\right] \quad (5.32)$$

and the term due to the source the $\mathbf{D}_{\mathbf{J}^{\mathrm{P}}}$:

$$\mathbf{D}_{\mathbf{J}^{\mathrm{P}}} = \left[-\sigma_1^{-1}\mathbf{v}_1\right] \quad (5.33)$$

Neumann-Neumann problem in $\Omega_2 \cup \Omega_3$: Equations for the Neumann boundary value problem: with Neumann data on the inside, and homogeneous Neumann on the outside *i.e.* $\mathbf{p}_3 = 0$.

equation on S_1 From Eq.(5.1)(plus):

$$-(\sigma_2\partial_{\mathbf{n}} u_{\Omega_2})^+_{S_1} = -\left(p - \partial_{\mathbf{n}} v_{\Omega_2}\right)^+_1 = \sigma_2\mathcal{N}_{\partial\Omega_2}[u_{\Omega_2}]_{\partial\Omega_2} + \left(\frac{\mathcal{I}_{\partial\Omega_2}}{2} - \mathcal{D}^*_{\partial\Omega_2}\right)[\partial_{\mathbf{n}} u_{\Omega_2}]_{\partial\Omega_2} \quad (5.34)$$

In Ω_2, we have $\partial\Omega_2 = S_1 \cup S_2$ and as there is no source in the second domain, $\partial_{\mathbf{n}} v_{\Omega_2} = 0$. Hence:

$$\begin{aligned} -\sigma_2\mathbf{N}_{11}\cdot\mathbf{V}_1 + \sigma_2\mathbf{N}_{12}\cdot\mathbf{V}_2 - \left(\frac{\mathbf{I}_{11}}{2} - \mathbf{D}^*_{11}\right)\cdot\mathbf{p}_1 - \mathbf{D}^*_{12}\cdot\mathbf{p}_2 &= -\mathbf{p}_1 \\ \sigma_2\mathbf{N}_{11}\cdot\mathbf{V}_1 - \sigma_2\mathbf{N}_{12}\cdot\mathbf{V}_2 + \mathbf{D}^*_{12}\cdot\mathbf{p}_2 &= \left(\frac{\mathbf{I}^*_{11}}{2} + \mathbf{D}^*_{11}\right)\cdot\mathbf{p}_1 \end{aligned} \quad (5.35)$$

equations on S_2 From Eq.(5.1) (plus-minus):

$$\begin{aligned}\sigma_2\mathbf{N}_{21}\cdot\mathbf{V}_1-\mathbf{D}^*_{21}\cdot\mathbf{p}_1-(\sigma_2+\sigma_3)\mathbf{N}_{22}\cdot\mathbf{V}_2+2\mathbf{D}^*_{22}\cdot\mathbf{p}_2+\sigma_3\mathbf{N}_{23}\cdot\mathbf{V}_3 &= 0 \quad (5.36)\\ -\sigma_2\mathbf{N}_{21}\cdot\mathbf{V}_1+(\sigma_2+\sigma_3)\mathbf{N}_{22}\cdot\mathbf{V}_2-2\mathbf{D}^*_{22}\cdot\mathbf{p}_2-\sigma_3\mathbf{N}_{23}\cdot\mathbf{V}_3 &= -\mathbf{D}^*_{21}\cdot\mathbf{p}_1\end{aligned}$$

and from Eq.(5.2) (plus-minus):

$$\begin{aligned}\mathbf{D}_{21}\cdot\mathbf{V}_1-\sigma_2^{-1}\mathbf{S}_{21}\cdot\mathbf{p}_1-2\mathbf{D}_{22}\cdot\mathbf{V}_2+(\sigma_2^{-1}+\sigma_3^{-1})\mathbf{S}_{22}\cdot\mathbf{p}_2+\mathbf{D}_{23}\cdot\mathbf{V}_3 &= 0 \quad (5.37)\\ \mathbf{D}_{21}\cdot\mathbf{V}_1-2\mathbf{D}_{22}\cdot\mathbf{V}_2+(\sigma_2^{-1}+\sigma_3^{-1})\mathbf{S}_{22}\cdot\mathbf{p}_2+\mathbf{D}_{23}\cdot\mathbf{V}_3 &= \sigma_2^{-1}\mathbf{S}_{21}\cdot\mathbf{p}_1\end{aligned}$$

equation on S_3 From Eq.(5.1) (minus):

$$-\left(\sigma_3\partial_{\mathbf{n}}u_{\Omega_3}\right)^-_{S_3}=0=\sigma_3\mathcal{N}_{\partial\Omega_3}\left[u_{\Omega_3}\right]-\left(\frac{\mathcal{J}_{\partial\Omega_3}}{2}+\mathcal{D}^*_{\partial\Omega_3}\right)\left[\partial_{\mathbf{n}}u_{\Omega_3}\right]_{\partial\Omega_3} \quad (5.38)$$

$$-\sigma_3\mathbf{N}_{32}\cdot\mathbf{V}_2+\mathbf{D}^*_{32}\cdot\mathbf{p}_2+\sigma_3\mathbf{N}_{33}\cdot\mathbf{V}_3 = 0 \quad (5.39)$$

Writing $\mathbf{H}_{NN}$ the Head matrix for the Neumann-Neumann problem, and $\mathbf{D}_{NhN}$ its right hand side, *i.e.* the source term due to the current imposed on S_1, we get the following matrix system to solve for $\mathbf{V}_1,\ \mathbf{V}_2,\ \mathbf{p}_2,\ \mathbf{V}_3$:

$$\mathbf{H}_{NN}\begin{bmatrix}\mathbf{V}_1\\ \mathbf{V}_2\\ \mathbf{p}_2\\ \mathbf{V}_3\end{bmatrix}=\mathbf{D}_{NhN}\,\mathbf{p}_1 \quad (5.40)$$

with the symmetric $\mathbf{H}_{NN}$:

$$\mathbf{H}_{NN}=\begin{bmatrix}\sigma_2\mathbf{N}_{11} & -\sigma_2\mathbf{N}_{12} & \mathbf{D}^*_{12} & \\ -\sigma_2\mathbf{N}_{21} & (\sigma_2+\sigma_3)\mathbf{N}_{22} & -2\mathbf{D}^*_{22} & -\sigma_3\mathbf{N}_{23}\\ \mathbf{D}_{21} & -2\mathbf{D}_{22} & (\sigma_2^{-1}+\sigma_3^{-1})\mathbf{S}_{22} & \mathbf{D}_{23}\\ & -\sigma_3\mathbf{N}_{32} & \mathbf{D}^*_{32} & \sigma_3\mathbf{N}_{33}\end{bmatrix} \quad (5.41)$$

and the $\mathbf{D}_{NhN}$:

$$\mathbf{D}_{NhN}=\begin{bmatrix}\frac{\mathbf{I}^*_{11}}{2}+\mathbf{D}^*_{11}\\ -\mathbf{D}^*_{21}\\ \sigma_2^{-1}\mathbf{S}_{21}\\ 0\end{bmatrix} \quad (5.42)$$

Similarly the convergence of the Neumann data is obtained by writing Eq.(4.46) with these matrices:

$$\mathcal{A}_{DN}=\left(\Sigma\ \nabla(\mathcal{N}_2(\mathcal{D}_1\ \cdot\ )|_\Gamma)\cdot\mathbf{n}\right)|_\Gamma \quad (5.43)$$

One can now write operators $\mathcal{D}_1, \mathcal{N}_2$ with the previous matrices which leads to the expression:

$$\mathbf{A}_{DN}=(1-\omega)\mathbf{I}+\omega\cdot\mathbf{H}_D^{-1}\cdot\mathbf{D}_D\cdot\mathbf{P}\cdot\mathbf{H}_{NN}^{-1}\cdot\mathbf{D}_N \quad (5.44)$$

5.2.3 BEM-BEM-BEM coupling, with the Sandwiched Neumann-Dirichlet coupling

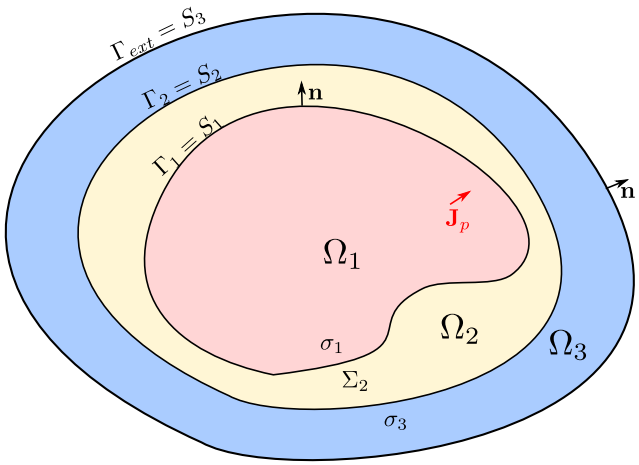

Figure 5.2 – *Domain partition for a BEM-BEM-BEM coupling.*

As explained in sec.(4.2.5), we treat this problem as a Neumann problem in a disjoint domain $(\Omega_1 \cup \Omega_3)$, and solve a Dirichlet problem in Ω_2. In our case this resorts to considering in total three independent BEM. The iterative problem writes:
Find V_1^k, V_2^k, V_3^k *for all* $k \geq 1$, *s.t.*:

$$\text{BEM Neumann} \quad \begin{cases} \sigma_1 \Delta V_1^{k+1} = \nabla \cdot \mathbf{J}_p & \text{in } \Omega_1 \\ \\ \sigma_1 \, \partial_{\mathbf{n}} V_1^{k+1} = \lambda_1^k & \text{on } \Gamma_1, \end{cases} \tag{5.45}$$

$$\text{BEM Neumann} \quad \begin{cases} \sigma_3 \Delta V_3^{k+1} = 0 & \text{in } \Omega_3 \\ \\ \sigma_3 \partial_{\mathbf{n}} V_3^{k+1} = \lambda_2^k & \text{on } \Gamma_2, \\ \sigma_3 \partial_{\mathbf{n}} V_3^{k+1} = 0 & \text{on } \Gamma_3, \end{cases} \tag{5.46}$$

$$\text{BEM Dirichlet} \quad \begin{cases} \sigma_2 \Delta V_2^{k+1} = 0 & \text{in } \Omega_2 \\ \\ V_2^{k+1} = V_1^{k+1} & \text{on } \Gamma_1 \\ V_2^{k+1} = V_3^{k+1} & \text{on } \Gamma_2, \end{cases} \tag{5.47}$$

where λ_1^k and λ_2^k are the relaxation variables such that:

$$\begin{pmatrix} \lambda_1^k \\ \lambda_2^k \end{pmatrix} = \lambda^k \tag{5.48}$$

with λ^k defined in Eq.(4.53). The stopping criterion of this scheme was defined as the condition on the relative residual:

$$\frac{\left\|\lambda^{k+1}-\lambda^k\right\|}{\|\lambda^k\|} \;<\; 10^{-6} \tag{5.49}$$

(exterior-)Neumann problem: The first Neumann system to solve is the one seen in Eq.(5.12).

Dirichlet-Dirichlet problem: The second sub-problem is now a pure Dirichlet boundary value problem with conditions on the two interfaces Γ_1 and Γ_2:

equation on S_1 From Eq.(5.2) (plus):
For the second domain, we have $\partial\Omega_2 = S_1 \cup S_2$ and as there is no source in the second domain, $v_{\Omega_2} = 0$. Hence:

$$(u_{\Omega_2})_1^+ = \mathcal{I}_{\partial\Omega_2} V_1 = \left(\frac{-\mathcal{I}_{\partial\Omega_2}}{2} - \mathcal{D}_{\partial\Omega_2}\right)[u_{\Omega_2}]_{\partial\Omega_2} + \sigma_2^{-1}\mathcal{S}_{\partial\Omega_2}[\partial_{\mathbf{n}} u_{\Omega_2}]_{\partial\Omega_2} \tag{5.50}$$

$$\begin{aligned}
\mathbf{I}_{11}\cdot\mathbf{V}_1 &= \left(\frac{\mathbf{I}_{11}}{2}+\mathbf{D}_{11}\right)\cdot\mathbf{V}_1 - \mathbf{D}_{12}\cdot\mathbf{V}_2 - \sigma_2^{-1}\mathbf{S}_{11}\cdot\mathbf{p}_1 + \sigma_2^{-1}\mathbf{S}_{12}\cdot\mathbf{p}_2 \\
\sigma_2^{-1}\mathbf{S}_{11}\cdot\mathbf{p}_1 - \sigma_2^{-1}\mathbf{S}_{12}\cdot\mathbf{p}_2 &= -\left(\frac{\mathbf{I}_{11}}{2}+\mathbf{D}_{11}\right)\cdot\mathbf{V}_1 - \mathbf{D}_{12}\cdot\mathbf{V}_2
\end{aligned} \tag{5.51}$$

equation on S_2 From Eq.(5.2) (minus):

$$(u_{\Omega_2})_1^- = V_2 = \left(\frac{\mathcal{I}_{\partial\Omega_2}}{2} - \mathcal{D}_{\partial\Omega_2}\right)[u_{\Omega_2}]_{\partial\Omega_2} + \sigma_2^{-1}\mathcal{S}_{\partial\Omega_2}[\partial_{\mathbf{n}} u_{\Omega_2}]_{\partial\Omega_2} \tag{5.52}$$

$$\begin{aligned}
\mathbf{V}_2 &= \mathbf{D}_{21}\mathbf{V}_1 + \frac{\mathbf{V}_2}{2} - \mathbf{D}_{22}\cdot\mathbf{V}_2 - \sigma_2^{-1}\mathbf{S}_{21}\cdot\mathbf{p}_1 + \sigma_2^{-1}\mathbf{S}_{22}\cdot\mathbf{p}_2 \\
-\sigma_2^{-1}\mathbf{S}_{21}\cdot\mathbf{p}_1 + \sigma_2^{-1}\mathbf{S}_{22}\cdot\mathbf{p}_2 &= -\mathbf{D}_{21}\cdot\mathbf{V}_1 + \left(\frac{\mathbf{I}_{22}}{2}+\mathbf{D}_{22}\right)\cdot\mathbf{V}_2
\end{aligned} \tag{5.53}$$

Writing $\mathbf{H}_{DD}$ the Head matrix for the Dirichlet-Dirichlet problem, and $\mathbf{D}_{DD}$ its right hand side, *i.e.* the source term due to the potential imposed on S_1 and S_2, we get the following matrix system to solve for $\mathbf{p}_1$ and $\mathbf{p}_2$:

$$\mathbf{H}_{DD}\begin{bmatrix}\mathbf{p}_1\\ \mathbf{p}_2\end{bmatrix} = \mathbf{D}_{DD}\cdot\begin{bmatrix}\mathbf{V}_1\\ \mathbf{V}_2\end{bmatrix} \tag{5.54}$$

with the symmetric $\mathbf{H}_{DD}$:

$$\mathbf{H}_{DD} = \sigma_2^{-1}\begin{bmatrix}\mathbf{S}_{11} & -\mathbf{S}_{12}\\ -\mathbf{S}_{21} & \mathbf{S}_{22}\end{bmatrix} \tag{5.55}$$

and the $\mathbf{D}_{DD}$:

$$\mathbf{D}_{DD} = \begin{bmatrix}-\frac{\mathbf{I}_{11}}{2}+\mathbf{D}_{11} & -\mathbf{D}_{12}\\ -\mathbf{D}_{21} & \frac{\mathbf{I}_{22}}{2}+\mathbf{D}_{22}\end{bmatrix} \tag{5.56}$$

Neumann-Neumann problem: Finally, the third sub-problem is a Neumann b.v.p, with a Neumann condition on the interior surface S_2 and an homogeneous Neumann condition on S_3 *i.e.* $\mathbf{p}_3 = 0$:

equation on S_2 From Eq.(5.1) (plus):

$$-(\sigma_3 \partial_{\mathbf{n}} u_{\Omega_3})^+_{S_2} = -\left(p - \partial_{\mathbf{n}} v_{\Omega_3}\right)^+_2 = \sigma_3 \mathcal{N}_{\partial\Omega_3}\left[u_{\Omega_3}\right]_{\partial\Omega_3} + \left(\frac{\mathcal{I}_{\partial\Omega_3}}{2} - \mathcal{D}^*_{\partial\Omega_3}\right)\left[\partial_{\mathbf{n}} u_{\Omega_3}\right]_{\partial\Omega_3} \tag{5.57}$$

In Ω_3, we have $\partial\Omega_3 = S_2 \cup S_3$ and as no source are in the second domain, $\partial_{\mathbf{n}} v_{\Omega_3} = 0$. Hence:

$$\begin{aligned} -\mathbf{p}_2 &= -\sigma_3 \mathbf{N}_{22} \cdot \mathbf{V}_2 + \sigma_3 \mathbf{N}_{23} \cdot \mathbf{V}_3 - (\frac{\mathbf{I}_{22}}{2} - \mathbf{D}^*_{22}) \cdot \mathbf{p}_2 \\ \sigma_3 \mathbf{N}_{22} \cdot \mathbf{V}_2 - \sigma_3 \mathbf{N}_{23} \cdot \mathbf{V}_3 &= (\frac{\mathbf{I}^*_{22}}{2} + \mathbf{D}^*_{22}) \cdot \mathbf{p}_2 \end{aligned}$$

equation on S_3 From Eq.(5.1) (minus):

$$\begin{aligned} 0 &= -\sigma_3 \mathbf{N}_{32} \cdot \mathbf{V}_2 + \mathbf{D}^*_{32} \cdot \mathbf{p}_2 + \sigma_3 \mathbf{N}_{33} \cdot \mathbf{V}_3 \\ -\sigma_3 \mathbf{N}_{32} \cdot \mathbf{V}_2 + \sigma_3 \mathbf{N}_{33} \cdot \mathbf{V}_3 &= -\mathbf{D}^*_{32} \cdot \mathbf{p}_2 \end{aligned}$$

Writing $\mathbf{H}_{NN}$ the Head matrix for the Neumann-Neumann problem, and $\mathbf{D}_{NhN}$ its right hand side, *i.e.* the source term due to the current imposed on S_2, we get the following matrix system to solve for $\mathbf{V}_2$ and $\mathbf{V}_3$:

$$\mathbf{H}_{NN} \cdot \begin{bmatrix} \mathbf{V}_2 \\ \mathbf{V}_3 \end{bmatrix} = \mathbf{D}_{NhN} \cdot \mathbf{p}_2 \ , \tag{5.58}$$

with the symmetric $\mathbf{H}_{NN}$:

$$\mathbf{H}_{NN} = \sigma_3 \begin{bmatrix} \mathbf{N}_{22} & -\mathbf{N}_{23} \\ -\mathbf{N}_{32} & \mathbf{N}_{33} \end{bmatrix} \tag{5.59}$$

Note that this problem is defined up to an constant, so this Head matrix has to be deflated to get a zero mean potential on the inner surface S_2. $\mathbf{D}_{NhN}$ is defined as:

$$\mathbf{D}_{NhN} = \begin{bmatrix} \frac{\mathbf{I}^*_{22}}{2} + \mathbf{D}^*_{22} \\ -\mathbf{D}^*_{32} \end{bmatrix} \tag{5.60}$$

Writing the operator $\mathcal{A}_{SND}$ in Eq.(4.57) with the sBEM yields:

$$\mathbf{A}_{SND} = (1-\omega)\mathbf{I} + \omega \cdot \mathbf{H}_D^{-1} \cdot \mathbf{D}_D \cdot \begin{pmatrix} \mathbf{H}_N^{-1} \cdot \mathbf{D}_N \\ \mathbf{P}\mathbf{H}_{NN}^{-1} \cdot \mathbf{D}_{NN} \end{pmatrix} \ , \tag{5.61}$$

with $\mathbf{P}$ an operator which extracts $\mathbf{V}_2$ from Eq.(5.58).

5.3 Numerical results on BEM-BEM coupled methods

In this section we propose to validate the proposed coupled methods, comparing for several mesh sizes their accuracy, time and memory consumption as well as their convergence. These comparisons are done on 3-layer spherical models for several dipoles which allow for the comparisons with an analytical solution.

5.3.1 Spherical models

The meshes used are made from icosahedra (12 points regularly sampled on the sphere), which are then regularly refined to approximate the sphere (see Fig.(5.3)). Let n be the number of vertices of one mesh, we have used several mesh resolutions, namely: $n \in \{42,\ 162,\ 642,\ 2\,562\}$. Out of these unit spheres 3-layer models were

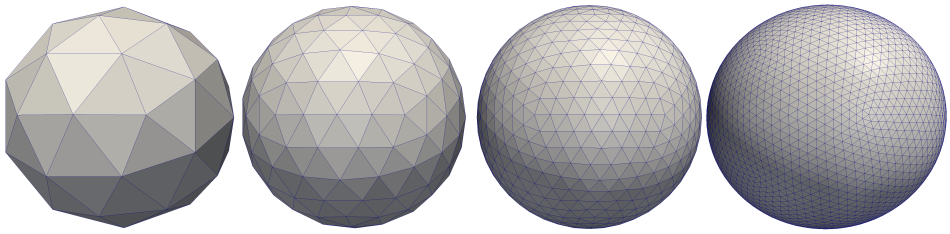

Figure 5.3 – *Spherical mesh at different resolutions:* 42, 162, 642, 2 562 *vertices.*

made whose layers represent the brain, the skull, and the scalp, with respective radii 0.87, 0.92, 1. To these layers were assigned the conductivities 1, 0.03, 1 respectively, as discussed in sec.(2.3.2.4). Comparisons were done using a set of 15 unit dipoles placed on the z-axis, with different orientations, namely:

positions: 5 positions on the z-axis: $z \in \{0.4650,\ 0.6150,\ 0.7650,\ 0.8075,\ 0.8415\}$.

momentum: 3 unit momentum given in Cartesian coordinates by: $\frac{1}{\sqrt{2}}[1,\ 0,\ 1]$, $\frac{1}{\sqrt{2}}[1,\ 1,\ 0]$, $[0,\ 0,\ 1]$.

as these dipoles approach the inner sphere, the error is as expected to increase, since the dipole is a singularity.
We propose to overlay the comparisons to the reference solution (analytic formula), for the sBEM (abbreviated BEM), the Neumann-Dirichlet BEM-BEM coupling (abbreviated BB_ND), and the Sandwiched Neumann-Dirichlet which is a BEM-BEM-BEM coupling (abbreviated BBB_SND).

5.3.2 Accuracies

We now plot the errors (RDM on first row, and MAG second row) of the three methods (BEM, BB_ND, and BBB_SND) where the x-axis represents the z-coordinates of the dipoles, and the three columns their orientations. This is done for the 4 model resolutions in Fig.(5.3) in order to see the convergence aspect (diminution of the errors) with respect to the mesh size. This is displayed in Fig.(5.4). Please note that the y-scale changes for each resolution.

One can see that the three methods are convergent with the grid size, *i.e.* both RDM, and MAG diminish when n increases. BEM, BB_ND, BBB_SND have similar accuracies, except in the more refined case ($n = 2\,562$), where the BBB_SND seems to converge more slowly than the others.

5.3.3 Convergence of the coupled methods

We evaluated numerically the spectral radius of the operators defined in Eq.(5.24)-(5.61), which defines the convergence property of the iterative scheme and we found the following values:

n	42	162	642	2 562	ω
$\rho(\mathbf{A}_{ND})$	0.140142	0.140077	0.14005	0.140092	1
$\rho(\mathbf{A}_{SND})$	0.699944	0.699941	0.699991	0.699993	0.3

Table 5.1 – *Estimated spectral radius of* $\mathbf{A}$.

These values do not seem to be dependent on the mesh size, but appear to be more specific to the electrophysiological model, we will come back to this further for a realistic geometry for the case of a BEM-FEM coupling. In [Berninger et al., 2007] such a behavior is also related for a 2D case.
For the BB_ND coupled method, these values are clearly below 1. and motivate the use of a non-relaxed scheme ($\omega = 1$) to accelerate convergence. Actually, for each of the head models, the scheme converged (with a relative residual lower than $\varepsilon = 1e-6$) for 8 iterations, *i.e.* only 16 b.v.p to solve. This is actually very fast once the main matrices are built and inverted, since it simply requires matrix multiplications. Note that taking the spectral radius to the power of 8 (the number of iteration) as in Eq.(5.24) gives $1.4878e-7$, which is below ε.
For the analysis of the convergence of the BBB_SND, we had to use a relaxation of $\omega = 0.3$ in order to get a good convergence rate. For $\omega > 0.45$, the scheme diverges, and for $\omega \simeq 0.45$, and $\omega < 0.45$, the scheme converges but oscillates a lot, thus the convergence was slow. The number of iterations to reach convergence at $\varepsilon = 1e-6$ was 33, for every head model.

It is interesting to see how the spectral radius of such operators evolves with the skull conductivity or the relaxation parameter. This is plotted in Fig.(5.5), for the case of the Neumann_Dirichlet coupled method. One can see that taking no relax-

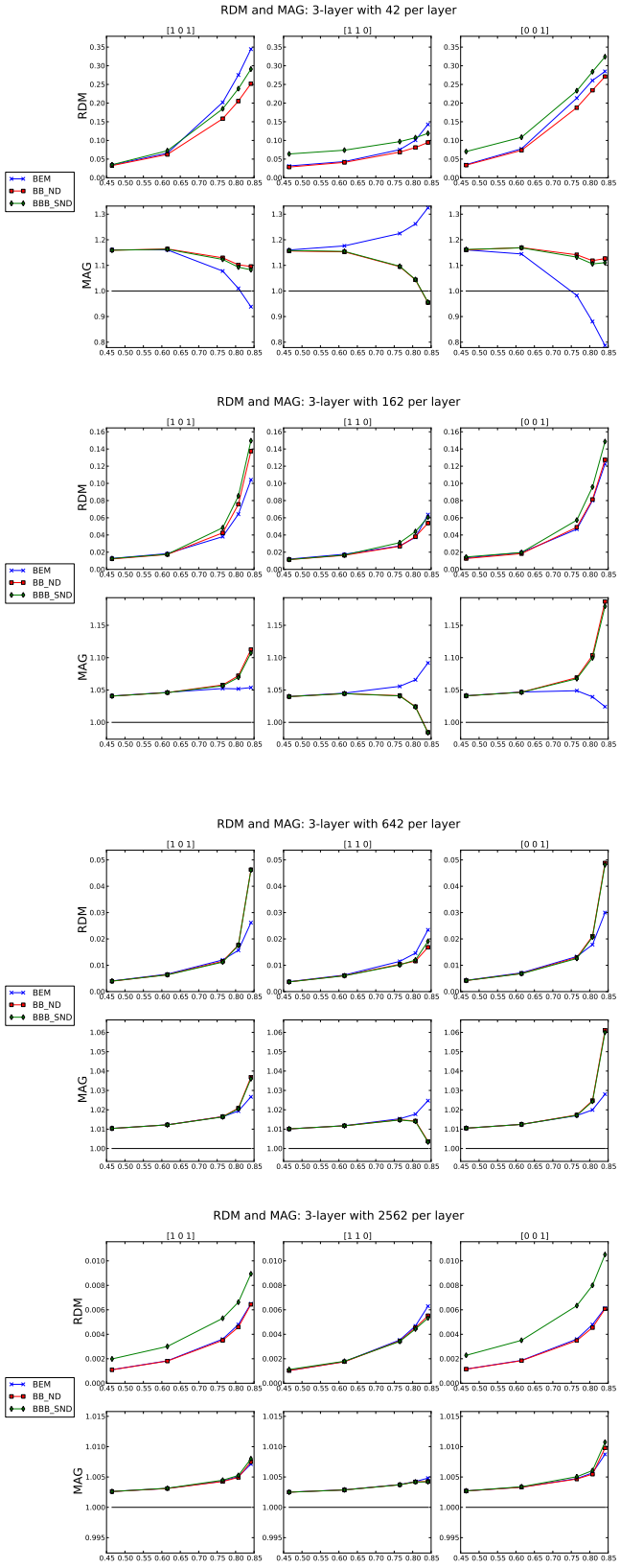

Figure 5.4 – *Errors of BEM-BEM coupled methods. Number of vertices per mesh is increased from top to bottom. For each resolution both RDM and MAG are shown depending on the orientation of the dipole (one orientation per column). The $x-$axis always represent the z-coordinate of the dipoles.*

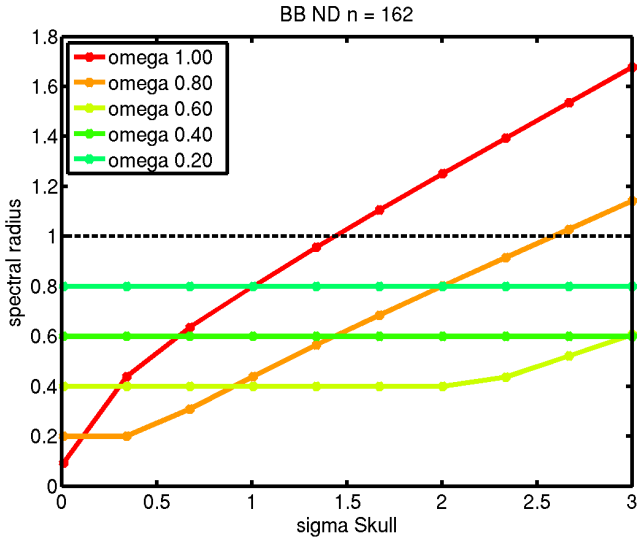

Figure 5.5 – *Spectral radius $\rho(\mathbf{A}_{ND})$ varying the skull conductivity and the relaxation parameter.*

ation (*i.e.* $\omega = 1$), the red curve has lower spectral values for small conductivities of the skull, which is our case, since the skull is considered to be 0.03 in our experiments. On the other hand, for higher skull conductivity > 1, the scheme would not converge without a relaxation. One can see that enforcing a strong relaxation leads to convergence in all cases, but with a low convergence rate.
For the case of the Dirichlet_Neumann coupled method, we could not find any relaxation parameter which would make the scheme convergent, even if it is in theory always possible to converge with an appropriate relaxation parameter. This might be due to an implementation problem. However we were able to solve successfully a Dirichlet_Neumann coupling using only two domains, *i.e.* the brain handled by a Dirichlet BEM, and the skull by a Neumann BEM (thus dropping the scalp.). This scheme was convergent for $\omega = 0.0001$, but its rate of convergence was extremely slow, after 2 000 iterations the best relative residual (for the first dipole) was only $\simeq 0.025$.

5.3.4 Time and memory comparisons

In Fig.(5.6), one can see plotted the elapsed time and memory consumption (peak RSS (Resident Set Size)) for the three methods, *i.e.* the standard sBEM, the BB_ND, and the BBB_SND.

These values are also summarized in table.5.2: One can see from these data, that the Neumann_Dirichlet_Neumann is the fastest, and almost 3 times faster than the classical BEM. The Neumann_Dirichlet coupled method (BB_ND) also spares a good percentage of time when compared to the classical BEM. These improvements

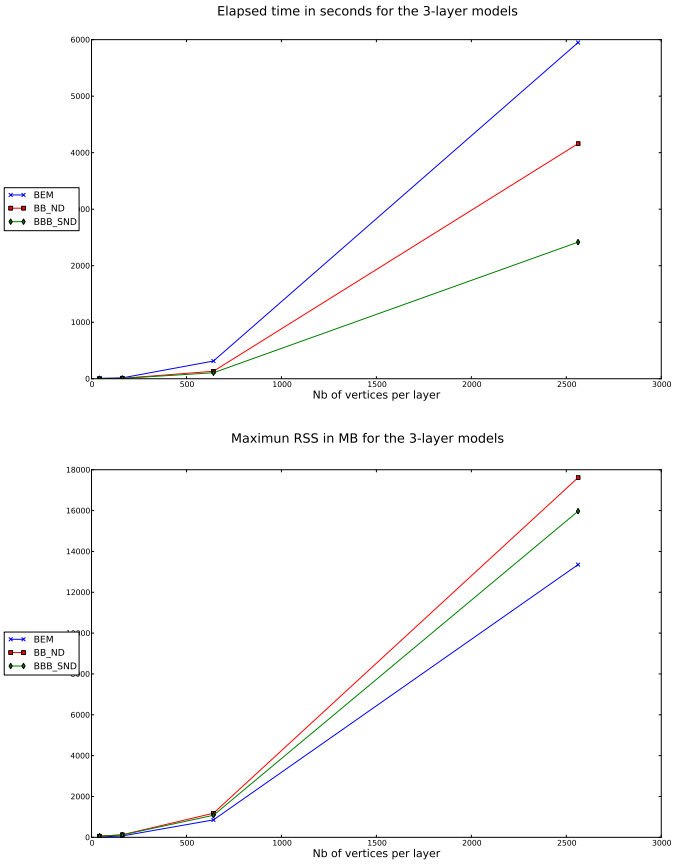

Figure 5.6 – *Elapsed time and memory peak (RSS).*

are due to the fact that the problems to solve are smaller thanks to the domain decomposition; there are more problems to solve but easier ones. Actually, the main gain in time is from the matrix inversion which is much reduced when reducing the matrix size. When looking at the memory consumption, the coupled methods are slightly more expensive than the classical method, since they require more RAM memory.

5.4 Conclusions on BEM-BEM coupled methods

We have seen how to couple BEM methods using iterative substructuring methods, thanks to the definition of b.v.p on sub-domains. Tools for studying the convergence properties of these coupling schemes were given in the numerical case. We have seen that the spectral properties of operator $\mathcal{A}$ guide the choice of a relaxation parameter. From a numerical point of view, these DD coupling techniques are very efficient since they reduce the time for similar accuracies. It moreover allows for parallelization *i.e* having one domain handled by only one machine, this can be very interesting

Methods	n	Elapsed time	User time	Peak RSS	worst RDM
Classic BEM	42	7.940	3.88	16	0.2849
	162	15.170	24.52	67	0.1227
	642	313.500	1 559.46	853	0.03000
(Lapack inversion)	2562	5948.720	11 355.00	13 353	0.0061
BEM-BEM	42	1.1	3.9	58	0.2710
	162	7.3	40.0	123	0.1274
	642	132.7	640.9	1 180	0.04884
(BB_ND)	2562	4 160.0	12 349.45	17 614	0.0061
BEM-BEM-BEM	42	1.0	3.8	57	0.3241
	162	6.0	34.4	118	0.1486
	642	106.0	529.2	1 079	0.0482
(BBB_SND)	2 562	2 417.0	9 274.5	15 970	0.01051

Table 5.2 – *Time and memory consumptions.*

in our case, since BEM are generally limited by memory consumption. Indeed one can thanks to these techniques deal with higher problem sizes in order to get very high definition solutions.

Chapter 6

Coupling BEM and FEM within a Domain Decomposition Framework

Using the previous conclusions made on the iterative substructuring methods, we choose to implement the Neumann-Dirichlet coupled method, with a BEM in the inner domain containing the source (*e.g.* the brain), coupled with a tetrahedral FEM handling the inhomogeneous conductivity profile of the skull, and the isotropic scalp. After validating the coupled formulation using analytical solutions on spheres, we will see a numerical example on a realistic head model, where the patient presents a highly inhomogeneous skull due to a craniotomy. Since no analytical solution exists, we will compare these results with the standard FEM and BEM.

Summary

Goals: Use the FEM in inhomogeneous or anisotropic domains (here the skull), and improve the forward EEG problem accuracy.

Tools: The Neumann-Dirichlet coupled method whose behavior was studied before, for the use with a tetrahedral FEM coupled with the sBEM.

Results: An effective, cheap coupling which improves the accuracy of the forward EEG problem.

The following sections are inspired from a submitted article in collaboration with Maureen Clerc, Théodore Papadopoulo and Mariette Yvinec.

Contents

6.1 Respective merits of FEM and BEM

Finite Element Methods (FEM) can in principle handle inhomogeneous or anisotropic conductivity fields such as the one of the skull. On the other hand Boundary Element Methods (BEM) can only handle piecewise homogeneous conductivity. Conversely, with the BEM, dipolar sources can be represented very accurately, whereas with the FEM they are more difficult to handle.
The choice of a model and of the numerical method to solve it are thus clearly inter-dependent: one has to consider whether or not a numerical method is able to cope with a conductivity and a source model. Furthermore, one must analyze the relative benefits of the model complexity and numerical accuracy, in order to balance the two sources of errors, and to avoid wasting resources.

The goal of this chapter is to introduce a method based on domain decomposition, which allows for the use of different numerical solver for each sub-domains; the objective is to take advantage of having the sources represented with the BEM, and also the conductivity profiles handled by the FEM for the other regions.

We refer to sec.(2.4.4) for the introduction of the general FEM, and recall here aspects of the tetrahedral FEM. We use a Galerkin FEM with tetrahedral elements, and the potential is represented with P1 basis functions.
When modeling a dipole source in a tetrahedron, the potential at its vertices is enforced weakly considering the P1-basis functions of the tetrahedron against the dipole function. The dipole function is then spread on these 4 vertices and the quality of representation strongly depends on the shape of this element, and its relative orientation to the dipole moment. This is the reason for the poor modeling of dipole sources with this FEM.
The system is then assembled into a huge but sparse stiffness matrix, and is solved for $\mathbf{v}_F$ the potential at vertices using a preconditioned conjugate gradient taking advantage of the positive definiteness of the problem:

$$\mathbf{A}_F \cdot \mathbf{v}_F = \mathbf{S}_F \ , \tag{6.1}$$

where $\mathbf{S}_F$ incorporates the imposed boundary value (either Dirichlet or Neumann) and/or an eventual source term.

6.1.0.1 Comparison:

Comparing BEM and FEM in terms of time and memory footprint to achieve a given accuracy is delicate. Both techniques do not share the same geometry, since the FEM requires a volumic partitioning of all the regions, and only surfacic meshes are needed for the BEM. When comparing BEM and FEM, one should then incorporate the cost of obtaining the discretized geometry plus running the codes. Furthermore, BEM to FEM comparison is delicate because both methods cannot handle the same conductivity profiles, and may only be compared on a restriction of the possible models. In this chapter we will show BEM to FEM comparisons for realistic problem sizes *i.e.* with a high number of elements for the BEM, and the FEM. See table (6.1) where their principal differences are summarized.

	Symmetric BEM	**Tetrahedral FEM**
Conductivity	piecewise constant	arbitrary
Mesh	surface	volume
Primitive element	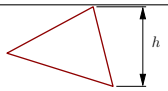	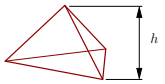
Typical number of vertices	$486 < N < 10\,248$	$20\,000 < N < 10\,000\,000$
Degrees of freedom (d.o.f)	$806 <$ d.o.f $< 17\,928$	$20\,000 <$ d.o.f $< 10\,000\,000$
System matrix	symmetric and dense per block	symmetric sparse ($\sim 8\%$ full)
Solver	Matrix inversion or GMres	(preconditioned-) conjugate gradient

Table 6.1 – *Summary on BEM and FEM.*

In the rest of this chapter the BEM acronym will denote the symmetric BEM, and FEM the tetrahedral FEM.
We propose first a method which combines the advantages of these two numerical methods, then a validation of this method on spheres where an analytical solution is available. Finally, we conclude by an application demonstrating the benefits of this approach on a realistic geometry incorporating inhomogeneity in the skull.

6.2 A domain decomposition framework for coupling BEM and FEM.

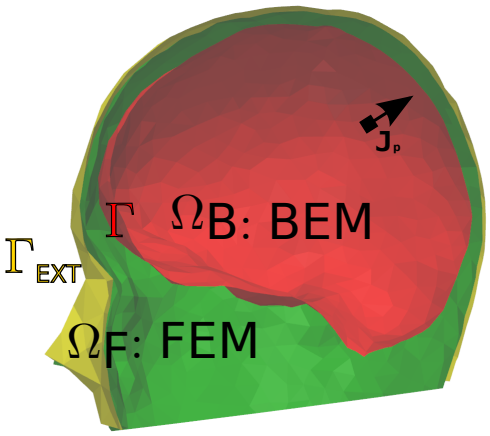

Figure 6.1 – *Domain partition for the coupled method.*

Splitting Ω into two nested regions Ω_B, (resp. Ω_F) with homogeneous constant conductivity σ (resp. inhomogeneous anisotropic conductivity tensor Σ), and con-

sidering the continuity conditions across the interface $\Gamma = \partial\Omega_B \cap \partial\Omega_F$, our Poisson equation becomes:

$$\begin{cases} \sigma\Delta V_B = \nabla \cdot \mathbf{J}_p & \text{in } \Omega_B \\ \\ V_B = V_F & \text{on } \Gamma \\ (\sigma\ \nabla V_B) \cdot \mathbf{n} = (\Sigma\ \nabla V_F) \cdot \mathbf{n} & \text{on } \Gamma \\ \\ \nabla \cdot (\Sigma \nabla V_F) = 0 & \text{in } \Omega_F \\ (\Sigma\ \nabla V_F) \cdot \mathbf{n} = 0 & \text{on } \Gamma_{ext} \end{cases} \tag{6.2}$$

where $\mathbf{n}$ denotes the outward normal to the surface (Γ or Γ_{ext}), and V_B (resp. V_F) denotes the BEM's (resp. the FEM's) solution.

We choose to alternate between Neumann-Dirichlet problems for BEM and FEM to reach a stationary state where BEM and FEM solutions fulfill the above system (6.2) in a sense to be defined.

6.2.1 Alternating on boundary condition Neumann/Dirichlet

We consider an iterative procedure solving first a Neumann boundary value problem (b.v.p) for the innermost domain Ω_B, and then a mixed Dirichlet/homogeneous Neumann b.v.p on the outer domains. The iterative procedure will stop when the proposed algorithm converges, in the sense that their boundary conditions reach a stationary state:

$k = 0$; $residual = 1$; $V_F^0 = 0$;
while ***residual*** $> 5.10^{-4}$ **do**

Solve with BEM

$$\begin{cases} \sigma\Delta V_B^{k+1} = \nabla \cdot \mathbf{J}_p & \text{in } \Omega_B \\ \\ (\sigma\nabla V_B^{k+1}) \cdot \mathbf{n} = (\Sigma\nabla V_F^k) \cdot \mathbf{n} & \text{on } \Gamma, \end{cases} \tag{6.3}$$

Solve with FEM

$$\begin{cases} \nabla \cdot (\Sigma\nabla V_F^{k+1}) = 0 & \text{in } \Omega_F \\ \\ V_F^{k+1} = V_B^{k+1} & \text{on } \Gamma \\ (\Sigma\nabla V_F^{k+1}) \cdot \mathbf{n} = 0 & \text{on } \Gamma_{ext}, \end{cases} \tag{6.4}$$

$$residual = \frac{\left\| (\sigma\nabla V_B^{k+1} - \Sigma\nabla V_F^{k+1}) \cdot \mathbf{n} \right\|_2}{\|\sigma\nabla V_B^{k+1} \cdot \mathbf{n}\|_2} \quad \text{on } \Gamma \tag{6.5}$$

$$k = k + 1$$

At first iteration, a homogeneous Neumann b.v.p is solved with the BEM, then using its potential values on Γ, a mixed Dirichlet/homogeneous Neumann b.v.p is set up, and solved using the FEM. For all following iterations, the FEM current

crossing a BEM triangle element is computed, and the scheme keeps on alternating between the two methods until convergence is reached.
Convergence was declared when the relative residual term on the BEM Neumann data was below 5.10^{-4}. We did not go below 10^{-6} as in the previous chapter on BEM-BEM couplings, to accelerate the problem resolution, furthermore the results did not evolve anymore significantly after reaching such a threshold.
At convergence, the BEM and FEM solutions satisfy Eq.(6.3) and Eq.(6.4) respectively. Concerning the continuity of the potential and of the normal current at interface Γ so that Eq.(6.2) is valid, this is explained in the next section.
As explained in [Quarteroni and Valli, 1999] p.12, the previous iterative scheme does not necessarily converge, depending on the shape and assigned conductivities of the domains Ω_B and Ω_F. But as seen in the previous chapter, the Neumann-Dirichlet coupling converges in the case considered here.

6.2.2 Interface:

One of the goals of the proposed coupled method is for the numerical solvers to be as independent as possible, so that independent meshes can be used for each solver. More specifically, the coupled method should support non-matching grids, *i.e.* meshes that do not share the same vertices at interface. This allows for having arbitrary discretization sizes which is desirable because the FEM requires smaller elements than the BEM to achieve the same accuracy.
Even if non-matching grids are used, the numerical methods must describe the same interface. Fig.(6.2) illustrates, in 2D, different kind of mesh and geometry compatibility at interface.

a) shows matching grids, where the BEM and the FEM share the same vertices at the interface, and thus assure the same geometry representation.

b) shows non-matching grids, in which the geometry representation of the FEM is more accurate than the one of the BEM. This case would introduce errors when interpolating from BEM to FEM boundary values.

c) shows non-matching grids sharing the same geometry representation.

Transmission between BEM and FEM variables at interface Γ, as seen in Eq.(6.3)-(6.4) must be defined. Using the same notation, the transmission of the BEM potential V_B to the FEM boundary value variable V_F is enforced point-wise; using the P1-finite elements of the BEM to compute the potential at FEM vertices location.

The transmission from FEM to BEM of the normal current crossing Γ is done considering a 16-point Gauss quadrature scheme on a BEM triangle [Bonnet, 1999].

Other transmission strategies can be considered for non-matching grids. Notably the mortar finite element method [Bernardi et al., 1994]. Instead of considering a point-wise continuity condition for the potential, the mortar method enforces

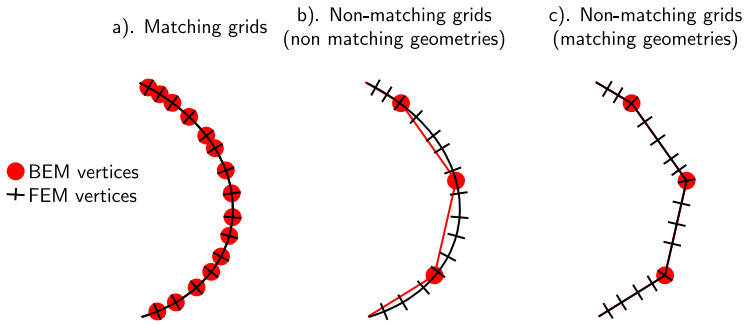

Figure 6.2 – *Matching and non matching grids and geometries. a). BEM and FEM share the same vertices on* Γ*, b). non-matching grids where both methods do not represent the same interface, c). non-matching grids and same geometry representation.*

weakly the continuity, using the test functions of both methods. This method has the advantage of providing an optimal bound for the a-priori error estimate. In 3D, it has rarely been used to our knowledge because of implementation difficulties (see [Belgacem, 2004]-[Ben Belgacem and Maday, 1997]). In this article, we restrict our attention to non-overlapping domains with non-matching grids, and to strongly enforced boundary conditions. We detail this issue in the next subsection.

6.2.3 Comments on non-matching grids, and meshes

DD techniques are meant to treat the sub-problems as independently as possible, in order to make use of parallelization techniques or to deal with different solver requirements. Mortar element methods [Bernardi et al., 1994] allow for the complete handling of non-matching grids at interface and provide convergence properties for iterative scheme as mentioned above. The key point in mortar finite elements is to enforce the continuity of variable weakly, using some Lagrangian parameter. Variables V_B, and V_F are represented within their finite element framework, with ϕ_i the family of BEM test functions and ψ_j for the FEM's. An example of such a representation of non-matching grids and different finite elements is shown in 2D Fig.(6.3), where the black dots represent the vertices for the domain on the left hand side, and the white diamonds the ones of the right hand side. We have represented P1 finite elements for ϕ_i and ψ_j, as it is the case here.

In order to have continuity of the potential called V_B in Ω_B, and V_F in Ω_F, one should have:

$$V_B = V_F \qquad \text{on } \Gamma \tag{6.6}$$

which may be impossible due to the representation of V_B and V_F within their respective finite elements *i.e.* there might be a jump between these solutions:

$$\forall \mathbf{r} \in \Gamma \quad u(\mathbf{r}) - v(\mathbf{r}) \neq 0 \ . \tag{6.7}$$

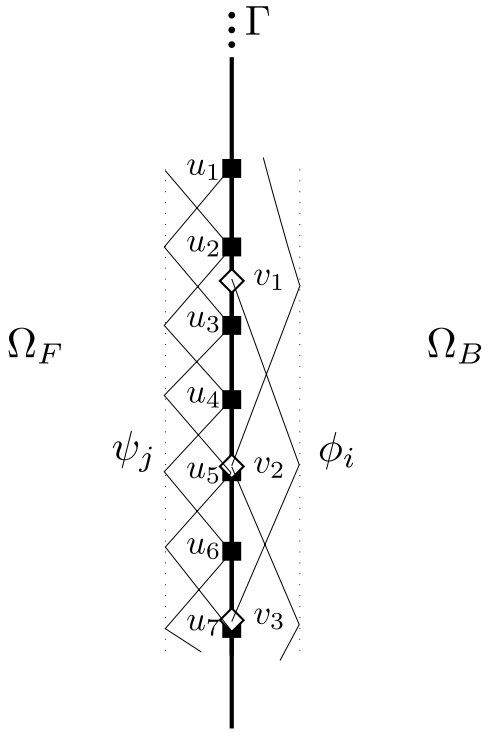

Figure 6.3 – *Example of non-matching grids at interface.*

Mortar finite elements enforce instead the following weak condition:

$$\int_\Gamma (u - v)\mu d\mathbf{s} = 0 \qquad \text{on } \Gamma \ , \tag{6.8}$$

where parameter μ must be expressed either in the finite elements basis of Ω_B, or of Ω_F. This defines a master domain and a slave. Still there are integral computations needed of one basis against the other since $V_B = \sum_i V_B^i \phi_i$, and $V_F = \sum_j V_F^j \psi_j$. This can be affordable in 2D, since it is the computation of the area of an intersection between triangles; but it becomes radically more complicated in 3D (see [Belgacem, 2004]-[Ben Belgacem and Maday, 1997]).
Another important point is the geometry defined by the two methods as discussed previously for Fig.(6.2). If we consider a planar interface in 3D, this is rather simple (see Fig.(6.4)).

In case of a non planar interface, the two meshes cannot be independent, one must impose one mesh to match at interface the geometry definition of the other, otherwise one is in the case b. of Fig.(6.2). In 2D, one way to achieve the same geometry representation for the two methods, is to impose the vertices of one mesh to the other, and then to refine the second mesh according to the convex hull defined by the first mesh. This is done in case c. of Fig.(6.2), where the BEM's nodes are imposed as FEM nodes. This leads to non-matching grid with matching interface representation.

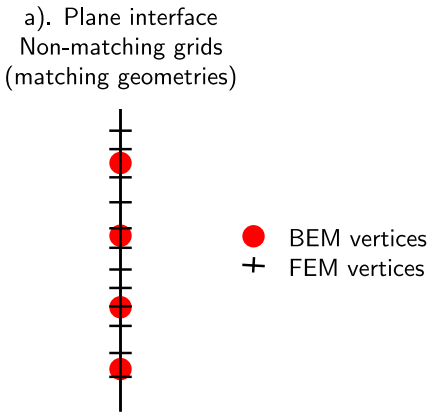

Figure 6.4 – *Example of non-matching grids at interface in 2D.*

In 3D this is more complicated. In fact, in order to keep the same interface representation by the two methods, one must enforce the edges (and not only the vertices) of the first mesh onto the other. This can be done using a brand new feature of CGAL called 'sharp edges', where one can impose edges to be matched, when meshing. One example is shown in Fig.(6.5), where the black edges correspond to the BEM mesh, and the finer white edges to the FEM mesh. One can see that the FEM mesh is simply (at the interface) a subdivision of the BEM mesh. Using

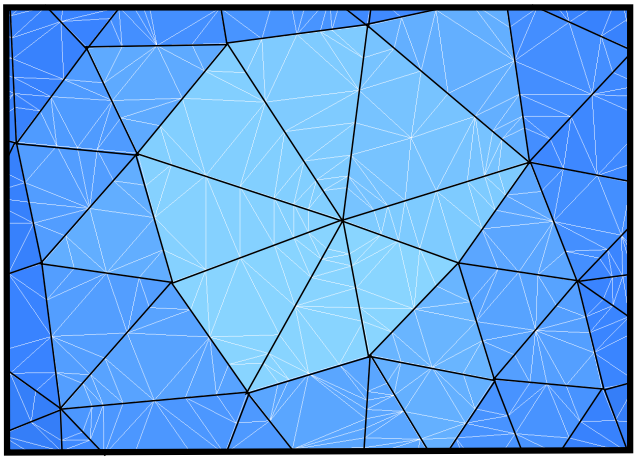

Figure 6.5 – *Non-matching grids in 3D, with matching geometry. (luminance codes for the 3D). The black triangles represent the BEM meshes, whereas the white the FEM's.*

such a mesh in a coupled method, such as we did with the BEM-FEM coupling, is very convenient. Actually, in the presented coupled method, we solved a Neumann problem with the BEM and then a mixed Dirichlet-Neumann problem using the FEM. We thus imposed the potential at Γ from the BEM potential (defined on the

BEM mesh) to the FEM potential (defined on the FEM mesh). And as we were using a P1 representation of the potential in both cases, we could assure that there was no jump at Γ *i.e.* contrarily to Eq.(6.7):

$$\forall \mathbf{r} \in \Gamma \quad V_{BEM}(\mathbf{r}) = V_{FEM}(\mathbf{r}) \ . \tag{6.9}$$

For these reasons, we did not use the mortar element method, which would have made the solution more complicated.
The main problem we had in the following experiments, was that this feature for handling sharps edges with CGAL, did not work for all meshes, *i.e.* we could not obtain all meshes as in Fig.(6.5). The problem was either due to bugs in this new feature or to a non-correct use of it. Instead we were able to generate the FEM meshes, where we used as input the BEM mesh vertices, but not its edges. In this case, we can say that the potential of the BEM at Γ V_B is 'almost' the same as V_F for all the points on Γ, since actually there are some triangles that do not fulfill this condition. Experiments were run with such meshes, and the Neumann-Dirichlet coupling with BEM-FEM was robust to that approximation.

6.2.4 Mesh generation:

Geometrical models with matching geometries and non-matching grids at interface were generated with CGAL (see sec.(2.6)). CGAL is able to give, from implicit functions or 3D gray level images, surfacic and volumic triangulations having good properties for numerical methods. These triangulations are Delaunay triangulations and provide well shaped elements [Rineau and Yvinec, 2011]. For the volumic meshes a special care is taken to eliminate slivers, these tetrahedra with a very small dihedral angle but fulfilling the Delaunay criterion, that introduce numerical errors in FEM. When generating these meshes with CGAL, all tetrahedra with a dihedral angle below 12° were removed. In order to get both surfacic and volumic meshes sharing the same geometry representation for the proposed coupling, we first generated the surfacic meshes, and set their vertices as input seeds for the volumic mesher; the mesher then inserted vertices at locations constrained by the input surfacic meshes.
In the next section we will compare the forward results of the BEM, the FEM, and the coupled BEM-FEM method for spherical head-models. The BEM meshes were generated using the implicit sphere function for the different radii; out of these BEM meshes were generated the volumic meshes. The FEM and the coupled BEM-FEM used the same meshes, although only the skull and the scalp part of the domains were used for the coupled method. Different resolution meshes were generated. For generating surfacic meshes out of sphere functions, the distance_bound criterion of CGAL was used. It controls the distance between the facets and the implicit surface. For the volumic meshes, two criteria have to be used, one surfacic, one volumic. The distance_bound ensures a maximal distance for the facets of the tetrahedra defining the surface to the input surface, and a criterion on tetrahedra sizes called cell_bound provides an upper bound on the circumradii of the mesh

tetrahedra. Note that even if we wanted the two meshes to describe the same interface, the mesher guarantees the same geometric representation up to the volumic mesher parameter distance_bound (which can be set very small).

6.2.5 A numerical convergence study:

In order to prove the convergence of the iterative scheme (6.3)-(6.5), it is necessary and sufficient to prove that the Neumann boundary condition $(\sigma \nabla V_B^k) \cdot \mathbf{n}$ converges when $k \to \infty$.

We express the Neumann boundary condition as a sequence with variable $c^k = (\sigma \nabla V_B^k) \cdot \mathbf{n}\big|_\Gamma$, under the form: $c^k = \mathbf{E}\, c^{k-1} + \mathbf{F}$, and study the norm of the operator $\mathbf{E}$.
At iteration k, $c^k = (\Sigma \nabla V_F^{k-1}) \cdot \mathbf{n}\Big|_\Gamma$; V_F^{k-1} in Eq.(6.4) is computed solving the linear system: $\mathbf{A}_F \cdot V_F^{k-1} = \mathbf{D}_F \cdot V_\Gamma^{k-1}$ where $\mathbf{A}_F$ denotes the FEM's stiffness matrix previously introduced, and $\mathbf{D}_F$ the source term dealing with the Dirichlet boundary condition on Γ. V_Γ^{k-1} represents the potential at the FEM vertices on Γ, which is computed solving the BEM system (6.3), and interpolating its boundary value, thanks to the BEM P1 approximation of the potential. Let $\mathbf{P}_{B2F}$ be this projector. V_Γ^{k-1} writes $V_\Gamma^{k-1} = \mathbf{P}_{B2F} \cdot \mathbf{A}_B^{-1} \cdot (\mathbf{S}_B + \mathbf{N}_B \cdot c^{k-1})$. Finally, when computing the current flow crossing Γ from the FEM's variable V_F, one can apply an operator $\mathbf{P}_{F2B}$ that computes the current density crossing each BEM triangle such that c^k writes:

$$\begin{aligned} c^k &= (\Sigma\ \nabla V_F^{k-1} \cdot \mathbf{n})|_\Gamma \\ &= \mathbf{P}_{F2B} \cdot V_F^{k-1} \\ &= \mathbf{P}_{F2B} \cdot \mathbf{A}_F^{-1} \cdot (\mathbf{D}_F \cdot V_\Gamma^{k-1}) \\ &= \mathbf{P}_{F2B} \cdot \mathbf{A}_F^{-1} \cdot (\mathbf{D}_F \cdot \mathbf{P}_{B2F} \cdot \mathbf{A}_B^{-1} \cdot (\mathbf{S}_B + \mathbf{N}_B \cdot c^{k-1})) \\ &= \mathbf{E} \cdot c^{k-1} + \mathbf{F}, \end{aligned} \tag{6.10}$$

where $\mathbf{E} = \mathbf{P}_{F2B}\mathbf{A}_F^{-1}\mathbf{D}_F\mathbf{P}_{B2F}\mathbf{A}_B^{-1}\mathbf{N}_B$.
Let us notice that the convergence of this sequence does not depend on the source $\mathbf{J}^{\mathrm{p}}$. Provided that $\rho(\mathbf{E}) = \max_i |e_i| < 1$, where the e_i denotes the eigenvalues of $\mathbf{E}$, the previous scheme is convergent. Using the power iteration method, we can evaluate the spectral radius of $\mathbf{E}$ for different meshes and see whether or not a relaxation is needed. This will be done for each new coupled BEM-FEM procedure with different geometries.

6.3 Numerical validation on spheres

Validation against analytical solutions is crucial when analyzing the accuracy of a method. Using the analytical solution provided by [Zhang, 1995] in case of multi-layer sphere model as reference, we propose to compare the solutions of the FEM, the BEM and the coupled BEM-FEM to the reference analytical solution.

Two spherical models were studied, the first one modeling 3 layers, the brain, the skull and the scalp, and the second model with 4 layers, splitting the brain into a gray matter and CSF component. Assigning a conductivity profile to the skull has been the topic of many papers; when considering an isotropic description the studies [Vallaghé and Clerc, 2009] and [Dannhauer et al., 2010] proposed to consider the radial conductivity of the skull as the skull conductivity for the isotropic model; on the other hand, when considering an anisotropic description the latter concludes that the tangential conductivity of the skull should be between 1.3 to 1.7 times higher than the radial one. This ratio between radial and tangential conductivities is not as big as the community used to believe (10 times lower); thus the results for a 1.5 anisotropy were not demonstrative and we chose to present here the method comparison on isotropic layers even if, in opposition to the BEM, the coupled BEM-FEM method also copes with anisotropy. Radii and conductivities used in this paper are shown table 6.2.

Models	Domains	Radii	Conductivities
3-layer	Brain	0.87	1.
	Skull	0.92	0.03
	Scalp	1.0	1.
4-layer	Brain	0.85	1.
	CSF	0.87	3.
	Skull	0.92	0.03
	Scalp	1.0	1.

Table 6.2 – *spherical models*

Forward computations were run for several dipoles placed on the z-axis with different positions and orientations, since the accuracy of all methods highly depends on these parameters. The next figures plot two errors measures: the RDM and the MAG (see sec.(2.5.2.4), Eq.(2.48) and Eq.(2.49)). The closer to 0, the better for the RDM, and to 1 for the MAG.
Several mesh resolutions were used to demonstrate the proper behavior of the proposed coupled method according to the BEM and FEM mesh sizes. For the surfacic meshes, we generated the 4 surfaces (out of the implicit sphere functions with radii $0.85, 0.87, 0.92, 1.0$) using the distance_bound criterion introduced before. We generated two sets of BEM meshes with 2 different bounds, leading to two resolutions

b1 and b2 (see table (6.3)). For the volumic meshes, meshes with two different cell sizes were generated out of the 2 sets of surfacic meshes for the two head models (3 and 4 layers). The resolution f1 ensures that cell sizes are below 0.05, and f2 below 0.02. These resolutions are shown in table (6.4) (and in Fig.(6.6) a FEM mesh is displayed), where the number of points represents the number of points per surface for the BEM, and the total amount of points (brain included) for the FEM.

Resolutions	Interfaces	Nb of points	Mean edge length
b1	Brain/CSF	1 112	0.09915
	CSF/Skull	1 145	0.09986
	Skull/Scalp	1 153	0.10533
	Scalp/Air	1 204	0.11202
b2	Brain/CSF	1 606	0.08241
	CSF/Skull	1 665	0.08304
	Skull/Scalp	1 658	0.08772
	Scalp/Air	1 665	0.09510

Table 6.3 – *Surfacic mesh resolutions*

Resolutions	Layers	Nb of points	Typical cell size
f1_b1	3	59 179	< 0.05
	4	80 895	< 0.05
f2_b1	3	387 016	< 0.02
	4	391 263	< 0.02
f1_b2	3	73 452	< 0.05
	4	95 952	< 0.05
f2_b2	3	393 374	< 0.02
	4	399 587	< 0.02

Table 6.4 – *Volumic mesh resolutions*

These mesh resolutions correspond to what is nowadays considered as a reasonable model, in terms of problem size. A very high precision FE mesh would have around five million vertices, and a very high precision BE mesh with 5 000 vertices per layer.
For the 3-layer model, the brain was handled by the BEM, and the skull as well as the scalp were handled by the FEM. For the 4-layer model, the BEM was used for the two inner regions: the brain and the CSF. In both cases, Γ was the inner skull surface.

Convergence of the proposed coupling was studied numerically by checking whether $\rho(\mathbf{E}) < 1$. The estimation of the spectral radius of the coupling opera-

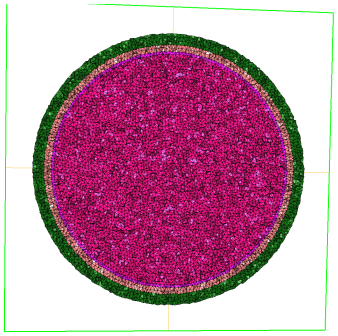

Figure 6.6 – *FE mesh resolution f2_b2 with 4 layers.*

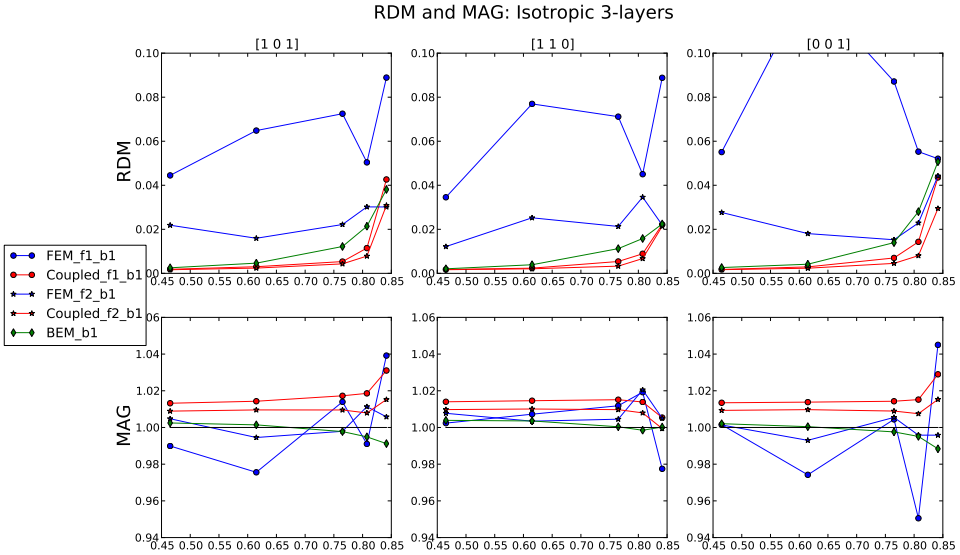

Figure 6.7 – *Forward solution comparisons for an isotropic 3-layer model – (b1).*

tor was for both the 3-layer and the 4-layer model between 0.11 — 0.14 for all mesh resolutions. Since $\rho(\mathbf{E})$ is clearly below 1, the coupled method scheme was convergent without need for relaxation. See table 6.5, for the computed spectral radii.

The number of iterations until the relative residual expressed in Eq.(6.5) reached 5.10^{-4}, was 4 or 5, *i.e.* only 8-10 boundary value problems to solve. Note also that most of the time was spent solving the sparse linear system of the FEM with the gradient descent; although each new iteration benefits from the near previous solution, and thus less time was needed after the first iteration. For the BEM part of the coupled method, once the main matrices were built, obtaining a new solution to a b.v.p was straightforward (just a matrix multiplication).

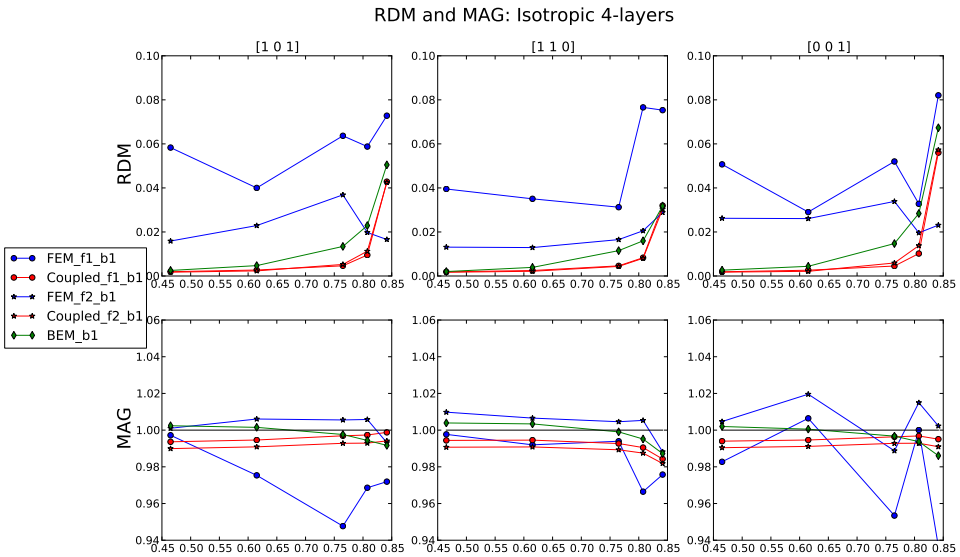

Figure 6.8 – *Forward solution comparisons for an isotropic 4-layer model – (b1).*

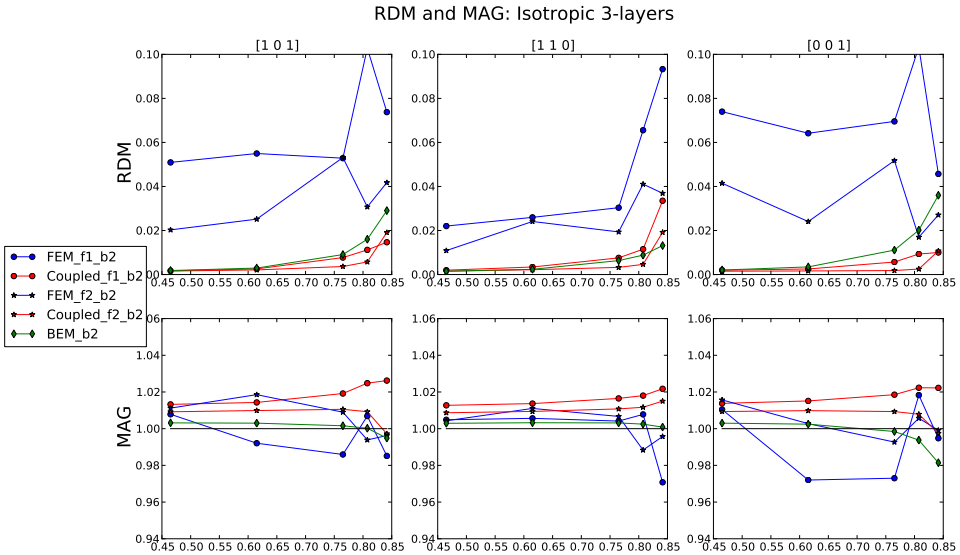

Figure 6.9 – *Forward solution comparisons for an isotropic 3-layer model – (b2).*

Results While the first row in Fig.(6.7)-(6.10) represents the RDM, the second shows the MAG error. Columns indicate the different dipole orientations, respectively Cartesian directions [1 0 1], [1 1 0], [0 0 1]. The horizontal axis represents the 5 dipole locations on the z-axis. The blue curves represent the solution of the

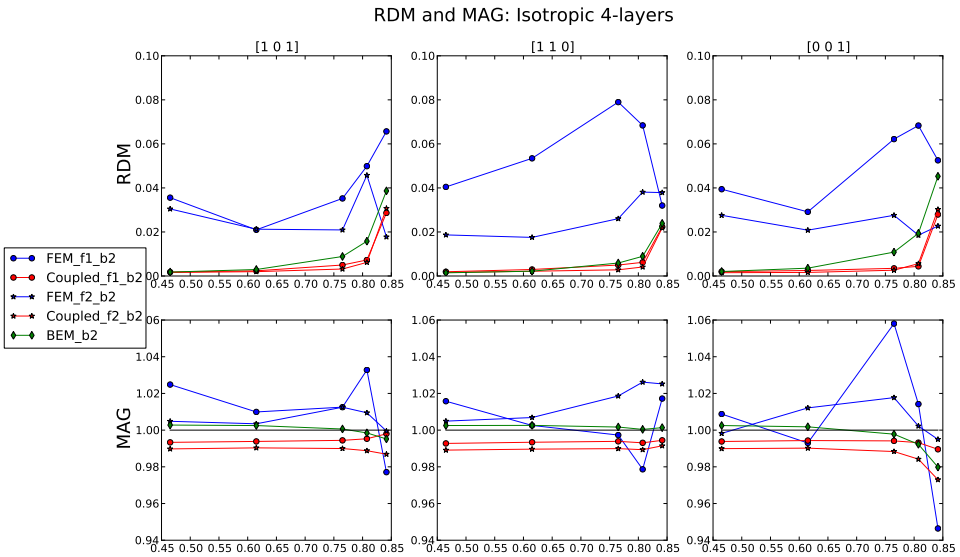

Figure 6.10 – *Forward solution comparisons for an isotropic 4-layer model – (b2).*

Coupled BE-FE mesh resolutions	3-layer	4-layer
b1+f1_b1	0.1304	0.1156
b1+f2_b1	0.1343	0.1191
b2+f1_b2	0.1307	0.1157
b2+f2_b2	0.1347	0.1192

Table 6.5 – *Estimated spectral radii:* $\rho(\mathbf{E})$.

pure FEM, one can see that at least for deep dipoles they display the lowest accuracies. One can also notice a staggering behavior for the FEM because, as discussed earlier, results depend on which tetrahedron the dipole falls in. The green error curves (BEM) are better than the FEM's, and degrade when the dipoles approach the inner surface, as expected. Finally, red curves show the coupled BEM-FEM error, better in almost all cases than their respective counterparts in BEM and FEM at same resolution. Since we are in an isotropic model, one can see that the improvement gained through the coupling compared to using the BEM alone, is due to the finer mesh resolution of the FEM. From another point of view, the poorer FEM results are due to the less accurate modeling of the source. Furthermore, we notice a limited gain using the coupled BEM-FEM, compared to the BEM, for a tangential dipole really close to the inner surface. Let us add that such tangential dipoles appear, when building a lead-field matrix for sources constrained by the white matter or gray matter surface, in the gyrus, thus not as close to the inner surface as the radial dipoles see Fig.(6.11).

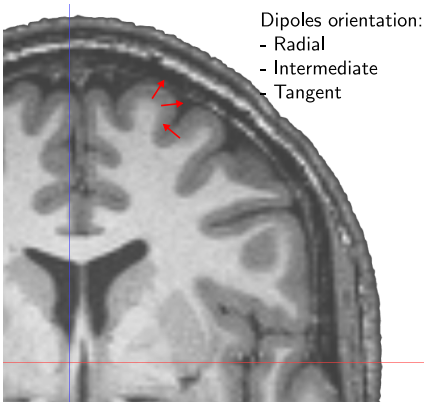

Figure 6.11 – *Typical dipoles orientations when constrained to be normal to the white/gray matter interface.*

Finally, while for the 3-layer models (Fig.(6.7) and Fig.(6.9)), one can see a significative improvement when increasing the FEM mesh size for the coupled method, the benefit is not obvious for the 4-layer models. This shows that the accuracy of the coupled method was limited by the FEM mesh in this case, and by the BEM mesh in the other cases. Also notice that the results of the three methods on the 4-layer models were a bit less good than for the 3-layer models, because the inner surface (in this case the brain/CSF interface) is closer to the dipoles.

Time and memory consumption Table (6.6) shows the time repartition and memory consumption for each method run for the highest mesh resolutions on the 4-layer model *i.e.* resolution b2 for the BEM, f2_b2 for the FEM, and b2+f2_b2 for the coupled method. The memory values shown are the maximum RSS (Resident Set Size) obtained when running the codes. Note that the FEM solver is the slowest but cheapest in term of memory usage. A better preconditioner than Jacobi would probably decrease the number of iterations of the conjugate gradient descent, but at the expense of the memory. The BEM solver is the fastest at the expense of a very high memory consumption. Finally, the coupled BEM-FEM method, is almost as fast as the BEM with the memory consumption of the FEM. Note that the coupled code has not been optimized yet, and considering a system resolution instead of inverting the BEM stiffness matrix $\mathbf{A}_B$ would save considerable time in this case (for less dipoles than problem unknowns). Furthermore, the time spent in the build of $\mathbf{P}_{F2B}$ is mostly due to a search in the FEM mesh structure and could be reduced by adding an octree representation for the FEM mesh.

Methods	Parts	CPU Time (in s)	Max RSS (in MB)
BEM	Assembling of $\mathbf{A}_B$	5 933	1 544
	Assembling of $\mathbf{S}_B$	4	77
	System resolution	1 436	12 738
	total for 15 dipoles	7 373	12 738
FEM	Assembling of $\mathbf{A}_B$ + 1 resolution	2 119	
	total for 15 dipoles	31 792	6 852
Coupled BEM-FEM	Assembling of $\mathbf{A}_B, \mathbf{N}_B, \mathbf{P}_{B2F}$	2 002	
	Inverting $\mathbf{A}_B$	2 378	
	Assembling of $\mathbf{A}_F$	21	
	Assembling of $\mathbf{P}_{F2B}$	2 307	
	total for 15 dipoles	10 239	6 995

Table 6.6 – *Time and memory repartition for the highest resolutions: b2, f2_b2 – 4 layers.*

6.4 BEM-FEM coupling on a realistic head shape

6.4.1 From MRI to meshes: segmenting and meshing:

Freesurfer[1] is a software suite for medical image processing (see [Dale et al., 1999] for cortical surface segmentation), which has been used to segment and obtain high resolution surfaces from a T1 anatomical MRI of resolution 256x176x256: the brain envelope, the inner skull, the outer skull, and the outer skin as seen Fig.(6.12).

Meshes generated by Freesurfer were of high resolution, and needed a re-meshing

Figure 6.12 – *Surfaces segmented by Freesurfer.*

to be usable on a BEM model. Volumic meshes with tetrahedra were also needed for the FEM. Using CGAL we were able to first re-mesh the surfaces with the desired number of vertices, and also provide volumic meshes out of these surfacic meshes, such that both surfacic and volumic meshes describe the same geometry (as discussed in subsection.6.2.4). In Fig.(6.13), the data processing from the MRI segmentation to the mesh generation is displayed.

[1] http://surfer.nmr.mgh.harvard.edu

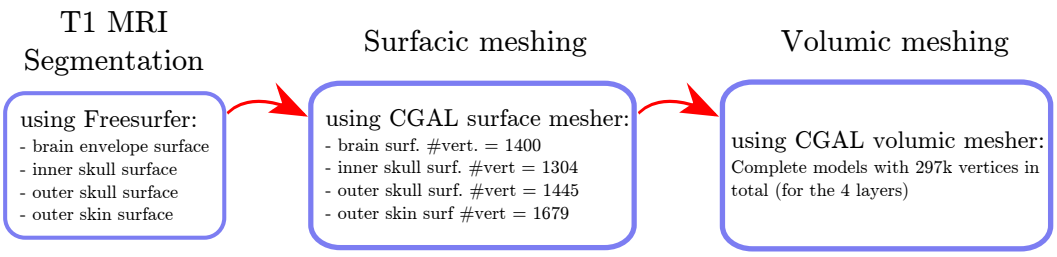

Figure 6.13 – *The meshing process from MRI to BEM and FEM meshes.*

6.4.2 Comparing methods

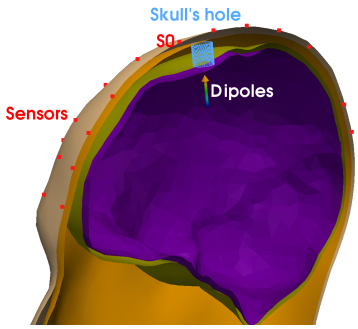

Figure 6.14 – *Realistic 4-layer model where the big arrow illustrates the set of dipoles oriented toward the z-axis, and approaching the skull hole.*

We propose here to model a cylindrical-shaped hole in the skull of a patient head. Such skull inhomogeneities occur in patients who have undergone brain surgery for a resection of an epileptogenic lesion. This hole was supposed to be of diameter 1cm and filled with a skin-like tissue material, and thus it was assigned a conductivity of 1. We located the hole at the top of the patient head, and ran the forward computations for 15 dipoles approaching the hole on the z-axis and oriented toward it. Such a hole has been modeled in BEM in [Bénar and Gotman, 2002, Oostenveld and Oostendorp, 2002], but requires a very fine meshing in its vicinity, and thus many elements. The current implementation of the sBEM in OpenMEEG does not allow for non-nested geometries proposed in [Kybic et al., 2006]. On the other hand the FEM is able to take into account the hole easily, and hence we propose to use the coupled BEM-FEM method and to handle the skull by the FEM in the proposed domain partition.
The FEM will use the model with the inhomogeneity produced by the hole. For the coupled BEM-FEM, the BEM will deal with the brain and the CSF, and the FEM with the skull (with the hole), and the scalp. We will show the results of the BEM for homogeneous layers, because of the previously mentioned difficulties for handling the hole. Table (6.7) presents the models used by the different methods,

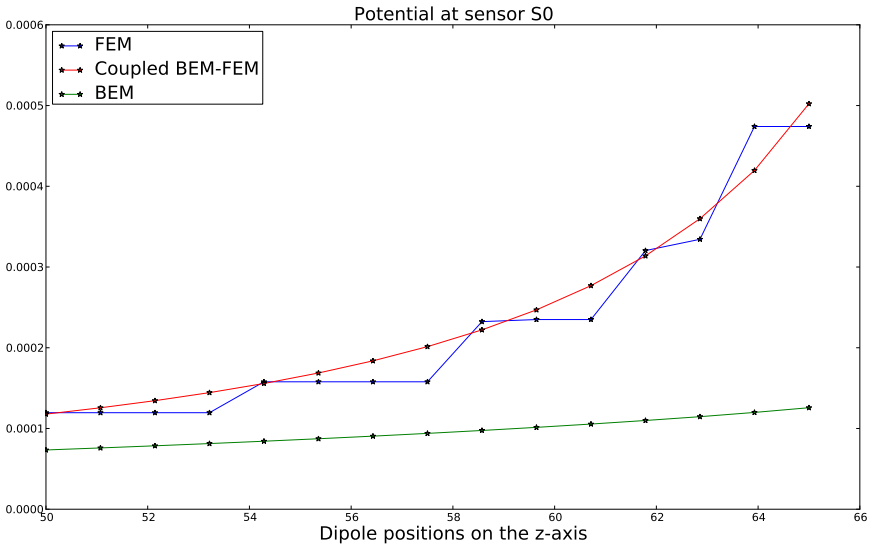

Figure 6.15 – *Potential at the closest sensor S0 to the hole.*

and the number of points.

Methods	Models	Conductivities	Number of vertices
BEM	Brain	1.	1 400
	CSF	3.	1 304
	Skull	0.03	1 445
	Scalp	1.	1 679
FEM	Brain	1.	96 551
	CSF	3.	134 127
	Skull	0.03	132 783
	Hole	1.	146
	Scalp	1.	115 672
Coupled BEM-FEM	Brain	1.	1 400
	CSF	3.	1 304
	Skull	0.03	132 783
	Hole	1.	146
	Scalp	1.	115 672

Table 6.7 – *Meshes resolution*

In order to analyze the results of the three methods, we plotted in Fig.(6.15) the potential at a sensor located very close to the hole on the patient scalp (labeled S0),

see Fig.(6.14). One can see from these curves that the BEM largely underestimates the potential by not modeling the very conductive hole; the BEM curve is almost linear, which is not the case for the two other methods. The staggering behavior of the blue curve (FEM result) is again due to the coarse dipole modeling within the FEM. The coupled BEM-FEM curve presents both advantages, with the high regularity of the BEM, and the good modeling of the hole, and thus the smooth exponential behavior when the dipole approaches the hole. It is likely, taking into account the results on the sphere models, that the coupled curve is the closest to reality. On Fig.(6.16), one can see the EEG topography plotted on the same scale for a 120-sensor helmet. Each line represents a method, the first one being the FEM, the second the coupled BEM-FEM method and lastly the BEM with intact skull. The columns represent 5 different dipole locations on z.

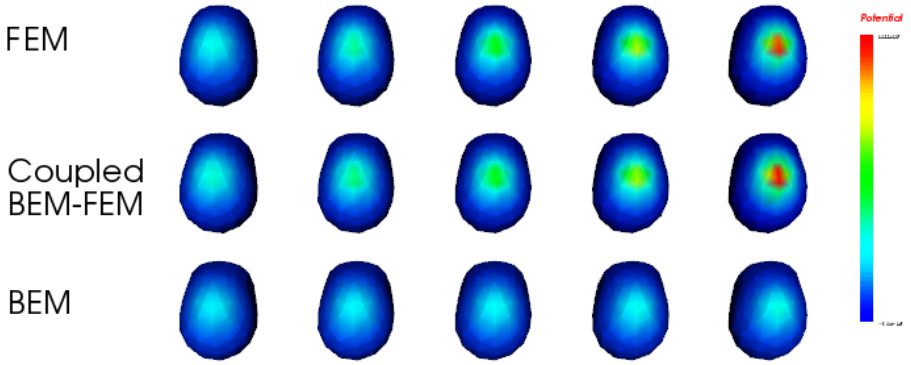

Figure 6.16 – *EEG topography results for different dipole positions approaching a hole in the skull on the z-axis. First row the FEM results, second row the coupled BEM-FEM results, and lastly the BEM results.*

6.4.3 Perspectives

Although [Wolters et al., 2006] have shown the tissues anisotropy in vicinity of the sources to be particularly influential on both EEG and MEG results, we have not incorporated it to our model, since the BEM was taking care of all the domains inside the inner skull, thus considering all the brain as homogeneous. Regarding the mesh generation, our first goal was to be able able to generate independent meshes for the BEM and the FEM. But the problems at interface regarding the interpolation between the two methods' variables constrained us to generate the FEM mesh out of the BEM ones in order to guaranty the same geometry definition (case c. in Fig.(6.2)). We have also run the coupled method for the spherical models with fully independent meshes (case b. in Fig.(6.2)), and obtained very similar results. These results let us think that the interpolation error is negligible (for these mesh sizes at least), and that fully independent meshes could be used for the coupled method.

6.4.4 Conclusion

In this chapter, a coupled BEM-FEM formulation has been studied. This coupled method used iterations between Neumann and Dirichlet boundary value problems until convergence. The convergence was guaranteed by an upper bound that can be verified numerically. The accuracy has been proved, and is better than using a pure FEM, furthermore it allows for more conductivity profiles than the standard BEM, allowing for inhomogeneities and anisotropy in the skull as shown on a realistic model.
In this discrete framework, we commented the convergence properties of the proposed scheme not in terms of the discrete version of the Poincaré-Steklov operator (often called Schur complement), but rather studying the norm of an operator which directly appears from our sub-problem expression (operator $\mathbf{E}$ in Eq.(6.10)).
Numerical results were shown, where one can see the improvements gained using DD techniques in order to get faster, and more accurate solutions of the forward EEG problem.

Chapter 7

Handling anisotropy or inhomogeneities in BEM

As seen in introduction, the brain contains white matter whose color is due to the myelin of axons. These axons have preferred orientations depending on the brain area. Although the white matter has a lower mean electrical conductivity than the gray matter, it is believed to be highly anisotropic $1:10$ along the fibers directions. As pointed out in recent studies, this anisotropy has influence on the result of MEEG. Moreover in EEG, inhomogeneities in the skull also influence highly the results. The BEM cannot handle inhomogeneities, and not anisotropies that are not homogeneous. In this chapter, we propose a new method for dealing with such conductivities.

Summary

Goals: Allow for the use of anisotropic or inhomogeneous conductivities within a BEM framework.

Tools: Consider a locally non isotropic conductivity tensor, as a main isotropic part plus a locally anisotropic or inhomogeneous part. Splitting the main operator into a component due to the isotropic part, and consider the rest as a perturbation.

Results: A very flexible formulation allowing for local anisotropy and/or inhomogeneity implemented with the sBEM.

Contents

7.1 Estimating the anisotropy of the white-matter

7.1.1 Diffusion MRI

Diffusion MRI allows to measure within voxels in a tissue the diffusion of water molecules. This diffusion would be isotropic if the medium were homogeneous. But because of the fiber structures present in the white matter, on can infer the principal directions of the diffusion by analyzing the diffusion tensor. This tensor can be represented as a symmetric 3×3 matrix for each voxel:

$$\mathbf{D} = \begin{pmatrix} D_{xx} & D_{xy} & D_{xz} \\ D_{xy} & D_{yy} & D_{yz} \\ D_{xz} & D_{yz} & D_{zz} \end{pmatrix} \tag{7.1}$$

After diagonalizing $\mathbf{D}$, one gets the eigenvalues $(\lambda_1, \lambda_2, \lambda_3)$ with their eigenvectors (v_1, v_2, v_3):

$$\mathbf{D} = \mathbf{S} \cdot \begin{pmatrix} \lambda_1 & & \\ & \lambda_2 & \\ & & \lambda_3 \end{pmatrix} \cdot \mathbf{S}^{\boldsymbol{T}}$$

where $\mathbf{S}$ corresponds to the transformation matrix made of the normalized eigenvectors. Diffusion tensor imaging (DTI) hence provides a 3D image, containing in each voxel a 3×3 tensor.

7.1.2 Fiber tractography

From these diffusion images a new imaging technique has arisen to recover the fiber structures: fiber tractography [Mori et al., 1999]-[Basser et al., 2000]. It provides images of the fibers contained in our brain (as seen in Fig.(2.5)). Tractographies are curvilinear structures defined by a high probability of having a white matter fiber in this direction at this location.

7.1.3 From the diffusion tensor to the conductivity tensor

Having the diffusion tensor for each voxel of a patient head, a relationship has been derived in [Tuch et al., 2001] showing that the conductivity tensor $\mathbf{\Sigma}$ and the diffusion tensor $\mathbf{D}$ share the same eigenvectors:

$$\mathbf{\Sigma} = \mathbf{S} \cdot \begin{pmatrix} \sigma_1 & & \\ & \sigma_2 & \\ & & \sigma_3 \end{pmatrix} \cdot \mathbf{S}^{\boldsymbol{T}} \, . \tag{7.2}$$

Knowing that, one still needs to establish a relationship between the eigenvalues of the tensors. Although a relation between their eigenvalues is given in the cited article, a few papers [Wang et al., 2008]-[Wolters et al., 2006] propose different formulas for estimating the eigenvalues. In [Shimony et al., 1999] the ellipsoidal profiles have been investigated in 12 regions of interest within the gray and white matter,

they most often relate prolate shapes for the tensor in white matter regions, whereas isotropic behavior was found in the gray matter. This comforts our intention of considering an isotropic conductivity for the gray matter, and to use only two values σ_l and σ_t to represent the anisotropy at a given location. The first parameter σ_l denotes the conductivity along the fiber's direction (*longitudinal*), while the second one denotes the transversal conductivity (which is thus considered the same in the two orthogonal transverse directions of the fiber). The conductivity tensor now writes:

$$\mathbf{\Sigma} = \mathbf{S} \cdot \begin{pmatrix} \sigma_l & & \\ & \sigma_t & \\ & & \sigma_t \end{pmatrix} \cdot \mathbf{S}^{\boldsymbol{T}} \tag{7.3}$$

We know that $\sigma_l \geq \sigma_t$, and sometimes have some insight on the mean conductivity of the white matter, which is believed to be ~ 2.5 times lower than the gray matter [Geddes and Baker, 1967]. The common anisotropic ratio used is $\sim 1:10$, which means $\sigma_l \simeq 10\sigma_t$ [Tuch et al., 2001]-[Shimony et al., 1999]. In fact the model for estimating the conductivity tensor detailed in [Tuch et al., 2001] predicts a strong linearity, explained by the fact that in the white matter both processes (diffusion and electrical conduction) happen mostly in the extracellular space.

7.2 Dealing with anisotropy in FEM

7.2.1 Existing studies

The FEM can deal with any kind of conductivity profile at an over-element resolution *i.e.* each mesh element (cells: *e.g.* tetrahedra) must have a constant anisotropic or isotropic conductivity value. A few studies relate the use of white matter anisotropy in FEM for the MEEG forward problems resolution [Haueisen et al., 2002]-[Wolters et al., 2006]-[Gullmar et al., 2006].
In [Haueisen et al., 2002] an eleven-compartment realistic head model was studied, with the use of anisotropic conductivities for the white as well as the gray matter. The relationship between the diffusion tensor and the conductivity tensor was supposed strongly linear as advised in [Tuch et al., 2001]:

$$\mathbf{\Sigma} = \frac{\sigma_e}{d_e}\mathbf{D} \ , \tag{7.4}$$

where the coefficients σ_e and d_e denote the extracellular conductivity and diffusivity, respectively. In this study they compared the EEG and MEG results using the full model (2 regions anisotropic, 9 isotropic) as reference to a simple 3-layer isotropic model. Similarly, [Wolters et al., 2006] has studied the influence of the white matter and skull conductivity profiles on the forward results for the EEG problem as well as the MEG problem on a realistic head model. There, two kinds of determination of the anisotropic value were examined, the so-called Wang constraint, which states that the following equality must hold:

$$\sigma_l \cdot \sigma_t = \sigma_{iso} \tag{7.5}$$

and a volume constraint, which compares the volume of the prolate tensor, with the spherical isotropic one:

$$\frac{4}{3}\pi\sigma_l(\sigma_t)^2 = \frac{4}{3}\pi\sigma_{iso}^3 \ . \tag{7.6}$$

In the latter study, no influence of the skull anisotropy on the MEG was found as expected, but up to 0.11 RDM (sec.(2.5.2.4)) error for the EEG leadfield. Both studies agree with a high influence of the white matter anisotropy on the MEG results (about 0.1 RDM and up to 0.15 for deep sources), and a weaker one for the EEG results (0.05 RDM and 0.1 for deep sources). Neglecting both skull and white matter anisotropies led to 0.13 RDM error for EEG (in mean and for both constraints).

7.2.2 Comments

In the cited studies the conductivity models were compared using the same geometry for all experiments. Thus the electrophysiological models were the same except for the conductivity part of the model. In the first one ([Haueisen et al., 2002]), a FEM with hexahedral (cubic) elements were used, whereas in the other tetrahedral elements were used. What we can conclude out of these studies is the importance of modeling the skull and white matter anisotropy for the EEG, and mostly the white matter anisotropy for the MEG. We still do not know if the results of an isotropic BEM would be better than those of an anisotropic FEM, since the true solution is then unknown. Two ways for validating such an approach could be explored:

Experimental way computing the forward leadfields with the two approaches, and comparing the inverse solution for a SEP (Somatosensory Evoked Potential) task, such as moving a finger whose activity is associated with some brain area in the motor cortex. In that case one could then affirm, the best solution (at least for this source location).

Diminishing the mesh size as the FEM should converge toward the true solution, a convergence study of the potential at sensors with regard to the mesh size could be investigated. One should then estimate after which mesh size the FEM results could be considered as stable, and compare the multi-compartment anisotropic FEM, the isotropic BEM, with the reference FEM solution at convergence.

The first case would be more appreciated, since the second one would also depend on the conductivity values assigned for every tissue which is still challenging to estimate, and could thus introduce errors. Note that, in the first case, the same inverse problem resolution should be applied on both leadfields.

7.3 Toward the handling of anisotropy/inhomogeneity in BEM

BEM methods do not allow for non-homogeneous anisotropic conductivities, no BEM formulation allows to handle a non constant anisotropic region for the 3D Laplace equation, even in the case of very structured anisotropy such as the one of the skull model, where the tangential conductivity is a few times larger than the radial one. This problem arises from the basis of BEM, the Green function for the Laplace equation which has to be invariant with space. A common trick when using a BEM in mechanics (elasticity) with an anisotropy in one Cartesian direction, is done considering an homothety dilation along that direction, with the value of the anisotropic ratio [Wang and Denda, 2007].
Anisotropy is quite common within the head, one example being the skull which is reported to be correctly modeled with an anisotropic ratio of 1.5 in the latest studies [Dannhauer et al., 2010]. Another anisotropy is due to the presence of white matter fibers very close to the sources and appears to play an important role on the forward EEG and MEG results as discussed previously.
In addition to anisotropy, inhomogeneity of conductivity is also also difficult to handle with the BEM. For example, after a surgery leading to a hole in the skull (craniotomy), this hole is often filled with a skin-like tissue which is highly conductive compared to the bone of the skull and thus can lead to big changes in current propagation (and thus the forward problem). Although this hole region is considered to be isotropic, it can be difficult to handle in a BEM framework since sharp edges at the interface of the skull/hole can lead to numerical errors (see Fig.(7.15)). BEM has anyway been successfully applied for the EEG problem with a hole in the skull in [Oostenveld and Oostendorp, 2002]-[Bénar and Gotman, 2002] but [Kybic et al., 2006] suggest a very high number of elements to avoid numerical errors.
In this section a method is proposed to handle a perturbation on the conductivity profile within the BEM framework. As a first step we will consider the anisotropy due to the white matter fibers.

7.3.1 A BEM handling local anisotropy

A standard EEG problem which is often solved with the BEM is a 3-layer nested model (see Fig.(7.1)). The equation solved is the Poisson equation, which in each domain Ω_k boils down to a Laplace equation, since the conductivity is constant:

$$\begin{cases} \sigma_k \Delta V & = \nabla \cdot \mathbf{J}_k^{\mathrm{p}} \quad \forall \mathbf{r} \in \Omega_k \\ [V_k] & = 0 \quad \forall \mathbf{r} \in \partial\Omega_k \\ \left[\sigma_k \frac{\partial V}{\partial \mathbf{n}}\right] & = 0 \quad \forall \mathbf{r} \in \partial\Omega_k \end{cases}, \tag{7.7}$$

where $\mathbf{J}_k^{\mathrm{p}}$ denotes the source term if there is one in the volume Ω_k. The bracket notation still stands for the jump across the interface, to show that the poten-

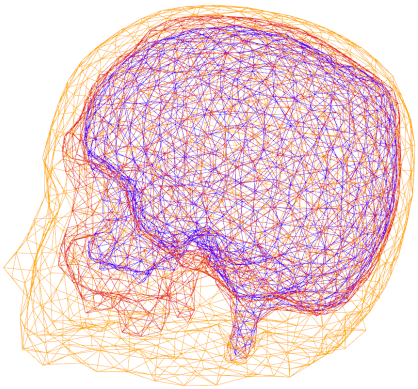

Figure 7.1 – *A typical 3-layer nested model for BEM.*

tial and the normal current are continuous. In Ω_1 let us introduce an anisotropic conductivity represented by the tensor Σ_1:

$$\nabla \cdot \Sigma_1 \nabla V = \nabla \cdot \mathbf{J}_1^{\mathrm{p}} \quad \forall \mathbf{r} \in \Omega_1 \tag{7.8}$$

The problem is that this equation cannot be dealt with the BEM since we do not have a Laplacian in the domain containing the anisotropy.

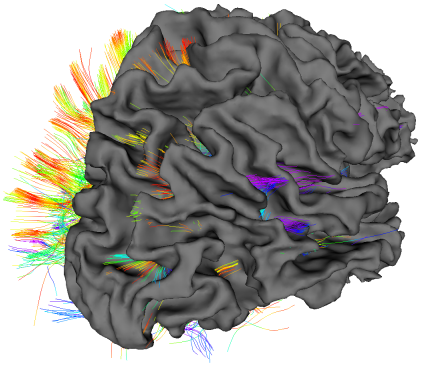

Figure 7.2 – *Some bundles of white matter fibers overlaid on the right white matter region.*

For the forward EEG problem, the most important part of this anisotropy, is the one due to the fibers that lie close to the source, because for a source lying far away from fibers this conductivity tensor can be well approximated by an isotropic one.

We propose to formulate a tensor expression, which takes into account the local anisotropy due to the fibers that are close to the source for which we solve the forward problem. Let us write $\Sigma = \Sigma_1$ the conductivity tensor in the innermost domain (the brain), and for sake of exposition we consider only one fiber f. In

this medium, the conductivity is thus perturbed along this fiber. One can consider the conductivity tensor of such medium containing the fiber f described with a characteristic function χ_f defined as:

$$\chi_f(\mathbf{r}) = \begin{cases} 1 & \text{if } \mathbf{r} \in f \\ 0 & \text{if } \mathbf{r} \in \Omega \setminus f \end{cases}, \tag{7.9}$$

We express the conductivity tensor as an isotropic one plus a perturbation due to the fiber conductivity $\Sigma_f(\mathbf{r})$, where we consider the conductivity of the fiber to be anisotropic along its local direction $\mathbf{n}_f(\mathbf{r})$ such that:

$$\Sigma_f(\mathbf{r}) = \sigma\mathcal{I} + (\sigma_f(\mathbf{r}) - \sigma)\mathbf{n}_f(\mathbf{r})\mathbf{n}_f^T(\mathbf{r}) \ , \tag{7.10}$$

with $\sigma_f(\mathbf{r})$ the conductivity along the fiber at location $\mathbf{r}$. The overall conductivity tensor then writes (see Fig.(7.3)):

$$\forall \mathbf{r} \in \Omega_1,\ \Sigma(\mathbf{r}) = \sigma\mathcal{I} + (\sigma_f(\mathbf{r}) - \sigma)\mathbf{n}_f(\mathbf{r})\mathbf{n}_f(\mathbf{r})^T\, \chi_f(\mathbf{r}) \tag{7.11}$$

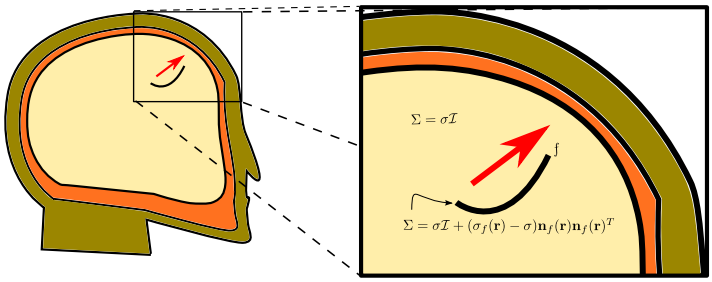

Figure 7.3 – *Perturbed conductivity tensor expression.*

Plugging in this tensor expression in the Poisson equation yields:

$$\begin{aligned} \nabla \cdot (\Sigma \nabla V) &= \nabla \cdot \mathbf{J}^{\mathrm{p}} \quad \text{in } \Omega_1 \\ \sigma \Delta V + \nabla \cdot ((\sigma_f(\mathbf{r}) - \sigma)\mathbf{n}_f(\mathbf{r})\chi_f(\mathbf{r})\nabla V \cdot \mathbf{n}_f(\mathbf{r})) &= \nabla \cdot \mathbf{J}^{\mathrm{p}} \quad \text{in } \Omega_1 \end{aligned} \tag{7.12}$$

We now have a Laplacian term, but the problem still cannot be solved with a BEM, since the correction term due to the fiber depends on the unknown V.
We next propose two methods for dealing with this correction term. In the first one, we consider discretizing the characteristic function χ_f into weighted points which is equivalent to discretizing the tensor. This was published in [Olivi et al., 2011a]. In the second method, we will instead try to take into account the full correction term instead.

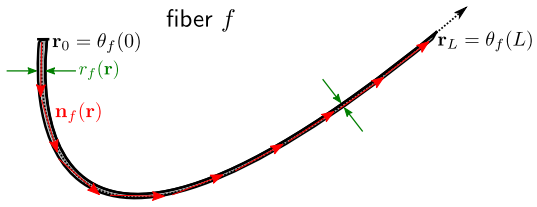

Figure 7.4 – *A sketch of a white matter fiber.*

7.3.2 First method: Discretizing the conductivity tensor

For sake of exposition, we consider one fiber f with (local-) cylindrical shape with radius $r_f(x)$, a total finite length L, with the previous notations for its direction, and conductivity. Such a fiber is displayed Fig.(7.4).

We now propose to discretize this fiber into weighted points, so that each discretization point will then play the role of a dipole later on.
The spatial extension of the fiber was denoted χ_f and we discretize it into N points along its curvilinear abscissa (denoted $\theta_f : \mathbb{R} \to \mathbb{R}^3$). Writing $\mathbf{r}_i$ the N points along the fiber, $s.t$ $\mathbf{r}_i = \theta_f\left(\frac{L}{N}(i - \frac{1}{2})\right)$, we write χ_f as:

$$\Delta_N(\chi_f) = \frac{L}{N}\pi \sum_{i=1}^{N} r_f(\mathbf{r}_i)^2 \delta\left(\mathbf{r} - \mathbf{r}_i\right) \ , \tag{7.13}$$

where δ denotes a Dirac distribution (in $\mathbb{R}^3$) centered at $\mathbf{r} = \mathbf{r}_i$.
Now, plugging in this discretized version of χ_f into Eq.(7.11), the conductivity tensor becomes:

$$\forall \mathbf{r} \in \Omega_1,\ \Sigma(\mathbf{r}) = \sigma\mathcal{I} + \sum_{i=1}^{N} \pi\frac{L}{N} r_f(\mathbf{r}_i)^2(\sigma_f(\mathbf{r}_i) - \sigma)\mathbf{n}_f(\mathbf{r}_i)\mathbf{n}_f(\mathbf{r}_i)^T\ \delta(\mathbf{r} - \mathbf{r}_i)\ . \tag{7.14}$$

This will allow pieces of fibers to be considered as weighted points.
From now we introduce the notation:

$$\varepsilon_i = \pi\frac{L}{N} r_f(\mathbf{r}_i)^2(\sigma_f(\mathbf{r}_i) - \sigma)\ , \tag{7.15}$$

$$\delta_i = \delta(\mathbf{r} - \mathbf{r}_i)\ , \tag{7.16}$$

$$\mathbf{n}_i = \mathbf{n}_f(\mathbf{r}_i)\ , \tag{7.17}$$

which leads the more digest expression:

$$\forall \mathbf{r} \in \Omega_1,\ \Sigma(\mathbf{r}) = \sigma\mathcal{I} + \sum_{i=1}^{N} \varepsilon_i \mathbf{n}_i\mathbf{n}_i^T\delta_i\ . \tag{7.18}$$

Re-writing the Poisson Eq.(7.12):

$$\sigma\Delta V = \ \nabla \cdot \left(\mathbf{J}^{\mathrm{p}} - \textstyle\sum_{i=1}^{N} \varepsilon_i \nabla V(\mathbf{r}_i) \cdot \mathbf{n}_i\mathbf{n}_i\delta_i\right) \quad \text{in } \Omega_1 \tag{7.19}$$

we then end up with an expression containing a Laplacian term, and on the right-hand side, terms due to the anisotropic part of the conductivity tensor that act like source terms. Indeed, writing $\mathbf{J}_i = \mathbf{m}_i\delta_i$, where $\mathbf{m}_i = \varepsilon_i \nabla V(\mathbf{r}_i)\cdot \mathbf{n}_i\mathbf{n}_i$, one recognizes the expression of a dipolar source term, as the one of the primary source current $\mathbf{J}^{\mathrm{p}}$.
Each $\mathbf{J}_i$ is a dipole located at a discretization point $\mathbf{r}_i$, with direction $\mathbf{n}(\mathbf{r}_i)$, and a momentum $\|\mathbf{m}_i\| = \varepsilon_i \nabla V(\mathbf{r}_i)\cdot \mathbf{n}_i$. In the following these new dipoles will be called virtual dipoles to differentiate them from the primary dipoles. Eq.(7.19) becomes:

$$\sigma\Delta V = \quad \nabla\cdot\left(\mathbf{J}^{\mathrm{p}} - \textstyle\sum_{i=1}^{N}\mathbf{m}_i\delta_i\right) \quad \text{in } \Omega_1 \tag{7.20}$$

The problem to solve now is that the strength of the source terms $\|\mathbf{m}_i\|$ depends on the actual unknown V.
Let us solve Eq.(7.19) using an iterative scheme (k), where we set up $V^0 = 0$:

$$\sigma\Delta V^{k+1} = \nabla\cdot\left(\mathbf{J}^{\mathrm{p}} - \sum_{i=1}^{N}\varepsilon_i\nabla V^k(\mathbf{r}_i)\cdot\mathbf{n}_i\mathbf{n}_i\delta_i\right) \text{ in } \Omega_1. \tag{7.21}$$

At the first iteration, an isotropic problem is solved. Then, we compute thanks to the internal operators of the BEM (described in sec.2.7.1) the value $\nabla V^k(\mathbf{r}_i)\cdot\mathbf{n}_i$, $\forall i$. At the second iteration, we then include the contribution of the fibers to the problem; the fibers contribution can be seen as virtual dipoles. The results obtained solving the second iteration are then the results of an anisotropic problem, where the anisotropy due to the fibers is taken into account. Actually this is only a first step, since the influence of the dipole onto the fibers is taken into account, but neither the fibers between fibers interaction nor the fiber and model interaction are considered, *e.g.* there is no conduction within the fiber as if it was an electric wire which should be almost the case in reality. A completion will be seen in the second method.
Let us present some numerical results of the proposed method at the second iteration. To do so, we expose here a validation experiment, where the FEM will be taken as reference, but first of all we expose the discrete problem for solving this iterative procedure using the symmetric BEM operators.

7.3.2.1 Discrete problem:

In this section we use the notation exposed in sec.2.7.1. At the first iteration, the isotropic solution $\mathbf{V}^1 = \mathbf{V}_{iso}$ is computed at sensors:

$$\mathbf{X}^1 = \mathbf{H}^{-1}\cdot\mathbf{D} \tag{7.22}$$
$$\mathbf{V}^1 = \mathbf{S}_{eeg}\cdot\mathbf{X}^1\ , \tag{7.23}$$

where the matrix $\mathbf{D}$ is the source term due to the primary source current $\mathbf{J}^{\mathrm{p}}$, *i.e.* it is the discretization of $\nabla\cdot\mathbf{J}^{\mathrm{p}}$. Then we need to compute the value $\nabla V^1\cdot\mathbf{n}_i(\mathbf{r}_i)$

in Eq.(7.21) at each discretization point. As explained in the section on internal operators (sec.2.7.1), the potential in a domain is composed of two parts; the one due to the dipole as if it was in an infinite medium, and the component due to the correction of the geometry, so that the potential at point $\mathbf{r}$ is:

$$V(\mathbf{r}) = \begin{cases} \mathbf{S_r} \cdot \mathbf{X} & \text{if } \mathbf{r} \in \Omega \text{ with no sources} \\ \mathbf{S_r} \cdot \mathbf{X} + \Phi_{\mathbf{r}}(\mathbf{J}^{\mathrm{p}}) & \text{if } \mathbf{r} \in \Omega \text{ with sources} \end{cases} , \tag{7.24}$$

where $\Phi_{\mathbf{r}}$ represents the analytical part (potential generated by a current dipole in an infinite medium of conductivity σ), and $\mathbf{S_r}$ the internal operators. As the white matter fibers are here considered to be in the same volume as the source $\mathbf{J}^{\mathrm{p}}$, we are in the second case.
The potential in an infinite medium of conductivity σ generated by a current dipole, is undefined at the exact location of the dipole, and is obtained analytically elsewhere with the formula $\Phi_{\mathbf{r}}(\mathbf{J}^{\mathrm{p}})$, where $\mathbf{J}^{\mathrm{p}} = \mathbf{m}_p \delta_{\mathbf{r}_p}$, as :

$$\Phi_{\mathbf{r}}(\mathbf{J}^{\mathrm{p}}) = \frac{1}{4\pi\sigma} \frac{\mathbf{m}_p \cdot (\mathbf{r} - \mathbf{r}_p)}{\|\mathbf{r} - \mathbf{r}_p\|^3} \tag{7.25}$$

But we need to compute the value $\nabla V^1(\mathbf{r}_i) \cdot \mathbf{n}_i$, and not the potential. Let us use a finite difference (parameter ε) to estimate it for the term depending on the internal operator, and use the analytical formula for the term due the source, *i.e*:

$$\partial_{\mathbf{n}_i} V^1(\mathbf{r}_i) = \frac{1}{\varepsilon}(\mathtt{S}_{\mathbf{r_i}+\frac{\varepsilon \mathbf{n_i}}{2}} - \mathtt{S}_{\mathbf{r_i}-\frac{\varepsilon \mathbf{n_i}}{2}}) \cdot \mathbf{X}^1 + \Psi_{\mathbf{n}_i,\mathbf{r}_i}(\mathbf{J}^{\mathrm{p}}) , \tag{7.26}$$

where $\Psi_{\mathbf{n}_i,\mathbf{r}_i}$ writes:

$$\begin{aligned} \Psi_{\mathbf{n}_i,\mathbf{r}_i}(\mathbf{J}^{\mathrm{p}}) &= \partial_{\mathbf{n}_i} \Phi_{\mathbf{r}_i}(\mathbf{J}^{\mathrm{p}}) \\ &= \frac{1}{4\pi\sigma}(\mathbf{m}_p \cdot \nabla) \frac{(\mathbf{r}_i - \mathbf{r}_p)}{\|\mathbf{r}_i - \mathbf{r}_p\|^3} \cdot \mathbf{n}_i = \frac{1}{4\pi\sigma}(\mathbf{m}_p \cdot \nabla)\nabla \left(\frac{-1}{\|\mathbf{r}_i - \mathbf{r}_p\|} \right) \cdot \mathbf{n}_i \\ &= \frac{1}{4\pi\sigma}(\mathbf{m}_{p_x}\partial_x + \mathbf{m}_{p_y}\partial_y + \mathbf{m}_{p_z}\partial_z) \left(\partial_x \frac{-1}{\|\mathbf{r}_i - \mathbf{r}_p\|}\mathbf{n}_x + \partial_y \frac{-1}{\|\mathbf{r}_i - \mathbf{r}_p\|}\mathbf{n}_y + \partial_z \frac{-1}{\|\mathbf{r}_i - \mathbf{r}_p\|}\mathbf{n}_z \right) \end{aligned} \tag{7.27}$$

The Hessian matrix H of $\frac{-1}{\|\mathbf{r}-\mathbf{r}_p\|}$ is needed:

$$H = \begin{pmatrix} \partial_x\partial_x & \partial_x\partial_y & \partial_x\partial_z \\ \partial_y\partial_x & \partial_y\partial_y & \partial_y\partial_z \\ \partial_z\partial_x & \partial_z\partial_y & \partial_z\partial_z \end{pmatrix} \left(\frac{-1}{\|\mathbf{r} - \mathbf{r}_p\|} \right) = 3\frac{(\mathbf{r} - \mathbf{r}_p) \otimes (\mathbf{r} - \mathbf{r}_p)}{\|\mathbf{r} - \mathbf{r}_p\|^5} - \frac{\mathcal{I}_3}{\|\mathbf{r} - \mathbf{r}_p\|^3} \tag{7.28}$$

so that it writes:

$$\begin{aligned} \Psi_{\mathbf{n}_i,\mathbf{r}_i}(\mathbf{J}^{\mathrm{p}}) = \frac{1}{4\pi\sigma} \quad (\quad & (\mathbf{m}_{p_x}\mathbf{n}_x)H_{1,1} + (\mathbf{m}_{p_y}\mathbf{n}_y)H_{2,2} + (\mathbf{m}_{p_z}\mathbf{n}_z)H_{3,3} \\ & +(\mathbf{m}_{p_y}\mathbf{n}_x + \mathbf{m}_{p_x}\mathbf{n}_y)H_{1,2} \\ & +(\mathbf{m}_{p_z}\mathbf{n}_x + \mathbf{m}_{p_x}\mathbf{n}_z)H_{1,3} \\ & +(\mathbf{m}_{p_y}\mathbf{n}_z + \mathbf{m}_{p_z}\mathbf{n}_y)H_{2,3} \quad). \end{aligned} \tag{7.29}$$

For sake of simplicity we introduce the operators:

$$\begin{aligned} \Delta_i &= \frac{1}{\varepsilon}(\mathbf{S}_{\mathbf{r}_i+\frac{\varepsilon\mathbf{n}_i}{2}} - \mathbf{S}_{\mathbf{r}_i-\frac{\varepsilon\mathbf{n}_i}{2}}) \\ \mathbf{T}_i^p &= \Psi_{\mathbf{n}_i,\mathbf{r}_i}(\mathbf{J}^{\mathrm{p}}) \end{aligned} \tag{7.30}$$

Thanks to these operators, the solution of the anisotropic problem at the second iteration is then:

$$\begin{aligned} \mathbf{X}^2 &= \mathbf{X}^1 - \mathbf{H}^{-1} \cdot \left(\sum_{i=1}^{N} \mathbf{D}_i^p \right) \\ \mathbf{V}^2 &= \mathbf{S}_{eeg} \cdot \mathbf{X}^2 \end{aligned} \tag{7.31}$$

where the RHS term $\mathbf{D}_i^p$ depends on $\mathbf{X}^1$ and $\mathbf{J}^{\mathrm{p}}$, and is the contribution of the i-th virtual dipole located at $\mathbf{r}_i$, oriented $\mathbf{n}_i$ with strength $\|\mathbf{m}_i\| = \varepsilon_i(\Delta_i \cdot \mathbf{X}^1 + \mathbf{T}_i^p)$.

7.3.2.2 Numerical validation:

In order to validate the proposed method we compared the results of the standard isotropic BEM (1^{st} iteration), the anisotropic BEM at 2^{nd} iteration, with the reference solution a high resolution FEM, on a 3-layer model displayed in Fig.(7.5) and Fig.(7.6) and defined as:

Model: 3-layer spherical model modeling the brain, the skull, and the scalp, with respective radii 0.87, 0.92, 1., and isotropic conductivity 1., 0.03, 1..

Fiber: We added a fiber oriented vertically (z-axis), with a cylindrical shape with radius $r_f = 0.04$, and a conductivity ten times higher than the brain one *i.e.* $\sigma_f = 10$ (along its direction $\mathbf{e}_z$). the fiber length was $L = 1$, starting at the Cartesian coordinates $[0.2, 0, -0.5]$ and ending at $[0.2, 0, 0.5]$.

Dipoles: We ran the computations for 24 dipoles oriented either parallel to the fiber $[0, 0, 1]$ (green arrows) or $[1, 0, 1]$ (orange arrows) with unit momentum. They were located on the z-axis at z-coordinates in $\{0.1, 0.2, 0.3, 0.4, 0.5, 0.6, 0.68, 0.72, 0.765, 0.79, 0.8075, 0.8415\}$.

Reference solution: A high resolution tetrahedral FEM was used with 590 747 vertices, which could take the anisotropy into account easily. We ran the forward computations for each dipole, and obtained the results for 642 nodes on the scalp.

BEM meshes had 642-vertices per layer.

The comparisons in term of RDM, and MAG errors (defined in sec.2.5.2.4 p.(2.48)) are displayed Fig.(7.7). The first row displays the results for the dipoles with orientation $[0, 0, 1]$ (RDM left and MAG at right), and the second row corresponds to $[1, 0, 1]$. The x-axis always represents the z-coordinate of the dipole.

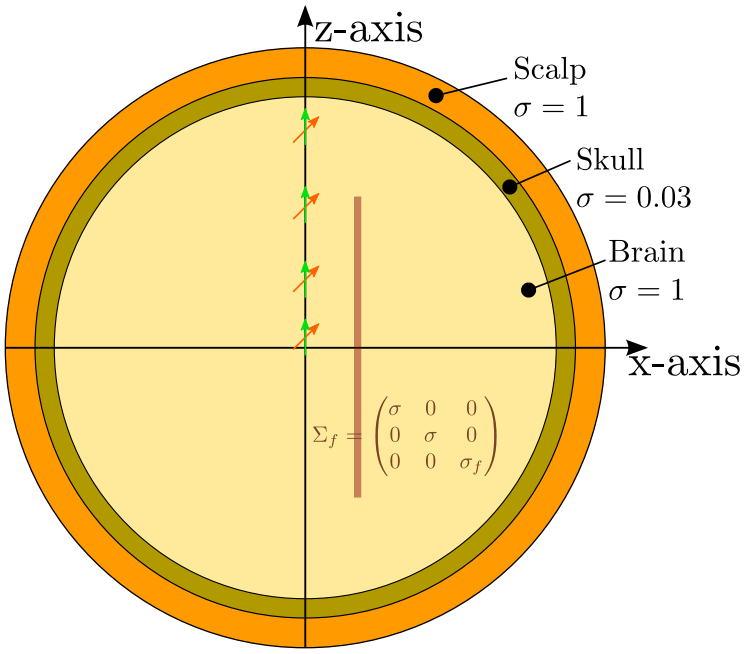

Figure 7.5 – *Validation model, 3-layer spherical model plus a fiber.*

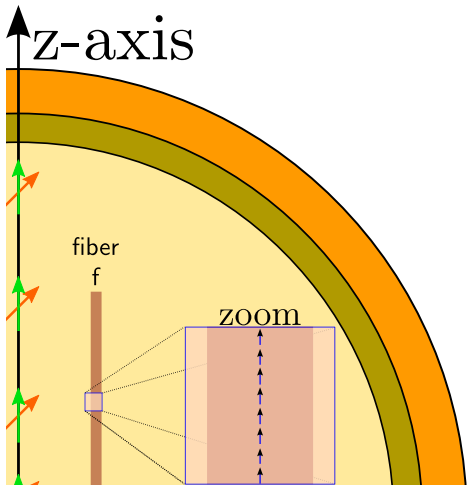

Figure 7.6 – *Zoom on the validation model and sketch of the virtual dipoles.*

In these plots we have computed the anisotropic results, discretizing the tensor in $N = 100$ points, *i.e.* the fiber was discretized into N points, and it acted like N virtual dipoles. Several comments can be made on these figures.

a. When looking at the first RDM curves (for $[0, 0, 1]$), the curves are very close to each other. For all other plots the green curve (anisotropic BEM) is the best solution (closer to 0 for the RDM and 1 for the MAG).

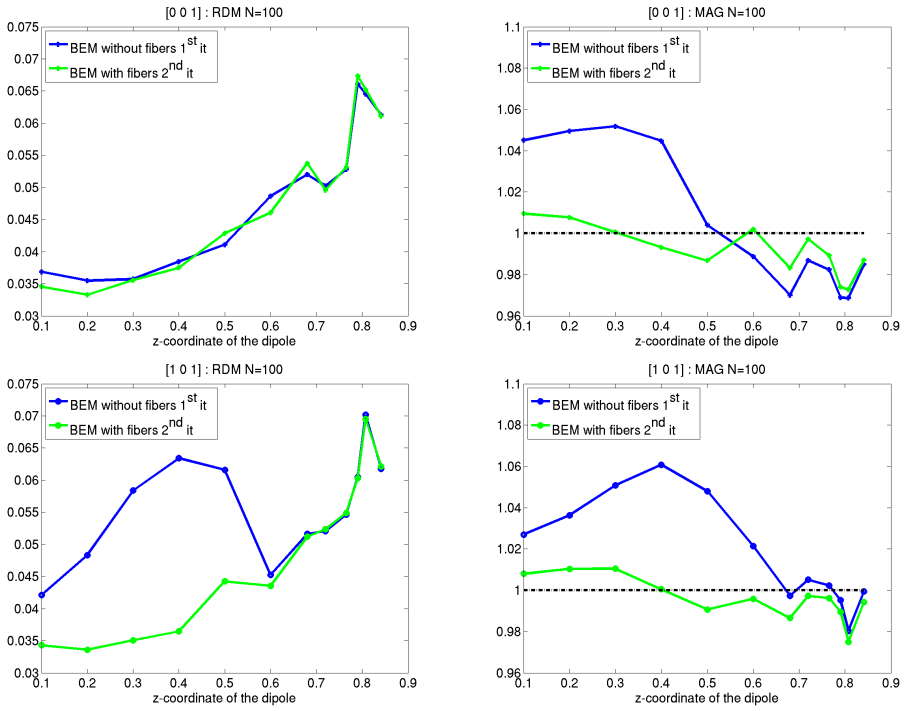

Figure 7.7 – *BEM results with and without fibers.*

b. For the first RDM results (for $[0, 0, 1]$) we can add that the virtual dipoles are oriented in the same direction as the real dipoles, which explains the small changes in the results (See Fig.(7.6)).

c. For any plot, the curves are very close to each other when the z-coordinate of the dipole is > 0.6, this seems coherent since the dipole is then far from the fiber (which ends at 0.5), and thus the fiber no longer has much influence on the results.

d. Finally one can comment saying that the FEM may not be that close to the true solution, because of its difficulty to handle dipolar sources as discussed in sec.2.5.1. Thus the errors might be biased by this aspect.

Let us investigate the last comment:

Dropping the fiber but otherwise keeping the same model, we propose to compare the BEM and the FEM results to the analytical ones to first check whether or not the high resolution FEM can be a reference solution. These results are shown Fig.(7.8). One can see the good RDM results of the FEM despite its staggering behavior already commented upon in the previous chapter. The BEM's MAG is slightly better than the FEM but both of them have a good behavior. This confirms the choice for the FEM to be taken as reference solution for the anisotropic problem (since we do not have analytical solution).

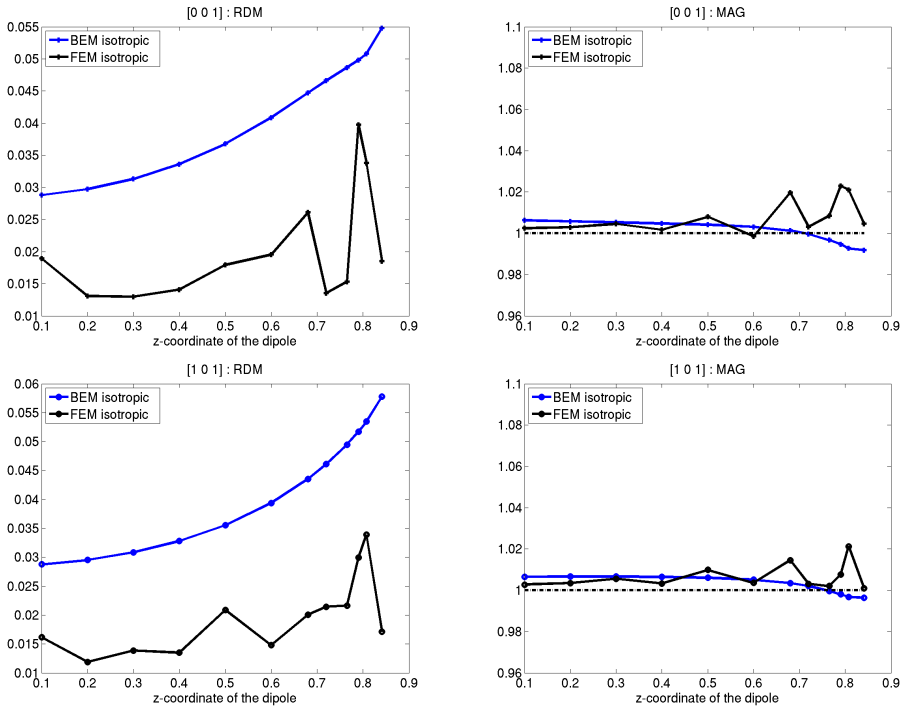

Figure 7.8 – *Isotropic BEM and FEM results compared with the analytical solution.*

It is interesting to plot the previous results shown in Fig.(7.7) with now overlaid the expected error between BEM and FEM, which is the comparison between the BEM and the FEM in the isotropic case. One can see Fig.(7.9) that the results using the anisotropic BEM are quite close to the expected error, it then means that the error on the model (the anisotropy model with discretization point) is well minimized after only one iteration (at least for this configuration of dipoles and fibers).

What about the influence of parameter N ? Actually we obtained similar results as soon as $N > 8$, which is a poor discretization of the fiber. This discretization parameter should depend on the problem geometry and overall on the distance of the fibers to the dipole, since the electromagnetic field becomes sharp (high variations) close to the dipole. Let us have a look at the RDM for the dipoles with direction $[1, 0, 1]$ for $N \in \{2, 4, 6, 8\}$. This is shown in Fig.(7.10). One can see that before $N = 6$ results are very bad, this is mostly due to the dipole which is too close to a discretization point and has a big weight. In fact the influence of the dipole on this point is the same when $N > 6$, but its weight is proportional to $\frac{1}{N}$ which reduces its influence.

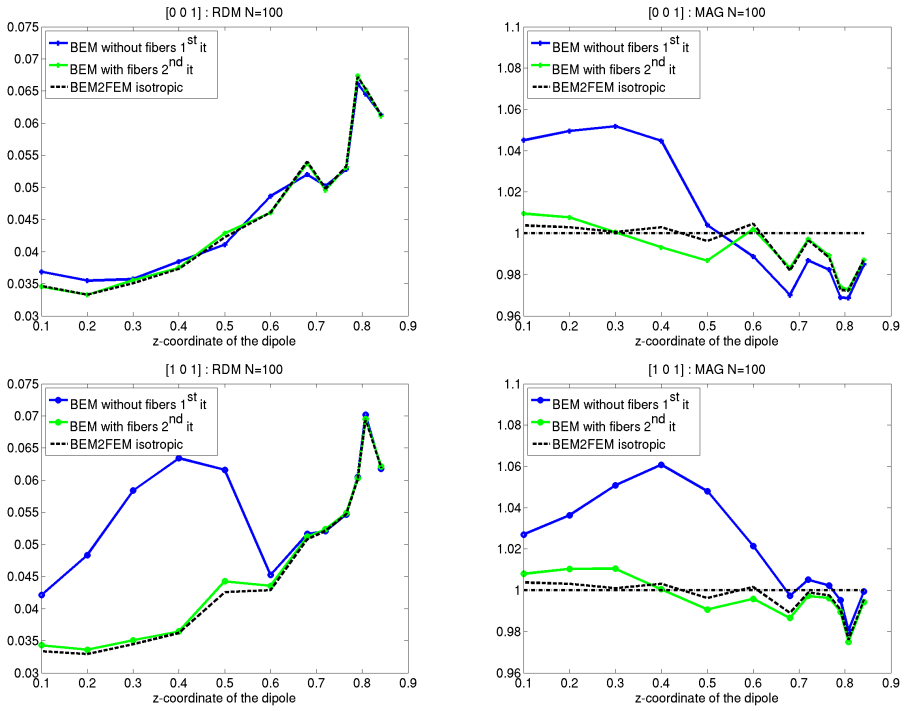

Figure 7.9 – *BEM results with and without fibers.*

What about the third iteration ? At the third iteration, the current to be computed is now indefinite at all fibers locations since there is a dipole on it. Indeed, $\nabla V^2(\mathbf{r}_i) \cdot \mathbf{n}_i$ needs to be computed, and this is at the exact location of the i-th virtual dipole. The analytical formula $\psi_{\mathbf{n}_i,\mathbf{r}_i}(\mathbf{J}_i)$ in Eq.(7.29), is indefinite at this location. It means that discretizing the conductivity tensor may not be the correct way to deal completely with our local anisotropy, even if the results at second iteration seem already promising.
This has led us to consider the second method.

7.3.3 Second method: Representing the conductivity tensor within the Poisson equation

Let us re-write the Poisson Eq.(7.12) which uses the conductivity tensor described in Eq.(7.11):

$$\sigma \Delta V \quad = \quad \nabla \cdot \mathbf{J}_p - (\sigma_f - \sigma) \nabla \cdot (\mathbf{n}_f(\mathbf{r}) \chi_f(\mathbf{r}) \nabla V \cdot \mathbf{n}_f(\mathbf{r})) \tag{7.32}$$

We now split the characteristic function χ_f into a sum of smaller characteristic functions χ_i^d (whose supports are centered at $\mathbf{r}_i = \theta_f\left(\frac{L}{N}(i - \frac{1}{2})\right)$):

$$\chi_f = \sum_{i=1}^{N} \chi_i^d \ , \tag{7.33}$$

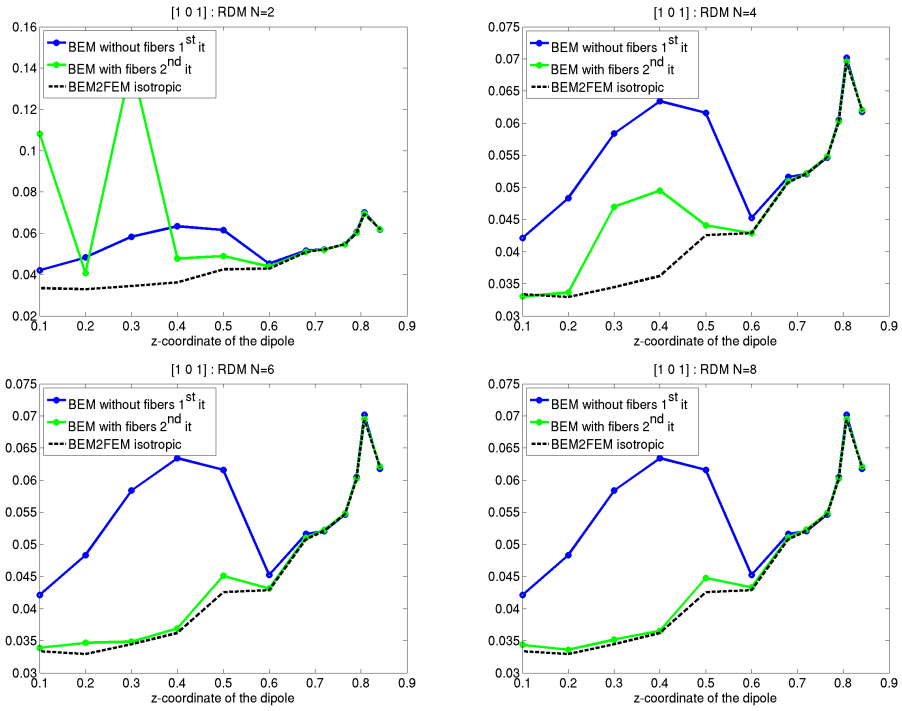

Figure 7.10 – *BEM RDM for dipoles oriented [1 0 1], with and without fibers varying N.*

actually each support of χ_i^d represents a small slice of cylinder of length d (see Fig.(7.11)).
We now look for the virtual dipole $\mathbf{J}_i = \mathbf{m}_i\delta_i = m_i\mathbf{n}_i\delta_i$ located in the center of the support of χ_i^d, that best approximates the conduction in this slice of cylinder *i.e.* $\forall i$ find $\mathbf{m}_i = m_i\mathbf{n}_i$ such that:

$$\forall \phi_i \in \mathcal{D}(\mathbb{R}^3), \left\langle (\sigma_f - \sigma)\nabla \cdot (\mathbf{n}_i\chi_i^d \nabla V \cdot \mathbf{n}_i), \phi_i \right\rangle \simeq \langle \nabla \cdot \mathbf{m}_i\delta_i, \phi_i \rangle = -m_i\mathbf{n}_i \cdot \nabla\phi_i(\mathbf{r}_i) \tag{7.34}$$

Then Eq.(7.32) can be approximated by:

$$\sigma\Delta V \quad = \quad \nabla \cdot \left(\mathbf{J}^{\mathrm{p}} - \sum_i^N \mathbf{m}_i\delta_i \right) \tag{7.35}$$

This equation looks the same as Eq.(7.12), and the main difference is the way of computing $m_i = \|\mathbf{m}_i\|$.
One can write the solution of this equation using linearity as:

$$V = V_p - \sum_{j=1}^{N} m_j V_j \tag{7.36}$$

where V_j, $j \in \{1..N\}$ solves: $\sigma\Delta V_j = \nabla \cdot \mathbf{J}_j$, and similarly V_p solves $\sigma\Delta V_p = \nabla \cdot \mathbf{J}^{\mathrm{p}}$.
Actually one simply needs to find these coefficients to get the (approximate) solution

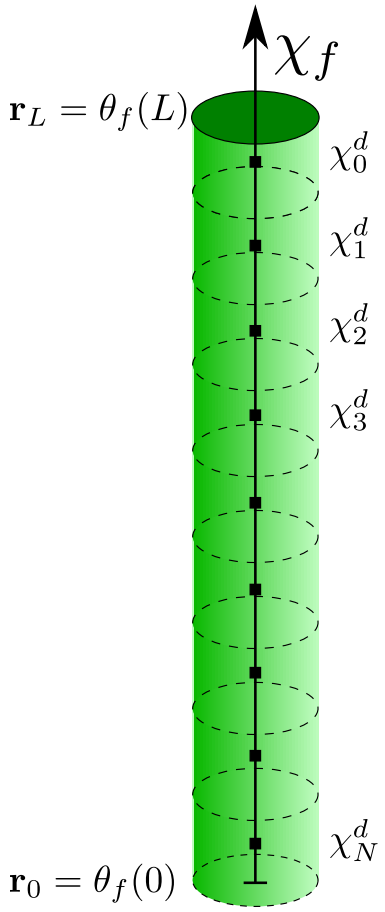

Figure 7.11 – *Example of a cylindrical fiber subdivided into smaller cylinders. A virtual dipole is located at each black dot.*

of an anisotropic problem.
Re-writing Eq.(7.34) we use the divergence theorem, and the nullity of the test functions on the border to get:

$$\begin{aligned} & \forall \phi_i \in \mathcal{D}(\mathbb{R}^3), \\ \left\langle (\sigma_f - \sigma)\nabla \cdot (\mathbf{n}_i \chi_i^d \nabla V \cdot \mathbf{n}_i), \phi_i \right\rangle &= -(\sigma_f - \sigma) \left\langle \mathbf{n}_i \chi_i^d \nabla V \cdot \mathbf{n}_i, \nabla \phi_i \right\rangle \\ &= -(\sigma_f - \sigma) \left(\left\langle \chi_i^d \nabla V_p \cdot \mathbf{n}_i \mathbf{n}_i, \nabla \phi_i \right\rangle - \sum_{j=1}^{N} m_j \left\langle \chi_i^d \nabla V_j \cdot \mathbf{n}_i \mathbf{n}_i, \nabla \phi_i \right\rangle \right) \end{aligned}$$

Considering $\nabla\phi_i$ constant in the support of χ_i^d, which can be reorganized as: $\forall i = 1 \dots N$,

$$\begin{aligned} m_i &= \left(A_i - \sum_{j=1}^{N} m_j B_i^j \right) \\ (1 + B_i^i) m_i &= \left(A_i - \sum_{j \neq i} m_j B_i^j \right) \end{aligned} \tag{7.37}$$

Eq.(7.37) is a linear system whose unknowns are the coefficients m_i, which gives the handling of the anisotropy.

$$\begin{pmatrix} 1 + B_1^1 & B_1^2 & \dots & B_1^N \\ B_2^1 & 1 + B_2^2 & \dots & B_2^N \\ \dots & \dots & \dots & \dots \\ B_N^1 & B_N^2 & \dots & 1 + B_N^N \end{pmatrix} \begin{pmatrix} m_1 \\ m_2 \\ \dots \\ m_N \end{pmatrix} = \begin{pmatrix} A_1 \\ A_2 \\ \vdots \\ A_N \end{pmatrix} \tag{7.38}$$

Let us specify the values of A_i, B_i^j, and B_i^i. These require the evaluation of $\nabla V_j \cdot \mathbf{n}_i$ for $\forall i$, and $\forall j \in \{1 \dots N, p\}$, which as explained previously are composed of an analytical part due to the dipole infinite medium component and the correction due to the boundedness of the domain. For the sequel, we will assume the second part to be smooth *i.e.* constant in χ_i^d, and concentrate on the analytical part which we will consider constant if we are far enough from the dipoles and not constant close to a dipole.

- Finding A_i: We can consider $\mathbf{r}_i$ is quite far from $\mathbf{r}_p$, and so consider $\nabla V_p \cdot \mathbf{n}_i$ as constant in χ_i^d, then:

$$\begin{aligned} A_i &= (\sigma_f - \sigma) \nabla V_p(\mathbf{r}_i) \cdot \mathbf{n}_i \int_{\mathbb{R}^3} \chi_i^d d\mathbf{r} \\ &= (\sigma_f - \sigma) \partial_{\mathbf{n}_i} V_p(\mathbf{r}_i) \int_0^{2\pi} \int_0^R \int_{-\frac{d}{2}}^{\frac{d}{2}} \rho d\rho d\theta dz \\ &= (\sigma_f - \sigma) \pi R^2 d \; \partial_{\mathbf{n}_i} V_p(\mathbf{r}_i) \end{aligned} \tag{7.39}$$

- For the B_i^j terms when $j \neq i$, $\nabla\phi_i$ is still considered constant:

$$\left\langle \chi_i^d \nabla V_j \cdot \mathbf{n}_i \mathbf{n}_i, \nabla \phi_i \right\rangle \tag{7.40}$$

therefore we write:

$$\begin{aligned} B_i^j &= (\sigma_f - \sigma) \int_{\mathbb{R}^3} \chi_i^d \nabla V_j(\mathbf{r}) \cdot \mathbf{n}_i d\mathbf{r} \\ &= C_i^j + (\sigma_f - \sigma) \int_{\mathbb{R}^3} \chi_i^d \Psi_{\mathbf{n}_i, \mathbf{r}}(\mathbf{J}_j) d\mathbf{r} \end{aligned} \tag{7.41}$$

where C_i^j expresses the correction term due to the boundedness of the domain. And as the dipole J_j is not in the support of χ_i^d, the value of $\partial_{\mathbf{n}_i} V_j(\mathbf{r})$ is obtained by the formula in Eq.(7.29) by $\Psi_{\mathbf{n}_i,\mathbf{r}}(\mathbf{J}_j)$. In other words, this integral can be computed easily either considering an analytical expression as we will do in the experiments or considering numerical integration, or if $\mathbf{r}_j$ is considered far enough from the support of χ_i^d, the function $\Psi_{\mathbf{n}_i,\mathbf{r}}(\mathbf{J}_j)$ can be considered as constant and the integral immediately computed.

- For the B_i^i terms, $\nabla\phi_i$ is still considered as constant:

$$\left\langle \chi_i^d \nabla V_i \cdot \mathbf{n}_i \mathbf{n}_i, \nabla\phi_i \right\rangle \tag{7.42}$$

This integral should be handled with care because of the singularity at $\mathbf{r}_i$. Let us now use polar coordinates (with the z-axis oriented toward $\mathbf{n}_i$) to write V_i. At a distance $\mathbf{r} > \varepsilon > 0$ from the source at $\mathbf{r}_i$, the potential is written as in Eq.7.25:

$$V_i(\mathbf{r}) = \frac{1}{4\pi\sigma} \frac{z}{\sqrt{\rho^2 + z^2}^3}$$

$$\begin{aligned}
B_i^i &= C_i^i + (\sigma_f - \sigma) \int_{S(\chi_i^d)} \frac{\partial V_i(\mathbf{r})}{\partial z} d\mathbf{r} \qquad (7.43)\\
&= C_i^i + (\sigma_f - \sigma) \left(\lim_{\varepsilon\to 0} \int_\varepsilon^R \int_0^{2\pi} \int_{-\frac{d}{2}}^{\frac{d}{2}} \frac{\partial V_i(\mathbf{r})}{\partial z} \rho d\rho d\theta dz \right)\\
&= C_i^i + (\sigma_f - \sigma) \left(\lim_{\varepsilon\to 0} 4\pi \int_\varepsilon^R \int_0^{\frac{d}{2}} \frac{\partial V_i(\mathbf{r})}{\partial z} \rho d\rho dz \right)\\
&= C_i^i + (\sigma_f - \sigma) \left(\lim_{\varepsilon\to 0} 4\pi \int_\varepsilon^R [V_i(\mathbf{r})]_0^{\frac{d}{2}} \rho d\rho \right)\\
&= C_i^i + \frac{\sigma_f - \sigma}{\sigma} \left(\lim_{\varepsilon\to 0} \int_\varepsilon^R \frac{d/2 \cdot \rho}{\sqrt{\rho^2 + d^2/4}^3} d\rho \right)\\
&= C_i^i + \frac{\sigma_f - \sigma}{\sigma} \left(\lim_{\varepsilon\to 0} \left[\frac{-d/2}{\sqrt{\rho^2 + d^2/4}} \right]_\varepsilon^R \right)\\
&= C_i^i + \frac{\sigma_f - \sigma}{\sigma} \left(\lim_{\varepsilon\to 0} \left(-\frac{d/2}{\sqrt{R^2 + d^2/4}} + \frac{d/2}{\sqrt{\varepsilon^2 + d^2/4}} \right) \right)\\
&= C_i^i + \frac{\sigma_f - \sigma}{\sigma} \left(1 - \frac{d}{\sqrt{4R^2 + d^2}} \right) \qquad (7.44)
\end{aligned}$$

where C_i^i expresses the correction term due to the boundedness of the domain.

7.3.3.1 Discrete problem:

Here for sake of simplicity, we consider the same shape and conductivity for all χ_i^d. Writing $\varepsilon = 4\pi R^2 d(\sigma_f - \sigma)$, and using the discrete operators defined in Eq.(7.30)

which we recall here, also introducing a new one:

$$\begin{aligned}\Delta_i &= \frac{1}{\varepsilon}(\mathbf{S}_{\mathbf{r}_i+\frac{\varepsilon\mathbf{n}_i}{2}} - \mathbf{S}_{\mathbf{r}_i-\frac{\varepsilon\mathbf{n}_i}{2}}) \\ \mathbf{T}_i^j &= \Psi_{\mathbf{n}_i,\mathbf{r}_i}(\mathbf{J}_j) \\ \mathbf{R}_i^j &= \int_{\chi_i^d} \Psi_{\mathbf{n}_i,\mathbf{r}}(\mathbf{J}_j)d\mathbf{r}\end{aligned}$$

so that the coefficients of system Eq.(7.38) are:

$A_i = \varepsilon_i(T_i^p + \Delta_i X^p)$

$B_i^j = \varepsilon_i\Delta_i X^j + (\sigma_f - \sigma)\mathbf{R}_i^j$ for $i \neq j$

$B_i^i = \varepsilon_i\Delta_i X^i + (\sigma_f - \sigma)(\frac{1}{\sigma} + \mathbf{R}_i^i)$

The algorithm is then as follows:

1. Assembling of $\mathbf{H}$, $\mathbf{D}$ and $\forall i \in \{1 \dots N\}$ $\mathbf{D}_i$, Δ_i and also $\forall j \in \{1 \dots N\}$, $\mathbf{R}_i^j$ and $\mathbf{T}_i^j$
2. Computation of $\mathbf{H}^{-1}$
3. Obtaining the solutions $\mathbf{X}_j$ $\forall j \in \{1 \dots N\} \cup \{p\}$ such that: $\mathbf{X}_j = \mathbf{H}^{-1}\mathbf{D}_j$
4. Resolution of the system $\mathbf{A} \cdot \mathbf{M} = \mathbf{E}$
5. Full solution: $\mathbf{X} = \mathbf{X}_p + \mathbf{M}\begin{bmatrix}\mathbf{X}_1 & \mathbf{X}_2 & \dots \mathbf{X}_N\end{bmatrix}$

7.3.3.2 Numerical validation:

We have now expressed the relation between the fiber coefficients relatively to the dipole, to the fibers themselves, and to the head model. The construction of such a system, only requires solutions in isotropic medium for the dipole, as well as for the virtual dipoles newly introduced, and internal operators. Several assumptions were made, notably:

1. the electrical conduction in the fiber can be modeled by a finite set of virtual dipoles along its axis.
2. the correction term denoted C_i^j was supposed constant in each χ_i^d.
3. the term $\nabla V_p \cdot \mathbf{n}_i$ was also supposed constant in each χ_i^d.

Knowing these assumptions the full system solution incorporates the interactions between the fibers, the model and the primary source. In contrast with the first method only interactions of the dipole, and the model onto the fibers were taken into account.
One can see Fig.(7.12) the result of this method denoted 'BEM with fibers' for the same experiment as sec.(7.3.2.2), on which we have overlaid the previous results.

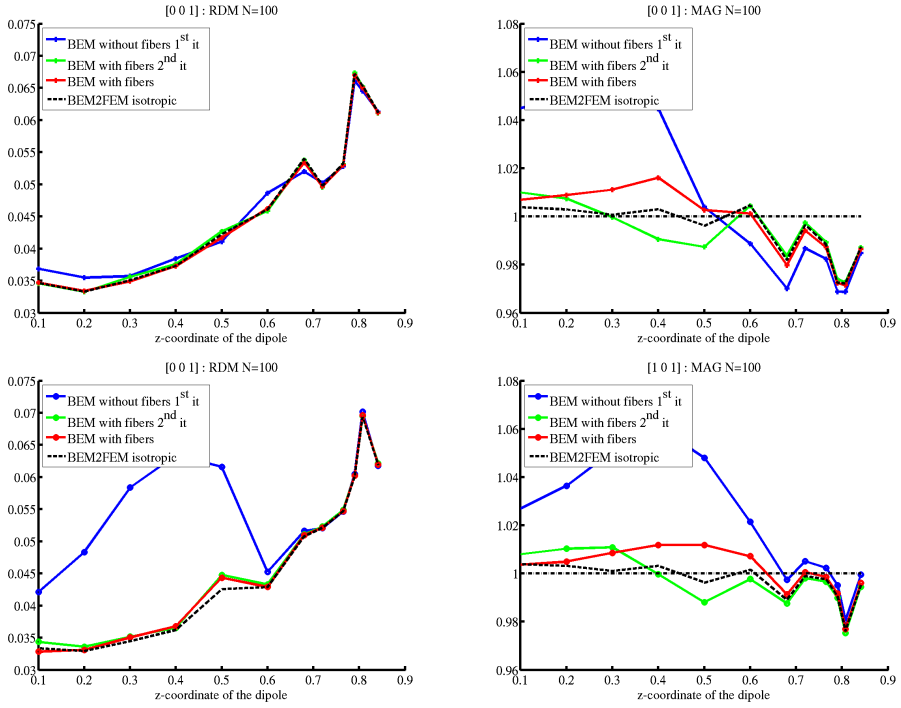

Figure 7.12 – *BEM results with and without fibers. Results of the red curves, as well as the green one, are for N=100.*

Note that the number of volumes χ^d was $N = 100$.
One can notice a slight improvement gained using the new method. But still new experiments should be done to say whether the second method is better than the first one. In Fig.(7.13), we have plotted the same results but this time running the experiment with $N = 6$ *i.e* the whole fiber discretized in only 6 cylinders. The results are still very good, much better than the ones of the first method with $N = 6$ in Fig.(7.10). This suggest that a coarser sampling would have been sufficient. The aspect of sampling (or discretization or decomposition) will be discussed in conclusion.

7.3.4 Application on a realistic model containing inhomogeneities in the skull

In this section, we will illustrate how one can easily handle inhomogeneities in BEM. In order to validate this method, we propose to work on the same realistic experiment as in the previous chapter for illustrating the BEM-FEM coupled method (sec.(6.4)). The geometry is a 4-layer realistic model, modeling the brain, the CSF, the skull and the scalp on which are placed the sensors. An artificial hole was performed in the skull with a diameter of 1cm, and the same conductivity as the scalp was assigned to the hole *i.e.* $\sigma_{hole} = 1$. This hole was of cylindrical shape along the

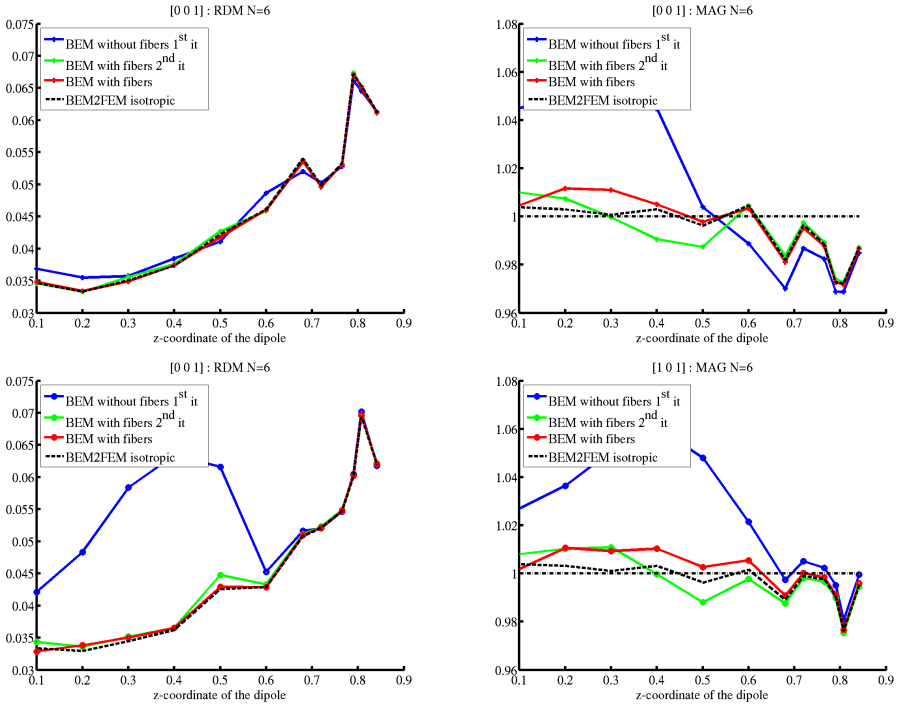

Figure 7.13 – *BEM results with and without fibers. Results of the red curves are for a fiber modeled as 6 smaller cylinders.*

$z-$axis.

Sequentially, the solutions are compared for 15 dipoles approaching the hole (see Fig.(7.14)). Four methods will be compared here: the tetrahedral FEM, the isotropic BEM (thus neglecting the hole), the BEM-FEM coupled method, and the method described in sec.(7.3.2) (the first of the two methods presented earlier). In the last method, we consider discretizing the conductivity tensor of the skull which we denote Σ with discretized points lying in the hole. Let us denote by χ_h the characteristic function of the hole which is a truncated cylinder at boundary due to the inner skull surface and the outer skull surface such as one can see Fig.(7.15). The cylinder has a radius of $R = 4.905$, is oriented toward the $z-$axis, and has a center located at point $[0, 0, 75.4]$[1]. As the radius of the hole is not so small (compared to the typical sizes) as was the radius of the fibers of the white matter studied before, we not only discretized along the $z-$direction of the hole but also in the plane section of the hole which defines a disc. We thus discretized the characteristic function of the hole, denoted χ_h, with equidistant points generated out of a Cartesian grid with at most n points in each direction, such that these points are in the cylinder and in the skull region (see Fig.(7.16) where $n = 10$ *i.e* at most 10 points in each direction.). Writing $\mathbf{r}_i$ the $N_h \simeq N = n^3$ points within

[1] the units on this realistic geometry are inherited from the MRI which was 256^3, that is why there are high value for coordinates.

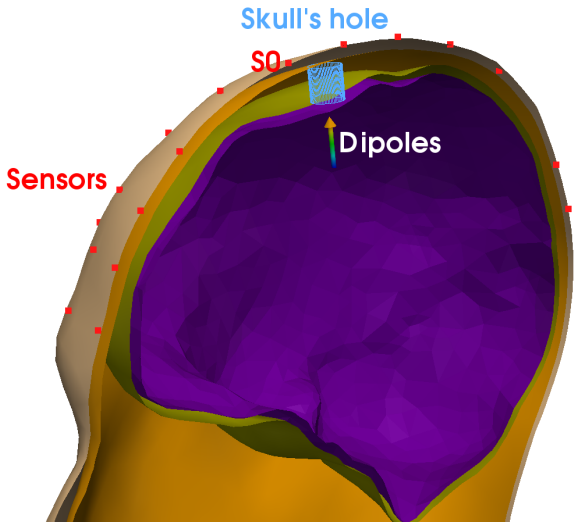

Figure 7.14 – *Realistic 4-layer model where the big arrow illustrates the set of dipoles oriented toward the z-axis, and approaching the skull hole.*

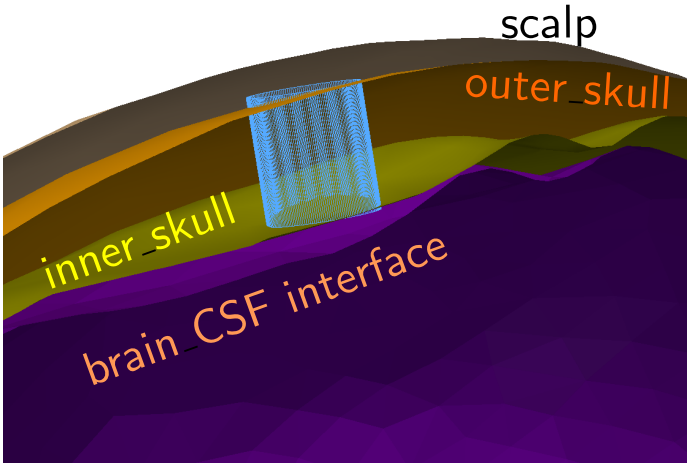

Figure 7.15 – *Zoom on the hole which can be modeled as a cylinder intersected by the inner and outer skull surfaces.*

the hole, we discretize χ_h into N_h weighted points:

$$\Delta_N(\chi_h) = \frac{V_h}{N_h} \sum_{i=1}^{N_h} \delta\left(\mathbf{r} - \mathbf{r}_i\right) \ , \tag{7.45}$$

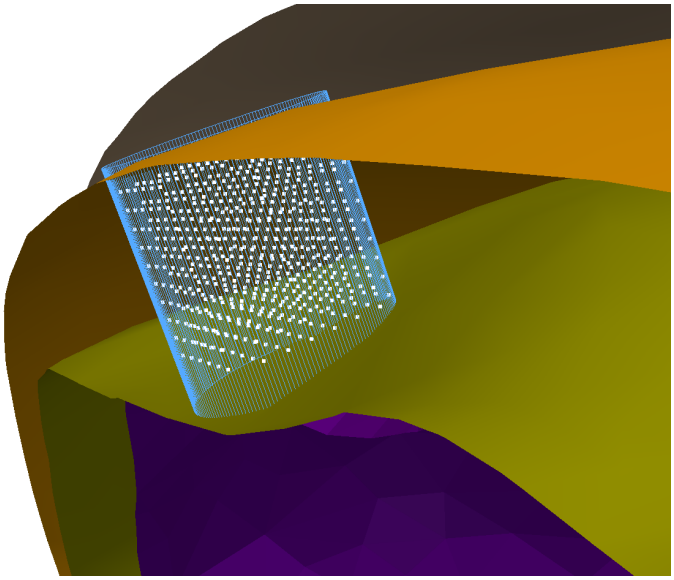

Figure 7.16 – *Zoom on the hole with the discretization points (white dots) placed on a Cartesian grid, with $n = 10$. These points will be the locations of the virtual dipoles.*

where V_h represents the volume of the hole, and N_h is the actual number of points within the hole. This expression is similar to Eq.(7.13), where we have an uncertainty regarding the volume of χ_h. We know that V_h is slightly bigger than the volume of the cylinder included in χ_d. Manually we have estimated the length of this cylinder to be $L \simeq 7.5$, which is the maximum length before the cylinder intersects the other surfaces (inner and outer skull), so that the volume V_h should be higher than $V(L = 7.5) = \pi R^2 L \simeq 567$.
Denoting the inhomogeneous conductivity tensor of the skull Σ, which is equivalent to a scalar conductivity $\sigma = 0.03$ out of the hole and $\sigma_h = 1$ in the hole, the Poisson equation in Ω_3, the skull, writes:

$$\begin{aligned} \nabla \cdot (\Sigma \nabla V) &= 0 \quad \text{in } \Omega_3 \\ \sigma \Delta V + \nabla \cdot (\chi_h(\mathbf{r})(\sigma_h - \sigma)\mathcal{I} \nabla V) &= 0 \quad \text{in } \Omega_3 \end{aligned} \tag{7.46}$$

and we write the homogeneous conductivity $(\sigma_h - \sigma)\mathcal{I}$ as the sum of anisotropic conductivities Σ_x,Σ_y, and Σ_z such that $(\sigma_h - \sigma)\mathcal{I} = \Sigma_x + \Sigma_y + \Sigma_z$:

$$\Sigma_x = (\sigma_h - \sigma)\mathbf{e}_x\mathbf{e}_x^T \quad , \quad \Sigma_y = (\sigma_h - \sigma)\mathbf{e}_y\mathbf{e}_y^T \quad , \quad \Sigma_z = (\sigma_h - \sigma)\mathbf{e}_z\mathbf{e}_z^T \tag{7.47}$$

such that Eq.(7.46) writes also plugging the discrete version of χ_h:

$$\sigma \Delta V = -\nabla \cdot \left(\sum_{i=1}^{N} (\mathbf{J}_i^x + \mathbf{J}_i^y + \mathbf{J}_i^z) \right) \text{ in } \Omega_3 \ , \tag{7.48}$$

with $\mathbf{J}_i^x = (\sigma_h - \sigma)\frac{V_h}{N}\mathbf{e}_x \nabla V(\mathbf{r}_i) \cdot \mathbf{e}_x \delta(\mathbf{r} - \mathbf{r}_i)$, and similarly for $\mathbf{J}_i^y$ and $\mathbf{J}_i^z$. Thus at each discretized point $\mathbf{r}_i$ we place 3 virtual dipoles oriented toward $\mathbf{e}_x$, $\mathbf{e}_y$, $\mathbf{e}_z$ respectively.
Similarly as in sec.(7.3.2.1), we use internal operators as well as analytical formulas to obtain the value of $\nabla V(\mathbf{r}_i)$, $\forall i$. There remains to find the value of the volume V_h and choose the number of discretization points n in each direction. Instead we will show the results and comment them for several values of n and L (and thus different volumes approximating V_h).

Results: In this paragraph we consider once more the results from the previous chapter (see sec.(6.4) p.152). We compare the plots of the potential at sensor S0 (the closest sensor to the hole) given by the FEM, the BEM coupled with the FEM (denoted BEMtFEM) and the inhomogeneous BEM (still denoted BEM fibers). We also compare the BEMtFEM taking the FEM as reference even if we commented already about its staggering behavior due to the coarse handling of dipolar sources. These plots are shown for different values of n, namely $n \in \{5, 10, 15\}$ (*i.e.* at most $N \in \{125, 1000, 3375\}$ discretized points and thus 3 times more virtual dipoles (one per direction)), and L the estimated length of the hole, namely $L \in \{7.,\ 7.5,\ 8.,\ 8.5\}$.

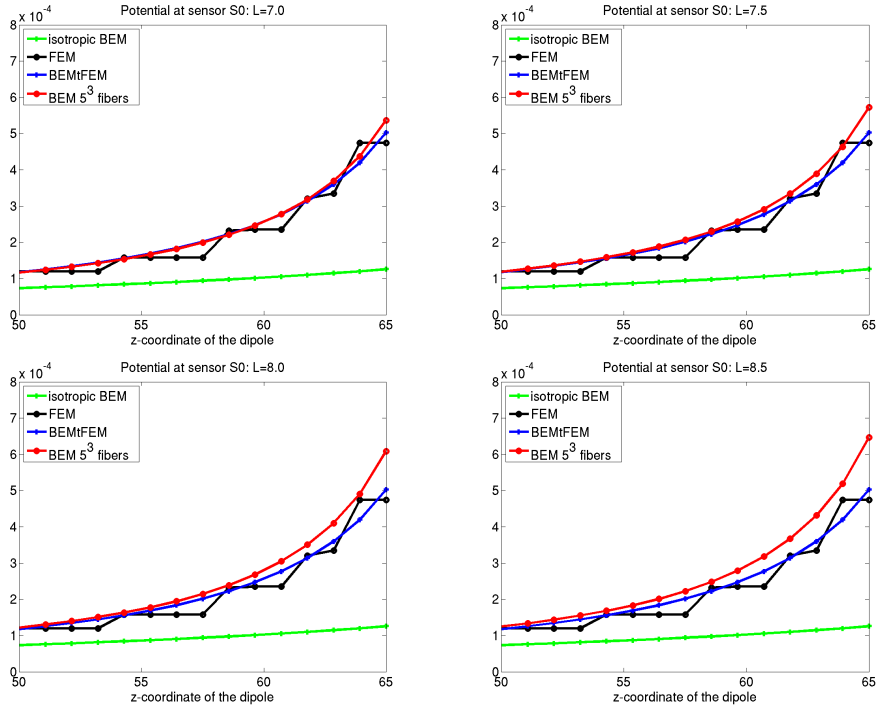

Figure 7.17 – *Potential at sensor S0 (close to the hole) given by the different methods. L, the estimated length of the hole, varies from 7. to 8.5 and so the results of the inhomogeneous BEM with fibers varies. $n = 5$.*

In Fig.(7.17), one can see plotted (similarly as in chapter 6 Fig.(6.15)) the potential at sensor S0, where we added the inhomogeneous BEM (still called BEM with fibers) with $n = 5$ *i.e.* $N_h \simeq 125$ points in total at most. One can see that the results are very similar to the ones of the BEMtFEM which we assume to be the closest to reality. Actually, one can compare the RDM and MAG values of this method, and the BEMtFEM method with the FEM as the reference. This is plotted in Fig.(7.18). One can see that the case with $L = 7.$ is the closest to the results of the BEMtFEM method (MAG curves similar), but is even more accurate than the BEMtFEM (*i.e.* it has a RDM curve closer to 0).

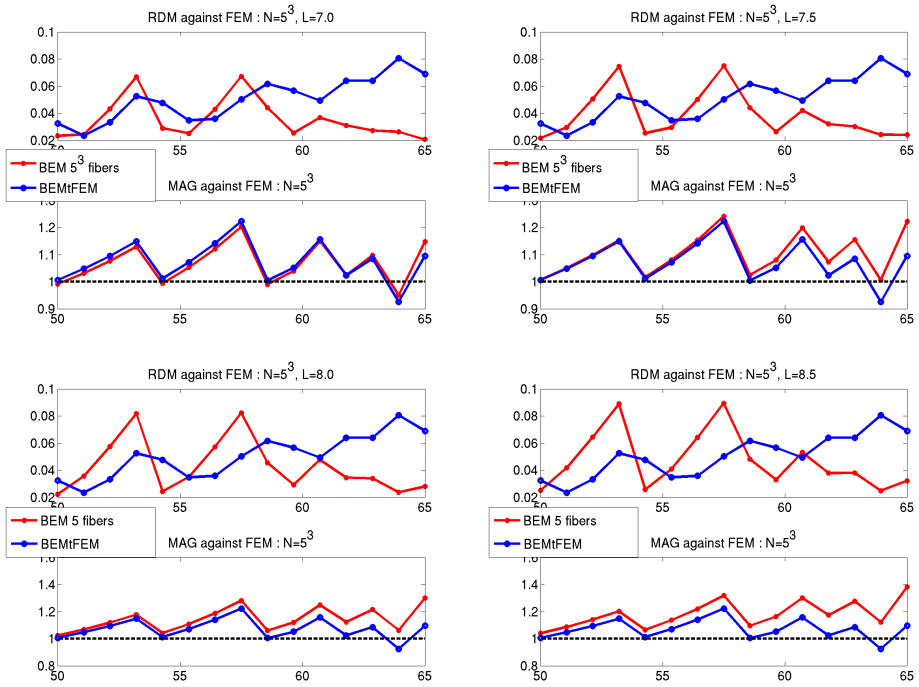

Figure 7.18 – *RDM and MAG values of the BEM with fibers and BEMtFEM compared to the FEM (reference). L varies from* 7. *to* 8.5. $n = 5$.

Finally, we can see the convergence of the proposed method showing the same plots for $L = 7.$, and n varying from 5 to 15. This is shown Fig.(7.19) and Fig.(7.20) where one can see the proper coherence of these results.

Concerning the computation time, the time needed to solve an anisotropic problem instead of an isotropic problem increased by 60 seconds for $n = 5$, by 12 minutes for $n = 10$ and by 48 minutes for $n = 15$. We recall that the total time for an isotropic solution with this 4-layer problem and 15 dipoles was about 2 hours.

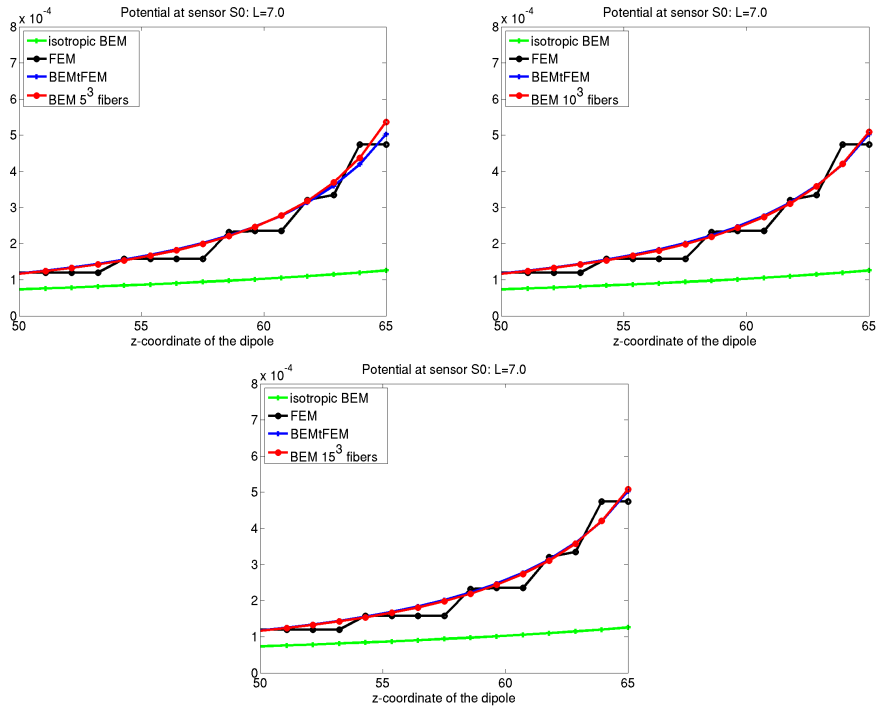

Figure 7.19 – *Potential at sensor S0 (close to the hole) given by the different methods. n varies from* 5,10 *and* 15.

7.4 Conclusion

In this chapter we have introduced new methods for handling local changes in the conductivity profiles within a BEM framework. Methods were given and commented. Still more analysis should be done in order to get clues concerning the discretization of the inhomogeneous part of the conductivity. The first method developed appears efficient and cheap. Tools should be developed in the future to allow the easy use of such a method by clinicians, such as:

1. build of an estimator of the smoothness of the value $\partial_{\mathbf{n}} V_i(\mathbf{r})$ within the domain to know where to have finer discretization (estimator of the smoothness of Eq.(7.26)).

2. easy computation of 3D volume (as for the case of the skull hole for example).

3. generation of discretized points in this volume following the density defined by the estimator.

Furthermore, let us add in the case of inhomogeneities such as the one we presented, that even if we put the theoretical values for the hole volume or its conductivity, the real (electrophysiological) values are unknown. For example, we can imagine that some of the CSF is actually spread into the hole, and thus increases its mean

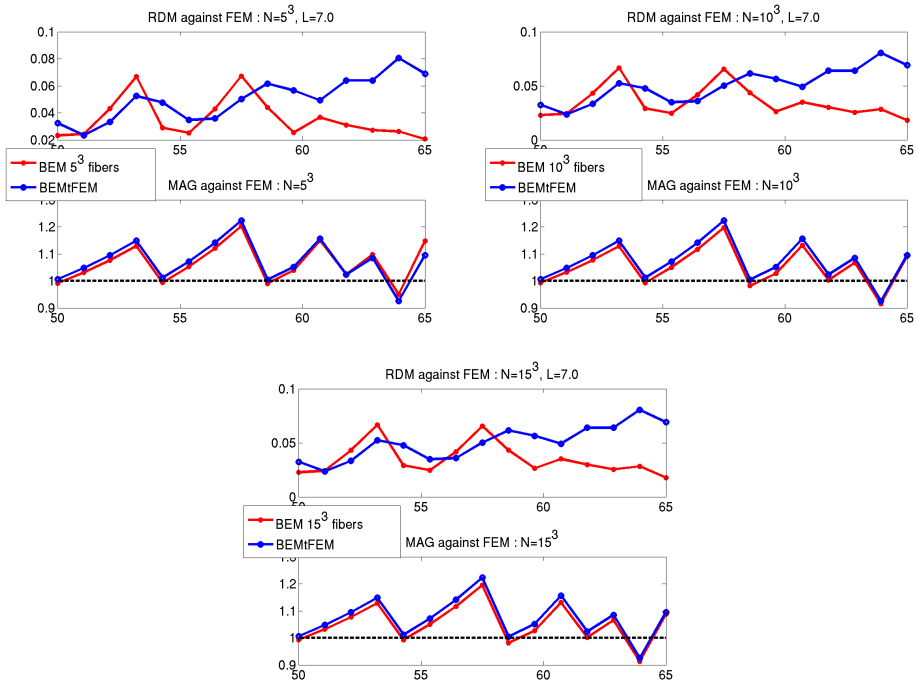

Figure 7.20 – *RDM and MAG values of the BEM with fibers and BEMtFEM compared to the FEM (reference). n varies from* 5,10 *and* 15.

conductivity. Clinical experiments should be designed in such a case, with first a calibration step, which aims at estimating whether or not the electrophysiological model chosen (and the respective conductivities) is in agreement with the experiments. EIT (Electrical Impedance Tomography) or SEP (Somato-sensory Evoked Potential) can be precious tools for this calibration.

Chapter 8

Conclusion

Summary

In this thesis, we focused on the resolution of the MEEG forward problems. MEEG achieve very good temporal resolution, but a relatively poor spatial resolution when compared to other brain imaging modalities (notably fMRI see Fig.(2.9) p.38). Improving this spatial resolution is then critical for the benefit of fine-grained spatio-temporal brain exploration in the future of MEEG. The good resolution of the forward problems aims at improving the comprehension of the electromagnetic behavior of the head. This problem is only part of the computational effort that one must achieve in order to recover the sources within the brain responsible for a measured signal. But the better the forward problem resolution, the better chances one has to get a higher spatial resolution.

We have seen the several numerical methods able to solve this problem in the state of the art exposed in introduction.

In Chapter (3), a method based on the adjoint problem of the forward problem was exposed. This method allows for a smarter (and thus faster) resolution of the forward problem (EEG and MEG) using any numerical method. An application was shown using a BEM; the method was particularly efficient in terms of time and memory consumption, which then allows the problem size to be increased and thus the accuracy of the solution to be improved.

To further improve the forward problem resolution, a domain decomposition framework was studied in chapter (4) in order to split the global computational domain made of several head layers, into smaller domains which could possibly be handled by different numerical solvers. This is particularly interesting, to balance the strengths and weaknesses of each numerical method when dealing with a specific problem or conductivity profile. Alternating between Neumann-Dirichlet boundary value problems, we have applied several coupled schemes in case of BEM-BEM coupling in chapter (5), and later for BEM-FEM coupling in chapter (6). Each method developed was particularly efficient, in terms of accuracy, time and memory consumption. A realistic case showed the gain when using such a coupled method for solving a forward EEG problem.

Finally, chapter (7) introduced a method for dealing with locally anisotropic or inhomogeneous media within a BEM framework. This method improves the accuracy of the forward problem by expanding the range of possible electrophysiological models that can be dealt with the BEM. Furthermore, the representation of the white matter fibers within a BEM framework, thanks to the good resolution of tractography, could be better in terms of precision than the classical conductivity

tensor which is then a more global expression of underlying phenomena. This would need further investigation, and moreover validation with clinicians.

Perspectives

Note that the methods presented independently in each chapter could be combined. Indeed one could think of using the adjoint for the BEM-BEM coupling, or the BEM-FEM coupling with a slightly different coupling scheme. Similarly the handling of local inhomogeneities in the BEM could be used with a BEM-BEM coupling. The author believe that using the adjoint approach with a BEM handling of local inhomogeneities can be achieved.
MEEG devices will play an important role in the future. Even if MEG has quite important constraints when compared to EEG devices, it is nevertheless interesting to study this modality because of its differences with EEG (slightly higher spatial resolution, and allowing for deep source observation). EEG is most surely a device which will keep on interesting scientists, clinicians but also industrials (like game designers), due to its low cost. BCI (Brain Computer Interfaces) are of great interest in several application domains (clinical, ergonomy, games, ...).
Source localization methods have been improving constantly and still are. The community is starting to validate what are good *a-priori* on the solutions sought with their correlations through time and through networks in the brain. The forward problem is the basis of a good inverse problem resolution, and the author believe that a subject-specific calibration step would highly increase its accuracy. Indeed, there are uncertainties about some quantities such as for example the conductivity of the skull or its inhomogeneities. In fact, one can thanks to EIT (Electrical Impedance Tomography) or SEP (Somato-sensory evoked potential) validate some solutions on an electrophysiological model, and estimate some of its parameters. One could design a calibration experiment which would have to be performed before the clinical application, which by using as much *a-priori* information as available, would improve the electrophysiological model for the next experiments. The method exposed in chapter (7) *i.e.* the inhomogeneous/anisotropic BEM is a good candidate, since one could think about placing virtual dipoles at possible inhomogeneities in the skull (like common locations for soft bone), and then run the validation step to estimate the strengths that these virtual dipoles should have. The highest coefficient should correspond to the soft bone compartments.
Furthermore, one could extend this calibration step, so that even subjects whose anatomical MRI is not available (and thus not their head geometry) could benefit from the analysis on template models. For example, one can imagine thanks to 3D reconstruction, that having some sets of pictures of a subject head, a software could estimate its scalp surface, out of which, could be deduced the skull and brain deformation one has apply onto the template model. This would yield EEG source localization methods available for all, without resorting to the painful steps of obtaining the MRI, segmenting it, and meshing the segmented surfaces. One can see

in [Acar and Makeig, 2010], such a possibility for wrapping a template with the sensor locations as input.

Bibliography

[Acar and Makeig, 2010] Acar, Z. and Makeig, S. (2010). Neuroelectromagnetic forward head modeling toolbox. *Journal of neuroscience methods*, 190(2):258–270. 189

[Agoshkov and Lebedev, 1990] Agoshkov, V. and Lebedev, V. (1990). Variational algorithms of the domain decomposition method. *Russian Journal of Numerical Analysis and Mathematical Modelling*, 5(1):27–46. 104, 108

[Akhtari et al., 2002] Akhtari, M., Bryant, H., Mamelak, A., Flynn, E., Heller, L., Shih, J., Mandelkern, M., Matlachov, A., Ranken, D., Best, E., DiMauro, M., Lee, R., and Sutherling, W. (2002). Conductivities of three-layer live human skull. *Brain Topography*, 14(3):151–167. 26, 53

[Alliez et al., 2011] Alliez, P., Rineau, L., Tayeb, S., Tournois, J., and Yvinec, M. (2011). 3D mesh generation. In *CGAL User and Reference Manual*. CGAL Editorial Board, 3.8 edition. http //www.cgal.org/Manual/3.8/doc_html/cgal_manual/packages.html#Pkg Mesh_3. 74

[Bashar et al., 2009] Bashar, M. R., Li, Y., and Wen, P. (2009). Eeg analysis on skull conductivity perturbations using realistic head model. In *Proceedings of the 4th International Conference on Rough Sets and Knowledge Technology*, RSKT '09, pages 208–215, Berlin, Heidelberg. Springer-Verlag. 23, 51

[Basser et al., 2000] Basser, P., Pajevic, S., Pierpaoli, C., Duda, J., and Aldroubi, A. (2000). In vivo fiber tractography using DT-MRI data. *Magnetic Resonance in Medicine*, 44:625–632. 6, 34, 159

[Baumann et al., 1997] Baumann, S., Wozny, D., Kelly, S., and Meno, F. (1997). The electrical conductivity of human cerebrospinal fluid at body temperature. *IEEE Transactions on Biomedical Engineering*, 44(3):220–223. 26, 54

[Baysal and Haueisen, 2004] Baysal, U. and Haueisen, J. (2004). Use of a priori information in estimating tissue resistivities - application to human data in vivo. *Physiol. Meas.*, 25:737–748. 23, 51

[Belgacem, 2004] Belgacem, F. B. (2004). A stabilized domain decomposition method with nonmatching grids for the stokes problem in three dimensions. *SIAM J. Numerical Analysis*, 42(2):667–685. 141, 142

[Ben Belgacem and Maday, 1997] Ben Belgacem, F. and Maday, Y. (1997). The mortar element method for three dimensional finite elements. *Modélisation mathématique et analyse numérique*, 31(2):289–302. 141, 142

[Bénar and Gotman, 2002] Bénar, C. G. and Gotman, J. (2002). Modeling of post-surgical brain and skull defects in the EEG inverse problem with the boundary element method. *Clinical Neurophysiology*, (113):48–56. 71, 153, 162

[Berg and Scherg, 1994] Berg, P. and Scherg, M. (1994). A fast method for forward computation of multiple-shell spherical head models. *Electroencephalogr. Clin. Neurophysiol.*, 90(1):58–64. 56

[Bernardi et al., 1994] Bernardi, C., Maday, Y., and Patera, A. T. (1994). A new nonconforming approach to domain decomposition: the mortar element method. In Pitman, editor, *Nonlinear Partial Differential Equations and Their Applications*, Collège de France Seminar XI, pages 13–51. H. Brezis and J.L. Lions. 140, 141

[Berninger et al., 2007] Berninger, H., Kornhuber, R., and Sander, O. (2007). On nonlinear dirichlet—neumann algorithms for jumping nonlinearities. *Domain Decomposition Methods in Science and Engineering XVI*, pages 489–496. 130

[Bjorstad and Widlund, 1986] Bjorstad, P. and Widlund, O. (1986). Iterative methods for the solution of elliptic problems on regions partitioned into substructures. *SIAM Journal on Numerical Analysis*, pages 1097–1120. 102

[Bonnet, 1995] Bonnet, M. (1995). *Equations intégrales et éléments de frontière*. CNRS Editions, Eyrolles. 62

[Bonnet, 1999] Bonnet, M. (1999). *Boundary Integral Equations Methods for Solids and Fluids*. John Wiley and Sons. 140

[Buzsáki, 2002] Buzsáki, G. (2002). Theta oscillations in the hippocampus. *Neuron*, 33(3):325 – 340. 18, 45

[Clerc et al., 2005a] Clerc, M., Adde, G., Kybic, J., Papadopoulo, T., and Badier, J.-M. (2005a). In vivo conductivity estimation with symmetric boundary elements. In Malmivuo, J., editor, *International Journal of Bioelectromagnetism*, volume 7, pages 307–310. 20, 48

[Clerc et al., 2005b] Clerc, M., Badier, J.-M., Adde, G., Kybic, J., and Papadopoulo, T. (2005b). Boundary element formulation for electrical impedance tomography. In *ESAIM: Proceedings*, volume 14, pages 63–71. EDP Sciences. 64, 81

[Clerc et al., 2011] Clerc, M., Badier, J.-M., Olivi, E., Gramfort, A., and Papadopoulo, T. (2011). Openmeeg for calibrating the conductivity of nested compartment models. In *EIT conference*. v

[Clerc et al., 2010] Clerc, M., Gramfort, A., Olivi, E., and Papadopoulo, T. (2010). The symmetric bem: bringing in more variables for better accuracy. In *Proceedings of Biomag*. v

[Cuffin, 1996] Cuffin, B. (1996). EEG localization accuracy improvements using realistically shaped head models. *IEEE Trans. on Biomed. Engin.*, 43(3). 24, 52

[Dale et al., 1999] Dale, A., Fischl, B., and Sereno, M. (1999). Cortical surface-based analysis I: Segmentation and surface reconstruction. *NeuroImage*, 9:179–194. 25, 52, 72, 152

[Dang and Ng, 2011] Dang, H. V. and Ng, K. T. (2011). Finite difference neuroelectric modeling software. *Journal of Neuroscience Methods*, 198(2):359 – 363. 59, 69

[Dannhauer et al., 2010] Dannhauer, M., Lanfer, B., Wolters, C. H., and Knösche, T. (2010). Modeling of the human skull in eeg source analysis. *Human Brain Mapping*. doi: 10.1002/hbm.21114. 27, 54, 146, 162

[Darvas et al., 2006] Darvas, F., Ermer, J., Mosher, J., and Leahy, R. (2006). Generic head models for atlas-based eeg source analysis. *Human brain mapping*, 27(2):129–143. 25, 52

[De Munck, 1988] De Munck, J. C. (1988). The potential distribution in a layered anisotropic spheroidal volume conductor. *J. Appl. Phys*, 64(2):464–470. 24, 52

[Descoteaux et al., 2009] Descoteaux, M., Deriche, R., Knosche, T. R., and Anwander, A. (2009). Deterministic and probabilistic tractography based on complex fibre orientation distributions. *IEEE Transactions in Medical Imaging*, 28(2):269–286. 6, 34

[Fischer et al., 2000] Fischer, G., Tilg, B., Modre, R., Huiskamp, G. J. M., Fetzer, J., Rucker, W., and Wach, P. (2000). A bidomain model based bem-fem coupling formulation for anisotropic cardiac tissue. *Annals of Biomedical Engineering*, 28(10):1229–1243. 10.1114/1.1318927. 99

[Fischl et al., 1999] Fischl, B., Sereno, M., and Dale, A. (1999). Cortical surface-based analysis II : Inflation, flattening, and a surface-based coordinate system. *Neuroimage*, 9(2):195–207. 25, 52

[Gabriel et al., 1996a] Gabriel, C., Gabriel, S., and Corthout, E. (1996a). The dielectric properties of biological tissues: I. literature survey. *Physics in Medicine and Biology*, 41:2231–2249. 26, 54

[Gabriel et al., 1996b] Gabriel, S., Lau, R., and Gabriel, C. (1996b). The dielectric properties of biological tissues: Ii. measurements in the frequency range 10 hz to 20 ghz. *Physics in Medicine and Biology*, 41:2251–2269. 21, 26, 48, 54

[Geddes and Baker, 1967] Geddes, L. and Baker, L. (1967). The specific resistance of biological material—a compendium of data for the biomedical engineer and physiologist. *Medical and Biological Engineering and Computing*, 5:271–293. 10.1007/BF02474537. 160

[Geselowitz, 1967] Geselowitz, D. B. (1967). On bioelectric potentials in an inhomogeneous volume conductor. *Biophysics Journal*, 7:1–11. 62

[Geselowitz, 1970] Geselowitz, D. B. (1970). On the magnetic field generated outside an inhomogeneous volume conductor by internal volume currents. *IEEE Trans. Magn.*, 6:346–347. 57

[Ghez and Fahn, 1985] Ghez, C. and Fahn, S. (1985). The cerebellum. *Principles of Neural Science, 2nd edition*, (2):502–522. 4, 32

[Gonçalves et al., 2003] Gonçalves, S., de Munck, J., Verbunt, J., Heethaar, R., and Lopes da Silva, F. (2003). In vivo measurement of the brain and skull resistivities using an EIT-based method and the combined analysis of SEF/SEP data. *IEEE Transactions on Biomedical Engineering*, 50(9):1124–1128. 27, 54

[Gramfort et al., 2008] Gramfort, A., Papadopoulo, T., Cottereau, B., Baillet, S., and Clerc, M. (2008). Tracking cortical activity with spatio-temporal constraints using graph-cuts. In *Biomag*. 20, 47

[Gramfort et al., 2010] Gramfort, A., Papadopoulo, T., Olivi, E., and Clerc, M. (2010). OpenMEEG: opensource software for quasistatic bioelectromagnetics. *BioMedical Engineering OnLine*, 9(45). v, 70, 76

[Gramfort et al., 2011] Gramfort, A., Papadopoulo, T., Olivi, E., and Clerc, M. (2011). Forward field computation with OpenMEEG. *Computational Intelligence and Neuroscience*. v, 77

[Gullmar et al., 2006] Gullmar, D., Haueisen, J., Eiselt, M.and Giessler, F., Flemming, L., Anwander, A., Knosche, T., Wolters, C., M., D., D., T., and J., R. (2006). Influence of anisotropic conductivity on EEG source reconstruction: investigations in a rabbit model. *IEEE Trans. on Biomed. Engin.*, 53(9):1841–1850. 160

[Hämäläinen et al., 1993] Hämäläinen, M., Hari, R., IImoniemi, R. J., Knuutila, J., and Lounasmaa, O. V. (1993). Magnetoencephalography— theory, instrumentation, and applications to noninvasive studies of the working human brain. *Reviews of Modern Physics*, 65(2):413–497. 13, 19, 21, 41, 46, 48

[Hämäläinen and Sarvas, 1989] Hämäläinen, M. S. and Sarvas, J. (1989). Realistic conductivity geometry model of the human head for interpretation of neuromagnetic data. *IEEE Trans. Biomed. Eng.*, 36(2):165–171. 62

[Haueisen et al., 2002] Haueisen, J., Tuch, D., Ramon, C., Schimpf, P., Wedeen, V., George, J., and Belliveau, J. (2002). The influence of brain tissue anisotropy on human EEG and MEG. *NeuroImage*, 15:159–166. 160, 161

[Hédou, 1997] Hédou, V. (1997). *Méthodes Numériques pour la Modélisation Electro-anatomique du Cerveau*. PhD thesis, Université de Rennes I. 56

[Hédou-Rouillier, 1999] Hédou-Rouillier, V. (1999). Realistic three-dimensional finite difference model of the human head: development and validation of electric potential computation. Technical Report 99.9, Université de Technologie de Compiègne. 59

[Hoekema et al., 2003] Hoekema, R., Wieneke, G., Leijten, F., van Veelen, C., van Rijen, P., Huiskamp, G., Ansems, J., , and van Huffelen, A. (2003). Measurement of the conductivity of skull, temporarily removed during epilepsy surgery. *Brain Topography*, 16(1):29–38. 26, 54

[Huang et al., 1999] Huang, M., Mosher, J., and Leahy, R. (1999). A sensor-weighted overlapping-sphere head model and exhaustive head model comparison for MEG. *Physics in Medicine and Biology*, 44:423. 25, 52

[Huiskamp et al., 1999] Huiskamp, G., Vroeijenstijn, M., van Dijk, R., Wieneke, G., and van Huffelen, A. C. (1999). The need for correct realistic geometry in the inverse EEG problem. *IEEE Trans. on Biomed. Engin.*, 46(11):1281–1287. 24, 52

[Kandel et al., 2000] Kandel, E., Schwartz, J., and Jessel, T. (2000). *Principles of Neural Science*. McGraw-Hill, 4th edition. 1, 29

[Kariotou, 2004] Kariotou, F. (2004). Electroencephalography in ellipsoidal geometry. *J. Math. Anal. Appl.*, (290):324–42. 24, 52

[Kybic et al., 2005] Kybic, J., Clerc, M., Abboud, T., Faugeras, O., Keriven, R., and Papadopoulo, T. (2005). A common formalism for the integral formulations of the forward eeg problem. *IEEE Transactions on Medical Imaging*, 24:12–28. 62, 63, 64

[Kybic et al., 2006] Kybic, J., Clerc, M., Faugeras, O., Keriven, R., and Papadopoulo, T. (2006). Generalized head models for MEG/EEG: boundary element method beyond nested volumes. *Physics in Medicine and Biology*, 51:1333–1346. 26, 54, 64, 65, 71, 153, 162

[Lai et al., 2005] Lai, Y., Van Drongelen, W., Ding, L., Hecox, K., Towle, V., Frim, D., and He, B. (2005). Estimation of in vivo human brain-to-skull conductivity ratio from simultaneous extra- and intra-cranial electrical potential recordings. *Clinical neurophysiology*, 116(2):456–465. 23, 26, 51, 54

[Lalancette et al., 2011] Lalancette, M., Quraan, M., and Cheyne, D. (2011). Evaluation of multiple-sphere head models for MEG source localization. *Physics in Medicine and Biology*. 25, 52, 68

[Lions, 1989] Lions, P. (1989). On the schwarz alternating method iii: a variant for nonoverlapping subdomains. In *Third International Symposium on Domain Decomposition Methods for Partial Differential Equations, held in Houston, Texas*, pages 20–22. 98, 103

[Malmivuo, 1980] Malmivuo, J. (1980). Distribution of m.e.g. detector sensitivity: an application of reciprocity. *Medical and Biological Engineering and Computing*, 18(3):365–370. 81

[Marini and Quarteroni, 1987] Marini, L. and Quarteroni, A. (1987). *An iterative procedure for domain decomposition methods: a finite element approach.* Ist., Consiglio. 102

[Marini and Quarteroni, 1989] Marini, L. and Quarteroni, A. (1989). A relaxation procedure for domain decomposition methods using finite elements. *Numerische Mathematik*, 55(5):575–598. 102

[Meijs and Peters, 1987] Meijs, J. W. H. and Peters, M. (1987). The eeg and meg using a model of eccentric spheres to describe the head. *IEEE Transactions on Biomedical Engineering*, 34:913–920. 24, 51

[Meijs et al., 1989] Meijs, J. W. H., Weier, O. W., Peters, M. J., and van Oosterom, A. (1989). On the numerical accuracy of the boundary element method. *IEEE Trans. Biomed. Eng.*, 36:1038–1049. 72

[Mori et al., 1999] Mori, S., Crain, B., Chacko, V., and Zijl, P. V. (1999). Three-dimensional tracking of axonal projections in the brain by Magnetic Resonance Imaging. *Annals of Neurology*, 45(2):265–269. 6, 34, 159

[Murakami and Okada, 2006] Murakami, S. and Okada, Y. (2006). Contributions of principal neocortical neurons to magnetoencephalography and electroencephalography signals. *The Journal of Physiology*, 575(3):925–936. 12, 13, 40, 41

[Nédélec, 2001] Nédélec, J.-C. (2001). *Acoustic and Electromagnetic Equations.* Springer Verlag. 60, 62

[Nolte, 2003] Nolte, G. (2003). The magnetic lead field theorem in the quasi-static approximation and its use for magnetoencephalography forward calculation in realistic volume conductors. *Physics in Medicine and Biology*, 48:3637–3652. 83

[Nunez, 1981] Nunez, P. (1981). *Electric fields of the brain.* Oxford University Press. 19, 46

[Olivi, 2007] Olivi, E. (2007). Comparaisons quantitatives de résultats de problème direct eeg. Research Report 6364, INRIA. 69

[Olivi et al., 2010a] Olivi, E., Clerc, M., and Papadopoulo, T. (2010a). Domain decomposition for coupling finite and boundary element methods in eeg. In *Proceedings of Biomag.* iv

[Olivi et al., 2010b] Olivi, E., Clerc, M., and Papadopoulo, T. (2010b). Domain decomposition for coupling finite and boundary element methods with non-matching grids in electro-encephalography. In *Proceedings of ECCM.* iv

[Olivi et al., 2011a] Olivi, E., Clerc, M., and Papadopoulo, T. (2011a). Handling white-matter anisotropy in bem for the eeg forward problem. In *Proceedings of ISBI*. v, 164

[Olivi et al., 2007] Olivi, E., Clerc, M., Yvinec, M., and Papadopoulo, T. (2007). Quantitative comparisons of forward problems in MEEG. Research Report 6364, INRIA. v

[Olivi et al., 2011b] Olivi, E., Gramfort, A., Papadopoulo, T., and Clerc, M. (2011b). Adjoint method for lead-fields computation in MEEG. In *HBM'2011*, Québec City, Canada. OHBM. POSTER. v

[Oostenveld and Oostendorp, 2002] Oostenveld, R. and Oostendorp, T. F. (2002). Validating the boundary element method for forward and inverse EEG computations in the presence of a hole in the skull. *Human Brain Mapping*, (17):192–192. 71, 153, 162

[Papadopoulo et al., 2006] Papadopoulo, T., Vallaghé, S., and Clerc, M. (2006). Implicit meshes for meg/eeg forward problem with 3d finite element method. In *Proceedings of the Biomag conference*. 68

[Papadopoulo et al., 2010] Papadopoulo, T., Vallaghé, S., and Clerc, M. (2010). The adjoint method for general eeg and meg sensor-based lead field equations. In *Proceedings of Biomag*. 85

[Piovano and Papadopoulo, 2008] Piovano, J. and Papadopoulo, T. (2008). Global region segmentation based on local statistics. In *Proceedings of the 10th European Conference on Computer Vision*, volume 5305 of *Lecture Notes in Computer Science*, pages 486–499. Springer–Verlag. 72

[Plonsey, 1963] Plonsey, R. (1963). Reciprocity applied to volume conductors and the ECG. *IEEE Trans. on Biomed. Engin.*, 10(1):9–12. 81

[Quarteroni and Valli, 1999] Quarteroni, A. and Valli, A. (1999). *Domain Decomposition Methods for Partial Differential Equations*. Oxford University Press, Oxford, UK. 99, 101, 102, 103, 107, 112, 140

[Ramon et al., 2006] Ramon, C., Haueisen, J., and Schimpf, P. (2006). Influence of head models on neuromagnetic fields and inverse source localizations. *BioMedical Engineering OnLine*, 5(55). 26, 53

[Rineau and Yvinec, 2011] Rineau, L. and Yvinec, M. (2011). 3D surface mesh generation. In *CGAL User and Reference Manual*. CGAL Editorial Board, 3.8 edition. 74, 144

[Rush and Driscoll, 1968] Rush, S. and Driscoll, D. (1968). Current distribution in the brain from surface electrodes. *Anesthesia and Analgesia*, 47:717–723. 24, 51

[Rush and Driscoll, 1969] Rush, S. and Driscoll, D. (1969). Eeg electrode sensitivity - an application of reciprocity. *IEEE Transactions on Biomedical Engineering*, 16(1):15–22. 81

[Ryynänen et al., 2004] Ryynänen, O., Hyttinen, J., Laarne, P., and Malmivuo, J. (2004). Effect of electrode density and measurement noise on the spatial resolution of cortical potential distribution. *IEEE Transactions on Biomedical Engineering*, 51(9):1547–1554. 20, 47

[Sarvas, 1987] Sarvas, J. (1987). Basic mathematical and electromagnetic concepts of the biomagnetic inverse problem. *Phys. Med. Biol.*, 32(1):11–22. 57, 58

[Shewchuk, 2002a] Shewchuk, J. (2002a). What is a good linear finite element ? In *Interpolation, conditioning, anisotropy and quality measures. unpublished preprint.* 73

[Shewchuk, 2002b] Shewchuk, J. (2002b). What is a good linear finite element? interpolation, conditioning, anisotropy, and quality measures (preprint). *University of California at Berkeley.* 73

[Shimony et al., 1999] Shimony, J. S., McKinstry, R. C., Akbudak, E., Aronovitz, J. A., Snyder, A. Z., Lori, N. F., Cull, T. S., and Conturo, T. E. (1999). Quantitative diffusion-tensor anisotropy brain mr imaging: Normative human data and anatomic analysis. *Radiology*, 212(3):770–784. 159, 160

[Spinelli et al., 2000] Spinelli, L., Andino, S., Lantz, G., Seeck, M., and Michel, C. (2000). Electromagnetic inverse solutions in anatomically constrained spherical head models. *Brain Topography*, 13(2):113–125. 24, 52

[Taheri et al., 1994] Taheri, B. A., Knight, R. T., and Smith, R. L. (1994). A dry electrode for eeg recording. *Electroencephalography and Clinical Neurophysiology*, 90(5):376 – 383. 15, 42

[Tuch et al., 2001] Tuch, D., Wedeen, V., Dale, A., George, J., and Belliveau, J. (2001). Conductivity tensor mapping of the human brain using diffusion tensor MRI. In *Proceedings of the National Academy of Sciences*, volume 98, pages 11697–11701. 159, 160

[Vallaghé and Clerc, 2009] Vallaghé, S. and Clerc, M. (2009). A global sensitivity analysis of three and four-layer eeg conductivity models. *IEEE Transactions on Biomedical Engineering*, 56(4):988–995. 27, 54, 146

[Vallaghé and Papadopoulo, 2010] Vallaghé, S. and Papadopoulo, T. (2010). A trilinear immersed finite element method for solving the electroencephalography forward problem. *SIAM Journal on Scientific Computing*, 32(4):2379–2394. 68

[Vallaghé et al., 2009] Vallaghé, S., Papadopoulo, T., and Clerc, M. (2009). The adjoint method for general eeg and meg sensor-based lead field equations. *Physics in Medicine and Biology*, 54:135–147. 85

[Van Uitert and Johnson, 2002] Van Uitert, R. and Johnson, C. (2002). Can a spherical model substitute for a realistic head model in forward and inverse MEG simulations? In *Proceedings of BIOMAG*. 25, 52, 68

[Wang and Denda, 2007] Wang, C.-Y. and Denda, M. (2007). 3d bem for general anisotropic elasticity. *International Journal of Solids and Structures*, 44(22-23):7073 – 7091. 162

[Wang et al., 2008] Wang, K., Zhu, S., Mueller, B., Lim, K., Liu, Z., and He, B. (2008). A new method to derive white matter conductivity from diffusion tensor mri. *IEEE Trans Biomed Eng*, 55(10):2481–6. 159

[Weinstein et al., 2000] Weinstein, D., Zhukov, L., and Johnson, C. (2000). Lead-field bases for electroencephalography source imaging. *Annals of Biomedical Engineering*, 28(9):1059–1164. 83

[Wohlmuth, 2001] Wohlmuth, B. (2001). *Discretization methods and iterative solvers based on domain decomposition*, volume 17. Springer Verlag. 112

[Wolters et al., 2007] Wolters, C., Anwander, A., Berti, G., and Hartmann, U. (2007). Geometry-adapted hexahedral meshes improve accuracy of finite-element-method-based eeg source analysis. *Biomedical Engineering, IEEE Transactions on*, 54(8):1446–1453. 69

[Wolters et al., 2006] Wolters, C. H., Anwander, A., Tricoche, X., Weinstein, D., Koch, M. A., and MacLeod, R. (2006). Influence of tissue conductivity anisotropy on EEG/MEG field and return current computation in a realistic head model: A simulation and visualization study using high-resolution finite element modeling. *NeuroImage*, (3):813–826. 70, 155, 159, 160

[Zhang, 1995] Zhang, Z. (1995). A fast method to compute surface potentials generated by dipoles within multilayer anisotropic spheres. *Phys. Med. Biol.*, 40:335–349. 56, 68, 72, 146